

BLDSC no: DX 205936



Pilkington Library

Author/Filing Title ALCOCK, R.D.

Accession/Copy No. 040165840

| | |
|---------------|------------------|
| Vol. No. | Class Mark |
|---------------|------------------|

LOAN COPY

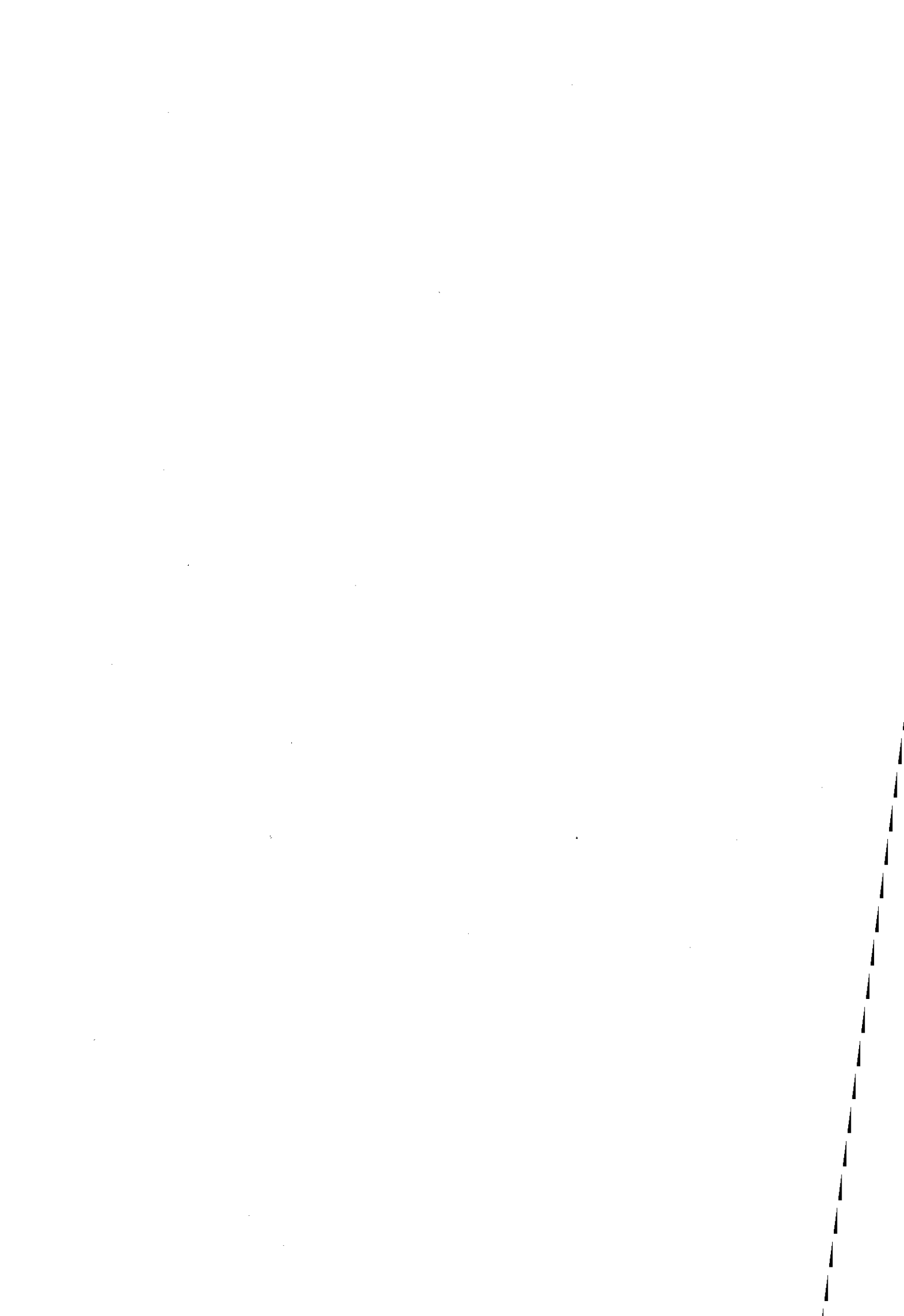
~~FOR REFERENCE ONLY~~

FOR REFERENCE ONLY

0401658406



BADMINTON PRESS
UNIT 1 BROOK ST
SYSTEM
LEICESTER LE7 1GD
ENGLAND
TEL : 0116 260 2917
FAX : 0116 269 6639



Transducers for Measuring Acoustic Transients

by


Robin Alcock, B.Sc.

A Doctoral Thesis

Submitted in Partial Fulfilment of the Requirements
for the Award of Doctor of Philosophy of
Loughborough University

August 1997

© R Alcock 1997

| |
|---|
|  Loughborough University Library |
| Date June 98 |
| Class |
| Acc No. 040165840 |

K0630304

To my wife, my parents,
and God

Acknowledgements

Throughout the many months of work put into this thesis there has been one person in particular that has given me a great deal of advice and encouragement. I would therefore first like to thank my project supervisor, Dr David Emmony, for all the time and energy he has put into guiding me and his continued commentary on the use of a spell checker.

I would like to acknowledge the considerable support given to me by the Physics Department technical staff, particularly John Oakley, Chaz and Raj for their equipment acquisition and construction skills. Thanks must also be given to my current employer, Dr Jeremy Coupland, who has been very understanding allowing me considerable time off for not only a round-the-world honeymoon trip, but also to finish this thesis.

During the years that I have spent in Loughborough, Dr Carl Sayer has provided me with many excuses to stop working on this thesis, especially to go out reservoir sampling around the Peak District. As a result I would fervently like to express my deep satisfaction for following his advice and keeping some sanity. Finally I would like to thank my wife, Ellen, for providing me with support, patience, and a constant flow of food and drinks during the final few months of this project.

Abstract

This thesis is concerned with the design and development of measuring devices for the characterisation of acoustic transients with high temporal and spatial resolution. Three new techniques are demonstrated characterising acoustic transients generated by Nd-YAG laser (1060nm, 30ns, 55mJ) assisted breakdown of water and air.

The first technique demonstrates the use of a high power semiconductor laser in a high speed multiple exposure imaging system. This system developed is capable of illuminating an event with up to 10 pulses of light at a maximum repetition rate of 5MHz, with a timing accuracy of ~5ns. Each semiconductor laser light pulse has a FWHM duration of 50ns, peak power of 30W, and a wavelength of 860nm. Images of individual acoustic transients are displayed on the same CCD camera frame, and it was found that this is best achieved using a dark field imaging technique such as Schlieren imaging.

The second technique described utilises the perturbations in the refractive index of water with pressure to give a measurable change in the reflectivity of light at a water-glass interface. High sensitivity is achieved by measuring the reflectivity of a probe light beam which is incident close to the critical angle for total internal reflection. The transducer has been demonstrated experimentally to be particularly useful for investigating optical cavitation in water, and has a temporal resolution of about 1ns, minimum resolvable pressure of 20bar, and a small sensitive area of 20x80 μ m.

Finally the third technique uses a large area planar piezoelectric transducer to measure the temporal pressure profile of spherically symmetric acoustic transients propagating in water. The technique addresses the problem of characterising acoustic transients that originate from sources which are small compared with the measuring device. An algorithm for deconvolving the temporal pressure profile from the output voltage of large area piezoelectric transducers has been derived, and the technique has been found to yield good results when the piezoelectric film is thin. Finally, the technique has been demonstrated resolving the sub 10ns rise time of shock fronts associated with optical cavitation.

Contents

| | Page |
|--|----------|
| Chapter One - Introduction | 1 |
| Chapter Two - The Generation and Detection of Acoustic Transients | 3 |
| Introduction | 3 |
| 2.1 - An introduction to acoustic transients | 3 |
| 2.1.1 - The equations of motion | 4 |
| 2.1.2 - The acoustic wave equation | 6 |
| 2.1.3 - Boundary conditions and co-ordinate systems | 9 |
| 2.1.4 - Non-linear effects and shock waves | 13 |
| 2.1.5 - The Rankine-Hugoniot Equations | 15 |
| 2.2 - The generation of acoustic transients | 21 |
| 2.2.1 - Shock tubes | 21 |
| 2.2.2 - High explosives | 24 |
| 2.2.3 - Laser interactions | 28 |
| (i) Gases | 29 |
| (ii) Liquids | 31 |
| (iii) Solids | 33 |
| 2.2.4 - Cavitation | 36 |
| 2.2.5 - Spark discharges | 37 |
| 2.2.6 - Piezoelectric transducers | 39 |
| 2.2.7 - Lithotrippers | 42 |
| 2.3 - The measurement and characterisation of acoustic transients | 44 |
| 2.3.1 - Piezoelectric transducers | 45 |
| 2.3.2 - Optical transducers | 49 |
| 2.3.3 - High speed photography | 55 |
| (i) Flash light sources | 55 |
| (ii) Shuttered cameras | 59 |
| 2.3.4 - Imaging techniques | 61 |
| (i) Shadowgraphy | 62 |
| (ii) Schlieren | 64 |
| (iii) Mach-Zehnder interferometry | 66 |
| (iv) Photoelastic imaging | 67 |
| (v) Holographic imaging | 70 |
| References | 70 |

| | |
|---|-----------|
| Chapter Three - High Speed Semiconductor Laser Photography | 84 |
| Introduction | 84 |
| 3.1 - High speed photography using pulsed semiconductor light sources | 84 |
| 3.2 - The Semiconductor Laser Diode | 87 |
| 3.2.1 - The Semiconductor junction diode | 87 |
| (i) The doping of semiconductor materials | 88 |
| (ii) p-n junctions | 90 |
| (iii) The p-n junction diode under forward bias | 91 |
| 3.2.2 - The light emitting diode | 91 |
| 3.2.3 - Homojunction semiconductor lasers | 95 |
| 3.2.4 - Properties of homojunction lasers | 98 |
| 3.2.5 - Heterojunction semiconductor lasers | 103 |
| 3.3 - Semiconductor laser drive circuitry | 105 |
| 3.3.1 - Single pulse | 105 |
| 3.3.2 - Experimental single pulse set-up | 112 |
| 3.3.3 - Problems with electromagnetic noise | 116 |
| 3.3.4 - Multiple pulse drive circuitry | 117 |
| 3.3.5 - Experimental multiple pulse drive circuit | 120 |
| 3.4 - Collimation Techniques | 121 |
| 3.4.1 - Commercial semiconductor laser collimators | 122 |
| 3.4.2 - Simplified experimental collimation set-up | 126 |
| 3.4.3 - Beam expansion | 130 |
| 3.5 - Imaging onto a CCD camera | 132 |
| 3.5.1 - General principles of charge coupled devices | 132 |
| 3.5.2 - CCD Camera systems | 133 |
| 3.5.3 - Brief calculations | 135 |
| 3.5.4 - Shadowgraphy and schlieren imaging | 137 |
| 3.6 - Synchronisation and timing of the semiconductor laser | 141 |
| 3.6.1 - Analogue delay system | 142 |
| 3.6.2 - Problems with analogue delays | 144 |
| 3.6.3 - Digital delays | 144 |
| 3.7 - Experimental single exposure imaging of laser ablation | 147 |
| 3.7.1 - Shadowgraphy results | 149 |
| 3.7.2 - Schlieren imaging results | 153 |

| | |
|---|------------|
| 3.8 - Multiple pulse imaging of acoustic transients | 154 |
| 3.8.1 - Shadowgraphic imaging of air born transients | 156 |
| 3.8.2 - Schlieren imaging of air born transients | 157 |
| 3.8.3 - Schlieren imaging of optical cavitation | 160 |
| Conclusion | 162 |
| References | 163 |
| | |
| Chapter Four - An Optical Transducer | 166 |
| Introduction | 166 |
| 4.1 - Refractive index transducers | 166 |
| 4.2 - Theory | 168 |
| 4.2.1 - Basic optics | 168 |
| 4.2.2 - Sensitivity of the reflectance | 171 |
| 4.2.3 - Divergent input beams and spatial resolution | 172 |
| 4.3 - The variation of refractive index with temperature and pressure | 174 |
| 4.3.1 - Refractive index relationships of water, perspex and glass | 176 |
| 4.3.2 - The refractive index ratio | 179 |
| 4.3.3 - Acoustic reflection at the interface | 180 |
| 4.4 - Prototype experimental transducer | 181 |
| 4.5 - Calibration | 182 |
| 4.6 - Experiments with the perspex transducer | 184 |
| 4.7 - Measurements made by glass fronted transducer | 189 |
| 4.7.1 - Acoustic transients | 189 |
| 4.7.2 - Negative or rarefaction waves | 191 |
| 4.7.3 - Cavitation bubble phenomena | 193 |
| Conclusions | 200 |
| References | 203 |

| | |
|--|----------------|
| Chapter Five - Large Area Planar Piezoelectric Transducer for Measuring Spherically Symmetric Acoustic Transients | 206 |
| Introduction | 206 |
| 5.1 - The problems of measuring acoustic transients from point sources | 206 |
| 5.2 - Acoustic wave interactions with a large area thin film piezoelectric transducer | 209 |
| 5.2.1 - The path of an acoustic wave from a point source | 211 |
| 5.2.2 - Evaluation of pressure in the high frequency limit | 213 |
| 5.2.3 - Accuracy of the high frequency approximation and piezoelectric materials | 215 |
| 5.2.4 - The transducer function | 217 |
| 5.3 - Computer simulations | 220 |
| 5.3.1 - The discrete form of convolution and deconvolution | 220 |
| 5.3.2 - Other techniques for evaluating a convolution | 221 |
| 5.3.3 - Simulated voltage output of the transducer | 222 |
| 5.3.4 - Deconvolution and the effects of a reduction in measurement accuracy | 225 |
| 5.4 - Experimental set-up | 228 |
| 5.4.1 - The equivalent circuit of a piezoelectric transducer | 230 |
| 5.4.2 - The use of a buffer amplifier | 234 |
| 5.4.2 - Shadowgraphy | 235 |
| 5.5 - Experimental results from 9 μ m thick PVDF transducer | 237 |
| 5.6 - Experimental results from 110 μ m thick PVDF transducer | 243 |
| Conclusions | 247 |
| References | 248 |
| Chapter Six - Conclusions | 251 |
| Appendix One - Digital Timing Circuitry | |
| Appendix Two - Maple Routines | |
| Appendix Three - Photographs | |

Table of Figures

| | page |
|--|------|
| 2.1 - The stresses which act upon an arbitrary uniform medium contained within a rectangular parallelepiped | 5 |
| 2.2 - Propagation of high and low amplitude acoustic transients with time | 5 |
| 2.3 - Properties of a shock front according to Rankine-Hugoniot theory | 16 |
| 2.4 - Pressure waves in simple shock tubes | 22 |
| 2.5 - Explosive detonation model | 22 |
| 2.6 - Laser generated acoustic transients in solids | 35 |
| 2.7 - Lithotripter shock wave generators | 35 |
| 2.8 - Piezoelectric hydrophones | 46 |
| 2.9 - Fibre optic probe hydrophones | 52 |
| 2.10 - Diode laser acoustic sensor | 52 |
| 2.11 - Experimental arrangement for schlieren probe method | 52 |
| 2.12 - Spark light sources | 56 |
| 2.13 - The basic principles of a L.A.S.E.R. | 56 |
| 2.14 - Multiple pulse photography | 56 |
| 2.15 - Cameras for high speed photography | 60 |
| 2.16 - Refraction of a light ray through a refractive index gradient | 63 |
| 2.17 - Direct shadowgraphy, where a parallel beam of light is disturbed by changes in the refractive index of the system | 63 |
| 2.18 - Example high speed photographs of shock waves at the focus of a lithotripter | 63 |
| 2.19 - Examples of schlieren imaging apparatus | 65 |
| 2.20 - Example high speed photographs examining the interaction of acoustic transients created by optical cavitation at a water-polycarbonate boundary | 65 |
| 2.21 - High speed photography using a Mach-Zehnder interferometer | 68 |
| 2.22 - Holographic interferometry of acoustic transients | 68 |
| 3.1 - Impurities in silicon | 89 |
| 3.2 - Schematic representation of a p-n junction | 89 |
| 3.3 - Forward biased p-n junction | 89 |
| 3.4 - Injection of minority carriers and subsequent recombination with majority carriers in a forward biased p-n junction | 93 |
| 3.5 - Interband transitions | 93 |
| 3.6 - Impurity centre recombinations | 93 |
| 3.7 - The light emitting diode | 93 |

| | |
|--|-----|
| 3.8 - Heavily doped p-n junction diode laser | 97 |
| 3.9 - Active region of a diode laser and cleaved planes | 97 |
| 3.10 - Electron levels in lasers | 97 |
| 3.11 - Diode laser band structure at the p-n junction | 99 |
| 3.12 - Radiant output intensity for a p-n junction semiconductor laser | 99 |
| 3.13 - Axial modes in a laser | 99 |
| 3.14 - Transverse modes | 102 |
| 3.15 - Output beam spread of a diode laser | 102 |
| 3.16 - The effect of an increase in temperature on the output of a diode laser | 102 |
| 3.17 - Hetrojunction lasers | 104 |
| 3.18 - Typical differences in output power between junction types | 104 |
| 3.19 - LJ30 pulsed laser diode typical characteristics and absolute ratings | 106 |
| 3.20 - SMP60N06-18 M.O.S.F.E.T. specifications | 106 |
| 3.21 - Standard drive circuit for high power pulsed diode laser | 108 |
| 3.22 - Pulsed laser drive circuit using MOSFET as a fast switch | 108 |
| 3.23 - The L-C-R approximation of the MOSFET diode laser driver circuit | 108 |
| 3.24 - Voltages measured from single pulse diode laser driver | 113 |
| 3.25 - Light pulse output of diode laser measured by photodiode | 115 |
| 3.26 - Multipulse timing control circuitry and diode laser controller schematics | 115 |
| 3.27 - Diode laser drive circuit | 119 |
| 3.28 - The optical output of the multi-pulsed semiconductor laser in comparison to the drive potential | 119 |
| 3.29 - Standard collimation methods, correcting astigmatism with a weak cylindrical lens | 123 |
| 3.30 - Geometric interpretation of the effects of a lens on the astigmatic output of the diode laser | 123 |
| 3.31 - Methods for the correction of the elliptical output from a semiconductor laser, where the correcting optics are placed in the minor plane | 125 |
| 3.32 - Energy transmission of commercial optical materials for 10mm thick window | 125 |
| 3.33 - Experimental collimation set-up used with the semiconductor laser | 125 |
| 3.34 - Collimation method | 128 |
| 3.35 - Image seen on CCD camera during stage I of semiconductor laser experimental collimation | 129 |
| 3.36 - Image seen by CCD camera during stage II of experimental collimation of diode laser | 129 |
| 3.37 - Laser diode collimation stage III, CCD camera image taken at the focus of a 50mm f/2.4 camera lens, with 0.072 filter attenuating the beam of light | 131 |

| | |
|---|-----|
| 3.38 - Output beam of collimated diode laser as seen by CCD camera, showing cross-section that is roughly circular approx. 5mm in diameter | 131 |
| 3.39 - Beam expansion set-up | 131 |
| 3.40 - The basic construction and operation of a CCD camera | 134 |
| 3.41 - CCD camera arrangements for reducing image smear | 134 |
| 3.42 - C.C.I.R. standard composite video signal | 136 |
| 3.43 - Scene illuminance | 136 |
| 3.44 - Response of the human eye | 136 |
| 3.45 - Typical response of CCD camera | 136 |
| 3.46 - Experimental schlieren and shadowgraphy set-up | 139 |
| 3.47 - Positioning of the schlieren knife edge | 139 |
| 3.48 - Adjustment of the knife edge in the focal plane of the imaging lens, going from shadowgraphy to schlieren imaging | 139 |
| 3.49 - Synchronisation between CCD camera, event, diode laser and frame grabber | 143 |
| 3.50 - Schematics of an analogue control system | 143 |
| 3.51 - Pre-delay after CCD camera synchronisation pulse | 143 |
| 3.52 - Analogue delay circuitry | 143 |
| 3.53 - Problems with E-M noise and analogue delays | 145 |
| 3.54 - Schematic representation of a digital delay system | 145 |
| 3.55 - The diode laser schlieren imaging system | 148 |
| 3.56 - Use of fibre optic photodetector for timing of output light pulses | 148 |
| 3.57 - Shadowgraphs taken of air born acoustic transients created by dye laser ablation, using single shot semiconductor laser imaging system | 150 |
| 3.58 - Average radius of air-born acoustic transient generated by laser ablation | 151 |
| 3.59 - Schlieren imaging of air shocks using single pulse laser diode illumination | 151 |
| 3.60 - Experimental set-up for multiple pulse semiconductor laser high speed photography | 155 |
| 3.61 - Semiconductor laser shadowgraphy in air | 155 |
| 3.62 - Schlieren imaging of air shocks with multiple pulse diode laser | 158 |
| 3.63 - Schlieren imaging of water shocks | 158 |
| 4.1 - Fresnel reflectance with incidence angle for Perspex-Water interface | 170 |
| 4.2 - Sensitivity of reflectance to changes in n for Perspex-Water interface | 170 |
| 4.3 - Angular spread | 173 |
| 4.4 - Reflectance for Perspex-Water interface varying with angular spread | 173 |
| 4.5 - Sensitivity of reflectance to angular spread for Perspex-Water interface | 173 |
| 4.6 - Refractive index variations with temperature and pressure for water | 177 |
| 4.7 - Refractive index variations with pressure for Perspex and Glass | 177 |

| | | |
|------|--|-------|
| 4.8 | - Calculated relative refractive index as a function of acoustic pressure | 178 |
| 4.9 | - Experimental set-up of Fresnel reflection transducer | 178 |
| 4.10 | - CW laser diode driver, monitor and detector photodiodes | 183 |
| 4.11 | - Calibration using measured reflectance with NaCl solution concentration | 183 |
| 4.12 | - Calculated reflectance as a function of acoustic pressure | 183 |
| 4.13 | - Perspex opto-transducer varying distance from event | 185 |
| 4.14 | - Expansion of figure 4.13 showing fast shock rise times | 185 |
| 4.15 | - Log scale plot of peak pressure recorded with acoustic transient radius | 187 |
| 4.16 | - The effect of acoustic wavefront curvature on the transducer time response | 187 |
| 4.17 | - Effects when source laser light strikes perspex transducer | 187 |
| 4.18 | - Glass opto-transducer varying distance from event | 190 |
| 4.19 | - Expansion of figure 4.18 showing fast shock rise times | 190 |
| 4.20 | - Reflection of acoustic transients off of water-air and water-copper boundaries | 192 |
| 4.21 | - Bubble detection at varying distances from the source | 195-6 |
| 4.22 | - Detection of acoustic transients during the 1st collapse of cavitation bubbles | 197 |
| 4.23 | - Improved design Fresnel reflection acoustic transient using glass equilateral prism | 202 |
| 5.1 | - Problems associated with the measurement of spherically shaped acoustic transients generated by optical cavitation | 208 |
| 5.2 | - Schematic diagram of the interaction between a spherically shaped acoustic transient and a piezoelectric transducer | 208 |
| 5.3 | - Acoustic transmission and reflection for waves with spherical symmetry at a boundary between two media | 208 |
| 5.4 | - Geometric wave approximation at boundary between two media | 216 |
| 5.5 | - Acoustic wave path predictions for a point source close to a boundary, using both geometric and wave equation approximations | 216 |
| 5.6 | - The transducer function in terms of the parameter τ | 219 |
| 5.7 | - Simulated voltage output for a 9 μ m thick transducer with varying step pressure pulse durations | 219 |
| 5.8 | - Simulated voltage output for a 9 μ m thick transducer with varying distance between point source and transducer | 219 |
| 5.9 | - Simulated voltage output of transducers with different film thicknesses | 224 |
| 5.10 | - Simulated voltage output for a 110 μ m thick transducer with varying step pressure pulse durations | 224 |
| 5.11 | - Simulated voltage output of a 110 μ m thick transducer with varying | |

| | |
|--|-----|
| distance between point source and transducer | 224 |
| 5.12 - Simulated problems associated with the deconvolution of a 'measured' voltage | 226 |
| 5.13 - As in figure 5.12 but for a 110 μ m thick piezoelectric transducer, showing an increase in noise during the calculation of the pressure profile from a voltage waveform with low resolution | 227 |
| 5.14 - Increasing number of applications of a least squares graduation formula reduces high frequency noise, but affects the temporal response of the transducer | 229 |
| 5.15 - Increasing the number of points used in smoothing formula reduces noise further, however it affects the temporal response of the transducer greatly | 229 |
| 5.16 - Experimental set-up for a PVDF thin film transducer measuring spherical acoustic transients from an optical cavitation event | 231 |
| 5.17 - Equivalent circuit of a PVDF film transducer connected to an amplifier | 231 |
| 5.18 - Experimental set-up for simultaneous high speed photography | 231 |
| 5.19 - Shadowgraph of the initial acoustic transient from optical cavitation event | 236 |
| 5.20 - Stages in the rise and fall of the output voltage | 236 |
| 5.21 - Results from experiment with 9 μ m PVDF film transducer placed 4mm away from the source of an optical cavitation event | 238 |
| 5.22 - Results from experiment with 9 μ m PVDF film transducer placed 2mm away from the source of an optical cavitation event | 240 |
| 5.23 - Results from experiment with 9 μ m PVDF film transducer placed 1mm away from the source of an optical cavitation event | 242 |
| 5.24 - Results from experiment with 110 μ m, 12.5mm ϕ PVDF film transducer placed 1mm away from the source of an optical cavitation event | 244 |
| | |
| A1.1 - Power Supply | |
| A1.2 - Video sync. separation and detection circuit with optical isolator | |
| A1.3 - External trigger switch arrangement | |
| A1.4 - Pre-delay and pulse shaping | |
| A1.5 - Fibre optic and opto isolated outputs | |
| A1.6 - Digital delay circuit | |
| A1.7 - BCD thumbwheel switches | |
| A1.8 - Multiple pulse timing circuitry | |
| A3.1 - Photograph of the prototype perspex semicircular optical transducer | |
| A3.2 - Photograph of the large area piezoelectric transducer with the high impedance amplification electronics attached | |

List of Tables

| | |
|---|-----|
| 2.1 - Typical values of the speed of elastic waves in materials | 5 |
| 2.2 - Commercially available pulsed lasers capable of generating acoustic transient | 22 |
| 2.3 - Properties of several piezoelectric materials | 46 |
| 4.1 - Refractive index properties of Water, Perspex and Glass | 178 |
| 5.1 - Graduation and smoothing formulae | 227 |

Chapter One

Introduction

The study of acoustic transients has over the last century or so been of great interest. Acoustic transients are generated in a large number of naturally occurring events, ranging in size from the large "crack" of thunder heard during lightning strikes, to the minute acoustic emissions made during the collapse of small bubbles around propeller blades. Different sources give rise to acoustic transients with somewhat different spatial and temporal pressure distributions. These characteristics can change considerably during the propagation of the acoustic transients, and under certain circumstances the transients can develop into shock waves. Although theoretical models exist for many sources, they are often inaccurate. It is therefore often necessary to measure acoustic transients in order to characterise the physical nature of their source. This thesis is concerned with the design of acoustic transient measuring devices with high spatial and temporal resolutions.

In the next chapter, which is entitled *The Generation and Detection of Acoustic Transients*, the basic theory of acoustic transients is outlined. A discussion then follows on the many different methods which can be used to generate acoustic transients under controlled conditions within the laboratory. The chapter finishes with a review of the numerous techniques that have been previously employed to measure acoustic transients, and covers high speed photography and probe transducers.

Chapter three, *High Speed Semiconductor Laser Photography*, describes the development of a multiple exposure imaging system that utilises a high powered semiconductor laser as a flash illumination source. The chapter includes a review of the physical properties of semiconductor lasers, before going on to discuss the construction of driving circuits and collimation optics for this application. Practical considerations are then discussed for shadowgraphic and schlieren imaging of acoustic transients with a CCD camera. The multiple exposure imaging system is demonstrated at the end of the chapter photographing the development of individual acoustic transients generated in air by dye laser ablation, and by Nd-YAG laser assisted breakdown in air and water.

In chapter four, *An Optical Transducer*, the development of a high speed optical reflection transducer for measuring acoustic transients propagating in water is discussed. The device is based upon the measurement of the optical reflectance at a boundary using a probe beam which is incident close to the critical angle. The relevant theory is

presented, and the transducer is demonstrated quantitatively measuring acoustic transients generated by Nd-YAG laser assisted dielectric breakdown in water. Results are also presented which show that the transducer is useful for studying the asymmetric collapse of cavitation bubbles close to solid boundaries.

Chapter five, *A Large Area Planar Piezoelectric Transducer for Measuring Spherically Symmetric Acoustic Transients*, introduces a technique that addresses the problem of characterising acoustic transients originating from sources which are smaller than the measuring device. The theory of the measurement of spherically symmetric acoustic transients using large piezoelectric transducers is presented, and simulations are performed which illustrate the problems involved with deriving the temporal pressure profile from the sampled voltage output of such transducers. Finally, the technique is successfully demonstrated experimentally measuring acoustic transients associated with optical cavitation in water, and the results are discussed.

Finally chapter six, *Conclusions and Further Work*, summarises the conclusions which have been made during the course of the this work and suggests possible areas for future development of the techniques described.

Chapter Two

The Generation and Detection of Acoustic Transients

Introduction

In this chapter the generation and detection of acoustic transients will be reviewed. The discussion is divided into three parts, and begins in section 2.1 with an introduction to the theory of acoustic transients. The many different methods for generating acoustic transients in the laboratory are then discussed in section 2.2. This includes commentary on shock tubes, explosives, laser interactions, cavitation phenomena, dielectric breakdown, lithotriptors, and piezoelectric transducers. Finally techniques for measuring acoustic transients are reviewed in section 2.3. The discussion is divided into two broad areas: probe transducers and high speed photography.

2.1 - An introduction to acoustic transients

Finite wave-like disturbances that propagate through media are often referred to as *acoustic transients*. The term covers the complete range of short duration elastic disturbances possible within a medium, that is either large or small in amplitude, and either planar or curved in shape. Small amplitude disturbances are generally known as *acoustic waves*. Such waves are essentially linear and are always propagated with a definite velocity with respect to the medium that they are travelling through, referred to as the *speed of sound*. The sound speed is dependant on the local thermodynamic properties of the medium, remaining the same for every conceivable small amplitude wave motion within the medium. Violent disturbances on the other hand, such as those created by the detonation of explosives, differ greatly from the linear phenomena of sound. Whereas in small amplitude wave motion initial discontinuities are preserved as they propagate, in large amplitude wave motion they are either smoothed out almost immediately or are propagated as *shock fronts*. In the latter the medium undergoes sudden and considerable changes in velocity and temperature. These *shock waves* are the most conspicuous phenomena in non-linear wave motion since they are propagated at supersonic velocities relative to the medium and, they can also be created without the need for an initial discontinuity. As a result of the non-linear nature of such violent disturbances, the familiar laws of refraction, reflection and superposition cease to be completely valid. For example, as a consequence excess pressures of interfering sound

waves are merely additive, whereas in contrast interactions and reflections of non-linear waves may lead to enormous increases in pressure.

2.1.1 - The equations of motion

An initial equation of motion for an isotropic medium can be derived by equating the net rate of increase of mass per unit volume to the rate of change in density. Suppose $\rho(x,y,z,t)$ denotes the density and $u(x,y,z,t)$ the displacement of particles within the rectangular parallelepiped shown in figure 2.1 as functions of position and time. The rate of inflow of mass through one face normal to the x-axis, say side OABC, will be equal to $\rho \frac{du}{dt} \delta y \delta z$, and that out of the other face (DEFG) will be $\left\{ \rho \frac{du}{dt} + \frac{\partial}{\partial x} \left(\rho \frac{\partial u}{\partial t} \right) \delta x \right\} \delta y \delta z$. Also the net rate of increase of mass from transport across these two faces will be $-\frac{\partial}{\partial x} \left(\rho \frac{du}{dt} \right) \delta x \delta y \delta z$. Furthermore, similar terms will also appear from the mass transfer across the other four faces and, equating the sum of these to the rate of change in density gives the first equation of motion:

$$\frac{\partial}{\partial x} \left(\rho \frac{\partial u}{\partial t} \right) + \frac{\partial}{\partial y} \left(\rho \frac{\partial v}{\partial t} \right) + \frac{\partial}{\partial z} \left(\rho \frac{\partial w}{\partial t} \right) + \frac{\partial \rho}{\partial t} = 0 \quad - (2.1)$$

A further set of equations of motion can be derived from Newton's second law of motion; that is by equating the products of density and acceleration in a given direction to the net forces acting per unit volume in that direction. Referring again to figure 2.1, it can be seen that the medium is subject to a total of 6 stresses acting in the x direction (that is 2 tensional and 4 shear stresses.) This gives rise to a total force in the x direction of:

$$\begin{aligned} & \left[\left(\sigma_{xx} + \frac{\partial \sigma_{xx}}{\partial x} \delta x \right) \delta y \delta z - \sigma_{xx} \delta y \delta z \right] \\ & + \left[\left(\sigma_{xy} + \frac{\partial \sigma_{xy}}{\partial y} \delta y \right) \delta x \delta z - \sigma_{xy} \delta x \delta z \right] \\ & + \left[\left(\sigma_{xz} + \frac{\partial \sigma_{xz}}{\partial z} \delta z \right) \delta x \delta y - \sigma_{xz} \delta x \delta y \right] \end{aligned} = \left(\frac{\partial \sigma_{xx}}{\partial x} + \frac{\partial \sigma_{xy}}{\partial y} + \frac{\partial \sigma_{xz}}{\partial z} \right) \delta x \delta y \delta z$$

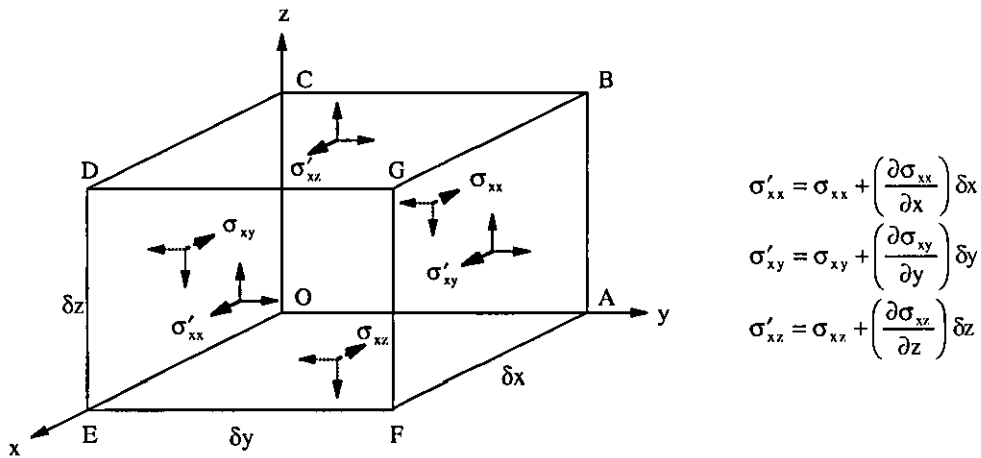
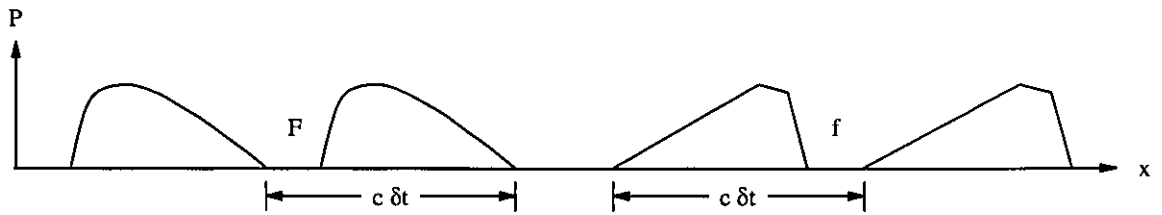
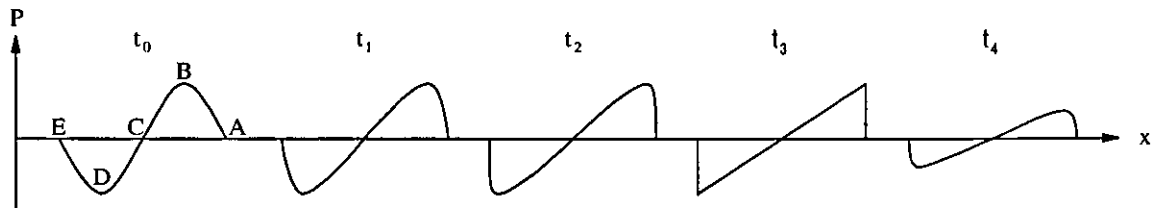


Figure 2.1 - The stresses which act upon an arbitrary uniform medium contained within a rectangular parallelepiped.



(a) Low amplitude - shape unchanged with time.



(b) High amplitude - high pressure peaks advance upon troughs with time.

Figure 2.2 - Propagation of high and low amplitude acoustic transients with time.

| Medium | c_L / ms^{-1} | c_E / ms^{-1} | c_S / ms^{-1} | c_{SR} / ms^{-1} | $\alpha / \text{neper m}^{-1}$ ($f = 10\text{MHz}$) | $\frac{B}{A}$ | d_s ($t_{1/2} = 50\text{ns}$) |
|---------|---------------------------|-------------------------|-------------------------|---------------------------|--|-----------------------------|--|
| Gases | 124 → 1285 (1) (2) | - | - | - | - | 0.024 → 0.69 (3.γ) (4.γ) | $10^{-8} \rightarrow 10^{-6} \text{ m}$ (5.γ) (2.γ) |
| Liquids | 920 → 1920 (6) (7) | - | - | - | 3 → 500 (8) (9) | 4.9 → 11.7 (10) (11) | 0.35 → 2.6mm (6) (7) |
| Solids | 1400 → 12900 (12) (13) | 500 → 6223 (14) (15) | 440 → 8880 (12) (13) | 1047 → 3655 (16) (17) | 0.01 → 1100 (18) (19) | - | - |
| Air | 331.46 | - | - | - | ~ 20 | 0.4 | 1/16 μm |
| Water | 1480 | - | - | - | ~ 2.5 | 4.9 | 1.5 mm |

Notes: 1 - Freon (113), 2 - Hydrogen, 3 - Ethyl ether, 4 - Krypton, 5 - Air, 6 - Carbon tetrachloride, 7 - Glycerol, 8 - Methyl alcohol, 9 - Castor Oil, 10 - Water, 11 - Ethyl alcohol, 12 - Teflon, 13 - Beryllium, 14 - Cork, 15 - Tungsten carbide, 16 - Polystyrene, 17 - Chromium, 18 - Quartz, 19 - Polyvinylidene fluoride. γ - Calculated from ratio of specific heats of gas.

Sources: (a) Kaye, G. W. C. and Laby T. H. (1995) - *Tables of Physical and Chemical Constants*, 16th Edition, Published by Longman.

(b) Tennent, R. M. (1990) - *Science Data Book*, Published by Oliver and Boyd.

(c) Beyer, R. T. (1960) - *Parameter of Nonlinearity in Fluids*, J. Acoust. Soc. Am. 32, pp719-721.

Table 2.1 - Typical values of the speed of elastic waves in materials.

The mass of fluid involved will be $\rho \delta x \delta y \delta z$, and so the rate of change of momentum will then be $(\rho \delta x \delta y \delta z) \frac{d^2 u}{dt^2}$ in the x-direction. Equating this using Newton's second law to the total force in the x-direction will give a conservation of momentum equation:

$$\rho \frac{d^2 u}{dt^2} = \frac{\partial \sigma_{xx}}{\partial x} + \frac{\partial \sigma_{xy}}{\partial y} + \frac{\partial \sigma_{xz}}{\partial z} \quad - (2.2a)$$

(ignoring body forces such as gravity.) Similarly, two further equations of motion can be derived for the y & z directions respectively:

$$\text{and } \left. \begin{aligned} \rho \frac{d^2 v}{dt^2} &= \frac{\partial \sigma_{yx}}{\partial x} + \frac{\partial \sigma_{yy}}{\partial y} + \frac{\partial \sigma_{yz}}{\partial z} \\ \rho \frac{d^2 w}{dt^2} &= \frac{\partial \sigma_{zx}}{\partial x} + \frac{\partial \sigma_{zy}}{\partial y} + \frac{\partial \sigma_{zz}}{\partial z} \end{aligned} \right\} \quad - (2.2b\&c)$$

2.1.2 - The acoustic wave equation

If the medium is assumed initially to be an isotropic solid, then the following linear elastic stress-strain relationships (which result from *Hooke's law*) can be inserted in the above momentum conservation equations [1]:

$$\left. \begin{aligned} \lambda \left(\frac{\partial u}{\partial x} + \frac{\partial v}{\partial y} + \frac{\partial w}{\partial z} \right) &= \sigma_{xx} - 2\mu \frac{\partial u}{\partial x} = \sigma_{yy} - 2\mu \frac{\partial v}{\partial y} = \sigma_{zz} - 2\mu \frac{\partial w}{\partial z} \\ \sigma_{xy} = \sigma_{yx} &= \mu \left(\frac{\partial u}{\partial y} + \frac{\partial v}{\partial x} \right) \quad \sigma_{xz} = \sigma_{zx} = \mu \left(\frac{\partial u}{\partial z} + \frac{\partial w}{\partial x} \right) \quad \sigma_{yz} = \sigma_{zy} = \mu \left(\frac{\partial v}{\partial z} + \frac{\partial w}{\partial y} \right) \end{aligned} \right\} \quad - (2.3)$$

where λ and μ are known as *Lame's constants* and can be expressed in terms of the *Young's modulus* E, *Poisson's ratio* ν and *Bulk modulus* K of the medium, such that [1]:

$$E = \frac{\mu(3\lambda + 2\mu)}{\lambda + \mu} \quad K = \frac{3\lambda + 2\mu}{3} \quad \nu = \frac{\lambda}{2(\lambda + \mu)} \quad - (2.4)$$

For simplicity here, it will be assumed that any disturbances within the medium will be a function of x and t only. Furthermore if it is assumed that there are only small particle displacements and velocities within the medium (i.e. that $d(u,v,w)/dt \sim \delta(u,v,w)/\delta t$), then the momentum conservation equations (2.2) with the elastic relations (2.3) simplify to:

$$\rho \frac{\partial^2 u}{\partial t^2} = (\lambda + 2\mu) \frac{\partial^2 u}{\partial x^2} \quad - (2.5)$$

$$\left. \begin{aligned} \rho \frac{\partial^2 v}{\partial t^2} &= \mu \frac{\partial^2 v}{\partial x^2} \\ \rho \frac{\partial^2 w}{\partial t^2} &= \mu \frac{\partial^2 w}{\partial x^2} \end{aligned} \right\} \quad - (2.6a\&b)$$

These equations give a complete description of small amplitude wave propagation along the x direction in an isotropic medium. The first equation of motion (2.5) describes the propagation of longitudinal vibrations along the x direction (i.e. displacement along the direction of propagation.) Such *acoustic* or *sound waves* have a velocity of $c_l = ([\lambda + 2\mu]/\rho)^{1/2}$ and are referred to as either *irrotational*, *dilatational*, *longitudinal bulk* or *P waves*. The other two equations of motion (2.6a&b), however, describe together a second type of wave which is propagated with particle displacement at right angles to the direction of propagation and, therefore represents a transverse wave. This is known as either a *shear*, *equivoluminal*, *rotational* or *S wave* and travels with velocity $c_s = (\mu/\rho)^{1/2}$ - which is slower than that of the P wave.

Note that there are several other wave types which can exist within a given medium. One of these is a modification of P waves, and exists only in straight and uniform bars or tubes with diameters significantly less than the wavelength of the waves. These waves travel at a velocity of $c_e = (E/\rho)^{1/2}$ - which is slower than c_l . Other types of vibration known as *Lamb* or *Plate waves* can be set-up at the interfaces between two or more solids in close proximity. One specific type called the Rayleigh wave propagates along the surface at a boundary between two media, one of them a solid. It has a velocity of $c_{RS} = a(\mu/\rho)^{1/2}$ where a is the least positive root of the following equation [2]:

$$\frac{a^6}{8(1-a^2)} + a^2 = \frac{1}{1-\nu} \quad - (2.7)$$

Further information on surface waves can be found in references [3] and [4]. For liquids and gases the rigidity μ is zero and as a result only longitudinal waves can exist within such media, travelling with a velocity of:

$$c = \sqrt{\frac{K}{\rho}} \quad - (2.8)$$

This can be derived simply from equations (2.4) and (2.5). The compressions and rarefactions of such waves occur rapidly and are therefore adiabatic, and this was considered by Laplace who derived the following relation using the definition of the bulk modulus:

$$c = \sqrt{\frac{\gamma P}{\rho}} \quad \text{or} \quad c \propto \sqrt{T} \quad - (2.9)$$

That is, the speed of sound is affected primarily by the ambient temperature T of the medium, but is not affected very much by the local pressure P since the density ρ varies linearly with the pressure. For solids however the ratio of specific heats γ is approximately unity and, as a result the compressions and rarefactions can be modelled as being isothermal equally as well as adiabatic. Typical values for the speed of sound in gases, liquids and solids are shown in table 2.1. In general sound travels at its greatest velocity in solids, followed next by liquids, and slowest in gases.

Solutions to the longitudinal wave equation (2.5) are generally of the form:

$$u = f(x - ct) + F(x + ct) \quad - (2.10)$$

where f and F are arbitrary functions which depend only on the initial boundary conditions. That is $f(x - ct)$ represents a plane wave which does not change shape as it propagates in the positive x direction. Likewise $F(x + ct)$ propagates unchanged with time in the negative x direction, as shown schematically in figure 2.2(a). The local pressure P is related to the above solution by the following relation:

$$P = -K \frac{\partial u}{\partial x} \quad (P = -\sigma_{xx} = -\sigma_{yy} = -\sigma_{zz}) \quad - (2.11a)$$

This also satisfies the longitudinal wave equation, which can be demonstrated by differentiating (2.5) through by $\partial/\partial x$. Also for plane waves or spherical waves at a distance the particle velocity $\partial u/\partial t$ and the intensity I , that is the time average of the energy flow per unit time over a unit area normal to the motion, are defined as [1]:

$$\dot{u} = \frac{\partial u}{\partial t} = \frac{P}{\rho_0 c} \quad \text{and} \quad I = \frac{\overline{p^2}}{\rho_0 c} \quad - (2.11b\&c)$$

2.1.3 - Boundary conditions and co-ordinate systems

In many more complicated problems in wave propagation involving a large number of boundary conditions it is often more convenient to solve the equations of motion using the velocity potential ϕ . This is defined for longitudinal waves propagating in an arbitrary direction in terms of the particle velocity components such that:

$$\frac{\partial u}{\partial t} = -\frac{\partial \phi}{\partial x} \quad \frac{\partial v}{\partial t} = -\frac{\partial \phi}{\partial y} \quad \frac{\partial w}{\partial t} = -\frac{\partial \phi}{\partial z} \quad - (2.12a)$$

where ϕ also satisfies the 3 dimensional wave equation:

$$\frac{\partial^2 \phi}{\partial t^2} = c^2 \left(\frac{\partial^2 \phi}{\partial x^2} + \frac{\partial^2 \phi}{\partial y^2} + \frac{\partial^2 \phi}{\partial z^2} \right) = c^2 \nabla^2 \phi \quad - (2.12b)$$

Furthermore the velocity potential is related to the physical quantity of pressure by:

$$P = \rho \frac{\partial \phi}{\partial t} \quad - (2.13)$$

The Laplacian operator ∇ can be re-expressed in an alternative co-ordinate system in order to aid the solution of a particular problem, the two most common systems being:

(i) *Spherical polar co-ordinates* in which there is complete symmetry about a single origin point, which is usually a point source. Here the Laplacian operator reduces to:

$$\nabla = \frac{\partial^2}{\partial r^2} + \frac{2}{r} \frac{\partial}{\partial r} \quad - (2.14a)$$

and gives rise to solutions in terms of the radial position r such that:

$$\phi = \frac{1}{r} f(r - ct) + \frac{1}{r} F(r + ct) \quad - (2.14b)$$

that is a spherically symmetric waves propagates both outwards and inwards from the origin unchanged in shape with time, however the amplitude of the waves reduces with distance from the origin.

(ii) *Cylindrically symmetric co-ordinates* where there is symmetry about a polar axis. In this case the Laplacian operator becomes:

$$\nabla = \frac{\partial^2}{\partial r^2} + \frac{1}{r} \frac{\partial}{\partial r} \quad - (2.15a)$$

where r is the radial distance measured from the axis. This has solutions of the form:

$$\varphi = \frac{1}{r^{1/2}} f(r - ct) + \frac{1}{r^{1/2}} F(r + ct) \quad - (2.15b)$$

that is cylindrically symmetric waves propagate in both in-going and out-going directions from the common axis, reducing in amplitude with the square root of the distance from the axis.

In order to solve the longitudinal wave equation described boundary conditions are required. These take two forms, firstly that of the initial conditions during the creation of the acoustic waves and, also those imposed when the waves meet a boundary between two media with differing physical properties. In the latter case two such boundary conditions are normally required to be met everywhere along the interface at all times so that there is never a situation where particles along the interface are subject to an infinite acceleration. These conditions are:

- (i) a continuity of pressure along the surface of the boundary and,
- (ii) continuity of the component of particle velocity in the direction perpendicular to the surface of the boundary.

Both of these conditions are used so that there is never a situation where particles along the interface are subject to an infinite acceleration. Of considerable interest is the case where a plane acoustic wave is incident at a planar boundary between two media and, is both transmitted and reflected in varying amounts according to the angle of incidence θ_i from the normal. The incident, reflected and transmitted waves can be expressed as follows:

$$\left. \begin{aligned} \varphi_i &= A \exp \left[i \left\{ \omega_i t + k(x \cos \theta_i + y \sin \theta_i) \right\} \right] \\ \varphi_r &= B \exp \left[i \left\{ \omega_r t - k(x \cos \theta_r + y \sin \theta_r) \right\} \right] \\ \varphi_t &= C \exp \left[i \left\{ \omega_t t + k(x \cos \theta_t + y \sin \theta_t) \right\} \right] \end{aligned} \right\} - (2.16)$$

each of which satisfy the 3 dimensional wave equation and the initial phases have been omitted for convenience. Here the boundary conditions take the form of:

$$\left. \begin{aligned} \frac{\partial}{\partial x}(\varphi_i + \varphi_r) &= \frac{\partial \varphi_t}{\partial x} & - \text{ } \perp \text{ particle} \\ & & \text{velocity} \\ \rho_1 \frac{\partial}{\partial t}(\varphi_i + \varphi_r) &= \rho_2 \frac{\partial \varphi_t}{\partial t} & - \text{ pressure} \end{aligned} \right\} \quad - (2.17)$$

These conditions, if met at all times and at all positions along the interface, give rise to the coefficients of all three exponentials in equations (2.16) to be equal. This condition results in the *law of refraction*, which is analogous to *Snell's law* in optics:

$$\frac{\sin \theta_i}{c_i} = \frac{\sin \theta_r}{c_i} = \frac{\sin \theta_t}{c_t} \quad - (2.18)$$

Solving for the amplitude terms gives rise to Rayleigh's reflection coefficients [5] using equation (2.13):

$$\left. \begin{aligned} \text{Reflection coefficient : } R &= \frac{P_r}{P_i} = \frac{Z_t \cos \theta_i - Z_i \left(1 - (c_t/c_i)^2 \sin^2 \theta_i\right)^{1/2}}{Z_t \cos \theta_i + Z_i \left(1 - (c_t/c_i)^2 \sin^2 \theta_i\right)^{1/2}} \\ \text{Transmission coefficient : } T &= \frac{P_t}{P_i} = \frac{2Z_t}{Z_t \cos \theta_i + Z_i \left(1 - (c_t/c_i)^2 \sin^2 \theta_i\right)^{1/2}} \end{aligned} \right\} \quad - (2.19)$$

where $Z_i = \rho_i c_i$ and $Z_t = \rho_t c_t$ which are known as the *acoustic impedances* of the two materials. At normal incidence the above relations reduce simply to:

$$R_0 = \frac{Z_t - Z_i}{Z_t + Z_i} \quad \& \quad T_0 = \frac{2Z_t}{Z_t + Z_i} \quad - (2.20)$$

Evaluating equations (2.19) and (2.20) for materials with differing sound speeds and densities gives rise to the following results:

- (i) $c_t < c_i$ - the reflection coefficient decreases as the angle θ_i increases away from the normal, reaching zero at an angle of incidence θ_0 such that:

$$\sin^2 \theta_0 = \left[\left(\frac{\rho_t}{\rho_i} \right)^2 - \left(\frac{c_t}{c_i} \right)^2 \right] / \left[\left(\frac{\rho_t}{\rho_i} \right)^2 - 1 \right] \quad - (2.21)$$

Beyond this angle there is a phase change, the reflected wave being π out of phase with the input wave and the reflection coefficient increases to unity. The transmission coefficient increases from T_0 with θ_i and it grows to beyond unity when the angle of incidence is larger than θ_0 , which is analogous to *Brewster's angle* in optics.

- (ii) $c_i > c_t$ - the reflection coefficient increases with θ_i from R_0 at normal incidence reaching unity at an angle θ_c defined by:

$$\theta_c = \arcsin\left(\frac{c_i}{c_t}\right) \quad - (2.22)$$

This is known as the critical angle at which total internal reflection occurs. Beyond this angle R remains at unity, but there is a phase difference ε between the reflected and incident waves which increases with angle from zero at θ_0 to π at grazing incidence, such that:

$$\varepsilon = 2 \arctan\left(\frac{\rho_i}{\rho_t} \sqrt{\frac{\sin^2 \theta_i - (c_i/c_t)^2}{1 - \sin^2 \theta_i}}\right) \quad - (2.23)$$

Whereas the transmission coefficient increases from T_0 at $\theta = 0$ to a peak value at θ_c of:

$$T_{\theta_c} = 2 \sqrt{1 - \left(\frac{c_i}{c_t}\right)^2} \quad - (2.24)$$

Beyond the critical angle the transmitted wave no longer exists physically, becoming imaginary since it is refracted along the surface of the discontinuity and therefore no energy is transmitted into the second medium. (Note: The imaginary wave, which is sometimes known as an evanescent wave, does penetrate the material but falls off in amplitude very quickly. A real wave is transmitted, however, if a further boundary exists close and parallel to the first interface in which the third material has c less than c_t .)

Finally attenuation of acoustic waves will be considered briefly. In general the absorption of plane sound waves conforms to:

$$I_d = I_0 \exp(-2d\alpha) \quad - (2.25)$$

where α is known as the *attenuation coefficient* and is expressed in *neper/unit length*. Typical values are shown in table 2.1. For liquids and monatomic gases α varies classically with the square of the frequency of the acoustic waves, however for solids α often varies linearly with frequency. Attenuation of acoustic waves is usually by viscous, thermal and rotational (mode change) mechanisms.

2.1.4 - Non-linear effects and shock waves

It has been assumed so far that the disturbances are of small amplitude and the media involved are perfectly elastic. The governing equations of motion that have been described are valid for most situations in acoustic transient propagation, however they do not hold for large amplitude waves. According to *Riemann's theory of waves* [1,6,7] this is predominantly due to the incorrect assumption that $du/dt \sim \delta u/\delta t$ which was used earlier to derive the wave equations (2.5) and (2.6). The correct relation connecting the partial and complete differentials with respect to time for large particle displacements and velocities is in fact closer to:

$$\frac{du}{dt} = \frac{\partial u}{\partial t} + \dot{u} \frac{\partial u}{\partial x} \quad - (2.26)$$

where $\dot{u} = du/dt$ (only the x-direction is considered here.) In general, given the appropriate thermodynamic law under which the motion takes place (e.g. adiabatic expansion,) the pressure can be expressed as an explicit function of the density using Taylor's expansion:

$$P = P_0 + \frac{A}{\rho_0}(\rho - \rho_0) + \frac{B}{2\rho_0^2}(\rho - \rho_0)^2 + \dots \quad - (2.27)$$

where $A = \rho_0 \left(\frac{\partial P}{\partial \rho} \right)_{\rho=\rho_0}$ and $B = \rho_0^2 \left(\frac{\partial^2 P}{\partial \rho^2} \right)_{\rho=\rho_0}$. Discarding the terms beyond the second order and applying this to equations (2.1) and (2.2), two new equations of motion can be derived which describe the non-linear motion of large amplitude elastic waves [8]:

$$\left. \begin{aligned} \left[\frac{\partial}{\partial t} + (c_0 + \beta \dot{u}) \frac{\partial}{\partial x} \right] (P + \beta \dot{u}) &= 0 \\ \left[\frac{\partial}{\partial t} + (c_0 - \beta \dot{u}) \frac{\partial}{\partial x} \right] (P - \beta \dot{u}) &= 0 \end{aligned} \right\} \quad - (2.28)$$

where β is known as the coefficient of non-linearity. These equations reveal that the quantity $(P + \beta \dot{u})$ is constant for a geometrical point moving with velocity $(c_0 + \beta \dot{u})$; and conversely that $(P - \beta \dot{u})$ is constant for a point moving with velocity $(c_0 - \beta \dot{u})$. For example: the wavelet shown in figure 2.2(b) is distorted from its initial sinusoidal shape as it propagates such that points with large excess pressures, and hence great particle velocities, such as point B, will travel faster than those with small amplitudes, such as points A, C and E. Conversely the rarefaction portion of the wavelet which has negative excess pressure, such as point D, will propagate with slower velocity. Given that point B advances on point A, a steep fronted wave known as a *shock front* will begin to develop after a short time. When this occurs the pressure gradient between the two points becomes very great, and as a result the effects of heat conduction and viscosity prevent point B from overtaking point A. These mechanisms also result in the *shock wave* eventually decaying. The terms $(P + \beta \dot{u})$ and $(P - \beta \dot{u})$ were first introduced by Earnshaw and Riemann, and are known as *Riemann invariance* [7].

The coefficient of non-linearity β is defined for any arbitrary fluid as:

$$\beta = 1 + \frac{B}{2A} \quad - (2.29)$$

where A and B relate to the first and second order terms in equation (2.27). The ratio B/A is of particular interest and some typical values are shown in table 2.1. It is worth noting the special case of an ideal gas where $P = P_0 (\rho/\rho_0)^\gamma$, the ratio of B/A becomes just:

$$\frac{B}{A} = \gamma - 1 \quad - (2.30)$$

Finally the distance a sinusoidal wavelet with angular frequency ω propagates before it distorts into a shock front can be calculated using the equation derived by Beyer and Letcher [9]:

$$d_s = \frac{c_0^2}{(B/2A + 1)\omega \dot{u}_0} \quad - (2.31a)$$

For a single pulse with peak pressure P_{\max} and duration $t_{1/2}$ which comprises of just the positive part of the sinusoid, this evaluates using equation (2.11b) to:

$$d_s = \frac{2\rho_0 c_0^3 t_{1/2}}{\pi(B/A + 2)P_{\max}} \quad - (2.31b)$$

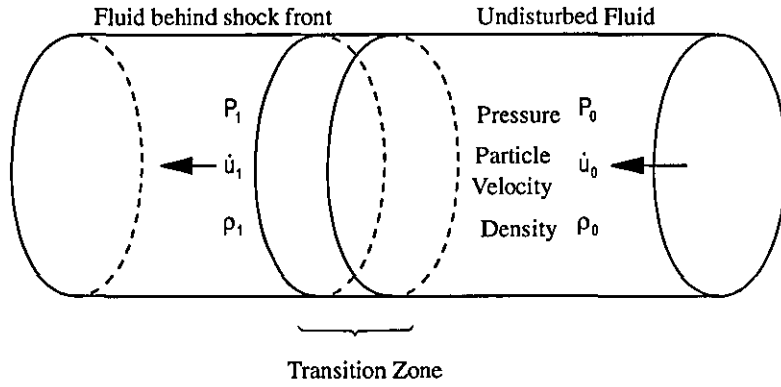
Typical values for 10MPa, 50ns duration pulses are shown in table 2.1. In general shock formation in gases occurs within a very short distance compared with that of liquids.

2.1.5 - The Rankine-Hugoniot equations

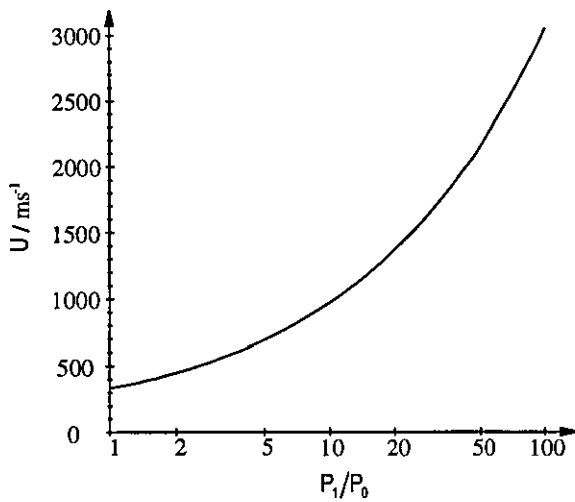
The most successful theory for the propagation of a shock front is that described by the Rankine-Hugoniot equations of motion. This theory uses the observation that shock fronts are often stable systems in which there is very little change in the profile of the shock front with time. That is, the shock front is assumed to be a region in which the fluid properties of temperature, pressure, density and flow velocity change within a constant distance. In reality this shock front thickness is in fact just a few mean free paths and thus it is often convenient to consider the fluid properties to change discontinuously at the shock front. The theory leading up to the Rankine-Hugoniot equations does not however rely upon this, but does require the shock thickness to remain constant. The derivation of these equations proceeds here as detailed in references [7] and [10].

Initially a steady state one-dimensional flow is considered where there are two regions in the fluid which are separated by a *transition zone* and, all the internal mechanisms of the system are neglected. The transition zone conditions are also steady and a frame of reference is chosen such that this zone is stationary. Such a situation where a cylinder of fluid of unit cross-section containing the shock front is shown in figure 2.3(a). The cylinder can be viewed here as being stationary with fluid flowing through it from right to left, or alternatively in a more conventional frame of reference the cylinder moves from left to right through the stationary fluid on the right hand side of the figure. The density and fluid velocity in the low pressure (right hand) region are represented here by ρ_0 and \dot{u}_0 respectively, and by ρ_1 and \dot{u}_1 in the high pressure (left hand) region of the fluid. Since the fluid cannot accumulate anywhere, the rate of mass flow across any section of fluid must be a constant, which will be denoted here as mass m per unit volume. Hence a first equation of motion can be written:

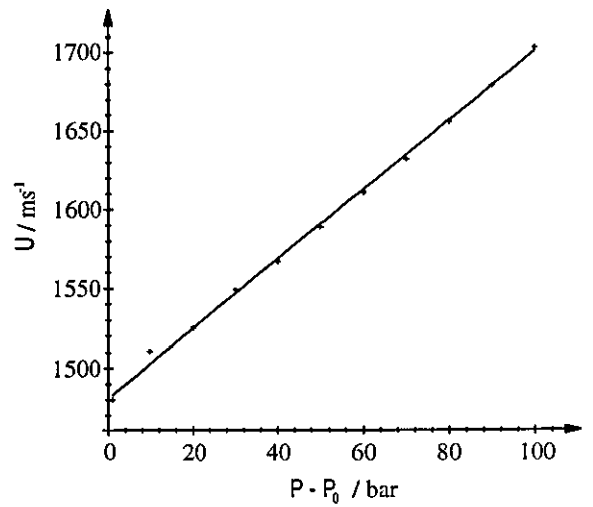
$$\text{Mass continuity :} \quad m = \rho_1 \dot{u}_1 = \rho_0 \dot{u}_0 \quad - (2.32)$$



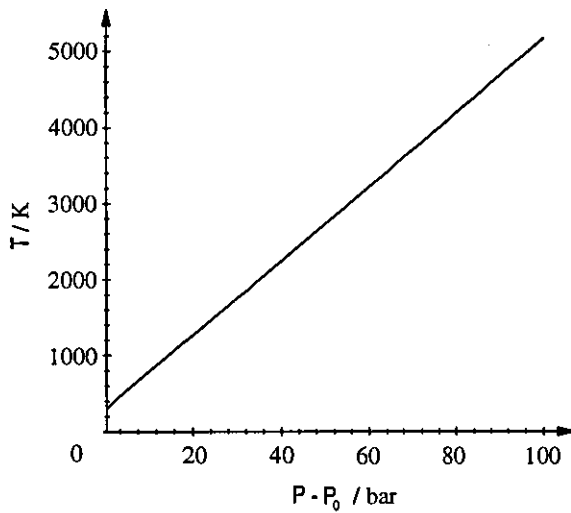
(a) A cylindrical mass of fluid with unit cross-section.



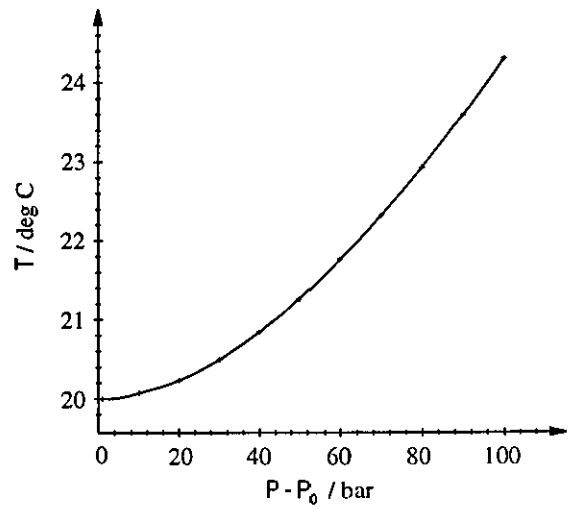
(b) Shock front velocity in air



(c) Shock front velocity in water



(d) Temperature rise in air



(e) Temperature rise in water

Figure 2.3 - Properties of a shock front according to Rankine-Hugoniot theory.

Since the shock compresses the fluid on the left hand side then $\rho_1 > \rho_0$ and, as a result of the above equation $\dot{u}_1 < \dot{u}_0$ giving rise to the length of the cylinder decreasing with time.

A second equation of motion can be developed by considering the rate of change of motion of the fluid, which is $m(\dot{u}_1 - \dot{u}_0)$ and this must be due to pressure difference at the two ends $P_0 - P_1$, giving:

$$\text{Momentum conservation : } P_0 - P_1 = m(\dot{u}_1 - \dot{u}_0) \quad - (2.33)$$

Also the work done by the cylinder of fluid in unit time is $P_1 \dot{u}_1 - P_0 \dot{u}_0$ and this work appears at the expense of both the internal and kinetic energy of the fluid. If E denotes the internal energy of the fluid per unit mass, then by conservation of energy:

$$\text{Energy conservation : } P_1 \dot{u}_1 - P_0 \dot{u}_0 = m \left(\left[E_0 + \frac{1}{2} \dot{u}_0^2 \right] - \left[E_1 + \frac{1}{2} \dot{u}_1^2 \right] \right) \quad - (2.34)$$

An equation describing the difference in internal energy between the two regions can then be found:

$$E_1 - E_0 = \left(\frac{P_0 + P_1}{2} \right) \left(\frac{1}{\rho_0} - \frac{1}{\rho_1} \right) \quad - (2.35)$$

This equation is independent of the frame of reference. Next the velocity, U , that the shock front advances into the stationary fluid is:

$$U = \dot{u}_0 = \sqrt{\frac{(P_1 - P_0)\rho_1}{(\rho_1 - \rho_0)\rho_0}} \quad - (2.36)$$

As the pressure difference between the two regions tends to zero, that is $P_1 \rightarrow P_0$, this relation reduces to just that of the speed of sound as in equation (2.8). Finally the mass flow velocity w behind the shock front is:

$$w = \dot{u}_0 - \dot{u}_1 = \sqrt{\frac{(P_1 - P_0)(\rho_1 - \rho_0)}{\rho_0 \rho_1}} \quad - (2.37)$$

Equations (2.35), (2.36) and (2.37) are known as the Rankine-Hugoniot shock wave equations after the English and French mathematicians who independently were the first to use them. The latter two equations for the shock front and mass flow velocities follow solely from the conservation of mass and momentum equations (2.32) and (2.33), hence

these apply even to shocks which cause chemical reactions and release energy such as in detonation waves.

Given the appropriate thermodynamic relation, the Rankine-Hugoniot equations can be solved to give a complete description of the propagation of a shock wave in a given medium. Specifically, for perfect gases the internal energy per unit mass is defined as:

$$E = c_v T = \frac{P}{\rho(\gamma - 1)} \quad - (2.38)$$

where γ is the ratio of specific heat at constant pressure c_p to that at constant volume c_v . Of particular interest is the velocity U that the shock advances into the stationary fluid. This can be solved for by first deriving the compression ratio ρ_1/ρ_0 from equations (2.35) and (2.38):

$$\frac{\rho_1}{\rho_0} = \frac{P_1 + \mu P_0}{P_0 + \mu P_1} \quad - (2.39)$$

where $\mu = \frac{\gamma - 1}{\gamma + 1}$. This can be substituted into equation (2.36) to give:

$$U = \sqrt{\frac{1}{\rho_0} \left(\frac{P_1 + \mu P_0}{1 - \mu} \right)} \quad - (2.40)$$

Again, at low pressures where $P_1 \rightarrow P_0$ this tends to the speed of sound as defined for adiabatic expansions in equation (2.9). A plot of the calculated shock front velocity U against pressure is shown in figure 2.3(b) for air which has a roughly constant specific heat ratio of $\gamma \sim 1.4$; this agrees with data collected experimentally by Payman and Shepherd [11]. It is briefly worth mentioning that according to this simple theory the fluid volume can only be compressed a limited amount no matter how much pressure is applied. This is shown in equation (2.39) which asymptotically tends to $(\gamma + 1)/(\gamma - 1)$ as $P_1/P_0 \rightarrow \infty$, giving for air a maximum compression of $\rho_1/\rho_0 \sim 6$ and for water $\rho_1/\rho_0 \sim 1333$.

For water the Rankine-Hugoniot equations are more difficult to solve since the P- ρ -T relationship is substantially more complex. Equation (2.35) can be solved numerically, however, using steam tables to calculate ρ_1 given an initial value for P_1 together with the properties of the undisturbed water at room temperature. This then allows the calculation

of the shock wave velocity U which has been done in figure 2.3(c) by interpolating data from the NBS/NRC Steam Tables [12]. It can be seen here that the shock front velocity is essentially linear with peak pressure up to at least 100 bar. According to Penney [10], although water is not an ideal gas it does behave roughly like one at high pressures with a γ of about 7.

Given the ideal gas relation the Rankine-Hugoniot equations can also be solved simply to give the increase in temperature of the fluid as the shock front passes through it:

$$\frac{T_1}{T_0} = \frac{P_1}{P_0} \left(\frac{P_0 + \mu P_1}{P_1 + \mu P_0} \right) \quad - (2.41)$$

This is plotted for air in figure 2.3(d), where it can be seen that there is a linear increase in temperature with peak shock front pressure. The increase in pressure can in fact be immense, say many thousands of degrees for strong shocks close to explosions. Also because of this temperature increase there is a considerable increase in entropy and, as a result of the law of energy conservation, an amount of energy equal to the increase in enthalpy of the fluid element will be taken from the pressure pulse itself. It can therefore be shown that if the pulse retains a constant shape then all of its energy will ultimately be dissipated in this way, with a permanent increase in temperature and volume in every part of the fluid [10]. The increase in temperature of water during shock propagation is almost negligible however, even for strong shocks. This is demonstrated in figure 2.3(e) which shows that there is only a 5°C increase above room temperature for a shock with a peak pressure of 100 bar. Again due to the complicated nature of the P- ρ -T relationship of water, this increase can only be calculated by interpolating steam table data.

Finally the velocity of the fluid flow on the high pressure side of the shock front for a perfect gas in a frame of reference in which the low pressure side is at rest is:

$$w = (P_1 - P_0) \sqrt{\frac{1 - \mu}{\rho_0 (P_1 + \mu P_0)}} \quad - (2.42)$$

For air this flow is supersonic for pressure ratios P_1/P_0 greater than ~ 4.6 , however for water this flow is always subsonic [10].

The preceding theory has assumed that the fluid involved is an ideal gas, however for real gases like air this theory begins to break down at high temperatures for two reasons:

- (i) If the gas is polyatomic, then when its temperature is raised sufficiently high molecular dissociation will begin to occur. Initially this means that a correction has to be applied to the ideal gas law to allow for the increase in the number of molecules in the gas. For example, the nitrogen molecules in air at high temperatures will begin to dissociate by the reaction $N_2 \rightarrow N+N$. If a fraction ζ of the original nitrogen molecules dissociate then the total number of particles in the gas will increase to $(1+\zeta)$, and hence the ideal gas law is modified to:

$$P = (1+\zeta)R\rho T$$

Similarly at still higher temperatures an appreciable degree of ionisation will begin to occur, the freed electrons will exert their own partial pressure and further modification to the ideal gas law will be needed.

- (ii) A more serious effect of dissociation and ionisation is that it leads to variations in the specific heat ratio of the medium. Although this is a reasonable approximation over a limited temperature range for many gases, in reality this assumption breaks down at some temperature for all gases. It is beyond the scope of this review to go into detail about such effects so the reader is referred to Wright's book [7]; but in general the specific heat of a gas increases somewhat after a certain temperature because of an increase in the number of degrees of freedom in the molecules of the gas. This is predominantly due to ionisation and, in polyatomic gases this is also due to molecular dissociation.

The net result of these two effects is a considerable increase in the specific heat c_p above its initial value. For air this increase occurs only above a threshold temperature of about 3000K, obeying a roughly linear relationship with temperature. The effect of this upon the shock front velocity U and flow velocity w is quite limited, there only being an increase of 5% on these properties for shocks with a peak pressure of 100 bar. There is however a large increase in the compression ratio ρ_1 / ρ_0 , for air there is a 50% increase above that calculated with a constant specific heat ratio at 100 bar. Also the compression ratio does not tend to the constant value predicted by equation (2.39) at high pressures but, continues to increase. Finally the increase in temperature of air as a shock temperature passes through decreases from that predicted with constant γ , the relationship becoming non-linear with pressure reducing the temperature increase for a 100 bar shock to just 75% of that calculated from equation (2.41).

2.2 - The generation of acoustic transients

In general any sudden disturbance within a medium, such as an explosion or sudden release of pressurised gas, can give rise to an acoustic transient. If the acoustic transient is small in amplitude then it will propagate into the surrounding media at the local speed of sound; however if it has a large amplitude then the medium in which it travels will be heated by its passage and, the changes in pressure, density and temperature together with its speed will be described by the Rankine-Hugoniot equations. In this section some of the many methods for generating acoustic transients in a laboratory will be outlined.

2.2.1 - Shock tubes

A relatively simple mechanism for generating acoustic transients is to allow a compressed gas to expand suddenly into a neighbouring region which has a significantly lower pressure [7]. Such a device is known as a *shock tube* and essentially consists of a rigid cylinder which is divided into two compartments by a gas tight diaphragm, as shown schematically in figure 2.4(a). The two compartments are both filled with gas, though not necessarily with gases of the same chemical type and, a pressure difference is applied across the diaphragm. The section with the higher pressure P' is known as the compression chamber and, that with lower pressure P_0 is referred to as the expansion chamber. When the diaphragm is ruptured the pressure tends to equalise by means of a shock wave travelling into the expansion chamber and a rarefaction wave which propagates into the compression chamber, as seen in figure 2.4(b). The gas flow from the shock front to the tail of the rarefaction wave has a uniform flow velocity since no pressure variations are allowed build up, thus giving rise to a constant pressure P_1 in this region. The dotted line in figure 2.4(b) represents the position of the gas which was initially at the diaphragm. The gas to the right has been compressed and heated by the shock wave, but the gas to the left of this line has expanded from the compression chamber and has therefore cooled. At this position there will therefore in general be a change of type, temperature and density of the gas, however the velocities are the same on both sides and this point is known as a contact discontinuity. Provided that the tube is of constant cross-section, the shock wave will be virtually unattenuated with distance and, both the pressure and particle velocity will remain constant over a certain distance behind the shock front. It is this property of the shock tube which allows the precise generation of shock waves and gas flows in media, together with its simplicity, which has made this technique invaluable in many investigations.

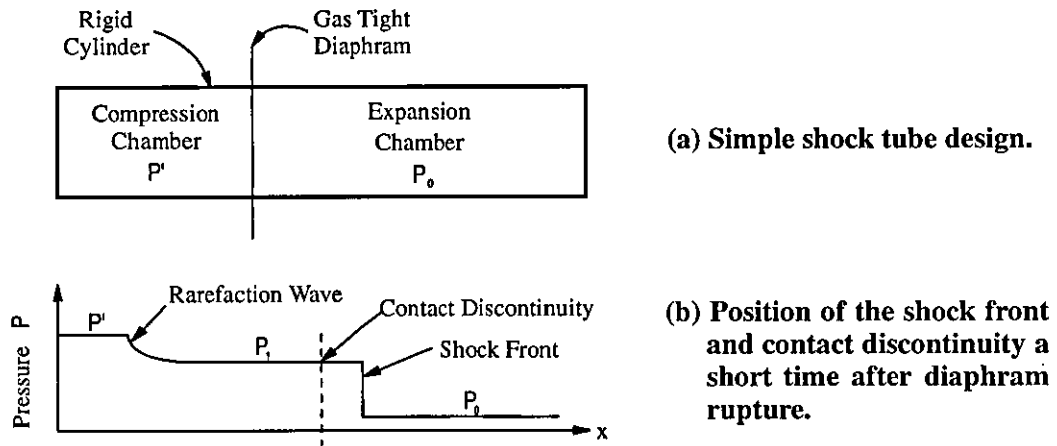


Figure 2.4 - Pressure waves in simple shock tubes.

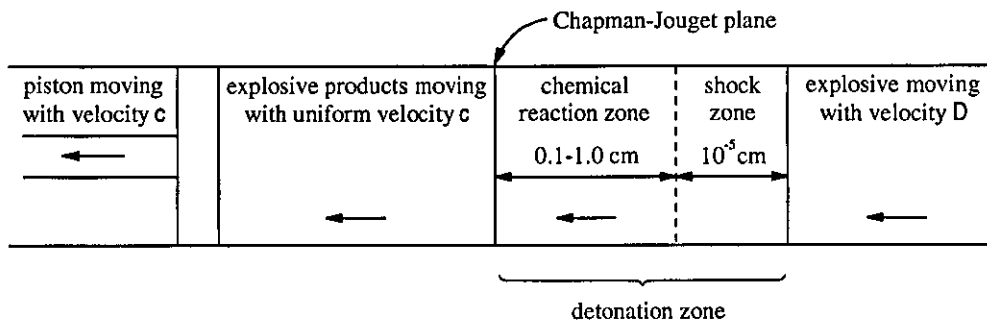


Figure 2.5 - Explosive detonation model.

| Lasing Medium | Emission Wavelength(s) | Maximum Output Power | Pulse Durations | Maximum Repetition Rate |
|------------------|------------------------|----------------------|--------------------|-------------------------|
| Nd : YAG | 1064 nm | 150 J | 30 ps - 20 ms | 50 kHz |
| Nd : Glass | 1064 nm | 10000 J | 100 ps - 2 ms | 120 Hz |
| Ruby | 694 nm | 400 J | 15 ns - 3 ms | 120 Hz |
| Carbon dioxide | 10.6 μ m | 2200 J | 6 ns - 1 ms | 10 kHz |
| Xenon chloride | 308 nm | 400 J | 30 ps - 80 μ s | 500 Hz |
| Xenon fluoride | 351 nm | 10 J | 8 ns - 1 μ s | 500 Hz |
| Dye | 400-1000 nm | 1 J | 1 ps - 2 μ s | 500 Hz |
| Krypton fluoride | 248 nm | 1.5 J | 30 ps - 200 ns | 500 Hz |
| Argon fluoride | 193 nm | 0.6 J | 5 ns - 25 ns | 500 Hz |
| Nitrogen | 337nm, 428 nm | 35 mJ | 50 ps - 10 ns | 100 Hz |
| Copper vapour | 510 nm, 578 nm | 30 mJ | 10 ns - 60 ns | 20 kHz |
| Fluorine | 157 nm | 30 mJ | 10 ns | 500 Hz |

Note : Maximum power, repetition rate and pulse duration not simultaneously possible in any one laser.
 Source : Scruby, C. B. and Drain, L. E. (1990) - *Laser Ultrasonics*, Published by Adam Hilger/IOP.

Table 2.2 -Commercially available pulsed lasers capable of generating acoustic transients.

The use of the shock tube began with Vielle [13] who showed that the shock wave was propagated down the tube with a velocity greater than that of sound. Some years later Payman and Shepherd [11] conducted a detailed analysis into air born acoustic transients propagating within a shock tube. It was not however until the second world war when the need to study blast waves (that is shock waves generated by explosives) arose that the shock tube came into general use. Since then shock tubes have been used as the source of high pressure acoustic transients in many investigations [7], including the reflection and diffraction of shocks at obstacles, calibration of piezoelectric pressure gauges, as well as numerous applications in aerodynamics involving aircraft and projectiles travelling at supersonic velocities.

In real shock tubes the shock strength achieved for a given initial pressure difference is somewhat weaker than that which would be predicted theoretically [7]. This is due to both influences from the diaphragm on the initial flow in the tube and also attenuation of the shock by viscous forces as it propagates. Initially the purpose of the diaphragm is to provide a gas tight seal between the compression and expansion chambers, and is generally required to be as light as possible so that when it shatters only a small amount of energy is used to accelerate the particles to the flow velocity of the gas. It is however found in reality that the weight of the material is important given the need for a sufficiently strong diaphragm, and results in the shock strength achieved being less than theoretically possible. As well as absorbing energy from the gases the pieces of shattered diaphragm tend to block the gas flow in the initial stages. Consequently the wave might have to travel several metres before a well defined shock is formed. Finally the diaphragm tends to destroy the one-dimensional character of the shock tube flow. That is, under the initial differential pressure the diaphragm starts to bow and as a result when the diaphragm is caused to rupture there will be a component of flow towards the walls of the shock tube, as well as directly along the central axis. This can result in a transverse wave system being produced. Typically the most widely used diaphragm material is cellulose acetate film, which gives consistent results since it shatters into very fine pieces. The material is allowed to burst spontaneously as the compression chamber is being pumped up or else the pressure differential is maintained at just below the bursting point and the centre of the diaphragm is pricked by a moving knife. At higher pressure metal foil is used with diagonal scratches marked on it so that when it is allowed to burst spontaneously the diaphragm folds open and potentially damaging fragments are not projected down the tube.

In practice it is observed that the shock fronts do not travel at constant speed down the tube but decelerate, and simultaneously the contact surface is seen to accelerate [7].

These effects are due to the viscous forces set up by the relative motion between the gas and the tube walls.

2.2.2 - High explosives

Explosions result from exothermic chemical reactions in which large quantities of gaseous products are released at great speed. The quantity of heat released by an explosion is in general relatively small compared with that released by combustion of ordinary fuels, however this release occurs at great speed, high explosives releasing all of their potential energy instantaneously. This sudden release of energy results in great mechanical forces and results not only in destruction locally, but also in a shock wave. The properties of explosive chemical compounds have been reviewed extensively by Taylor [14] and also by Johansson and Persson [15], on which the following summary is based.

The speed of a chemical reaction usually depends on both temperature and the intimacy with which the reactants can be brought together. If the reaction produces heat which cannot be dissipated rapidly, then since chemical reactions are accelerated by increases in temperature, self-heating and auto-acceleration will occur. Not all exothermic reactions result in explosions however, for example *thermite* burns at a slow rate with very intense heat emission but gives rise to very few gaseous products. On the other hand the early and well known explosive mixture named *black powder*, or *gun powder*, (formed from charcoal, potassium nitrate and sulphur ground up intimately) produces not only an exothermic reaction but also a large volume of gas as it burns, resulting in an explosion.

When black powder is ignited the grains burn from the surface inwards so that the reaction front advances everywhere normal to the nearest free surface, and at a speed proportional to the gas pressure surrounding the grains. The temperature and gas pressure govern the behaviour of the reactions taking place, the composition containing its own oxygen for combustion, liberating gas and its burning speed is accelerated by the gas pressure produced. If such a reaction is allowed to burn in the open the gas will escape freely and consequently the gas pressure will not rise greatly, the combustion speed remaining at a rate determined by the chemical nature of the composition and the granule size (i.e. the ratio of surface area to volume.) If however the composition is confined so that the gas pressure can rise, then the reaction becomes self-accelerating and an explosion results. Explosive compositions capable of following this regime are known as burning, propulsive or deflagrating explosives. There are many compositions

which exhibit this behaviour, most typical is black powder and cordite, as well as powders used in gun and rocket propulsion. The speed of deflagration along a column of such explosives rarely exceeds 100m/s and is often only a few m/s.

More powerful explosions can be obtained by making the chemical mixture more intimate. This can be done by making the chemical constituents miscible liquids where the contact is virtually molecular, however the ultimate degree of intimacy is achieved when the same molecule contains all the reactants required. Reactions are then found to occur at speeds far greater than that of deflagration; subsequently the chemical reactions are initiated by a high intensity pressure pulse which passes through the medium and are no longer dependant upon the surrounding ambient gas pressure. This pressure pulse generally develops into a shock wave, its speed typically being of the order of several km/s. This process is termed a *detonation* and substances which give rise to such a pressure wave, or *detonation wave*, or *blast wave*, are known as *high explosives*.

There is an enormous number of intrinsically explosive compounds, ranging between the extremes of those so unstable as to be only just capable of isolation, such as nitrogen trichloride, and others that can only be detonated by an exceptionally powerful impulse, for example ammonium nitrate. Within these limits exists the chemical compounds that can be made to detonate when suitably initiated, they are not restricted to any form or state, and may be solid, liquid or gaseous. When explosive substances are arranged in descending order of sensitiveness a continuously graded series is obtained, however 3 general groupings can be distinguished [14]:

- (i) *Primary or initiating explosives* - these in small quantities are capable of ready ignition by flame, spark or percussion. They rapidly increase their reaction velocity to full detonation and, can then generate detonation in an adjacent mass of high explosive, which is their main use. Such substances are essentially dangerous to handle since they are very sensitive to ignition, but a surprising degree of safety can be obtained if the initiator is pressed into a thin walled metal shell or capsule. Typical explosives in this class include mercury fulminate, first used by Nobel, and lead azide.
- (ii) *Secondary or high explosives* - are less easily brought to detonation by ordinary physical means, usually requiring the shock from a detonation initiating explosive in close contact. Many high explosives can however be initiated by mechanical impact, such as being nipped between two hard metal surfaces. The most typical solid explosive of this class is TNT (trinitrotoluene.)

(iii) *Tertiary explosives* - these compounds are not usually regarded as explosives under normal conditions since they require extreme provocation to induce detonation, such as from a powerful high-explosive primer. A typical member of the group is ammonium nitrate.

The problem of modelling the properties of a blast wave which is self sustained by a chemical reaction in a gaseous medium was first tackled by Chapman [16], and independently also by Jouget [17]. The reader is however referred to other works for a more comprehensive approach, such as the discussion by Penney *et al* [18] and the book by Sedov [19]. Chapman began by defining the detonation wave as the region in which the chemical reactions are induced, and went on to derive the minimum velocity for this wave for which conditions in this zone are steady. In a similar manner to that used by Rankine-Hugoniot (see section 2.1.5), the shock front travelling with velocity U into the undisturbed medium was reduced to rest in a new frame of reference. In other words the explosive material moves from right to left at the detonation velocity and passes into the detonation zone which is stationary in space. This situation is shown schematically in figure 2.5 in which 3 zones are distinguishable:

- (i) the undisturbed medium ahead of the shock wave
- (ii) an extremely rapid pressure rise at the shock front which leads to chemical reaction generation behind this, which proceed until complete at the Chapman-Jouget plane. This zone is often considered to have negligible thickness, and as observed in the derivation of the Rankine-Hugoniot equations the particle velocity of the material decreases as it passes through the detonation zone, typically to between 50 to 80% of the detonation velocity U . Also the temperature within this zone cannot be defined precisely since the material is not in thermal equilibrium.
- (iii) a region where the pressure and temperature are steadily maintained by the exploded gas. This can be represented by a piston which moves away from the reaction zone at the same speed as the products emerge from the reaction zone. According to Penney [18] this speed is equal to the speed of sound in the gaseous products.

This situation is similar to that discussed in section 2.1.5, and equation (2.35) can easily be modified to represent an ideal gas undergoing an explosive chemical reaction [19]:

$$E_1 - (E_0 + Q) = \frac{P_1}{\rho_1(\gamma_1 - 1)} - \frac{P_0}{\rho_0(\gamma_0 - 1)} - Q = \left(\frac{P_0 + P_1}{2} \right) \left(\frac{1}{\rho_0} - \frac{1}{\rho_1} \right) \quad - (2.43)$$

where Q represents the amount of energy released during the chemical reaction and, γ_0 & γ_1 are the specific heat ratios of the gas before and after the reaction or detonation wave front. This can be solved as before for the compression ratio:

$$\frac{\rho_1}{\rho_0} = \frac{P_0 + P_1 / \mu_1}{P_0 / \mu_0 + 2Q\rho_0 + P_1} \quad - (2.44)$$

Given that the detonation wavefront velocity U is known to be very much greater than the speed of sound as defined by equation (2.9), then it can easily be seen that $U^2 \gg P_0 / \rho_0$. The compression ratio can then be solved for by using this and substituting P_1 using equation (2.36):

$$\left(\frac{\rho_0}{\rho_1}\right)^2 - \left(\frac{2\gamma_1}{\gamma_1+1}\right)\frac{\rho_0}{\rho_1} + \left(\frac{\gamma_1-1}{\gamma_1+1}\right)\left(1 + \frac{2Q}{U^2}\right) = 0 \quad - (2.45)$$

giving:

$$\frac{\rho_1}{\rho_0} = \frac{\gamma_1+1}{\gamma_1 \pm \sqrt{1 - \frac{2Q}{U^2}(\gamma_1^2 - 1)}} \quad - (2.46)$$

For large explosions $Q \gg 0$ giving a maximum compression ratio of:

$$\left(\frac{\rho_1}{\rho_0}\right)_{\text{MAX}} = \frac{\gamma_1+1}{\gamma_1} \quad - (2.47)$$

This is the Chapman-Jouget condition for steady conditions in the detonation zone. It can be clearly seen that the maximum compression ratio for a detonation wave is less than that for a simple shock, as found in equation (2.39). The velocity of such a detonation wave can then be found simply by inserting equation (2.47) into (2.45):

$$U = \sqrt{2Q(\gamma_1^2 - 1)} \quad - (2.48)$$

Taylor [20] modelled the formation and propagation of a blast wave produced by a very intense explosion, namely that of an atomic explosion. By assuming that the initial enthalpy and pressure are negligible compared to those behind the shock, it was found that the spherical shock front is propagated outwards with radius r which is related to the time t after the explosion started by:

$$r = S(\gamma) \left(\frac{Q}{\rho_0}\right)^{1/5} t^{2/5} \quad - (2.49)$$

where a finite amount of energy Q is instantaneously released in an infinitely concentrated form and, $S(\gamma)$ is a calculated function of the ratio of specific heats γ ; which for air this is approximately equal to 1. Taylor commented that the effect of such an explosion would be to force most of the air within the shock front into a thin shell just inside of the front. The theory is only valid however for intense explosions and becomes invalid when the peak pressure falls below about 10 atm since the initial atmospheric pressure can no longer be neglected. Taylor also commented that it is apparent that a blast wave from a very intense explosion is more efficient in heating the gas behind the shock front than explosions where the explosive products are not negligible. Hence the shock is attenuated much more quickly than lower intensity shocks because more of its energy is converted into entropy. Finally, Sedov [19] used similarity methods to show that the radial component r of the shock front of intense explosions in air conforms to:

$$r \approx \left(\frac{Q}{\rho_0} \right)^{\frac{1}{2+\nu}} t^{\frac{2}{2+\nu}} \quad - (2.50)$$

where ν represents the symmetry of the system such that $\nu=1$ is a plane blast wave, $\nu=2$ is a cylindrical one, and $\nu=3$ a spherical blast wave.

2.2.3 - Laser interactions

The use of modulated light for the generation of sound was first suggested by Alexander Graham Bell in 1881 [21], who modulated sunlight incident upon a metal plate causing sound emission from the plate. This sound emission was due to the light heating the plate causing thermal expansion and, it was observed that the pitch of the sound emitted followed the frequency at which the sun light was modulated. It was not until the laser was invented in the early 1960's, however, that the use of pulsed light to cause acoustic emissions came to a peak. As sources of light, lasers have a number of unique characteristics, such as their ability to generate a collimated, intense beams of coherent light at precisely defined wavelengths from infrared to ultraviolet. They have the ability to produce a continuous beam of light, or alternatively pulsed beams with durations from a few milliseconds down to picoseconds. The generation of acoustic transients by optical interactions with gases, liquids or solids, utilises in general only the high intensity and collimation characteristics of lasers. Table 2.2 shows the properties of several different types of laser which are capable of generating acoustic transients. Although pulsed high

powered laser beams have been used to create acoustic transients directly, the output can also be accurately focused to give a very intense point source of spherical waves.

A substantial quantity of work has been done by numerous authors on laser induced acoustic transients in media. It has been found that there are a number of mechanisms by which acoustic transients may be generated. These include the thermo-elastic effect, vaporisation, electrostriction and dielectric breakdown, or ablation. However not all these mechanisms play a part in the generation of acoustic transients in every material, that is the dominant processes depend upon whether the medium is a gas, liquid or a solid. It is beyond the scope of this thesis to review all the work published on acousto-optic interactions, so the reader is referred to Jin [22] for a detailed account of research done on liquid and gas interactions, Scruby and Drain [23] for solids, and Hutchins [24] for all media. A summary of the main processes involved will however be presented here.

(i) Gases

In general the processes involved in acoustic transient generation in gases have been likened to those in high explosive detonations. Given that the majority of gases are transparent, the main mechanism for acoustic transient creation within a gas has been found to result from dielectric breakdown. This process can be divided into two regimes: firstly the detonation or heating of the gas, and then secondly, the subsequent expansion of the spark and acoustic transient after the laser pulse has ended.

Ramsden and Savic [25] were the first to study both of these phases. They proposed a model to explain the time dependence of the luminous spark produced experimentally by a Q-switched ruby laser pulse (5MW, 20ns) focused with a 8mm focal length lens into air at atmospheric pressure. Using this a relation was derived for the shock front displacement towards the lens and away from the focal point, and found that this was proportional to $W^{2/5} t^{3/5}$ during the duration of the laser pulse, where W is the energy absorbed from the laser beam and t is time. The constant of proportionality was found to depend only on the geometry of the system and, the 3/5 power law came as a consequence of the inverse square fall off of the electric field as the shock front moves towards the lens. They verified this experimentally finding that the plasma front obeyed a $t^{0.65}$ power law for the duration of the laser pulse, the plasma having preferential growth towards the focusing lens. It was postulated that the initial non-linear growth of the plasma was caused by a shock wave generated at the air breakdown site. This was thought to lead to further ionisation of the air immediately behind the shock front giving

rise to increased optical absorption behind the front, and hence the shock front would subsequently be maintained by greater absorption of energy from the laser beam. It was considered that this situation was equivalent to that of a detonation, where the reaction energy in a detonation gas mixture is replaced by the energy absorbed from the laser beam.

Ramsden and Savic also found experimentally that after the laser pulse ended the shock front displacement followed a $t^{0.38}$ relationship. This situation was considered to be identical to that investigated by Taylor [20] (see section 2.2.2), who found that the time displacement of spherically symmetric blast waves caused by chemical and nuclear explosions followed a $t^{2/5}$ power law (equation 2.49).

Daiber and Thompson [26] obtained results which conflicted with those by Ramsden and Savic. They studied the growth of a gas breakdown plasma, as well as the resulting shock front, over a range of gas pressures from 1-75atm in air, helium, argon and hydrogen using a ruby laser giving 25ns pulses with energies between 2 to 10 joules. It was found that the displacement relationship of the plasma followed a t^N relationship, but N varied between 0.5 to 0.9 depending upon the initial gas pressure, laser energy and focal length of the focusing lens used. Daiber and Thompson thought that higher values of N could be explained by taking into account the shape of the laser pulse. They assumed the pulse to have a gaussian shape and found that the breakdown occurred at earlier times for higher powered pulses. Later Emmony [27] pointed out that apparent discrepancies in the value of N are almost entirely dependant upon the geometry of the system and the laser pulse shape. That is for $N < 0.6$ geometrical considerations were considered dominant, whereas laser pulse shape and breakdown time accounted for displacements where $N > 0.6$.

After the cessation of the pulse Daiber and Thompson found that the displacement of the shock front followed a $t^{0.2}$ relationship for all conditions of gas, laser power, pulse duration and focusing lens geometry. This differed considerably from Ramsden and Savic's results, and it was suggested that blast wave theory giving $N \sim 0.4$ only applies when the shock wave radius exceeds that in which the energy is added.

Subsequently Raiser [28-30] made a comprehensive analysis of laser induced shock wave generation in gases, in which three separate but related mechanisms were identified:

- (a) *Breakdown wave* - dielectric breakdown first occurs at the focal point of the lens where the electric field is at its greatest, giving rise to intense ionisation and heating.

That is the high intensity laser light ionises molecules which emit free electrons. These electrons are accelerated by absorbing light and subsequently go on to cause further ionisation in other nearby molecules by inelastic collisions processes, the total number of free electrons building up exponentially in an avalanche process. Given that the rate at which this process occurs is dependant upon the electric field intensity, the breakdown process will take longer to occur a points further away from the focus where the light intensity is not as strong. Hence the ionisation, or plasma, front will appear to grow as a breakdown wave towards the lens. Whereas breakdown on the other side of the focal point, remote from the lens, will occur at a slower rate since the laser light is attenuated by the strongly ionised plasma at the focal point.

- (b) *Shock wave mechanism* - the plasma at the focus of the lens expands quickly and creates a shock wave. As this propagates out into the surrounding gas, the gas is locally heated giving rise to an increased optical absorption coefficient. Given that high intensity light is only present in the focal cone of the lens, further energy is absorbed accelerating the shock, resulting in distortion in the overall shape of the shock front.
- (c) *Radiative mechanism* - the relatively cold outer regions of the plasma absorb thermal (blackbody) radiation from the hot inner core, become ionised and are subsequently able to absorb lower energy photons from the beam.

(ii) Liquids

According to Hu [31], there are four main mechanisms responsible for the stress production and the resulting acoustic transients in liquids by laser irradiation, namely dielectric breakdown, electrostriction, vaporisation and the thermoelastic effect. The properties of these effects are summarised below:

- (a) *Vaporisation* - this occurs when the total light energy absorbed in the medium is greater than the boiling threshold for the liquid, giving rise to evaporation and an explosion. A typical value for the vaporisation threshold of water is about 537 cal/cm³. This mechanism has been studied in some detail by Bell and Maccabee [32], Sigrist and Kneubuhl [33], Emmony [34], and theoretically by Bunkin and Komissarov [35].

- (b) *Thermoelastic effect* - this is the dominant mechanism when the total absorbed energy is too small for evaporation to take place, but it can still give rise to large acoustic waves. The effect is produced in the medium when the energy is injected in a very short time, say of the order of 10^{-8} sec. Absorption and heating results in very rapid thermal expansion of the liquid, the inertia of this giving rise to a large reaction force on the surrounding medium, even though the total expansion is small. Under this large reaction force the medium becomes slightly extensible and compressible giving rise to an acoustic wave. Sigrist and Kneubuhl [33] have studied this mechanism and vaporisation using a CO₂ laser. They observed using high speed photography that the geometry of the resulting acoustic transients was determined by the optical absorption coefficient α of the liquid at the laser beam's wavelength (10.6 μ m). With high α only a hemispherical wave was generated, originating from where the laser radiation intersects the surface of the liquid; however in liquids with low α it was found that the laser beam penetrates the liquid creating a cylindrical wave in addition to the hemispherical wave. The thermo-elastic effect in liquids has been studied in some detail by many authors, including Carome *et al* [36], Hunter *et al* [37], Westervelt and Larson [38], and theoretically by Bushanan and Barnes [39] and Hu [31].
- (c) *Electrostriction* - this mechanism becomes important in a few transparent liquids, such as N₂ and O₂ at cryogenic temperatures, where the absorption coefficient is too small to give appreciable absorption of energy. It occurs in the beam of some Q-switched lasers that are capable of generating electric fields as high as 10^7 V/cm. This high electric field causes polarised molecules to move in or out of the field according to their charge, resulting in a density gradient and thus an acoustic transient. The electrostriction effect has been experimentally observed by Sullivan and Tam [40], and by Chaio *et al* [41], and considered theoretically by Lai and Young [42], and Heretier [43].
- (d) *Dielectric Breakdown* - this is the most efficient means of producing high intensity acoustic transients, however it is often the most difficult effect to produce since extremely large electric fields and intensities are required, typically of the order of 10^{10} Wcm⁻². Also it was the first mechanism to be utilised for the generation of acoustic transients in liquids, being first reported by Askar'yan *et al* [44] who used a 1 μ s duration high power Ruby laser pulse which was either focused or directed straight into water. It has been found to be useful for producing not only spherically symmetrical acoustic transients, but also a cavitation bubble which grows to some maximum diameter before collapsing and producing more acoustic transients [22].

The effect in pure liquids is attributed to molecules becoming ionised by an extremely high electric field, the liberated electrons are subsequently accelerated by the radiation field and collide with other molecules causing further ionisation, and hence the number of freed electrons grows exponentially in an avalanche process. Breakdown is however produced at significantly lower intensities (few kWcm^{-2} [44]) in inhomogeneous liquids, where small impurities such as dust or dissolved gases absorb the light energy and become 'hot spots'. These impurities subsequently produce free electrons via inelastic collisions with other impurities, which then go on to produce the avalanche effect as before. A great number of papers have been published on acoustic transients generated by laser induced dielectric breakdown in liquids [45-48], and also more recently on its applications to surgery [49-53] and the study of cavitation phenomena [52-54]. Finally it can be commented that the energy and power densities that have been obtained during laser generated breakdown in liquids, between 10^{10} to 10^{12} Jcm^{-2} and 10^{20} to 10^{22} Wcm^{-2} respectfully, are much greater those achieved in high-current electrical discharges and chemical explosions (10^4 Jcm^{-2} and 10^9 Wcm^{-2}). Infact the densities are of order of those achieved during nuclear explosions [55], even though the total amount of energy is small.

(iii) Solids

According to Scruby and Drain [23], there are a number of different processes that can take place when a solid surface is illuminated by pulsed laser light. At low intensities these include heating, the generation of thermal and elastic waves by the thermo-elastic effect and, in materials such as semiconductors electric currents may also be generated. Whereas at higher intensities material may be ablated from the surface and a plasma formed, while in the material there may be melting, plastic deformation, combustion and even the formation of cracks. In addition to longitudinal (sound) waves, transverse and surface waves can also be generated within solids by these mechanisms.

The generation of elastic waves in solids *thermoelastic effect* was first observed in solids by White [56], and occurs when the incident power of the laser radiation is relatively low, say 10^4 to 10^6 W/cm^2 . When a solid with a high absorption coefficient is illuminated by a short pulse of light from a Q-switched laser, some of the radiation is reflected at the surface, whereas the rest is transmitted into the solid and absorbed within a short distance. For conductors this distance is defined by the *skin depth*, where conduction band electrons close to the surface either reflect or absorb the light, screening those deeper in from the radiation. Next, the absorbed energy heats the surface region of the solid and, this energy propagates into the material as a short lived thermal wave. The

subsequent rapid and localised increase in temperature results in thermal expansion, setting up stress and strain fields which propagate out as elastic waves deep into the material. In the simplest case where the surface is unconstrained, as shown in figure 2.6(a), there will be very little stress developed normal to the surface, giving rise to a radial source of acoustic transients.

Significant changes in the stress distribution can be obtained by adding liquid or solid layers to the surface prior to irradiation [24]. In the case shown in figure 2.6(b), where a thin film of liquid is applied to the surface, forces normal to the surface can be generated by momentum transfer if the liquid evaporates in addition to the radial stresses caused by thermo-elastic effect. Alternatively if a completely transparent (at the wavelength of the light) layer of solid material is bonded rigidly to the surface, as shown in figure 2.6(c), the absorbing material will be completely constrained in all directions. This results in stresses being developed in both the normal and radial directions during the rapid thermal expansion, thereby creating elastic waves which propagate in all directions.

Given that the light pulse is very short, it is the total energy absorbed per pulse which determines the amplitudes of the elastic waves generated by the thermo-elastic effect. There is however no general rule as to the relative proportions of longitudinal, transverse and surface waves generated. The maximum amplitude of such waves generated by the thermo-elastic effect is defined by the damage threshold of the irradiated media, which is typically reached with beam intensities of the order of 10^7 Wcm^{-2} . Beyond this threshold the temperature of the surface is raised above the boiling point of the solid, resulting in some of the material being vaporised and ejected from the surface. Often this accompanied by a spark, the vaporised material becoming ionised and forming a plasma. This process is called *ablation*, and the momentum transfer from the ejected material will cause stresses to be formed normal to the irradiated area. At high laser power densities these stresses will dominate over the more radial thermo-elastic stresses, giving rise to very strong elastic waves which will propagate into the solid, together with sound waves which propagate towards the laser in the surrounding gaseous medium. Vaporisation and ablation of solids by laser radiation can be produced most easily at the focal point of a lens. Typically a 30ns duration 100mJ pulse of light from a Q-switched laser will give rise to a power density of the order of 10^9 Wcm^{-2} when focused, much greater than the vaporisation threshold of $\sim 10^7 \text{ Wcm}^{-2}$ for most metals [23]. For further information on ablation the reader is referred to the book by Ready [57], and for experimental work the paper by Krehl et al [58]. The generation of acoustic transients in solids by the thermoelastic effect is covered in great detail in the book by Scruby and Drain [23], and also in the paper by Hutchins [24].

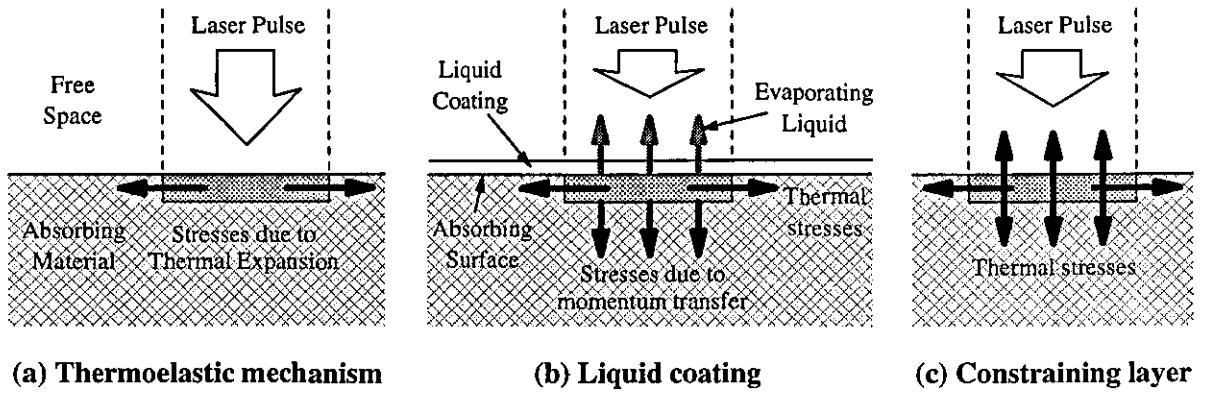


Figure 2.6 -Laser generated acoustic transients in solids.

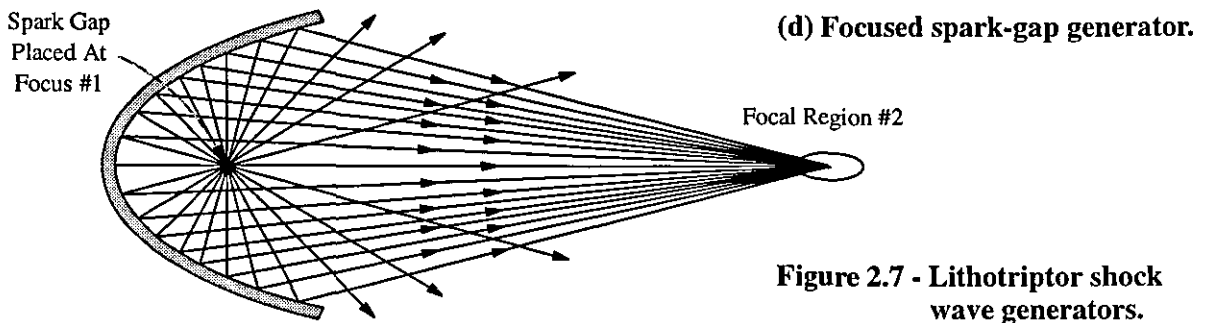
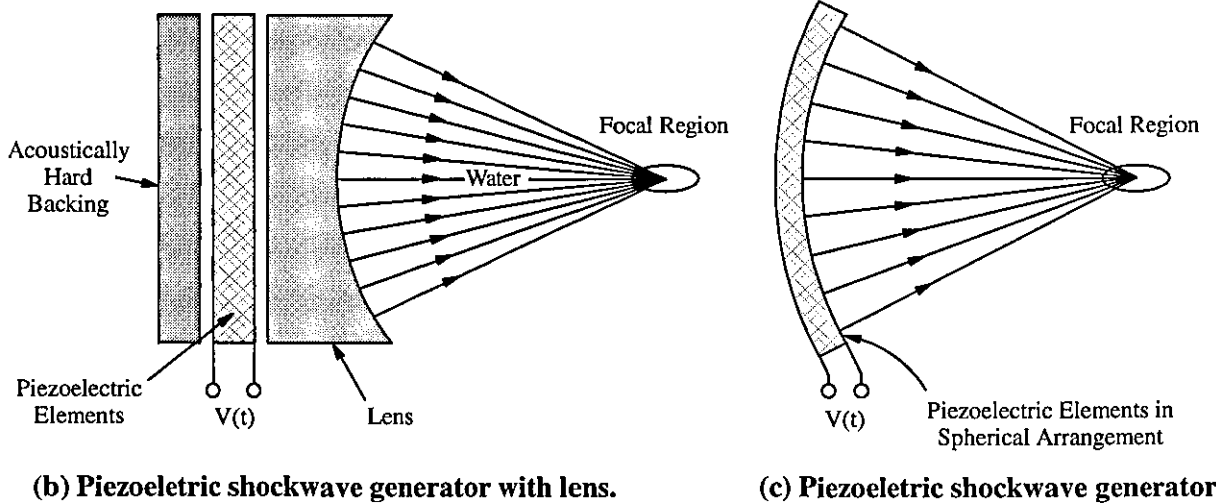
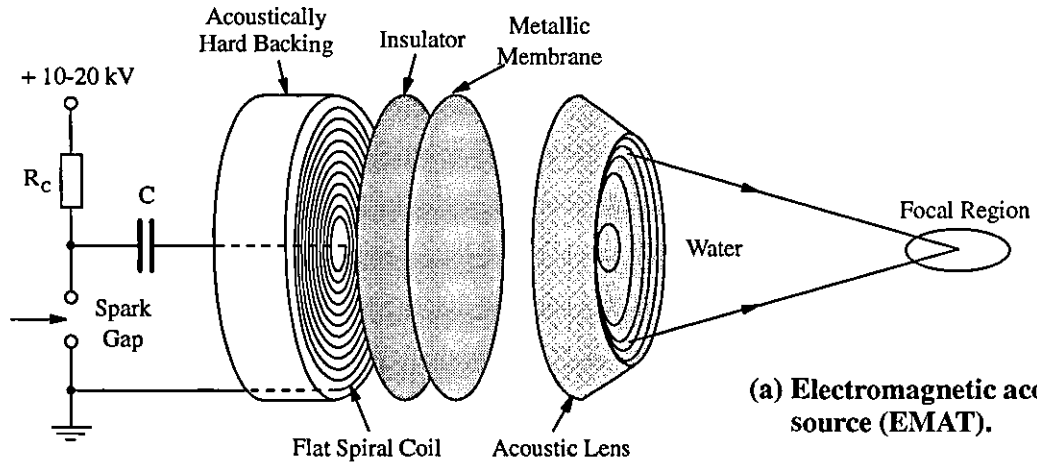


Figure 2.7 -Lithotripter shock wave generators.

2.2.4 - Cavitation

The phenomenon of cavitation was first discovered by Reynolds in 1873 [59]. It was observed that when water flowed through a tube containing a local restriction, bubbles or cavities were formed in regions of low pressure which subsequently collapsed and vanished upon entering a region of higher pressure. Later Barnaby and Thornycroft [60] observed that bubbles were created around rotating ship propeller blades and were caused by the pressure drop around the blades. They observed that rapid erosion of the blades occurred due to the bubble formation and gave the phenomenon the name *cavitation*. Infact cavitation has been found as the main cause of damage in most hydraulic machinery, and in severe cases causes complete destruction of moving parts.

Cavitation bubbles were first modelled theoretically by Rayleigh [61] who considered spherically symmetric bubbles. Rayleigh showed that although the total energy involved is small, the spherical convergence of a collapsing bubble can give rise to enormous energy densities and pressures as it reaches its minimum volume. Cavitation bubbles were also shown to undergo several cycles of expansion and collapse and this was first photographed in detail by Lauterborn [62,63]. The consequence of this is that every time cavitation bubbles collapse to their minimum volume it is found that acoustic transients are produced; since at minimum volume the pressure and rate of change of pressure is at its highest around the bubbles. Also the extreme pressures can initiate other phenomena, such as the emission of light (*sonoluminescence*) and the initiation of chemical reactions.

Since the discovery of cavitation much effort has been put into researching and understanding the precise mechanisms involved and, ultimately to search for a means of controlling cavitation damage. Several authors have suggested that shock waves are the predominant mechanism for damage [64,65]. These are created during the collapse of a spherical cavitation bubble, and also as such a bubble is arrested by solid boundary placed close by. Another mechanism which has been suggested is that the damage is caused by a *liquid jet* or *water hammer*, which is formed within the asymmetric collapse of a cavitation bubble when it is close to a solid boundary. This idea was first put forward by Kornfeld and Suvorov [66] and observed later experimentally by Naude and Ellis [67]. No consensus has been reached in the literature, however, as to which mechanism is dominant. Some experimental investigators such as Hickling and Plesset [64], as well as Fujikawa and Akamatsu [68,69], have produced evidence that it is the shock waves which damage the solid. Whereas other authors have come to the conclusion that the damage is caused by a liquid jet, these include Benjamin and Ellis [70], Plesset and Chapman [71], Lauterborn and Bolle [63], and Jin [22].

Although mechanical methods of generating cavitation have been used to investigate the mechanisms involved, such techniques make the observation of the history of a single bubble impractical because of the inherent random nature of cavitation. Hence cavitation is often artificially generated in water by either electrical spark discharge, the blowing of hot vapour into the liquid, underwater chemical explosion, high intensity sound field and, also by focused laser irradiation to give dielectric breakdown in water. All of these methods rely upon violently changing the pressure within the liquid to create the bubble. Generation of cavitation bubbles by high intensity acoustic fields has been studied in some detail by Flynn [72]. *Acoustic cavitation*, as it is termed, results when the negative pressure (or positive tension) in the rarefaction parts of an acoustic wave exceeds the tensile strength of the liquid. This has been measured for pure water by Briggs [73] and found to be about -275 bars; however it has been found to be more easily produced in impure water with 1/10 to 1/100 of the pressure, the cavitation being initiated at inhomogeneities present called *nuclei* or *microbubbles*. Generation of cavitation bubbles by laser induced liquid dielectric breakdown, called *optical cavitation*, has been studied in some detail by Jin [22] and comes about by the same interactions described in the last section. This technique has a distinct advantage over many of the others because the bubble can be easily generated at a chosen point and, it leaves the region clear of obstacles enabling high speed photographing of the event.

2.2.5 - Spark discharges

If a small potential difference is applied across two electrodes in an insulating or dielectric medium then under normal conditions only a small, negligible current will flow. When the potential is increased to some critical magnitude, the dielectric medium abruptly becomes conducting and a large current begins to flow. Localised intense heating of the gas occurs giving rise to rapid thermal expansion and the generation of an acoustic transient together with a bright spark. This phenomena known as *dielectric breakdown*, *sparking*, or *arc discharge* occurs under a number of conditions: at its greatest during lightning strikes and at its smallest between low voltage switch contacts. The potential at which this begins to occur is called the *breakdown potential* or *sparking potential*; the magnitude of which depends upon the dielectric medium involved, the time variation of the potential, and also the size, shape, material and separation of the electrodes. For example, air typically breaks down at potentials between 8.6kV and 30kV for point like and parallel plate electrodes respectively with 1cm separation [74].

The many processes involved in electrically induced breakdown of gases were first studied by J. J. Thompson [75] and J. S. Townsend [76], and have been extensively reviewed Llewellyn-Jones [77]. Initially when a potential difference is established across two electrodes in a gas, electrons which are naturally produced at the cathode are accelerated towards the anode by the electric field. During their travel these electrons ionise gas molecules through inelastic collisions, thereby producing more electrons which are also accelerated and go on to collide with other gas molecules. This gives rise to an avalanche effect, where the electron population rises exponentially with distance from the cathode, until they are eventually neutralised at the anode.

Secondary electron generation processes also exist which become dominant at the breakdown potential. At low gas pressures additional electrons are generated at the cathode by the incidence of either accelerated positive ions, excited metastable gas atoms, and also by photons which have been released through the photoelectric effect during gas molecule ionisation. These photons can also be absorbed by unexcited gas molecules giving rise to ionisation, and both the photons and electrons can excite already ionised molecules to release more electrons. Dielectric breakdown occurs when the rate of electron generation just exceeds the loss of electrons through mechanisms such as diffusion and drift. Since an electron gas, or plasma, is formed the electrical resistance of the gas falls to almost zero allowing a very great current to flow which is limited only by the electrical circuit supplying the electrodes. Typically currents of up to 10kA can flow and, it is possible for up to 50% of the supplied electrical energy to be converted into mechanical energy [83].

At higher pressures however, including atmospheric pressure, very few extra electrons are generated at the cathode and, Loeb's *streamer* theory [77,78] of breakdown then applies. Here narrow luminous tracks are observed upon spark breakdown, indicating that additional electrons are generated mainly by photo-ionisation by photons produced in the primary electron avalanche. This ionisation only becomes rapid, however, when the original field is heavily distorted by a positive space charge at the head of the avalanche. These new electrons then initiate additional avalanches near the head of the main avalanche, producing rapid effective propagation of the avalanche across the gap. Breakdown occurs when the streamer reaches the cathode [78].

Less is known about the mechanisms behind electrically induced dielectric breakdown in liquids since the processes involved are not necessarily the same under all conditions. In general it is thought that the Loeb's streamer theory also applies to liquids accompanied by low-density disturbances near the cathode [79], such as cavitation bubbles. Liquids

have a higher dielectric strength than gases; typically water has a breakdown potential in the region of a few hundred kV/cm. This is however very dependant upon the purity of the water, since impurities can be draw up into the high field region causing partial bridging of the high potential gap and so precipitate breakdown.

Finally it is worth noting that the first high speed photographs of acoustic transients were taken by Toepler [80] who used spark gaps not only as pulsed light sources, but also to generate the shock waves. Other techniques for generating dielectric breakdown exist, such as by using a *theta pinch* in which breakdown is caused by high electric fields developed within a single turn coil [81]. Lastly, further information about the design of spark discharge systems can be found in Frungel's books [82-85].

2.2.6 - Piezoelectric transducers

The phenomena in which materials develop an electrical polarisation when mechanically stressed and, conversely, change their shape in an electric field is called *Piezoelectricity* [86]. It was first discovered in 1880 by Pierre and Jacques Curie [87,88], who found the effect in several naturally occurring minerals, such as *Rochelle salt* (potassium sodium tartrate), *quartz* (nearly colourless silicon dioxide) and *tourmaline* (a silicate). Their discovery came as a consequence of studying the relationship between *Pyroelectricity* (generation of electrical charge by changes in temperature) and crystal symmetry, and the phenomenon was later given the name Piezoelectricity by Hankel since *Piezo-* is derived from the Greek word for *press*. The effect remained a laboratory curiosity until 1916 when Langevin demonstrated the first acoustic transducers, utilising quartz placed between two metal electrodes as both the source and detector of sound in a simple sonar system [89].

In 1940 the first synthetic piezoelectric substance, *barium titanate*, was fabricated [90]. This is a *ferroelectric ceramic* which becomes piezoelectric by poling the material in an electric field above its *Curie temperature*, and it has piezoelectric properties comparable to those of Rochelle salt. Being a ceramic barium titanate has several more favourable properties, such as that it is not water soluble, can withstand higher temperatures and can be moulded into almost any physical shape, whereas the naturally occurring crystalline materials could only be cut with diamond saws. This material was quickly followed by other man-made substances offering yet better performances. These include *ethylene diamine tartrate* (EDT), *dipotassium tartrate* (DKT), *ammonium dihydrogen phosphate* (ADP), *lead metaniobate*, *lead zirconate titanate* (PZT), and synthetic quartz.

Piezoelectric effects also exist in polymers. This was first discovered as early as 1924 [91], however it was not until the work of Fukada [92,93] in the 1950's and 1960's that such materials were examined in detail. The real breakthrough came in 1969 when Kawai [94] discovered a strong piezoelectric effect in Polyvinylidene Fluoride, better known as either PVDF or PVF₂. This material exhibits considerably stronger piezoelectric activity than other polymers, which is in part due to its high dielectric constant [95].

The most typical configuration for piezoelectric transducers is that of a piezoelectric substance placed between two parallel plate electrodes, with the piezo material polled in the direction perpendicular to the plates. If a voltage V is applied across these plates the dimensions of the material will, to a good approximation, change linearly with electric field along all three axes. As a result the strains in the material parallel ($\Delta w/w$) and perpendicular ($\Delta s/s$) to the plates under stress-free conditions will be:

$$\frac{\Delta w}{w} = d_{31} \left(\frac{V}{s} \right) \quad \text{and} \quad \frac{\Delta s}{s} = d_{33} \left(\frac{V}{s} \right) \quad - (2.51)$$

where s and w are the thickness and length of the material, Δs and Δw are the changes in thickness and length, and d_{33} and d_{31} are the respective *piezoelectric strain constants*. Here the first subscript denotes the direction of the applied electric field (3 for perpendicular to plates) and the second subscript gives the direction of mechanical strain (1 or 2 for the two directions parallel to plates.) Also note that positive strain results from when the electric field is applied in the same direction as the original poling field of the piezoelectric material.

The strains developed in a piezoelectric material under stress-free conditions can also be calculated in terms of the open-circuit charge Q applied to the electrodes:

$$\frac{\Delta w}{w} = -g_{31} \left(\frac{Q}{A} \right) \quad \text{and} \quad \frac{\Delta s}{s} = -g_{33} \left(\frac{Q}{A} \right) \quad - (2.52)$$

where A is the area of the electrodes and, g_{31} and g_{33} are the *piezoelectric stress constants* of the material. Typical values for the piezoelectric stress and strain constants are shown in table 2.3 [96-100] (see page 46), together with two other important constants. The *electromechanical coupling factor* k expresses the ability of a transducer to convert the applied electrical energy into mechanical energy, and visa versa. Whereas the *acoustic*

impedance Z can be used to find the amount of energy reflected R_E and transmitted T_E at the interface between the transducer and the external medium as follows:

$$R_E = \left(\frac{Z_{\text{tran}} - Z_{\text{ext}}}{Z_{\text{tran}} + Z_{\text{ext}}} \right)^2 \quad \text{and} \quad T_E = \frac{4Z_1 Z_2}{(Z_1 + Z_2)^2} \quad - (2.53)$$

where Z_{tran} and Z_{ext} are the acoustic impedances of the piezoelectric and external media respectively. These relations follow from equations (2.11c) and (2.20) for normally incident waves at an interface. As a result the best piezoelectric materials will have acoustic impedances close to that of the external medium, this is so that the amount of energy transmitted is maximised.

Of the piezoelectric materials available, PZT has become the most popular for the generation of acoustic waves due to its comparatively high coupling factor. The acoustic impedance of PZT is, however, very much greater than that of air ($425 \text{ kgm}^{-2}\text{s}^{-1}$) and water ($1.5 \times 10^6 \text{ kgm}^{-2}\text{s}^{-1}$). As a result most of the acoustic energy is reflected back into the transducer. To some extent this can be reduced by using an impedance matching layer, called a *couplant*, placed between the transducer and the external medium. Alternatively the polymer polyvinylidene fluoride can be used as the transducer material, since this has an acoustic impedance much closer to that of water. For acoustic sources the piezoelectric characteristics of PVDF are however not as good as those of PZT; both the coupling factor and the strain constants are smaller, meaning that a higher driving voltage is required to give the same output from a PVDF transducer compared with one made from PZT.

Further information on piezoelectric transducers can be found in a review article by Crecraft [100], and for piezoceramic transducers in a paper by Gallego-Juarez [97]. For a detailed comparison between ceramic and polymer piezoelectric materials the reader is referred to a paper by Lancee *et al* [101]. Details of the applications of piezoelectric transducers can be found in a book by Shields [102], and the crystal structures of piezoelectric materials can be found in an article by Sworakowski [103]. Finally piezoelectricity is not to be confused with the much smaller effect called electrostriction, which is seen in all dielectric materials and follows the square of the applied electric field [96].

2.2.7 - Lithotriptors

In this section pulsed high pressure acoustic sources will be briefly investigated. These devices have been used predominantly in the medical field for the fragmentation of *Gall* and *Biliary stones*, and given this application such transducers have come to be known as *Lithotriptors*, which is derived from the Greek for 'stone breakers'.

The idea of fragmenting Gall stones, sometimes called *calculi*, by using high pressure continuous ultrasound was first investigated independently by several authors in the 1940's and 1950's [104-106]. It was found that even the largest continuous pressure waves produced had too small an intensity to effectively fragment the stone and, these waves caused damage to human tissue through ultrasonic heating. It took a further two decades before Forßmann et. al. [107] solved these problems by using single pulses of ultrasonic energy generated by a spark gap focused by an elliptical reflector onto the stones, fragmenting them with the shock wave developed. As a result Dornier [108,109] produced the first clinically applicable system, pioneering the field of *extracorporeal shock wave lithotripsy*; which was followed later by similar systems from the Siemens medical group and Wolf.

Typically the compressive strength of stones found in kidneys is about 11MPa [110] and, there are several high pressure acoustic sources which are capable of generating peak pressures in excess of this:

- (i) *Electromagnetic acoustic source* (EMAS) - this design of emitter is shown schematically in figure 2.7(a). A spirally wound coil is mounted onto an acoustically hard and electrically insulating backing. When an electric current pulse is passed through the coil it produces a rapidly increasing magnetic field which induces eddy currents (according to Lenz's law) in a metallic membrane. Electrostatic repulsion occurs between the currents in the coil and membrane, giving the membrane kinetic energy which is transmitted into the water as an acoustic wave. The acoustic transient is then focused by an acoustic lens made from polystyrene, which has the effect of increasing the peak pressure generated and accelerating the formation of a shock wave. Mathematical analyses of this type of source are given by Alcock [111] and Eisenmenger [112], whereas design and construction considerations can be found in several papers by Carnell, Emmony and Alcock [113,114]. Typically peak pressures in the region of 60MPa [115] can be generated using this type of emitter. This form of transducer also has applications in oceanography and in the investigation of chemical equilibria [116].

- (ii) *Planar piezoelectric source* - when an external electric field is applied across a planar piezoelectric crystal, the external dimensions of the piezo material change as described in the last section. Provided that the electric field is pulsed high enough, a pressure wave is produced which is then focused using an acoustic lens, as shown schematically in figure 2.7(b). Peak pressures of up to 115MPa have been reported for this type of transducer [115].
- (iii) *Hemispherical piezoelectric source* - shown schematically figure 2.7(c). The principle for this type of emitter is similar to that of the planar piezoelectric source, except that the transducer is spherically shaped and is therefore self-focusing. Although modern piezoelectric ceramics can be fabricated into the required shape, it is more usual for the source to be comprised of small flat elements arranged in a curved mosaic. This type of shock wave generator is consumes more space (up to 50cm diameter [117]) than other designs and, the life time of the piezoelectric crystals is limited by mechanical damage due to peeling off of the piezo-ceramic elements and by electrical breakdown of the materials insulation.
- (iv) *Spark gap source* - this design for a high pressure acoustic source was the first to be applied as a Lithotripter by Dornier [108,109] and is shown in figure 2.7(d). The basic principle is that energy is released suddenly in a small volume using a spark gap (see section 2.2.5,) thus generating an exploding plasma which then expands with supersonic velocity. The resulting shock wave is then focused by an elliptical reflector. Typically peak pressures of about 80MPa can be generated using such a system [115], however this form of shock wave generator suffers from extreme variations in intensity (up to $\pm 45\%$) [118] due to the transient nature of spark gaps.

When applied to lithotripsy, the dimensions of these systems are a compromise between several factors. If the device is too large skeletal parts obscure and absorb the acoustic waves, whereas a small aperture leads to a higher power density at the body's point of entry, thereby causing pain sensation if not also tissue damage [119].

2.3 - The measurement and characterisation of acoustic transients

In the last section it has been seen that acoustic transients can be generated by a large number of different mechanisms. These sources cannot always be accurately modelled theoretically, and different sources give rise to acoustic transients with very different temporal and spatial properties. It is therefore beneficial to measure experimentally generated acoustic transients to either characterise the source, or examine the effects of the transients upon objects placed in their path. Among numerous other examples, the characterisation of acoustic transients has been shown to be useful for examining urinary and biliary stone damage in extracorporeal lithotripsy [110-113,116,119], blast wave effects from intense explosions [11,18,20], and cavitation bubble damage to surfaces [54,64-65,68-69].

There are a great number of techniques that have been developed in the last century for the detection and characterisation of acoustic transients. The most successful of these measurement techniques can be broadly divided into two categories:

- (a) *Transducers* - in which the measurement of pressure takes place at a single point in the path of an acoustic transient. Transducers give rise to a signal $S(t)$ measured with respect to time. There are two general types of transducer, firstly *piezoelectric transducers* which will be discussed in the next section, and secondly *optical probes* which will be reviewed in section 2.3.2.

- (b) *High Speed Photography* - where an acoustic transient is frozen at one of more points in time and imaged onto a recording medium. This technique gives rise to an image with intensity $I(x,y)$ which varies according to spatial co-ordinates. Temporal resolution, that is how effectively the image of the acoustic transient being measured is frozen in time, can be achieved using either (i) a *pulsed light source* or (ii) a *shuttered camera*. Both of these techniques will be discussed in section 2.3.3. In general photographic techniques can only be used for transients propagating in transparent media. Furthermore acoustic transients are invisible, however the refractive index of the medium local to the transient is pressure dependant giving rise to the refraction of light. The effects of this can be imaged, and techniques for doing this are described in section 2.3.4.

2.3.1 - Piezoelectric transducers

Acoustic transients may be detected and characterised using piezoelectric transducers. As commented earlier in section 2.2.6, this was first demonstrated in 1916 by Langevin [89] who showed that a quartz crystal placed between two metal electrodes could be used as both source and detector of sound in a simple sonar system. Devices for measuring acoustic transients propagating in water are called *hydrophones*. Traditionally hydrophones have been fabricated out of poled ceramic materials such as barium titanate (BaTiO_3), lead zirconate titanate (PZT), quartz, and lead metaniobate. Extensive reviews of the physical properties of ceramic piezoelectric materials can be found in papers by Gallego-Juarez [97] and Berlincourt [120], as well as in the book by Ikeda [96]. Ceramic piezoelectric materials have been extensively used as both sources and detectors in the medical field (e.g. ultrasound scanning and lithotriptors), as well as in non-destructive testing (e.g. flaw detection in materials) [97,100]. Since the discovery of a large piezoelectric effect in the organic polymer polyvinylidene fluoride (PVDF) [92,93], this polymer has become probably the most popular material for use in hydrophones. This material has been used in a number of configurations ranging from thin film detectors to needle hydrophones. Furthermore it has been used extensively in the characterisation of acoustic transients associated with cavitation [22,121-124], laser interactions [22,55,125], and lithotripsy [110,113,115-116,119,126].

The piezoelectric properties of ceramic and polymer piezoelectric materials are shown in table 2.3, and have been compared in Woodward [127] and also by Lancee *et al* [101]. Of particular importance in the design of hydrophones is the *piezoelectric stress constant* g_{33} . In the case of a simple transducer where the piezoelectric material is sandwiched between two metal electrodes and is poled in the direction normal to these plates, the open circuit voltage V generated upon the electrodes due to a compressive pressure P_3 applied perpendicular to the plates will be:

$$V = -g_{33}P_3s \quad - (2.54)$$

where s is the thickness of the piezoelectric material. From table 2.3 it can clearly be seen that the magnitude of the stress constant of the polymer PVDF is 13 times higher than that of ceramic materials such as PZT. Clearly from the above equation the same amount of pressure applied to similar dimension transducers fabricated out of PZT and PVDF will give rise to a far higher voltage output from the polymer.

| | $k_{33} / \%$ | $d_{33} / \text{pC/N}^1$ | $d_{31} / \text{pC/N}^1$ | $g_{33} / 10^3 \text{VmN}^1$ | $g_{31} / 10^3 \text{VmN}^1$ | $Z / 10^6 \text{kgm}^2\text{s}^{-1}$ |
|------------------|---------------|--------------------------|--------------------------|------------------------------|------------------------------|--------------------------------------|
| Rochelle salt | 76 | 550 | - | - | - | - |
| Quartz (crystal) | 10 | 2.3 | - | - | - | 15.2 |
| Barium titanate | 50 | 150 | -58 | 14 | -5.5 | 27 |
| Lead Metaniobate | 38 | 80 | -10 | 36 | -4.5 | - |
| PZT-4 | 70 | 290 | -123 | 26 | -11 | 30 |
| PVDF | 20 | -33 | 23 | -339 | 216 | 4 |

Sources : Ikeda, T. (1990) - *Fundamentals of Piezoelectricity*, Published by Oxford University Press.

Gallego-Juarez, J. A. (1989) - *Piezoelectric Ceramics and Ultrasonic Transducers*, J. Phys. E: Sci. Instrum. 22, pp804-816.

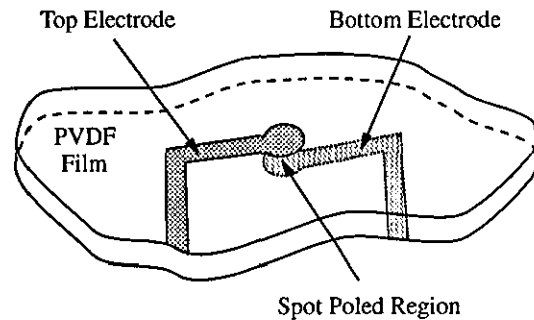
Brush-Clevite Ltd. (1966) - *Piezoelectricity, A Data Book for Designers*, Brush Clevite Ltd. Data Book., U.K.

Gulton Industries Inc. (1961) - *Glennite Piezoceramics*, Gulton Industries Data Book, U.S.A..

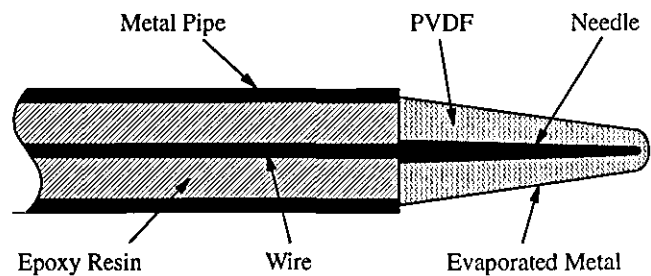
Crecraft, D. I. (1983) - *Ultrasonic Instrumentation : Principles, Methods and Applications*, J. Phys. E: Sci. Instrum. 16, pp181-189.

Table 2.3 - Properties of several piezoelectric materials.

(a) Polyvinylidene-fluoride membrane hydrophone.



(b) Polyvinylidene-fluoride needle hydrophone.



(c) Miniture ultrasonic ceramic hydrophone.

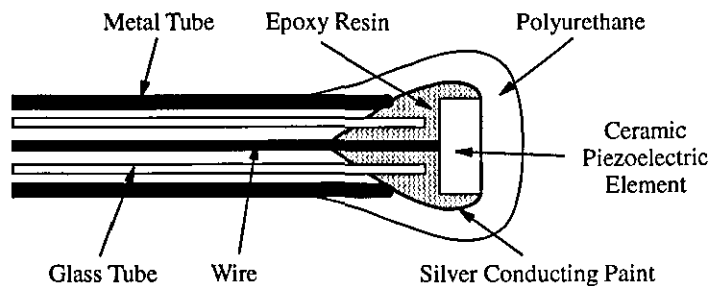


Figure 2.8 - Piezoelectric hydrophones.

An other important factor is the coupling factor k_{33} , which represents the ability of a given piezoelectric material to convert mechanical energy into electrical energy. From table 2.3 it can be seen that the coupling factor of PZT is 3.5 times larger than that of PVDF, making PZT a much more efficient material. Lastly the acoustic impedance Z of a transducer material determines the amount of an incident acoustic transient which is transmitted into the transducer at the water-transducer interface, as defined earlier by the Rayleigh's reflection coefficients [5] in equation (2.19), and equation (2.20) for normally incident waves. Clearly the polymer PVDF has a much closer acoustic impedance to water than PZT, and is therefore a much better material for detecting acoustic transients propagating in water. Typically 80% of the energy in a normally incident acoustic transient is transmitted into a PVDF transducer, whereas only 18% is transmitted into the ceramic PZT. Furthermore acoustic reflection at the transducer boundary can also significantly perturb the acoustic field being measured. Clearly the low acoustic impedance and the relatively high value for the piezoelectric stress constant makes PVDF a far more superior hydrophone material than a ceramic.

A great number of piezoelectric hydrophones have been built and it is beyond the scope for this review to detail them all. For further information the reader is referred to reviews by Gallego-Juarez [97] for ceramic transducers, and Sessler for PVDF hydrophones [95]. Several transducer designs will however be described here briefly because of their relevance to detecting water born acoustic transients with high spatial and temporal resolution.

The simplest and most common form of piezoelectric transducer comprises of a thin film of piezoelectric material sandwiched between two metallic electrodes, the piezoelectric material being poled in the direction which is normal to the plates. A typical fabrication process for PVDF film transducers can be found in reference [128], and in this material the piezoelectric effect has been found to work well for frequencies up to 10GHz [129]. The frequency response of a free standing film transducer is predominantly limited by the acoustic resonance of the film. The (half wavelength) resonant frequency f_r of the film can be calculated using the time of flight of an acoustic transient entering the film, being reflected at the rear interface, and returning to the front interface:

$$f_r = \frac{c_{trans}}{2s} \quad - (2.55)$$

where c_{trans} is the sound speed in the film which has thickness s . Typically a 9 μ m thick PVDF film transducer will have a resonant frequency of about 120MHz. Greater

temporal resolution can be obtained with thinner piezoelectric films, however this gives rise to a reduced output voltage as indicated in equation (2.54). Furthermore the voltage resolution is reduced because the amount of noise is proportional to the frequency range measured, as stated by the bandwidth theorem.

Clearly thick film transducers will have relatively poor temporal resolution. This can to some extent be improved by backing the film transducer with a material which has the same acoustic impedance and relatively large dimensions. This eliminates reflection of the acoustic transient at the rear interface back into the transducer, and gives rise to a rise time which is equal to the time for the transient to traverse the film. The wave transmitted into the backing material is then either eventually absorbed, or returns to the film via other reflections well after the signal of interest has finished. Furthermore when the rise time of the film transducer is taken into account, the pressure profile of a normally incident planar acoustic transient can be temporally resolved to a higher resolution than that of the voltage output of the transducer [130].

The parallel plate construction of film transducers also makes the device inherently capacitive, making voltage output frequency dependant. The resulting electrical impedance Z_e of such devices at a frequency f is defined by:

$$Z_e = \frac{1}{2\pi f C} = \frac{s}{2\pi f \epsilon A} \quad - (2.56)$$

where C is capacitance of the device, which varies with the area of the electrodes A and the permittivity ϵ of the piezoelectric material.

One problem with large area film transducers is that such devices have poor spatial resolution due to their size. Higher spatial resolutions can be achieved by reducing the area of the film, such as in the *spot poled membrane* transducer design [131-134] which was first demonstrated by DeReggi [131]. In this technique a thin sheet of unpolarised PVDF film, typically 25 μ m thick, is stretched over a drum and is metalised in a limited area by vacuum deposition, as shown schematically in figure 2.8(a). The electrodes on both sides of the film only overlap in the centre, and typically the resulting active area can be as little as 0.3mm in circular diameter [134]. Poling of the piezoelectric material is then performed by applying the appropriate voltage to the electrodes (an electric field of ~1MV/cm [131]) at a temperature of ~390°C for about 15 minutes. Spot poled membrane hydrophones have been shown to exhibit minimal perturbation to the acoustic field being probed, and have a broad-band and smoothly varying frequency response.

Such devices are not omni-directional however, and have a maximum frequency of up to 100MHz [132] which is sometimes too low for resolving shock fronts. This type of hydrophone has however been extensively used characterising acoustic transients generated by medical lithotriptors [115-116,119,126].

An alternative transducer design is that of the *needle hydrophone*, which is shown schematically in figure 2.8(b). This transducer was first demonstrated by Platte [135-137] and has recently been found useful for studying both acoustic transients generated by optical cavitation [121,138] and lithotripsy [110,119]. In this design a metal needle, rounded at its tip, is coated with a thin layer of polyvinylidene fluoride. The needle forms one of the transducer electrodes, and the other is vacuum deposited onto the outside of the piezoelectric material. A small spot poled zone at the needle point approximately 200 μ m in diameter forms the sensitive region of the hydrophone, which gives the transducer extremely high spatial resolution. The thickness of the PVDF layer is also smallest at the needle point, typically 20 μ m thick. As a result the device has an acoustic resonant frequency of about 55MHz giving the transducer high temporal resolution. Furthermore the curved shape of the sensitive region gives rise to non-directivity in a wide angular range.

Finally miniature hydrophones have also been constructed out of piezoelectric ceramics such as barium titanate [139,140] and lead zirconate titanate (PZT) [139]. Figure 2.8(c) shows a typical construction in which a small plate of piezoelectric material (typically 400 μ m thick and 0.8mm square [139]) is attached to a platinum wire. The piezoelectric crystal is pre-poled in the direction of the wire, which also serves as one of the electrodes. An epoxy resin is used to support the crystal at the end of a glass capillary tube, and this is coated with silver conductive paint which acts as the second electrode. Ceramic based miniature hydrophones have been found useful in the characterisation of acoustic transients originating from lithotriptors [116,126], and also in the study of optical cavitation [121,138].

2.3.2 - Optical transducers

Acoustic transients may also be accurately characterised using optical probe transducers. Almost all of these optical transducers are based upon fibre optic technology and have been reviewed in some detail by Giallorenzi *et al* [141], Bucaro and Cole [142-144], Davis [145], and most recently by Bilaniuk [146]. The idea of an acousto-optic transducer has existed since Bell [147] proposed his *photophone* in 1880, however the

first practical design for an optical acoustic sensor was probably that of Von Ohain [148] in 1935 in which an interferometer would sense vibrations on a membrane. The first acousto-optic hydrophone developed was probably the phase dependant *moving mirror* hydrophone [149]. In this arrangement light is reflected diagonally back and forth down the length of two parallel mirrors. One of the mirrors is movable and is attached to a diaphragm which responds to incident acoustic waves, thus modulating the total optical path length through the mirror system. The device forms one path of a Mach-Zehnder interferometer which is used to detect the changes in path length.

More recently Bucaro [150-151] and Cole [152] have introduced the use of optical fibre interferometers for acoustic detection. In these arrangements the moving mirror is replaced by a high quality glass fibre. The acoustic waves to be detected are allowed to interact with a portion of the fibre, and the resulting compression gives rise to a change in the refractive index the fibre core which induces phase modulation. Again the phase modulation is converted into an amplitude signal using a Mach-Zehnder interferometer. Hydrophones of this nature have been demonstrated to have a reasonably high frequency response ($>1\text{MHz}$ [153]). Furthermore perhaps the most attractive feature of these hydrophones is that it is possible to arrange the sensing fibre in almost any configuration desired: linear, spiral, and cylindrical have all been demonstrated.

Another recent hydrophone design is that of the *fibre microbend sensor* [154-155]. This device utilises induced bending loss in an optical fibre when deformed using a series of ridges connected to a diaphragm which moves under the influence of the acoustic field being detected. *Evanescent or coupled waveguide sensors* [156-158] on the other hand, have two parallel fibres placed in very close contact so that light is coupled between the two fibre cores. If light is incident along only one of these fibres then the amount of transmitted to the other is a function of the interaction length, refractive indices and separation of the cores [157]. The refractive indices and core separation can be altered by an incident acoustic wave, and therefore give rise to a signal in the second fibre.

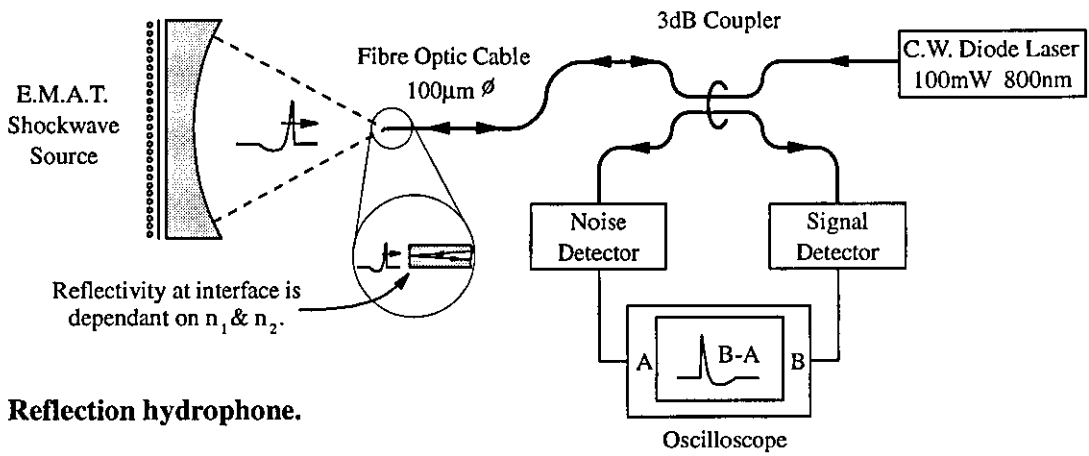
The *moving fibre hydrophone* [159] employs two fibres which are mounted such that their end surfaces are parallel, coaxial, and separated by about $2\mu\text{m}$. The acoustic waves incident induce relative motion between the two fibres, one of which is fixed and the other is free to move in the acoustic field. Relative motion varies the light coupled between the two fibre ends and thus modulates the transmitted light intensity. A more sensitive arrangement based upon *frustrated total internal reflection* has been demonstrated by Spillman and McMahon [160]. In this arrangement the two fibre ends are cleaved at the critical angle so that total internal reflection occurs for all modes

propagating in the fibres, and the fibres are positioned sufficiently close to each other so that a large amount of the light power is transmitted across the gap. If one of the fibres is fixed and the other is connected to a diaphragm, then vertical displacements caused by acoustic interactions with the diaphragm give rise to modulation of the light power coupled between the two fibres.

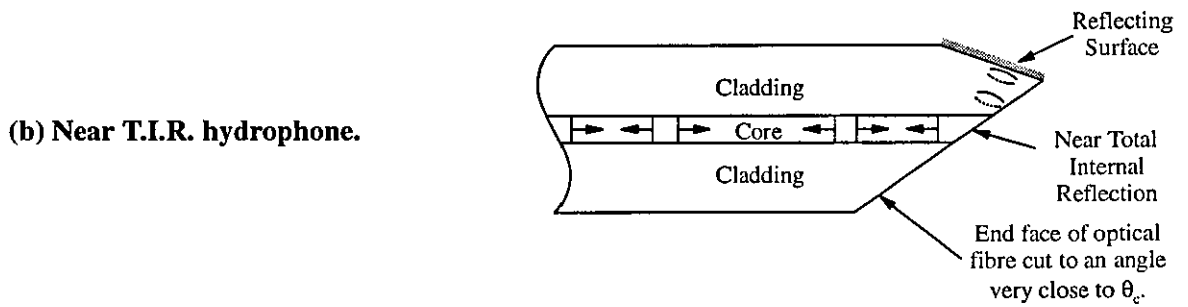
Hydrophones based upon changes in the polarisation of light propagating down a single mode fibre have also been demonstrated [161-162]. In these devices a coil of fibre is placed in tension by wrapping it around a small compliant cylinder, which induces a large birefringence in the fibre. When a linearly polarised input beam is used, changes in the polarisation of the light induced by an incident acoustic transient can be simply detected using analysing polarisers. Another sensor, the *Schlieren* [163] or *grating* [164] hydrophone, uses two parallel diffraction gratings of which one is attached to a diaphragm and the other is fixed. These are mounted in a collimated probe beam, and the relative movement the gratings perpendicular to the light beam induced by the incident acoustic field at the diaphragm gives rise to modulation of the light beam. This sensor has advantages over others in that tight mechanical tolerances are not required.

Although proven to be extremely useful in many underwater applications, the transducers described above do not address the problem of measuring acoustic transients with high spatial and temporal resolution. Infact due to their physical size many of the above are unable to resolve the fast rising curved wavefront shock waves generated by, say, optical cavitation. One fibre optic sensor which is capable of measuring acoustic transients with high spatial resolution has been demonstrated by Staudenraus and Eisenmenger [165-167]. This transducer is shown schematically in figure 2.9(a), and is based upon changes in the reflection of light at the end of a single mode glass fibre which is submerged in water. The reflectance at the fibre tip is perturbed by changes in the refractive index of the water arising from an acoustic transient incident upon the front face, and a probe beam generated by a semiconductor laser (100mW, 800nm) is then used to measure this effect. A 3dB fibre coupler is used to sample the reflected light so that the signal can be measured by a photodiode. Furthermore noise generated by the semiconductor laser is removed by sampling the probe beam before reflection, and subtracting it from the measured signal.

The spatial resolution of the fibre optic hydrophone is determined by the diameter of the glass fibre, which in the case of the device demonstrated by Eisenmenger [165] is 100 μ m. As commented above, the sensitivity of the transducer to acoustic waves is dependant upon the reflectance at the glass-water interface. Since the refractive index of glass is



(a) Reflection hydrophone.



(b) Near T.I.R. hydrophone.

Figure 2.9 - Fibre optic probe hydrophones.

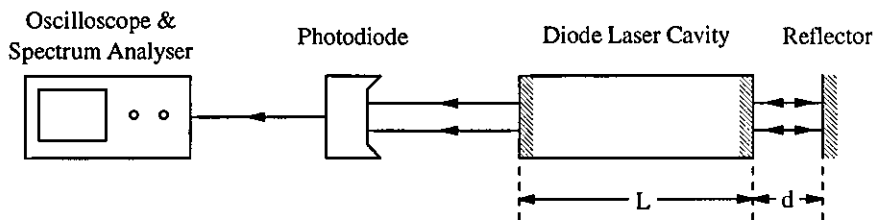


Figure 2.10 - Diode laser acoustic sensor.

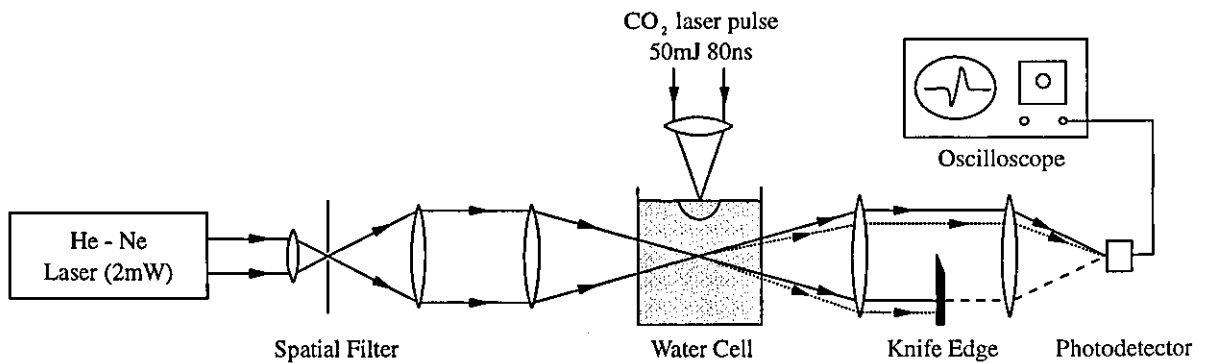


Figure 2.11 - Experimental arrangement for Schlieren probe method.

relatively insensitive to stress, the reflectance is predominantly determined by changes in the refractive index of the water. Unfortunately the change in the refractive index of water due to an applied pressure is rather small ($\Delta n/\Delta p \sim 1.4 \times 10^{-5} \text{ bar}^{-1}$ [165]), and therefore the overall sensitivity of the device is also small. As a result the signal measurement requires the detection of a small decrease in reflected light intensity against a relatively large background. Furthermore only 0.4% of the probe beam is reflected back down the fibre to the photodiode. This fails to utilise all of the probe beam intensity, and almost all of the powerful ($\sim 100 \text{ mW}$ [165]) probe beam is transmitted into the water making eye protection necessary, which makes this device difficult to use. This device has however been demonstrated characterising the acoustic output of lithotriptors [119,165].

Phillips [168] suggested a similar fibre optic reflection hydrophone with a much higher sensitivity. The design is shown schematically in figure 2.9(b) and is based upon a single mode fibre which is cleaved close to the critical angle. The reflectance of the water-to-fibre interface is defined by the *Fresnel equations* [169], which are functions of the incident angle and polarisation of the probe beam, as well as the refractive indices of the media involved. The greatest sensitivity of the reflectance to small changes in the refractive index is found to be at, or just below, the critical angle. Furthermore at this angle almost all of the probe beam is reflected back down the fibre to the photodetector. This results in the signal measurement being made against a much smaller background radiation level, and allows the use of a much less powerful probe beam source. The *near total internal reflection hydrophone* has however never been demonstrated practically, and it is thought that this was because the cleaved fibre end disrupted the single mode properties of the fibre giving rise to high beam divergence, thus reducing the sensitivity of the device. This will be discussed in more detail in chapter four.

Other techniques for improving the sensitivity of a reflection probe hydrophone have also been demonstrated and are described by Davis [145]. One method is to coat the plane cleaved end of a fibre with a mirror, and incorporate this as one arm of a *Michelson interferometer*. If the fibre tip is placed in the path of an acoustic transient, then changes in the refractive index of the fibre will give rise to a change in the relative path length of the interferometer arms. This is detected by a photodiode when the two (coherent) light beams combine and interfere at the beam splitter. A second technique involves coating the fibre tip with a half silvered mirror, followed by thin film of transparent material, and on top of this a fully reflecting mirror. This arrangement forms a *Fabry-Perot interferometer* in which interference of a coherent probe beam takes place at the half silvered interface. Again an incident acoustic transient causes changes in the refractive

index of the fibre. This gives rise to phase modulation of the probe beam, which is converted to an amplitude modulation by the interferometer.

An other sensor capable of measuring acoustic transients with high spatial resolution has been demonstrated by Dandridge *et al* [170]. This device is shown schematically in figure 2.10 and utilises a single mode semiconductor laser with an external second mirror. The external reflector, placed in the path of the acoustic transient, feeds light back into the laser cavity, and the phase of the reflected light is determined by the displacement of the mirror. When the reflected light is in phase with that inside the laser cavity the effect is to raise the reflectance of the front laser facet, whereas when the light is out of phase the facet reflectance is lowered. The resulting modulation of the laser output intensity is monitored by a photodiode placed near to the rear facet of the laser. The great advantage of this device is that it is extremely sensitive and is capable of detecting displacements as small as 10^{-4} nm [170]. Furthermore the sensor can be made very small thus giving it high spatial resolution.

A technique for measuring the amount of refraction experienced by a narrow probe beam while being traversed by an acoustic transient has been demonstrated by Davidson and Emmony [171]. The basic set-up for the *schlieren probe* is shown schematically in figure 2.11, in which the probe beam is generated by a He-Ne laser which is spatially filtered and focused by a camera lens. After passing through the test area the beam is collimated to a parallel beam and then re-focused on to a fast photodiode. A knife edge is used to mask off some of the re-collimated light, and deflection of the beam at the focus gives rise to a modulation of the beam intensity at the photodiode. The spatial resolution of the technique is determined by the diffraction limit of the probe beam and the temporal resolution by the response of the photodiode detector. Similar techniques have also been used in the study of cavitation [121,138] and laser induced breakdown [40,53,172-173].

Finally there are also a range of probe beam techniques for studying surface waves. It is beyond the scope of this review to discuss them here, and the reader is referred to a number of reviews by Monchalin [174], Sontag and Tam [175], Wagner [176] and Dewhurst [177], as well as a paper by Halliwell *et al* [178].

2.3.3 - High speed photography

High speed photography has been extensively reviewed by a number of authors including Field [179], Fuller [180-185] and in books by Holder and North [186], Jones [187] and Saxe [188]. In this technique an image of the event is "frozen" at one or more points in time and recorded on, say, photographic film so that it can be reviewed at a later stage. Some form of temporal resolution is required however, and this can be achieved using one of two techniques: (i) by illuminating the event using a flash light source, or (ii) by photographing the event using a camera with a high speed shutter. These techniques are discussed below.

(i) Flash light sources

A short duration flash light source can be used to illuminate the acoustic transient with a bright pulse of light, which is subsequently imaged onto a relatively slow recording medium such as a CCD camera or photographic film. In order to temporally resolve the acoustic transient, that is minimise the image blur, the pulse duration needs to be as short as possible. The most desirable situation is that the movement of the image during the light pulse is smaller than the thickness of the acoustic transient shock front. Acoustic transients typically last for up to about $1\mu\text{s}$, and shock fronts in water are typically of 10ns duration. At present only spark discharge light sources and lasers are capable of providing such short exposure times.

Spark discharge sources are technically the simplest method of obtaining a short duration pulse of light, and have been reviewed in some detail by Frungel [82-85]. Historically the first high speed photographs of acoustic transients were taken by Toepler [80] using this method, applying the flash photography technique first demonstrated in 1851 by the inventor of modern photography, William Fox Talbot [179,182]. The internal processes of spark discharge have already been described earlier in section 2.2.5. Obtaining sparks of sub-microsecond duration which are bright enough to expose film has been found to be very difficult. It requires careful control of the geometry and material of the electrodes, the gas surrounding the spark gap, and the electrical parameters of the driving circuit [179]. Typical designs for use as high speed photographic light sources are shown in figure 2.12, and include the *sandwich*, *Liberstarr* and *Schlieren* spark gaps [82-85].

The *laser* is a more recent development having been used since the mid 1960's as both a useful source of acoustic transients (see section 2.2.3) and a short duration pulsed illumination source in high speed photography. The acronym L.A.S.E.R. stands for Light

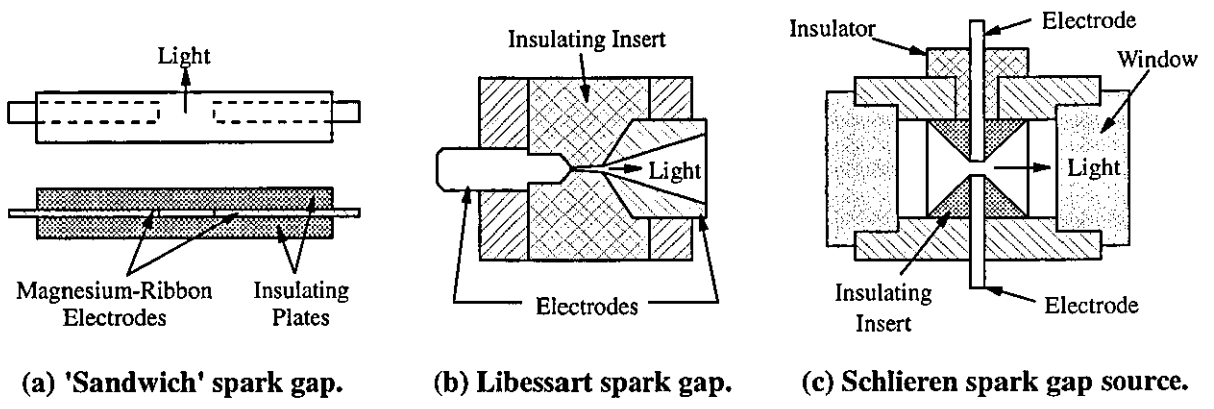


Figure 2.12 - Spark light sources.

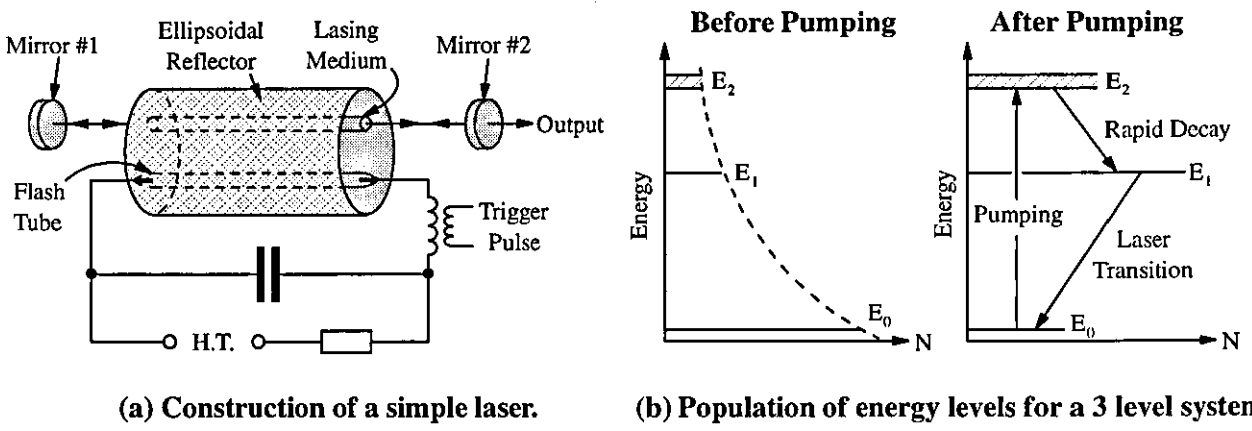


Figure 2.13 - The basic principles of a L.A.S.E.R.

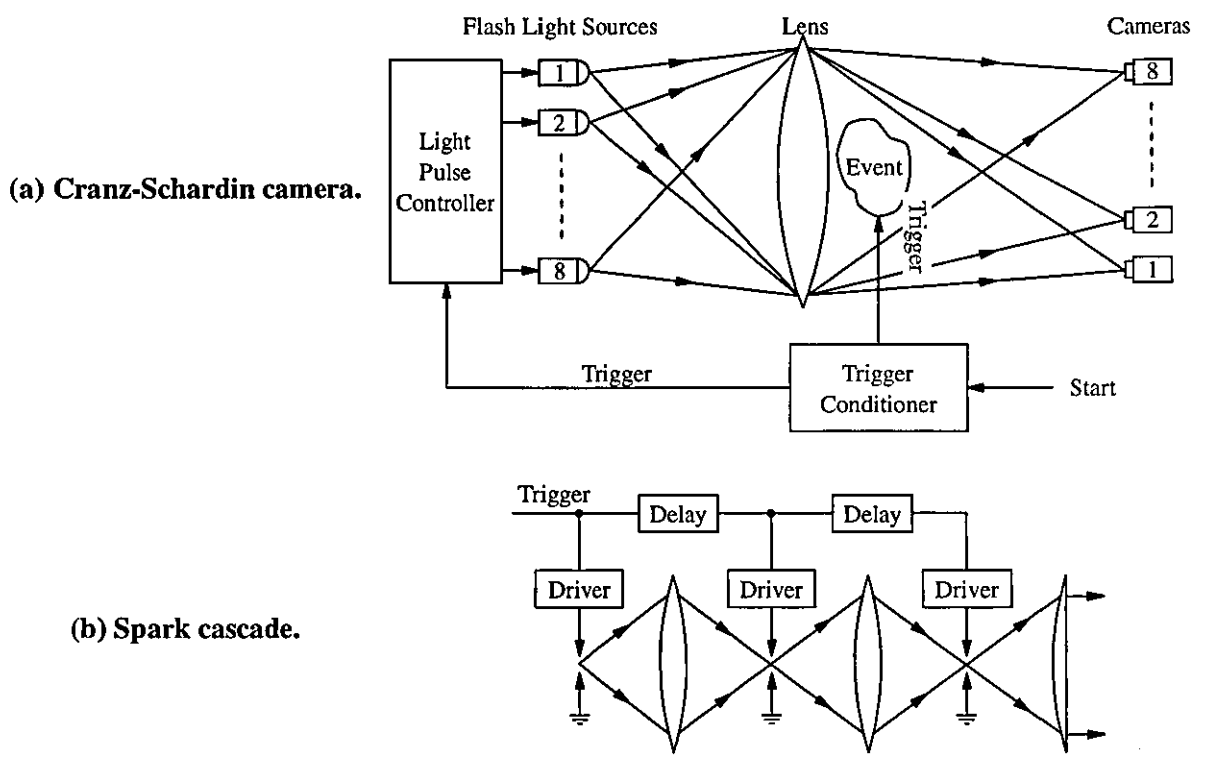


Figure 2.14 - Multiple pulse photography.

Amplification by Stimulated Emission of Radiation. Lasers work by virtue of stimulated emission between two atomic energy levels. This was first shown theoretically by Einstein in 1917 [189], however it was not until 1960 that Maiman [190] first demonstrated laser operation in the visible spectrum using a ruby crystal.

The construction of a simple ruby laser is shown schematically in figure 2.13(a), and operates as follows. Under normal circumstances the electron levels of the ruby crystal are occupied according to Boltzmann statistics, such that the higher energy levels have relatively few electrons, as shown in figure 2.13(b). When light from a conventional source such as a photographic flash tube is "pumped" into the crystal, electrons are raised into excited states (E_2) before rapidly decaying into a single lower metastable state (E_1). When the pumping is intense enough the metastable state will have more electrons than the ground state (E_0), which is called population inversion. If a single photon is then spontaneously emitted by an electron transition from the metastable state to the ground state, then after propagating a short distance it will stimulate the emission of a second photon with the same wavelength (energy), phase, direction and polarisation. In this situation stimulated emission is far more likely than absorption of the original photon because of population inversion. These two photons then go on to stimulate further photon emission in the same way, and an avalanche effect builds up giving rise to a large flux intensity. The lasing medium is placed in a Fabry-Perot etalon (mirrors #1 and #2) which provides optical feedback, enhancing the amplification process by redirecting escaping laser light back into the medium. In the early stages of the lasing process spontaneous photons are emitted in all directions, and all except those propagating along the mirror axis are lost. This gives rise to an output beam which is both highly collimated and coherent. Furthermore the mirror cavity gives rise to longitudinal and transverse standing waves, the characteristics of which are determined by the separation of the mirrors. The resonant modes of the cavity are considerably narrower in frequency than the bandwidth of the normal spontaneously emitted photons. This acts such that light of only a certain narrow wavelength band is selected and amplified, giving rise to a monochromatic output beam.

Many different types of laser exist, and are reviewed in some detail by numerous authors, including Wilson and Hawkes [191-192] and Hecht [193]. The output properties of several pulsed laser sources are summarised in table 2.2 [23]. In general the most suitable lasers for high speed photography are Q-switched. In these lasers a fast optical switch is placed within the Fabry-Perot cavity which initially inhibits the lasing action such that the population inversion is enhanced. The Q-switch is turned on when the population inversion reaches its peak, and this gives rise to a tremendously fast and

powerful output light pulse as the electrons drop to the lower states in unison. In practice, dye [54,123-124], nitrogen [34], ruby [32,46,113-114] and Nd-YAG [46,194] lasers have been used for the study of acoustic transients. More recently semiconductor lasers have begun to be used in high speed photography and this will be discussed in more detail in chapter three.

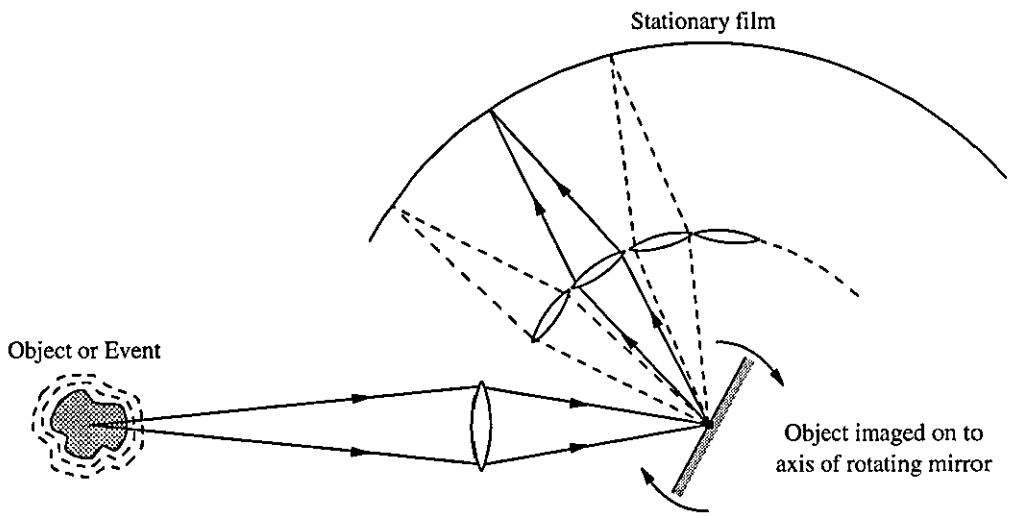
A single flash of light illuminating an acoustic transient is capable of producing just one picture. If the event can be repeated accurately, then a sequence of pictures can be built up by simply repeating the experiment and altering the delay between the emission of the acoustic transients and the light pulse. Most dynamic events are however not easily repeated, and it is therefore necessary to obtain the sequence of images from just a single event. One approach is to use the Cranz-Schardin camera which is shown schematically in figure 2.15(a). In this arrangement several pulsed light sources are spaced out in a grid pattern and are triggered at different times. The resulting sequence of images of the event are recorded on either a single camera [195] or an array of cameras [196]. One disadvantage with this type of camera is that unless rather complicated optics are used, the images are taken at different angles and therefore suffer from problems with parallax. The great advantage with this technique is that framing rates of above 1 million frames per second are achievable. Other techniques involve either a single source pulsed a number of times, or alternatively a number of (schlieren) spark gap sources placed in the cascade arrangement shown in figure 2.15(b). In these techniques the sequence of events build up on the same image, and a dark field imaging method such as Schlieren is often required so that the image is not swamped by the background light.

The image(s) of the acoustic transients can be recorded on a variety of recording media, the most popular being photographic film and CCD cameras. Photographic film has the advantages of being highly sensitive with high spatial resolution, however it is inconvenient as it is slow to wet process. Whereas CCD cameras are often more useful because their output is a continuous electronic signal which is observable in real time on a TV monitor, and can be stored on a frame grabber. The disadvantages of CCD cameras is that they suffer from relatively low resolution compared with photographic film and are often not as sensitive. Typically a black and white photographic film such as Ilford HP5 [197-198] requires an exposure of 10^{-3} lux-seconds, whereas CCD cameras on the other hand require a more powerful light source providing about 1 lux over a 1/50 second field [199]. Further details on the workings of CCD cameras can be found in chapter three.

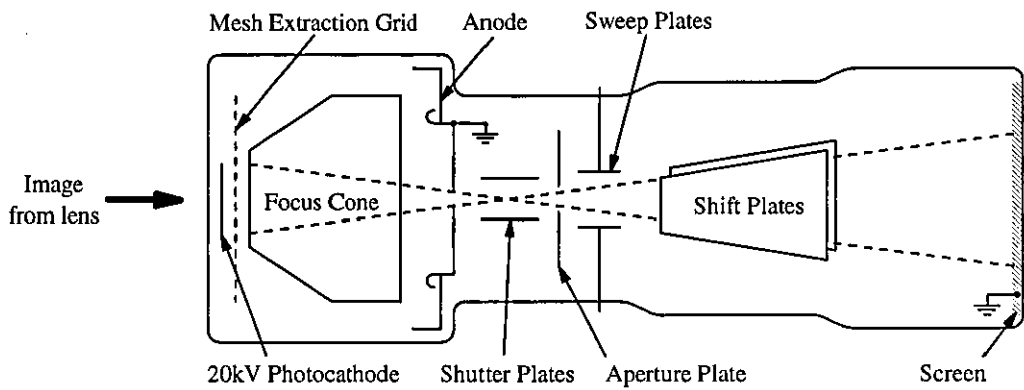
(ii) Shuttered cameras

As commented above, in high speed photography the exposure time must be shorter than the duration of the transient in order to resolve the acoustic transient spatially on the recorded image. This can be achieved using shuttered cameras, in which the light is blocked off from the recording medium either mechanically or electronically for all time except during the exposure. A sequence of events can be built up from a number of exposures which can then be recorded on either the same picture or a sequence of different pictures. Traditional moving picture cameras such as the Cinecamera (or intermittent pin-register camera [179,181]) are far too slow for this application and are limited by film strength and other mechanical tolerances. The stresses placed upon the film can be overcome somewhat by supporting the film in motion such as in a drum camera [181], and moving the image of the event with the motion of the film using rotating prisms [179,181] or lens arrays [181]; however framing rates of up to 10,000 frames per second (f.p.s.) can only be achieved. High speed photography of acoustic transients can however be achieved using the following camera designs:

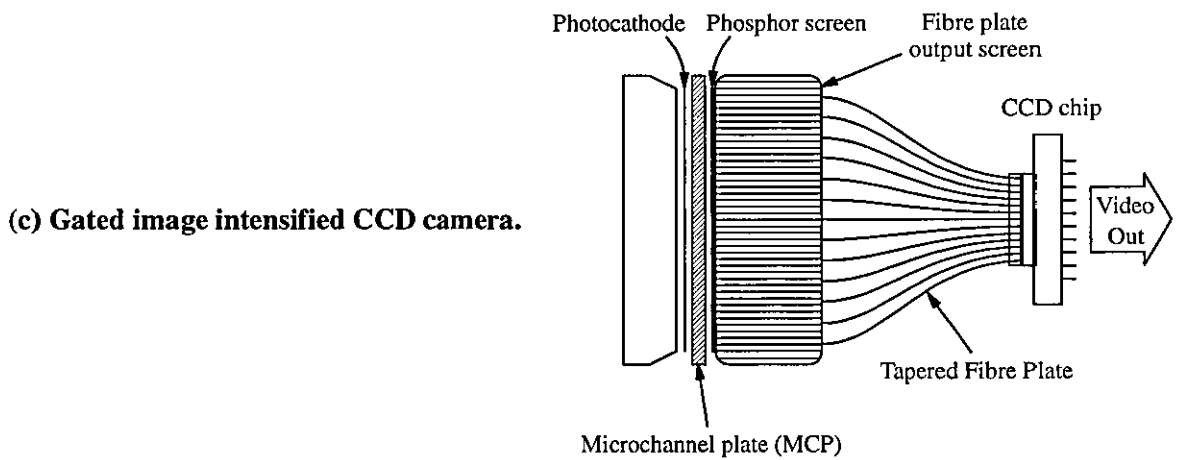
- (a) *Rotating mirror or frame camera* - still higher frame speeds can be achieved when the event is first imaged on a rotating mirror, shown in figure 2.15(a) which then re-images the light through framing lenses onto the stationary film held on a drum. Temporal resolution of the images is provided by the lens apertures as the light is continually moved by the mirror over the lens arrays. The event, light source, and camera are usually synchronised so that double exposure does not take place as the mirror is continually rotating. Typically top framing rates of up to 25 million f.p.s. can be achieved using this arrangement, and depending on the design up to 200 frames can be stored [179].
- (b) *Image Converter camera* - in this type of camera, shown in figure 2.15(b), the light falls first onto a sensitive photocathode which releases electrons according to the image intensity. In a single frame a short duration electronic pulse is applied to the shutter plates, which then allows a short burst of electrons to be imaged on a phosphor screen which is then recorded using a conventional camera. Furthermore in an *image converter framing camera*, a series of deflecting sweep and shift plates moves the electron beam to different parts of the screen giving a set of frames over several consecutive exposures. Image converter cameras can provide framing rates of up to 600 million f.p.s. and typically up to 20 frames [179]. The image converter framing camera has become extremely popular for studying acoustic transients



(a) Moving mirror or frame camera.



(b) Image converter camera (Ima-con).



(c) Gated image intensified CCD camera.

Figure 2.15 - Cameras for high speed photography.

[25-26,33], and further information on this type of high speed camera can be found in a review paper by Garfield [200].

- (c) *Streak cameras* have been used to characterise the development of laser generated acoustic transients [25-26,49-50]. In a simple streak camera the event is first imaged on to a slit. This takes a one dimensional sample of the image which is then re-imaged and scanned across a recording medium with constant velocity by a mirror. The development of the event is then reviewed on the recording medium with one axis representing time. One advantage with this technique is that the event can be studied with extremely high temporal resolution (i.e. sub-nanosecond), however the primary disadvantage is that only a one dimensional sample of the event can be studied.

- (d) *Gated microchannel plates* are the latest development in high speed camera technology. Figure 2.15(c) shows schematically a gated microchannel plate attached to a CCD camera, although it could also be incorporated into image converter cameras [201]. In this case the optical image is focused on to the photocathode where it is converted into a photoelectron image. When a negative shutter voltage pulse is applied to the cathode the electrons are accelerated by the electric field onto the microchannel plate (MCP). The microchannel plate consists of a large number of small tubes, in which the electrons are accelerated further and their number are amplified through collisions with the tube walls. Finally the intensified electron image is converted into light which is subsequently coupled to the CCD camera through a fibre optic array. Further information on this type of high-speed camera can be found in several papers by Kume et al [201-202].

2.3.4 - Imaging techniques

Many problems in science and engineering involve substances that are colourless, transparent and non-luminous, so that their observation by direct visual or photographic methods is inherently difficult. This is particularly true for the study of acoustic transients propagating in transparent media, as well as in other situations such as the investigation of air flow around aeroplane wings and jet engine compressor blades. It is often the case that the phenomena of interest is related to changes in refractive index, and this can be visualised using one of several optical techniques which depend upon the refraction of light. These techniques will be reviewed in this section.

The refractive index of a medium may vary across the field of interest because different substances are present at different points in the field, or because the density of the substance changes because of its temperature and pressure are non-uniform. In the case of acoustic transients, the latter effect is important since the density of the medium being imaged is dependant upon the pressure of the acoustic transient. Taite [203-204] discovered during the mid 1870's that a simple linear equation can accurately describe the changes in density of sea water with applied pressure. It has since been found that the Taite equation of state accurately describes the changes in density of many materials for applied pressures up to 100MPa [204]. Furthermore in the late 1850's Gladstone and Dale [205-206] discovered that there is a linear relationship between the refractive index and density of many optical materials for excess pressures of up to about 100bars [207]. This will be discussed in greater detail in chapter four, section 4.3.

Figure 2.16 shows the effect that a refractive index gradient has upon a ray of light. Here the density and hence refractive index gradient is perpendicular to the incident ray. The ray suffers no change in course upon entering the new region, however clearly the light starts to bend towards the higher refractive index region immediately after entry. Upon reaching the far side of the refractive index disturbance the ray is refracted further according to Snell's law [169]. As a result of this the imaging techniques described below are in general only sensitive to refractive index gradients perpendicular to the direction of the illumination beam.

(i) Shadowgraphy

Shadowgraphic imaging is a comparatively simple technique which is used for the visualisation and measurement of positions and dimensions, and was first introduced as a scientific technique in 1880 by Dvorak [208]. The technique can be applied usefully in high speed photography by illuminating the event of interest with a point or collimated light source, and recording the shadow of the object using a camera. In the case of an opaque object, such as a cavitation bubble, the method can only give an umbra, that is a region of complete shadow. Whereas for a transparent object such as an acoustic transient, the intensity of the image depends upon the refractive index variations across the field of view. This situation, called *direct shadowgraphy*, is shown schematically in figure 2.17. Light is deflected away from its normal path by the changes in refractive index, and this results in intensity fluctuations which are recorded by the camera (Σ). An increase in the refractive index gradient perpendicular to the illumination beam gives rise to a decrease in the recorded light intensity; whereas a decrease gives rise to an increases in the light intensity. Infact in direct shadowgraphy the recorded image intensity is

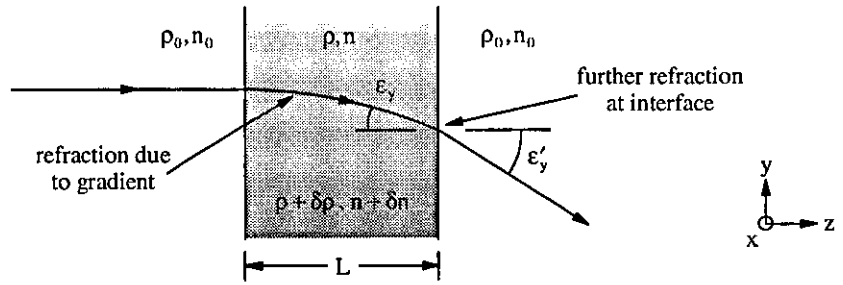


Figure 2.16 - Refraction of a light ray through a refractive index gradient.

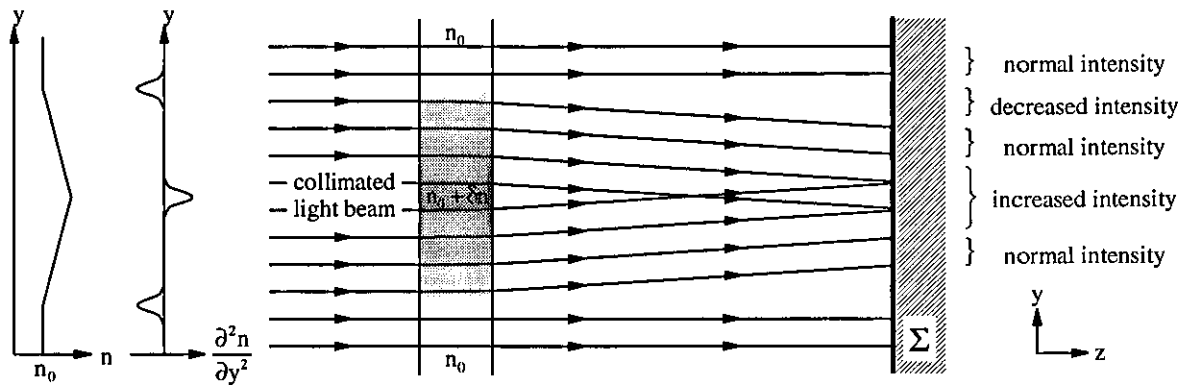
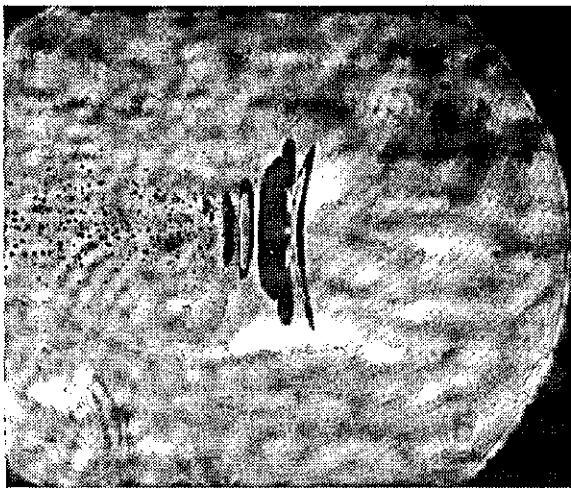
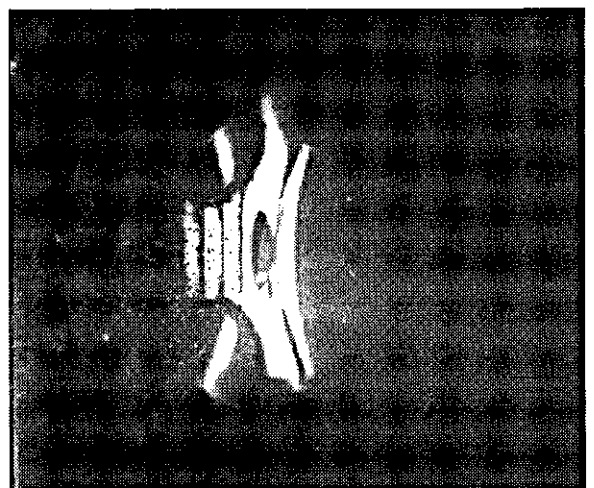


Figure 2.17 - Direct Shadowgraphy, where a parallel beam of light is disturbed by changes in the refractive index of the system.



(a) Shadowgraph imaging.



(b) Schlieren imaging.

Pictures taken from "Optical Imaging of Shock Waves Produced by a High-Energy Electromagnetic Transducer" by M.T.Carnell, R.D.Alcock & D.C.Emmony, Phys. Med. Biol. v38, 1993, p1575.

Figure 2.18 - Example high speed photographs of shock waves at the focus of a lithotripter.

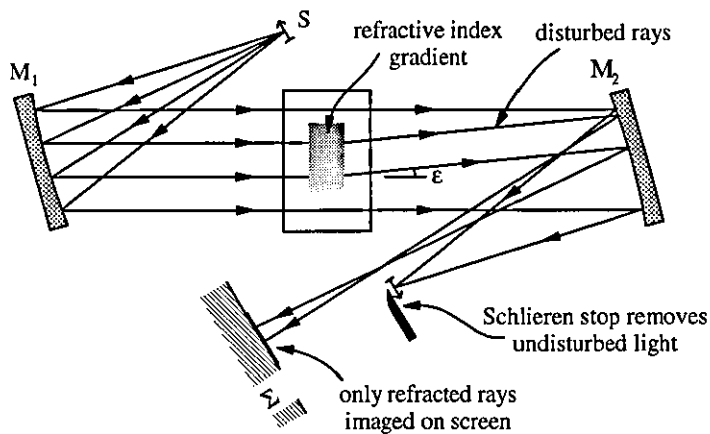
proportional to the second derivative of the refractive index with respect to distance in the plane perpendicular to the illumination. As result however, quantitative measurements of intensity variations are not sufficient to provide enough information deduce the spatial distribution of refractive index and hence pressure field of the medium.

In *focused shadowgraphy* the refractive index disturbance is imaged onto the camera using a lens, and the undeflected collimated input illumination beam is brought to a focus at the focal plane of the lens. Refraction of light in the object plane of the lens does not give rise to any changes in the image intensity recorded by the camera. Infact increases in the local image intensity recorded are only due to light being deflected before or after the object plane, and this light is imaged out of focus and displaced on the resulting image. Consequently decreases in the local image intensity occur where this light would have normally been imaged to, and are also due to light being deflected beyond the aperture of the imaging lens. Again it is not possible to quantitatively derive the pressure field using this technique, and shadowgraphic imaging is not as sensitive as other imaging techniques such as Schlieren and Mach-Zehnder interferometry. This technique has however been found to be very useful for studying the propagation of acoustic transients generated by optical cavitation in liquids [34,46,125,194,209] and in lithotripsy [113-114]. An example of a high speed photograph taken using the shadowgraphic imaging technique of an acoustic transient generated by an electromagnetic lithotripter (see section 2.2.7) can be seen in figure 2.18(a). Further details on the shadowgraphic imaging technique can be found in chapter three, section 3.5.4, and in the book by Holder and North [186].

(ii) Schlieren

Focused shadowgraphy can be made much more sensitive to perturbations in the refractive index of the medium by placing an opaque stop at the focus of the imaging lens to remove the undeflected zeroth-order light beam. This technique is called *schlieren imaging* and was first introduced by Toepler in 1864 [80,210], initially for examining defects in optical elements, and later for visualising compressible fluid flows. The technique has since been developed for studies in many different areas such as ballistics [183,185], aerodynamics [186], and the propagation of acoustic transients in fluids [22,48,113-114,123-124,218].

Two different arrangements for schlieren imaging of refractive index disturbances are shown in figures 2.19(a) and (b) respectively. In both arrangements light from an extended source is collimated using either a concave mirror or lens, and is used to



(a) Schlieren method using concave mirrors.

(b) Schlieren imaging using lenses.

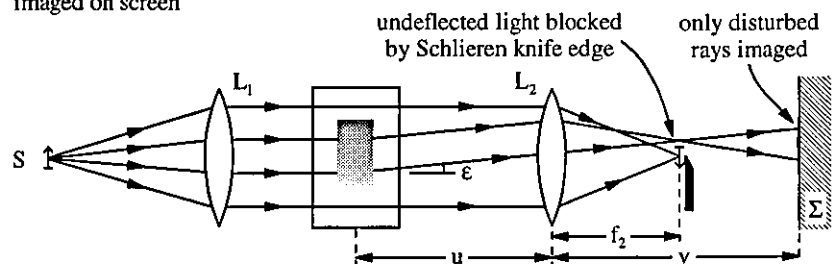
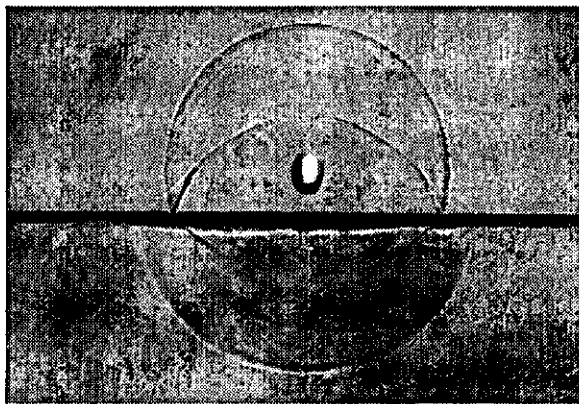
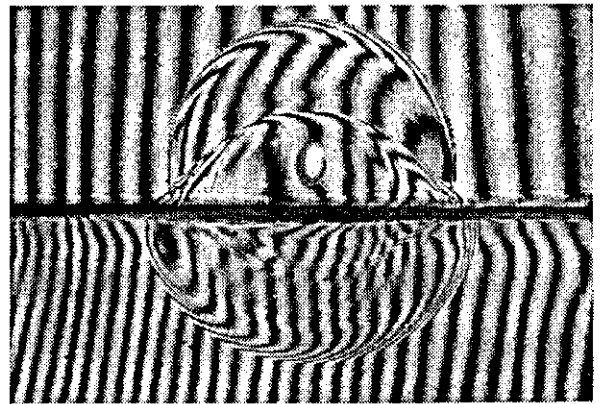


Figure 2.19 - Examples of Schlieren imaging apparatus.



(a) Schlieren imaging.



(b) Mach-Zehnder interferometry.



(c) Circular polariscope imaging.

Pictures supplied by kind permission of Y. H. Jin, from "Optical Investigations of Cavitation", Loughborough University Thesis.

Figure 2.20 - Example high speed photographs examining the interaction of acoustic transients created by optical cavitation at a water-polycarbonate boundary.

illuminate a test region containing the event, which is subsequently imaged on to a screen (Σ) using either a second concave mirror or camera lens. In the Toepler method a knife edge *schlieren stop* is brought in to the focal region of the imaging mirror or lens, which partially obscures the image of the extended source (S). A refractive index gradient in the test area gives rise to an angular beam deflection ϵ which displaces the image of the source on the knife edge. This results in a change in the image intensity recorded on the screen, the intensity increasing if the deflection is away from the knife edge. If the knife edge is carefully positioned so that it obscures the whole of the image of the source, the imaging system becomes a high pass filter in which the intensity variations across the image plane are proportional to the first derivative of the refractive index perturbations in the test region with respect to distance. Furthermore although quantitative Schlieren methods exist, they are however extremely difficult and are comparatively inaccurate compared with more quantitative techniques such as Mach-Zehnder interferometry, which is described below.

An example high speed photograph of a shock wave generated by an electromagnetic lithotripter [113-114] taken using the schlieren imaging technique can be seen in figure 2.18(b). By comparing this image with that taken with the same source using shadowgraphic imaging, which is shown in figure 2.18(a), it can clearly be seen that the schlieren technique is much more sensitive to perturbations in the refractive index of the medium and shows the image on a dark background. Furthermore, an other example of a schlieren image is shown in figure 2.20(a) [22]. In this picture optical cavitation has been generated in water close to a transparent solid. The initial acoustic transient originating from the dielectric breakdown of the water can clearly be seen propagating with spherical symmetry in the upper half of picture, together with its reflection at the liquid-solid boundary, and also in the solid shown in the lower half of the picture. Finally the schlieren imaging technique is described in greater detail in chapter three, section 3.5.4, and is reviewed in the classic text by Holder and North [186].

(iii) Mach-Zehnder interferometry

Since its development by Zehnder [211] and Mach [212] in 1891 in the fields of ballistics and air jets, the *Mach-Zehnder interferometer* has been found to be extremely useful for the quantitative measurement of refractive index disturbances. The great advantage of using interferometry is that it provides a technique for visualising a dynamic field and, perhaps more importantly, it makes possible numerical analysis of the interferograms in situations where schlieren images are quite inadequate.

A high speed Mach-Zehnder interferometry set-up for studying acoustic transients generated by Nd-YAG laser optical cavitation is shown schematically in figure 2.21. It comprises a short duration pulsed coherent light source, beam preparation optics, two semireflecting plane beam splitters (B1 and B2) and two fully reflecting mirrors (M1 and M2). The optical paths of the two interferometer paths are matched using a compensating sample, and the two light beams are recombined at the second beam splitter (B2) giving rise to interference fringes. The cavitation event created within the test sample is imaged on to a CCD camera using a camera lens, and the resulting image is stored on a frame grabber and viewed using a television monitor. Perturbations in the refractive index of the fluid in the test sample give rise to changes in the optical path length of the interferometer. This results in a displacement of the fringes recorded by the CCD camera which can subsequently be analysed quantitatively using computational techniques. This has been demonstrated by Ward and Emmony who derived the radial pressure profiles of spherically symmetric acoustic transients produced during optical cavitation using the Abel-inversion technique [54,209,213-215].

An example Mach-Zehnder interferogram can be seen in figure 2.20(b) [22] in which optical cavitation has been generated in water close to a transparent solid. Significant fringe displacements can be clearly identified in both the water and the solid, and are due to the initial acoustic emission from the plasma. Furthermore these fringes extend over greater distances than the intensity variations observed using schlieren imaging in figure 2.20(a), and it can therefore be said that Mach-Zehnder interferometry technique is more sensitive.

(iv) Photoelastic imaging

Although schlieren and shadowgraphic imaging are very useful for studying the propagation of acoustic transients in fluids, these techniques are quite inadequate for the highly complicated situation of waves travelling solids. The reason for this lies in the fact that whereas in fluids only longitudinal sound waves can exist (see section 2.1.2), in solids transverse and surface waves are also possible. Shadowgraphy and schlieren imaging are only capable of resolving changes in the refractive index of media resulting from longitudinal waves, and are completely insensitive to shear waves in which the local pressure remains unchanged. Since the discovery of the phenomena of *double refraction* induced by mechanical stress in amorphous transparent materials by Brewster [216] in 1815, the technique of photoelastic imaging has become extremely useful for analysing stresses within solid materials.

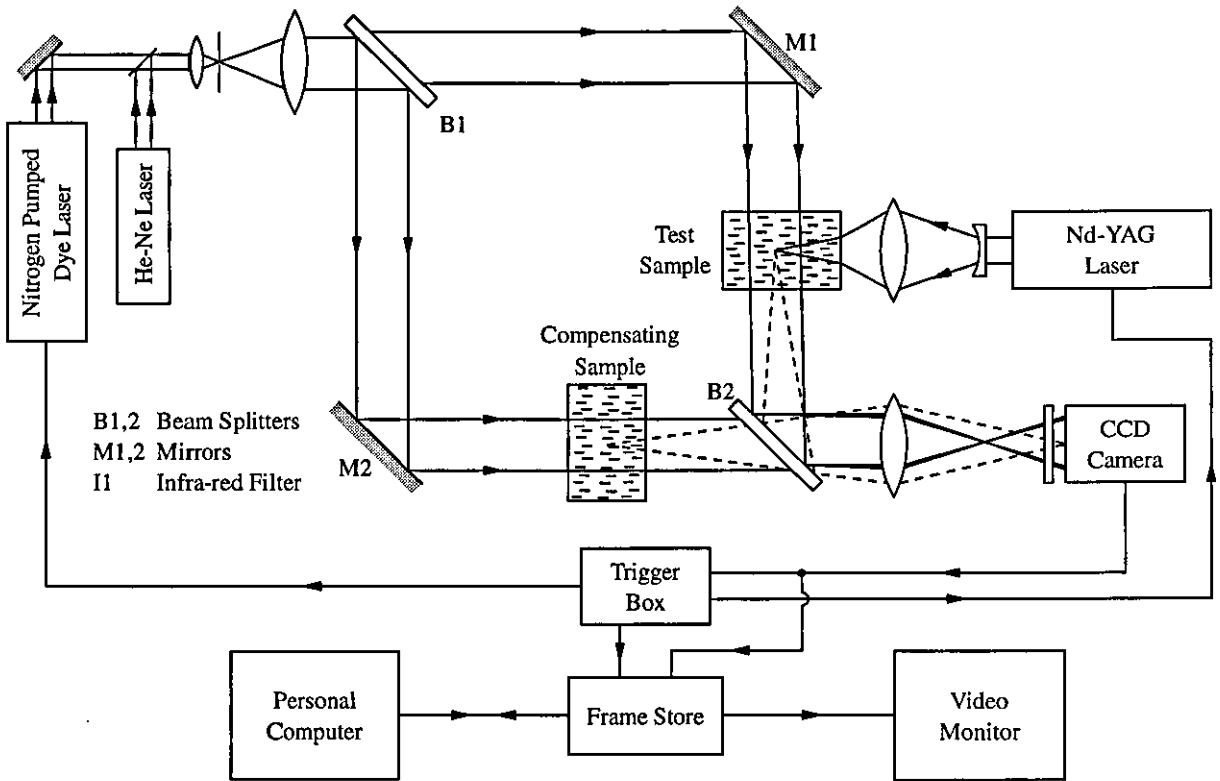


Figure 2.21 - High speed photography using a Mach-Zehnder interferometer.

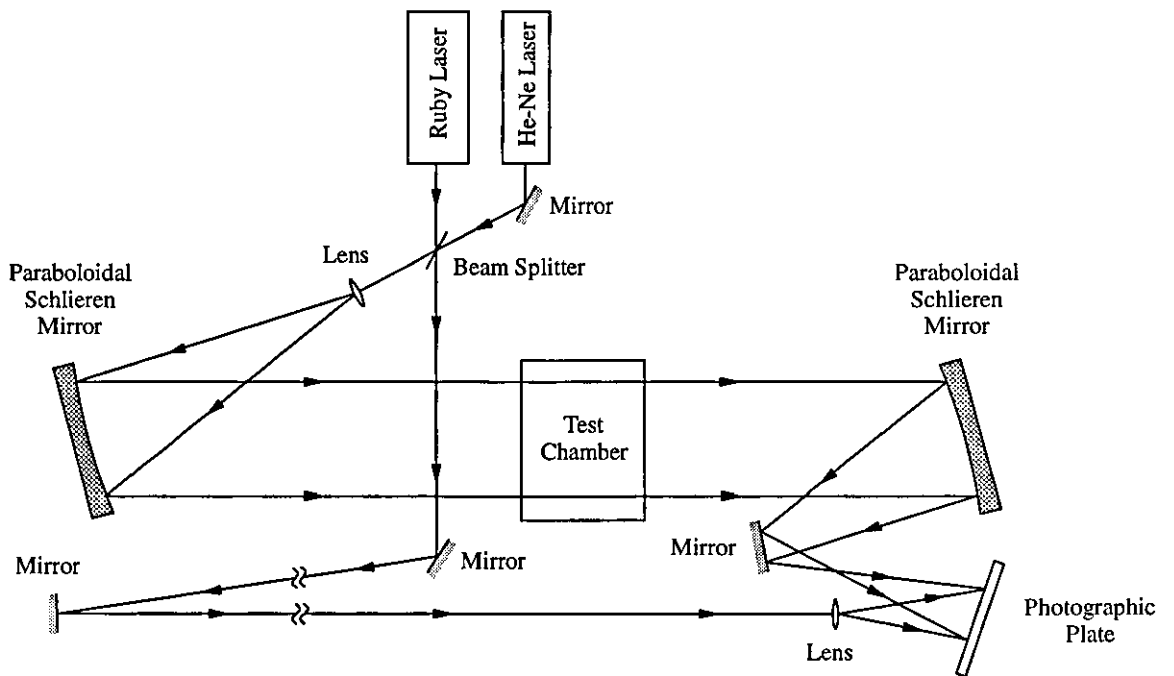


Figure 2.22 - Holographic interferometry of acoustic transients.

Many transparent non-crystalline materials which are optically isotropic under stress free conditions become anisotropic and *birefringent* when they are stressed. When linearly polarised light propagates through a stressed material the electric field can be resolved into components along the principal stress directions at any point in the material. According to the Maxwell-Neumann stress-optic law [217], the changes in the refractive indices of these two components are linearly related to the stresses or strains applied to a linearly elastic material. Changes in the optical path between the two components lead to rotation of the polarised light which can then be analysed by a crossed output polariser. The medium then displays regions of dark and light known as isoclinic fringes which are superimposed onto isochromatic fringes. Isochromatic fringes are the most useful for studying shear waves and can be isolated from the isoclinic fringes by the use of circularly polarised light.

In *dynamic photoelasticity* a pulsed light source is passed through a polariser and converted to circularly polarised light by a quarter wave plate aligned with its optical axis at 45° . Having passed through the photoelastic material containing the acoustic transients of interest, the beam is subsequently analysed using a further quarter wave plate and polariser. The photoelastic imaging system can be operated in either the light or dark field modes by rotation of the final polariser, and the region of interest is imaged on to a camera using an appropriate camera lens. High speed dynamic photoelastic imaging has been demonstrated by Jin *et al* [22,218-219] to study the effects of cavitation close to a polycarbonate surface, and by Asundi and Sajan [220] for impacts on a polyurethane beam. An example photograph taken using this technique can be seen in figure 2.20(c), in which Nd-YAG laser breakdown has been created in the water in the top half of the picture close to a polycarbonate surface, which is at the bottom half of the image [22]. The longitudinal acoustic transients are imaged as in focused shadowgraphy, and by comparing this picture with the similar schlieren and Mach-Zehnder images, figures 2.20(a) and (b) respectively, it can clearly be seen that additional disturbances exist in the solid which can be attributed to the propagation of shear waves in the solid. One problem with this technique is that the isochromatic fringes only represent the difference between the principle stresses and do not directly give the absolute values of the principal stresses. A second problem is that the solid has a three dimensional stress field and it is extremely difficult to derive this from the fringes.

(v) Holographic imaging

A holographic imaging technique has been demonstrated by Takayama *et al* [221-223] for studying acoustic transients created in water by a lithotripter [221], and in air by a shock tube [222]. In this technique, which is shown schematically in figure 2.22, an acoustic transient propagating in the test chamber is illuminated by a short duration pulse of light from the ruby laser, and is imaged onto a high resolution photographic plate using a paraboloidal mirror. At the same time a second "reference" beam of light is split off using the beam splitter and superimposed on to the image of the acoustic transient. Two exposures are taken using light pulses from the ruby laser, and the photographic plate is developed and fixed using appropriate chemicals. The first exposure is performed without the acoustic transient present in the imaging field, and the second exposure taken at the time of interest with the acoustic transient present. The hologram records local phase changes in the coherent ruby laser beam induced by the disturbance in the refractive index. As a result the holographic interferogram measures only the part of the phenomena which changed between the two exposures, and is therefore insensitive to the quality of the optical elements used and any inhomogeneities in the media involved. Finally, after developing the hologram can be reviewed simply using the reference beam. The main advantage with this technique is that the recorded fringe information can be used to visualise and quantitatively derive the characteristics of acoustic transients. Furthermore holographic imaging has the potential to provide quantitative three dimensional photographs of acoustic transient phenomena.

References

- [1] Officer, C. B. (1958) - *An Introduction to the Theory of Sound Transmission With Application to the Ocean*, Published by McGraw-Hill Book Company Inc.
- [2] Kaye, G. W. C. and Laby, T. H. (1995) - *Tables of Physical and Chemical Constants*, 16th Edition, Published by Longman, pp76-77,95-103.
- [3] Viktorov, I. A. (1967) - *Rayleigh and Lamb Waves - Physical Theory and Applications*, Published by Plenum Press.
- [4] Achenbach, J. D. (1973) - *Wave Propagation in Elastic Solids*, Published by North-Holland Publishing Co., pp187-195.
- [5] Strutt, J. W. (Lord Rayleigh) (1945) - *The Theory of Sound*, Volume II, Published by Dover Publications / The Macmillan Company, pp78-86.
- [6] Courant, R. and Friedrichs, K. O. (1948) - *Supersonic Flow and Shock Waves*, Published by Interscience Publishers Ltd, pp87-101.

- [7] Wright, J. K. (1961) - *Shock Tubes*, Published by Methuen & Co. Ltd, pp1-39.
- [8] Hamilton, M. F. and Blackstock, D. T. (1988) - *On the Coefficient of Nonlinearity β in Nonlinear Acoustics*, J. Acoust. Soc. Am. **83**, pp74-77.
- [9] Beyer, R. T. and Letcher, S. V. (1969) - *Physical Ultrasonics*, Published by Academic Press, pp202-241.
- [10] Penney, W. G. and Pike, H. H. M. (1950) - *Shock Waves and the Propagation of Finite Pulses in Fluids*, Reports on Progress in Physics **13**, pp46-82.
- [11] Payman, W. and Shepherd, W. C. F. (1946) - *Explosion Waves and Shock Waves VI. The Disturbance Produced by Bursting Diaphragms with Compressed Air*, Proc. Roy. Soc. **A186**, pp203-321.
- [12] Haar, L., Gallagher J. S. and Kell, G. (1984) - *NBS/NRS Steam Tables: Thermodynamic and Transport Properties and Computer Programs for Vapour and Liquid States of Water in SI Units*, Published by Hemisphere Publishing Corporation/McGraw-Hill International Book Company.
- [13] Vieille, P. (1899) - *Propagation of Explosive Air Waves*, Comptes Rendus **129**, pp1228-1230.
- [14] Taylor, W. (1959) - *Modern Explosives*, The Royal Institute of Chemistry Lectures, Monographs and Reports No. 5.
- [15] Johansson, C. H. and Persson, P. A. (1970) - *Detonics of High Explosives*, Published by Academic Press.
- [16] Chapman, D. L. (1899) - *On the Rate of Explosion in Gases*, Lond. Edinb. Dubl. Phil. Mag. **47**, pp90-104.
- [17] Jouget, E. (1905) - *Sur la Propagation des Reactions Chimiques dans la Gaze*, J. Math. Pures. Appl. **60**, p347, **61**, p1.
- [18] Penney, W. G. *et. al.* (1950) - *A Discussion on Detonation*, Proc. Roy. Soc. **A204**, pp1-33.
- [19] Sedov, L. (1959) - *Similarity and Dimensional Methods in Mechanics*, Published by Infosearch Ltd., pp157-164, pp210-232.
- [20] Taylor, G. I. (1950) - *The Formation of a Blast Wave by a Very Intense Explosion, I. Theoretical Discussion, and, II. The Atomic Explosion of 1945*, Proc. Roy. Soc. **A201**, pp159-174 and pp175-186. Reprinted in *The Scientific Papers of Sir Geoffrey Ingram Taylor, Volume III, Aerodynamics and the Mechanics of Projectiles and Explosions*, Published by Cambridge University Press, pp493-509 and pp510-521.
- [21] Bell, A. G. (1881) - Phil. Mag. **11**, pp510-528.
- [22] Jin, Y. H. (1995) - *Optical Investigations of Cavitation*, PhD Thesis, Loughborough University.

- [23] Scruby, C. B. and Drain, L. E. (1990) - *Laser Ultrasonics - Techniques and Applications*, Published by Adam Hilger / IOP Publishing Ltd.
- [24] Hutchins, D. A. (1988) - *Ultrasonic Generation by Pulsed Lasers*, Physical Acoustics - Principles and Methods **18**, pp21-123.
- [25] Ramsden, S. A. and Savic, P. (1964) - *A Radiative Detonation Model for the Development of a Laser-Induced Spark in Air*, Nature **203**, pp1217-1219.
- [26] Daiber, J. W. and Thompson, H. M. (1967) - *Laser-Driven Detonation Waves in Gases*, The Physics of Fluids **10**, pp1162-1169.
- [27] Emmony, D. C. (1968) - *Some Properties of Laser Generated Plasmas and Shocks*, PhD. Thesis, University of Strathclyde, pp150.
- [28] Raizer, Yu. P. (1966) - *Breakdown and Heating of Gases Under the Influence of a Laser Beam*, Physics Uspekhi **8**, pp650-673.
- [29] Raizer, Yu. P. (1965) - *Heating of a Gas by a Powerful Light Pulse*, Zh. Eksper. Teor. Fiz. (USSR), pp1503-1519, and, Soviet Physics JETP **21**, pp1009.
- [30] Mandel'shtam, S. L., Pashinin, P., Prokhorov, A. M., Raizer, Yu. P., and Sukhodrev, P. N. (1966) - *Investigation of the Spark Discharge Produced in Air by Focusing Laser Radiation II*, Soviet Physics JETP **22**, pp91-96.
- [31] Hu, C. L. (1969) - *Spherical Model of an Acoustic Wave Generated by Rapid Laser Heating in a Liquid*, J. Acoust. Soc. Am. **46**, pp728-736.
- [32] Bell, C. E. and Maccabee, B. S. (1974) - *Shock Wave Generation in Air and in Water by CO₂ TEA Laser Radiation*, Applied Optics **13**, pp605-609.
- [33] Sigrist, M. W. and Kneubuhl, F. K. (1978) - *Laser-Generated Stress Waves in Liquids*, J. Acoust. Soc. Am. **64**, pp1652-1663.
- [34] Emmony, D. C. (1985) - *Interaction of IR Laser Radiation with Liquids*, Infrared Phys. **25**, pp133-139.
- [35] Bunkin, F. V. and Komissarov, V. M. (1973) - *Optical Excitation of Sound Waves*, Sov. Phys. Acoust. **19**, pp203-211.
- [36] Carome, E. F., Clark, N. A., and Moeller, C. E. (1964) - *Generation of Acoustic Signals in Liquids by Ruby Laser-Induced Thermal Stress Transients*, Appl. Phys. Lett. **4**, pp95-97.
- [37] Hunter, S. D., Jones, W. V., and Marlborough, D. J. (1981) - *Nonthermal Acoustic Signals from Absorption of a Cylindrical Laser Beam in Water*, J. Acoust. Soc. Am. **69**, pp1563-1567.
- [38] Westervelt, P. J. and Larson, R. S. (1973) - *Laser-Excited Broadside Array*, J. Acoust. Soc. Am. **54**, pp121-122.
- [39] Busshanam, G. S. and Barnes, F. S. (1975) - *Laser-Generated Thermoelastic Shock Waves in Liquids*, J. Appl. Phys. **46**, pp2074-2084.

- [40] Sullivan, B., and Tam, A. C. (1984) - *Profile of Laser-Produced Acoustic Pulse in a Liquid*, J. Acoust. Soc. Am. **75**, pp437-441.
- [41] Chiao, R. Y., Townes, C. H., and Stoicheff, B. P. (1964) - *Stimulated Brillouin Scattering and Coherent Generation of Intense Hypersonic Waves*, Phys. Rev. Lett. **12**, pp592-595.
- [42] Lai, H. M. and Young, K. (1982) - *Theory of the Pulsed Optoacoustic Technique*, J. Acoust. Soc. Am. **72**, pp2000-2007.
- [43] Heretier, J. M. (1983) - *Electrostrictive Limit and Focusing Effects in Pulsed Photoacoustic Detection*, Opt. Comm. **44**, pp267-736.
- [44] Askar'yan, G. A., Prokhorov, A. M., Chanturiya, G. F. and Shipulo, G. P. (1963) - *The Effects of a Laser Beam in a Liquid*, Sov. Phys. JETP **17**, pp1463-1465.
- [45] Carome, E. F., Moeller, C. E., and Clark, N. A. (1966) - *Intense Ruby-Laser-Induced Acoustic Impulses in Liquids*, J. Acoust. Soc. Am. **40**, pp1462-1466.
- [46] Bell, C. E. and Landt, J. A. (1966) - *Laser Induced High-Pressure Shock Waves in Water*, Appl. Phys. Lett. **10**, pp46-48.
- [47] Barnes, P. A. and Rieckhoff, K. E. (1968) - *Laser Induced Underwater Sparks*, Appl. Phys. Lett. **13**, pp282-284.
- [48] Felix, M. P. and Ellis, A. T. (1971) - *Laser-Induced Liquid Breakdown - a Step-By-Step Account*, Appl. Phys. Lett. **19**, pp484-486.
- [49] Docchio, F., Regondi, P., Capon, M. R. C., and Mellerio, J. (1988) - *Study of the Temporal and Spatial Dynamics of Plasmas Induced in Liquids by Nanosecond Nd:YAG Laser Pulses. 1: Analysis of the Plasma Starting Times*, Applied Optics **27**, pp3661-3668.
- [50] Docchio, F., Regondi, P., Capon, M. R. C., and Mellerio, J. (1988) - *Study of the Temporal and Spatial Dynamics of Plasmas Induced in Liquids by Nanosecond Nd:YAG Laser Pulses. 2: Plasma Luminescence and Shielding*, Applied Optics **27**, pp3669-3674.
- [51] Zysset, B., Fujimoto, J. G., and Deutsch, T. F. (1988) - *Time-Resolved Measurements of Picosecond Optical Breakdown*, Appl. Phys. B **48**, pp139-147.
- [52] Vogel, A., Schweiger, P., Frieser, A., Asiyo, M. N., Birngrubber, R. (1990) - *Intraocular Nd:YAG Laser Surgery: Light-Tissue Interaction, Damage Range, and Reduction of Collateral Effects*, IEEE J. Quantum Electronics **26**, pp2240-2260.
- [53] Doukas, A. G., Zweig, A. D., Frisoli, J. K., Birngrubber, R., and Deutsch, T. F. (1991) - *Non-Invasive Determination of Shock Wave Pressure Generated by Optical Breakdown*, Appl. Phys. B **53**, pp237-245.
- [54] Ward, B. and Emmony, D. C. (1990) - *Interactions of Laser-Induced Cavitation Bubbles With a Rigid Boundary*, Proc. SPIE **1358**, pp1035-1045.

- [55] Martynenko, O. G., Stolovich, N., Rudin, G. I., and Levchenko, S. A. (1981) - *Shock Waves in Water Induced by Focused Laser Radiation*, Shock Waves, Explosions and Detonations, Progress in Astronautics and Aeronautics **87**, pp64-70.
- [56] White, R. M. (1963) - *Elastic Wave Generation by Electron Bombardment or Electromagnetic Wave Absorption*, J. Appl. Phys. **34**, pp2123-2124.
- [57] Ready, J. F. (1971) - *Effects of High Power Laser Radiation*, Published by Academic Press.
- [58] Krehl, P., Schwirke, F., and Cooper, A. W. (1975) - *Correlation of Stress-Wave Profiles and the Dynamics of the Plasma Produced by Laser Irradiation of Plane Solid Targets*, J. Appl. Phys. **46**, pp4400-4406.
- [59] Reynolds, O. (1873) - Trans. Inst. Naval Arch. **14**, Sci. Papers 1, pp56.
- [60] Barnaby, S. W. and Thornycroft, Sir John (1895) - *Torpedo Boat Destroyers*, Proc. Inst. Civ. Engrs. **122**, pp57.
- [61] Rayleigh, Lord. (1917) - *On the Pressure Developed in a Liquid During the Collapse of a Spherical Cavity*, Phil. Mag. **34**, pp94-98.
- [62] Lauterborn, W. (1974) - *Kavitation Durch Laserlicht*, Acustica **31**, pp51-78.
- [63] Lauterborn, W. and Bolle, H. (1975) - *Experimental Investigations of Cavitation-Bubble Collapse in the Neighbourhood of a Solid Boundary*, J. Fluid. Mech. **72**, pp391-399.
- [64] Hickling, R. and Plesset, M. S. (1964) - *Collapse and Rebound of a Spherical Bubble in Water*, Phys. Fluids. **7**, pp7-14.
- [65] Tomita, Y. and Shima, A. (1977) - *On the Behaviour of a Spherical Bubble and the Impulse Pressure in a Viscous Compressible Liquid*, Bull. Japan Soc. Mech. Eng. **20**, pp1453-1460.
- [66] Kornfeld, M. and Suvorov, L. (1944) - *On the Destructive Action of Cavitation*, J. Appl. Phys. **15**, pp495-506.
- [67] Naude, C. F. and Ellis, A. T. (1961) - *On the Mechanism of Cavitation Damage by Nonhemispherical Cavities Collapsing in Contact with a Solid Boundary*, Trans. A.S.M.E. D: J. Basic. Eng. **83**, pp648-656.
- [68] Fujikawa, S. and Akamatsu, T. (1978) - *Experimental Investigations of Cavitation Bubble Collapse by a Water Shock Tube*, Bull. Japan Soc. Mech. Eng. **21**, pp223-230.
- [69] Fujikawa, S. and Akamatsu, T. (1980) - *Effects of the Non-Equilibrium Condensation of Vapour on the Pressure Wave Produced by the Collapse of a Bubble in a Liquid*, J. Fluid. Mech. **97**, pp481-512.

- [70] Benjamin, T. B. and Ellis, A. T. (1966) - *The Collapse of Cavitation Bubbles and the Pressure Thereby Produced Against Solid Boundaries*, Phil. Trans. R. Soc. Lond. **A260**, pp221-240.
- [71] Plesset, M. S. and Chapman, R. B. (1971) - *Collapse of an Initially Spherical Vapour Cavity in the Neighbourhood of a Solid Boundary*, J. Fluid. Mech. **47**, pp283-290.
- [72] Flynn, H. G. (1964) - *Physics of Acoustic Cavitation in Liquids*, Physical Acoustics - Principles and Methods **1B**, pp57-172.
- [73] Briggs, L. J. (1950) - *Limiting Negative Pressure of Water*, J. Appl. Phys. **21**, pp721-722.
- [74] Forsythe, W. E. (1951) - *Smithsonian Physical Tables*, 9th Ed., Published by the Smithsonian Institution, pp421-423.
- [75] Thompson, J. J. (1906) - *Conduction of Electricity Through Gases*, Published by Cambridge University Press.
- [76] Townsend, J. S. (1915) - *Electricity in Gases*, Published by Oxford: Clarendon Press.
- [77] Llewellyn-Jones, F. (1957) - *Ionization and Breakdown in Gases*, Published by Methuen and Co. Ltd.
- [78] Howatson, A. M. (1965) - *An Introduction to Gas Discharges*, Published by Pergamon International Library, pp71-73.
- [79] Parker, S. P. (1993) - *McGraw-Hill Encyclopaedia of Physics*, 2nd Ed., Published by McGraw-Hill, pp283-284.
- [80] Toepler, A. (1866) - *Beobachtungen Nach Einer Neuen Optischen Methode*, Poggendorff's Ann. d. Phys. u. Chem. **127**, pp556.
- [81] Phillips, N. J. (1962) - *The Formation and Implosion of a Current Sheet in a Gas Discharge Containing Reversed Magnetic Fields*, Proc. Phys. Soc. **79**, pp171-179.
- [82] Frungel, F. B. A. (1965) - *High Speed Pulse Technology - Volume I, Capacitor Discharges, Magnetohydrodynamics, X-Rays, Ultrasonics*, Published by Academic Press.
- [83] Frungel, F. B. A. (1965) - *High Speed Pulse Technology - Volume II, Optical Pulses, Lasers, Measuring Techniques*, Published by Academic Press.
- [84] Frungel, F. B. A. (1976) - *High Speed Pulse Technology - Volume III, Capacitor Discharge Engineering*, Published by Academic Press.
- [85] Frungel, F. B. A. (1980) - *High Speed Pulse Technology - Volume IV, Sparks and Laser Pulses*, Published by Academic Press.
- [86] Cady, W. G. (1949) - *Piezoelectricity*, Published by McGraw-Hill.
- [87] Curie, J. and Curie, C. (1880) - C. R. Acad. Sci. Paris **91**, pp294, **91**, pp383.

- [88] Mason, W. P. (1981) - *Piezoelectricity, Its History and Applications*, J. Acoust. Soc. Am. **70**, pp1561-1566.
- [89] Langevin, P. (1918) - Brev. Franc., pp505, pp703.
- [90] Roberts, S. (1947) - *Dielectric and Piezoelectric Properties of Barium Titanate*, Physical Review **71**, pp890-895.
- [91] Brain, H. (1924) - *Piezo-Electric Effects with Dielectrics*, Proc. Phys. Soc. (London) **36**, pp81-93.
- [92] Fukada, E. (1968) - *Mechanical Deformation and Electrical Polarization in Biological Substances*, Biorheology **5**, pp199-208.
- [93] Fukada, E. (1968) - *Piezoelectricity in Polymers and Biological Materials*, Ultrasonics **6**, pp229-234.
- [94] Kawai, H. (1969) - *The Piezoelectricity of Poly(vinylidene Fluoride)*, Japan J. Appl. Phys. **8**, pp975-976.
- [95] Sessler, G. M. (1981) - *Piezoelectricity in Polyvinylidene fluoride*, J. Acoust. Soc. Am. **70**, pp1596-1608.
- [96] Ikeda, T. (1990) - *Fundamentals of Piezoelectricity*, Published by Oxford University Press.
- [97] Gallego-Juarez, J. A. (1989) - *Piezoelectric Ceramics and Ultrasonic Transducers*, J. Phys. E: Sci. Instrum. **22**, pp804-816.
- [98] Brush Clevite Company Ltd (1966) - *Piezoelectricity, a data book for designers*, Published by Brush-Clevite Company Ltd., U.K.
- [99] Gulton Industries Inc. (1961) - *Glennite Piezoceramics*, Published by Gulton Industries Inc., U.S.A.
- [100] Crecraft, D. I. (1983) - *Ultrasonic Instrumentation : Principles, Methods and Applications*, J. Phys. E: Sci. Instrum. **16**, pp181-189.
- [101] Lancee, C. T., Souquet, J., Ohigashi, H. and Bom, N. (1985) - *Ferro-Electric Ceramics Versus Polymer Piezoelectric Materials*, Ultrasonics **23**, pp138-142.
- [102] Shields, J. P. (1966) - *Basic Piezoelectricity*, Published by W. Foulsham & Co. Ltd.
- [103] Sworakowski, J. (1992) - *Molecular Electronics*, Edited by G. J. Ashwell, Published by Research Studies Press Ltd./John Wiley & Sons Inc., pp266-331.
- [104] Coates, E. C. (1956) - *The Applications of Ultrasonic Energy to Urinary and Biliary Calculi*, J. Urology **75**, pp865-876.
- [105] Berliniche, M. L. and Schenette, F. (1951) - *Über Beeinflussung von Gallenteinen Ultraschall in vitro*, Kilinische Wonchenzeitschrift, pp390.
- [106] Mulvaney, W. P. (1953) - *Attempted Disintegration of Calculi by Ultrasonic Vibrations*, J. Urology **70**, pp704.

- [107] Forßmann, B, Hepp, W., Chaussy, C., and Eisenberger, F. (1977) - *Eine Methode zur Beruhigung Sfreien Zertummerung von Nierensteinen durch Stoßwellen*, Biomed. Tecknik **22**, pp164 et seq.
- [108] Chaussy, Ch, Brendel, W. and Schmiedt, E. (1980) - *Extracorporeally Induced Destruction of Kidney Stones by Shock Waves*, The Lancet **11**, pp1265-1267.
- [109] Hoff, G. and Behrendt, A. (1973) - *Einrichtung zum Zertrummern von im Korper eines Lebewesens befindlichen Konkrementen*, German Patent Application 2.351.247.
- [110] Granz, B. and Köhler, G. (1992) - *What Makes a Shock Wave Efficient in Lithotripsy?*, J. Stone Disease **4**, pp123-128.
- [111] Alcock, R. D. (1992) - *A Brief Study into the Design of an Electromagnetic Lithotriptic Device*, thesis for BSc (Hons) Physics Degree, Loughborough University of Technology.
- [112] Eisenmenger, W. (1962) - *Elektromagnetische Erzeugung von Ebenen Druckstossen in Flussigkeiten*, Acustica **12**, pp185-202.
- [113] Carnell, M. T., Alcock, R. D. and Emmony, D. C. (1993) - *Optical Imaging of Shock Waves Produced by a High-Energy Electromagnetic Transducer*, Phys. Med. Biol. **38**, pp1575-1588.
- [114] Emmony, D. C., Carnell, M. T. and Alcock, R. D. (1993) - *Optical Diagnostics of Cavitation and Ultrasound in Materials*, Ultrasonics International 93 Conference Proceedings, pp619-622.
- [115] Coleman, A. J. and Saunders, J. E. (1993) - *A Review of the Physical Effects of the High Amplitude Acoustic Fields used in Extracorporeal Lithotripsy*, Ultrasonics **31**, pp75-89.
- [116] Reichenberger, H. (1988) - *Lithotripter Systems*, Proc. IEEE **76**, pp1236-1246.
- [117] Folberth, W. (1989) - *Non-Invasive Treatment of Urinary and Biliary Stones with Extracorporeal Shockwave Lithotripsy*, Atomkern-Energie Kerntechnik-Independant Journal on Energy Systems and Radiation **53**.
- [118] Whelan, J. P. and Finlayson, B. (1988) - *An Experimental Model for the Systematic Investigation of Stone Fracture by Extracorporeal Shock Wave Lithotripsy*, J. Urology **140**, pp395-400.
- [119] Pfeiler, M., Matura, E., Ifflander, H. and Seyler, S. (1989) - *Lithotripsy of Renal and Biliary Calculi: Physics, Technology and Medical-Technical Application*, Electromedica **57**, pp52-63.
- [120] Berlincourt, D. (1981) - *Piezoelectric Ceramics: Characteristics and Applications*, J. Acoust. Soc. Am. **70**, pp1586-1595.

- [121] Vogel, A., and Lauterborn, W. (1988) - *Acoustic Transient Generation by Laser-Produced Cavitation Bubbles Near Solid Boundaries*, J. Acoust. Soc. Am. **84**, pp719-731.
- [122] Vogel, A., Hentschel, W., Holzfuss, J. and Lauterborn, W. (1986) - *Cavitation Bubble Dynamics and Acoustic Transient Generation in Ocular Surgery with Pulsed Neodymium:YAG lasers*, Ophthalmology **93**, pp1259-1269.
- [123] Schiffers, W. P., Shaw, S. J., Jin, Y. H., and Emmony, D. C. (1997) - *High Speed Photographic Studies of the Interaction of Cavitation Bubbles with a Boundary*, High Speed Photography and Photonics, Proc. SPIE **2869**, pp308-331.
- [124] Shaw, S. J., Jin, Y. H., Schiffers, W. P. and Emmony, D. C. (1996) - *The Interaction of a Single Laser-Generated Cavity in Water with a Solid Surface*, J. Acoust. Soc. Am. **99**, pp2811-2824.
- [125] Sigrist, M. W., and Kneubuhl, F. K. (1978) - *Laser-Generated Stress Waves in Liquids*, J. Acoust. Soc. Am. **64**, pp1652-1663.
- [126] Reichenberger, H., and Naser, G. (1986) - *Electromagnetic Acoustic Source for the Extracorporeal Generation of Shockwaves in Lithotripsy*, Siemens Forsch. - u. Entwickl.-Ber. Bd. **15**, pp187-194.
- [127] Woodward, B. (1977) - *The Suitability of Polyvinylidene Fluoride as an Underwater Transducer Material*, Acustica **38**, pp264-268.
- [128] Ambrosy, A. and Holdik, K. (1984) - *Piezoelectric PVDF Films as Ultrasonic Transducers*, J. Phys. E: Sci. Instrum. **17**, pp856-859.
- [129] Kynar data sheet, Supplied by AMP Piezo Film Sensors-Europe, Stanmore, UK.
- [130] Schoeffmann, H., Schmidt-Kloiber, H. and Reichel, E. (1988) - *Time-Resolved Investigations of Laser-Induced Shock Waves in Water by use of Polyvinylidenefluoride Hydrophones*, J. Appl. Phys. **63**, pp46-51.
- [131] DeReggi, A. S., Roth, S. C., Kenney, J. M., and Edelman, S. (1981) - *Piezoelectric Polymer Probe for Ultrasonic Applications*, J. Acoust. Soc. Am. **69**, pp853-859.
- [132] Lewin, P.A. (1981) - *Miniature Piezoelectric Polymer Ultrasonic Hydrophone Probes*, Ultrasonics **19**, pp213-216.
- [133] Shotton, K. C., Bacon, D. R., and Quilliam, R. M. (1980) - *A PVDF Membrane Hydrophone for Operation in the Range 0.5MHz to 15MHz*, Ultrasonics **18**, pp123-126.
- [134] Harris, G. R. (1982) - *Sensitivity Considerations for PVDF Hydrophones Using the Spot-Poled Membrane Design*, IEEE Trans. Sonics Ultrason. **SU-29**, pp370-377.
- [135] Platte, M. (1985) - *A Polyvinylidene Fluoride Needle Hydrophone for Ultrasonic Applications*, Ultrasonics **23**, pp113-118.

- [136] Müller, M., and Platte, M. (1985) - *Einsatz Einer Breitbandigen Piezodrucksonde Auf PVDF-Basis Zur Untersuchung Konvergierender Stosswellen in Wasser*, *Acustica* **58**, pp215-222.
- [137] Platte, M. (1983) - *Ultraschallwandler Aus Polyvinylidendifluorid Mit Breitbandigem Übertragungsverhalten Und Fokussierenden Eigenschaften*, *Acustica* **54**, pp23-32.
- [138] Vogel, A., Lauterborn, W. and Timm, R. (1989) - *Optical and Acoustic Investigations of the Dynamics of Laser-Produced Cavitation Bubbles Near a Solid Boundary*, *J. Fluid. Mech.* **206**, pp299-338.
- [139] Moffett, M. B., Powers, J. M., and Clay, W. L. (1988) - *Ultrasonic Microprobe Hydrophones*, *J. Acoust. Soc. Am.* **84**, pp1186-1194.
- [140] Romanenko, E. V. (1957) - *Miniature Piezoelectric Ultrasonic Receivers*, *Sov. Phys. Acoust.* **3**, pp364-370.
- [141] Giallorenzi, T. G., Bucaro, J. A., Dandridge, A., Sigel, G. H., Cole, J. H., Rashleigh, and Priest, R. G. (1981) - *Optical Fiber Sensor Technology*, *IEEE. J. Quantum Electron.* **QE-18**, pp626-665.
- [142] Bucaro, J. A., Lagakos, N., Cole, J. H. and Giallorenzi, T. G. (1982) - *Fiber Optic Acoustic Transduction*, in *Physical Acoustics - Principles and Methods Volume XVI*, Chapter 7, Edited by Mason, W. P, and Thurston, R. N., Published by Academic Press, pp385-445.
- [143] Bucaro, J. A. and Cole, J. H. (1979) - *Acousto-Optic Sensor Development*, *Proc. EASCON 1979*, IEEE Pub. 79CH1476-1 AES, pp572-580.
- [144] Bucaro, J. A., Cole, J. H., Jarzynski, J., Burns, W. K. and Giallorenzi, T. G. (1981) - *Optical Fiber Sensor Development*, in *Physics of Fibres, Vol. 2, Advances in Ceramics*, *Proc. 82nd American Ceramic Soc.*, pp493-514.
- [145] Davis, C. M. (1985) - *Fibre Optic Sensors: An Overview*, *Opt. Eng.* **24**, pp347-351.
- [146] Bilaniuk, N. (1997) - *Optical Microphone Transduction Techniques*, *Appl. Acoustics* **50**, pp35-63.
- [147] Hecht, J. (1985) - *Victorian Experiments and Optical Communications*, *IEEE Spectrum*, February, pp69-73.
- [148] Pabst von Ohain, H. J. (1935) - *Ein Interferenzlightrelais Für Weißes Licht*, *Annalen der Physik*, pp431-441.
- [149] Shajenko, P. (1976) - *Fibre Optic Acoustic Array*, *J. Acoust. Soc. Am.* **59**, ppS27A.
- [150] Bucaro, J. A., Houston, B. H., and Williams, E. G. (1991) - *Fibre-Optic Air-Backed Hydrophone Transduction Mechanisms*, *J. Acoust. Soc. Am.* **89**, pp451-453.
- [151] Bucaro, J. A., Dardy, H. D., and Carome, E. F. (1977) - *Fiber-Optic Hydrophone*, *J. Acoust. Soc. Am.* **62**, pp1302-1304.

- [152] Cole, J. H., Johnson, R. L., and Bhuta, P. G. (1977) - *Fibre-Optic Detection of Sound*, J. Acoust. Soc. Am. **62**, pp1136-1138.
- [153] Culshaw, B., Davies, D. E. N., and Kingsley, S. A. (1977) - *Acoustic Sensitivity of Optical-Fibre Waveguides*, Electronics Letters **13**, pp760-761.
- [154] Lagakos, N., Litovitz, T., Macedo, R., Mohr, R., and Meister, R. (1981) - *Multimode Optical Fibre Displacement Sensor*, Appl. Opt. **20**, pp167-168.
- [155] Fields, J. N., and Cole, J. H. (1980) - *Fibre Microbend Acoustic Sensor*, Appl. Opt. **19**, pp3265-3267.
- [156] Carome, E. F., and Koo, K. P. (1980) - *Multimode Coupled Waveguide Acoustic Sensors*, Opt. Lett. **5**, pp359-361.
- [157] Sheem, S. K., and Cole, J. H. (1979) - *Acoustic Sensitivity of Single Mode Optical Power Dividers*, Opt. Lett. **4**, pp322-324.
- [158] Beasley, J. D. (1980) - *Multimode Optical Evanescent-Wave Acoustic Sensor*, J. Acoust. Soc. Am. **68**, pp595-598.
- [159] Spillman, W. B., and Gravel, R. L. (1980) - *Moving Fibre-Optic Hydrophone*, Opt. Lett. **5**, pp30-31.
- [160] Spillman, W. B., and McMahon, D. H. (1980) - *Frustrated-Total-Internal-Reflection Multimode Fibre-Optic Hydrophone*, Appl. Opt. **19**, pp113-117.
- [161] Rashleigh, S. C. (1980) - *Acoustic Sensing with a Single Coiled Monomode Fiber*, Opt. Lett. **5**, pp392-394.
- [162] DePaula, R. P., Flax, L., Cole, J. H., and Bucaro, J. A. (1981) - *Single Mode Fiber Ultrasonic*, IEEE J. Quantum Electron. **QE-18**, pp680-683.
- [163] Spillman, W. B., and McMahon, D. H. (1980) - *Schlieren Multimode Fibre-Optic Hydrophone*, Appl. Phys. Lett. **37**, pp145-147.
- [164] Tietjen, B. W. (1981) - *The Optical Grating Hydrophone*, J. Acoust. Soc. Am. **69**, pp993-997.
- [165] Staudenraus, J., and Eisenmenger, W. (1992) - *Fibre-Optic Probe Hydrophone for Ultrasonic and Shock-Wave Measurements in Water*, Ultrasonics **31**, pp267-273.
- [166] Staudenraus, J., and Eisenmenger, W. (1988) - *Optisches Sondenhydrophon*, Fortschritte der Akustik-DAGA'88, pp467-470.
- [167] Staudenraus, J., and Eisenmenger, W. (1992) - *Optisches Sondenhydrophon für Ultraschall- und Stoßwellenmessungen mit Einem Meßbereich von 0.1bar bis 1000bar*, Fortschritte der Akustik-DAGA'92, pp301-304.
- [168] Phillips, R. L. (1980) - *Proposed Fiber-Optic Acoustical Probe*, Optics Letters **5**, pp318-320.
- [169] Hecht, E. and Zajac, A. (1974) - *Optics*, Published by Addison-Wesley.
- [170] Dandridge, A., Miles, R. O., and Giallorenzi, T. G. (1980) - *Diode Laser Sensor*, Electron. Lett. **16**, pp948-949.

- [171] Davidson, G. and Emmony, D. C. (1980) - *A Schlieren Probe Method for the Measurement of the Refractive Index Profile of Shock Wave in a Fluid*, J. Phys. E: Sci. Instrum. **13**, pp92-97.
- [172] Sigrist, M. W. (1986) - *Laser Generation of Acoustic Waves in Liquids and Gases*, J. Appl. Phys. **60**, R83-R121.
- [173] Fujimoto, J. G., Lin, W. Z., Ippen, E. P., Puliafito, C. A., and Steinert, R. F. (1985) - *Time Resolved Studies of Nd-YAG Laser Induced Breakdown*, Invest. Ophthalmol. Vis. Sci. **26**, pp1771-1777.
- [174] Monchalin, J. P. (1986) - *Optical Detection of Ultrasound*, IEEE Trans. Ultrason. Ferroelect. and Frequency Control **UFFC-33**, pp485-499.
- [175] Sontag, H., and Tam, A. C. (1986) - *Optical Detection of Nanosecond Acoustic Pulses*, IEEE Trans. Ultrason. Ferroelect. and Frequency Control **UFFC-33**, pp500-506.
- [176] Wagner, J. W. (1990) - *Optical Detection of Ultrasound*, in Physical Acoustics, chapter 5, edited by R. N. Thurston and A. D. Pierce, Published by Academic Press, pp201-266.
- [177] Dewhurst, R. J. (1996) - *Laser-Ultrasound: Concepts and Applications*, IOP Appl. Opt. Div. Conf., pp289-298.
- [178] Pickering, C. J. D., Halliwell, N. A., and Wilmshurst, T. H. (1986) - *The Laser Vibrometer: A Portable Instrument*, J. Sound. Vib. **107**, pp471-485.
- [179] Field, J. E. (1982) - *High Speed Photography: Techniques and Applications*, Optical Engineering **21**, pp709-717.
- [180] Fuller, P. W. W. (1994) - *Aspects of High Speed Photography - 1 - Introduction*, J. Photogr. Sci. **42**, pp42-43.
- [181] Fuller, P. W. W. (1994) - *Aspects of High Speed Photography - 2 - Cameras*, J. Photogr. Sci. **42**, pp66-71.
- [182] Fuller, P. W. W. (1994) - *Aspects of High Speed Photography - 3 - Lighting for Cine and Still High Speed Photography*, J. Photogr. Sci. **42**, pp100-105.
- [183] Fuller, P. W. W. (1994) - *Aspects of High Speed Photography - 4 - The Study of Fluid Flow*, J. Photogr. Sci. **42**, pp133-139.
- [184] Fuller, P. W. W. (1994) - *Aspects of High Speed Photography - 5 - Some Specific Applications*, J. Photogr. Sci. **42**, pp169-177.
- [185] Fuller, P. W. W. (1994) - *Aspects of High Speed Photography - 6 - Photography in Ballistics*, J. Photogr. Sci. **42**, pp210-217.
- [186] Holder, D. W. and North, R. J. (1963), *Schlieren Methods*, National Physics Laboratory Notes on Applied Science No. 31, Published by HMSO.
- [187] Jones, G. A. (1952) - *High Speed Photography*, Published by Chapman and Hall.
- [188] Saxe, R. F. (1966) - *High Speed Photography*, Published by Focal Press.

- [189] Einstein, A. (1917) - *Zur Quantentheorie de Strahlung (On the Quanta Theory of Radiation)*, Zeitschrift fur Physik **18**, pp121-128.
- [190] Maiman, T. H. (1960) - *Stimulated Optical Radiation in Ruby Masers*, Nature **187**, pp493.
- [191] Wilson, J. and Hawkes, J. F. B. (1989) - *Optoelectronics - An Introduction*, 2nd Ed., Published by Prentice Hall International (UK) Ltd.
- [192] Wilson, J. and Hawkes, J. F. B. (1987) - *Lasers: Principles and Applications*, Published by Prentice Hall.
- [193] Hecht, J. (1992) - *The Laser Guidebook*, 2nd Ed., Published by McGraw-Hill Inc.
- [194] Vogel, A., Busch, S., and Asiyo-Vogel, M. (1993) - *Time-Resolved Measurements of Shock-Wave Emission and Cavitation-Bubble Generation in Intraocular Laser Surgery with ps- and ns-Pulses and Related Tissue Effects*, Ophthalmic Technologies III, Proc. SPIE **1877**, pp312-322.
- [195] Cranz, C. and Schardin, H. (1929) - *Kinematographie auf ruhendem Film und mit extrem hoher Bildfrequenz*, Zeitschrift fur Physik **56**, pp147-183.
- [196] Bretthauer, B., Meier, G. E. A. and Stasicki, B. (1991) - *An Electronic Cranz-Schardin Camera*, Rev. Sci. Instrum. **62**, pp364-368.
- [197] HP5 Data Sheet, Ilford Photographic Ltd., UK.
- [198] Stroebel, L., Compton, J., Current, I., and Zakia, R. (1986) - *Photographic Materials and Processes*, Published by Focal Press / Butterworth Publishers.
- [199] PE530 data sheet, Pulnix Europe Ltd, Basingstoke, UK.
- [200] Garfield, B. R. C. (1992) - *Developments in Image Converter Streak/Framing Camera Systems*, High-Speed Photography and Photonics, Proc. SPIE **1801**, pp192-203.
- [201] Kume, H., Nakamura, H., and Suzuki, M. (1990) - *Gatable Photonic Detectors and It's Image Processing*, High Speed Photography and Photonics, Proc. SPIE **1358**, pp1144-1155.
- [202] Kume, H., Koyama, K., Nakatsugawa, K., Suzuki, S., and Fatlowitz, D. (1988) - *Ultrafast Microchannel Plate Photomultipliers*, Appl. Opt. **27**, pp1170-1178.
- [203] Taite, P. G. (1888) - *Physics and Chemistry of the Voyage of H.M.S. Challenger*, Vol. 2, Part 4, Published by Her Majesty's Stationary Office.
- [204] Dymond, J. H. and Malhotra, R. (1988) - *The Tait Equation: 100 Years On*, Int. J. Thermophysics **9**, pp941-951.
- [205] Dale, T. P. and Gladstone, J. H. (1858) - *On the Influence of Temperature on the Refraction of Light*, Phil. Trans. Roy. Soc. London **148**, pp887-894.
- [206] Gladstone, J. H. and Dale, T. P. (1863) - *Researches on the Refraction, Dispersion, and Sensitiveness of Liquids*, Phil. Trans. Roy. Soc. London **153**, pp317-343.

- [207] Partington, J. R. (1953) - *An Advanced Treatise on Physical Chemistry, Volume Four: Physico-Chemical Optics*, Published by Longman, pp6-21.
- [208] Dvorak, V. (1880) - *Über Eine Neue Einfache Art Der Schlieren-Beobachtung*, Ann. Phys. Chem. **9**, pp502-512.
- [209] Ward, B., and Emmony, D. C. (1991) - *Interferometric Studies of the Pressures Developed in a Liquid During Infrared-Laser-Induced Cavitation-Bubble Oscillation*, Infrared Phys. **32**, pp489-515.
- [210] Toepler, A. (1864) - *Beobachtungen Nach Einer Neuen Optischen Methode*, Published by Max Cohen and Sohn.
- [211] Zehnder, L. (1891) - *Ein Neuer Interferenz-Refrakter*, Z. Instrumentkd. **11**, pp275-285.
- [212] Mach, L. (1893) - *Über Einen Interferenz-Refraktor*, Z. Instrumentkd. **12**, pp89-93.
- [213] Ward, B., and Emmony, D. C. (1990) - *Conservation of Energy in the Oscillations of Laser-Induced Cavitation Bubbles*, J. Acoust. Soc. Am. **88**, pp434-441.
- [214] Ward, B. (1990) - *The Energies and Pressures of Acoustic Transients Associated with Optical Cavitation in Water*, J. Mod. Opt. **37**, pp803-811.
- [215] Ward, B. (1991) - *Generation of Acoustic Waves by Focused Infrared Neodymium-Laser Radiation*, PhD Thesis, Loughborough University of Technology.
- [216] Brewster, D. (1815) - Phil. Trans. Roy. Soc. **60**.
- [217] Maxwell, J. C. (1853) - *On the Equilibrium of Elastic Solids*, Trans. Roy. Soc. Edinburgh **20**, Part 1, pp87-120.
- [218] Suaidi, M. K. B., Jin, Y. H., Ward, B. and Emmony, D. C. (1992) - *Dynamic Photoelastic Studies of Laser Interaction with Water at a Solid Boundary*, J. Photo. Sci. **40**, pp23-28.
- [219] Emmony, D. C., Suaidi, M. K. B., Jin, Y. H., and Ward, B. (1992) - *A High Resolution Dynamic Photoelastic Study of Laser Generated Sound in Polymer*, High-Speed Photography and Photonics, Proc. SPIE **1801**, pp380-391.
- [220] Asundi, A., and Sajan, M. R. (1995) - *Multiple LED Camera for Dynamic Photoelasticity*, Appl. Opt. **34**, pp2236-2240.
- [221] Takayama, K., Obara, T., and Onodera, O. (1990) - *Holographic Interferometric Observation of Shock Wave Focusing to Extracorporeal Shock Wave Lithotripsy*, 19th Int. Cong. High-Speed Photography and Photonics, Proc. SPIE **1358**, pp1180-1190.
- [222] Takayama, K. (1992) - *A Holographic Interferometric Study of Shock Wave Phenomena*, High-Speed Photography and Photonics, Proc. SPIE **1801**, pp304-313.
- [223] Takayama, K. (1983) - *Application of Holographic Interferometry to Shock Wave Research*, Proc. SPIE **389**, pp174-179.

Chapter Three

High Speed Semiconductor Laser Photography

Introduction

This chapter will deal with the design and development of a high speed multiple exposure imaging system utilising a high powered semiconductor diode laser as a flash illumination source. It begins by reviewing the general problems of high speed photography using semiconductor illumination sources and, a system for Schlieren imaging of an acoustic transient on a CCD camera is proposed utilising a pulsed semiconductor laser source. A general review of the construction and operating properties of semiconductor lasers then follows in section 3.2, leading onto the design of drive circuits and collimation optics for such lasers in sections 3.3 and 3.4 respectively. The practical considerations of Shadowgraphic and Schlieren imaging with CCD cameras are then investigated in section 3.5, followed by the timing circuitry required in section 3.6. The use of high power single pulse semiconductor lasers in high speed photography is illustrated in section 3.7, and is applied to the imaging of air born acoustic transients created during dye laser ablation. Finally a multiple pulse semiconductor laser high speed imaging system utilising dark field Schlieren imaging is described in section 3.8 and, it is used to image the development of individual acoustic transients with time propagating in both air and water created by Nd-YAG laser assisted breakdown. The system is demonstrated by illuminating an optical cavitation event with up to 10 pulses of light at a repetition rate of 5MHz, the spatially and temporally resolved images of the resulting acoustic transient being displayed on the same CCD camera frame.

3.1 - High speed photography using pulsed semiconductor light sources

It has already been seen in chapter 2 that high speed photography of acoustic events involves either having a camera with an extremely fast shutter speed, or by illuminating the event with a short duration flash of light and recording this with a relatively slow camera. The latter is often the simplest of the two techniques to perform in practice, given the need to resolve the acoustic transient with good spatial and temporal resolution. That is, it has been seen that sufficiently short duration light pulses are capable of 'freezing' the motion of the acoustic transient when it is imaged on a recording medium. This light pulse is conventionally achieved by use of one of a range of pulsed light

sources, for example a Q-switched Ruby laser [1], or a Nitrogen pumped Dye laser [2]. These devices are however often difficult, expensive and complex to operate and maintain.

Semiconductor light sources on the other hand have proved to be simple and cost effective devices to operate, requiring only appropriately timed current pulses to drive them. Recent developments in these devices have provided extremely bright sources of near infrared light which are ideally suited for detection by CCD cameras. It has already been seen that the Light Emitting Diode (LED) when over-driven can be a bright pulsed light source powerful enough to suitably expose a CCD camera [3-5]. This has been done for a variety of high-speed photographic applications with typical single exposure times of between 50ns and 2 μ s, emitting up to ~1W [3,5] in light output power at a framing rate of up to 165kHz [5] (80 frames max.) when applying the Cranz-Schardin camera arrangement [6]. However, although LEDs are superior light sources in terms of their stability [7], they are extended light sources and suffer from high beam divergence. As a result they are not as suited to Schlieren imaging applications as say lasers or other conditioned light sources [7].

A further disadvantage of LEDs compared with pulse semiconductor laser diodes is their distinct lack of light output power, for example pulsed LEDs can only supply up to ~1W [3,5] in a single pulse compared with a single chip pulsed diode laser with 30W [8]. Further improvements in output power of a semiconductor laser can be achieved by stacking several relatively low power single chip lasers together [9], giving in excess of 100W output light power [8]. Furthermore diode lasers are ideally suited to detection by CCD cameras, the near infrared peak response wavelength of CCD cameras (see figure 3.45) matching the peak output of the most powerful semiconductor lasers (~860nm.) This can however also be a disadvantage during beam alignment and in terms of safety, since the human eye cannot see output light at these wavelengths.

Semiconductor diode lasers have begun to be used in high speed photography, first as a single pulsed light source in Schlieren imaging systems [10], and then with several sources in a Cranz-Schardin camera arrangement [9]. However, both semiconductor lasers and LED sources suffer from limitations in their *Duty Cycle*, that is the time that a device is switched 'on' multiplied by the repetition rate at which it is pulsed. In a high speed camera system this restricts the number of exposures that can be made within a finite period. For example an LED giving out 1W of light power can be pulsed at a rate of up to 5kHz [3] and, diode laser sources have duty cycles of up to 0.025% corresponding to repetition rates ~5kHz for 50ns output pulses [8] (see section 3.2.4).

One method of overcoming this problem is to use several sources, such as in the Crazz-Schardin camera arrangement [5,6], however this has a disadvantage in that Schlieren imaging is not possible.

Higher repetition rates can be obtained for semiconductor lasers if only a small number of light pulses are required. In practice repetition rates typically a 1000 times higher than that stated for continuous operation can be achieved without permanent damage to the laser [9], providing that the overall number of output pulses for any one event is kept small. This allows repetition rates in excess of 2MHz, which can be usefully applied to high-speed imaging of non-repetitive events that occur over a very short duration, such as with acoustic transients. Acoustic transients in air travel at speeds equal to or greater than the sound speed of $\sim 330\text{ms}^{-1}$, so for a framing rate of 2MHz might travel a distance of $\sim 0.165\text{mm}$ between each exposure. Whereas in water the sound speed is $\sim 1500\text{ms}^{-1}$, corresponding to about 0.75 mm of travel. High speed mechanical framing cameras (see chapter 2) can be used in conjunction with semiconductor laser sources applied in this way, giving systems capable of taking 80 individual photographs with 7ns exposures at framing rates of up to 2MHz [9]. There are problems associated with this type of system in that the event, camera and diode laser have to be very carefully synchronised with each other.

A better and less complicated solution can be found for non-repetitive acoustic events. In many cases the transient usually only occupies a small proportion of the image field at any one point in time. Therefore the progress of the acoustic transient at several instances in time could be viewed effectively on just one frame. An appropriate imaging technique has to be chosen given that for multiple exposure photography the background scene must be a dark field, otherwise the required image in one frame will be swamped by the background light intensity integrated over several exposures. Such a technique is Schlieren imaging in which the resulting first order changes in refractive index in the plane of the acoustic transient are displayed on a dark field.

A multiple exposure imaging system could be constructed for non-repetitive events, using an over-driven semiconductor laser as the flash light source and, the variations in refractive index Schlieren imaged onto a CCD camera. This provides a very cost effective solution to the examination of the progress of an acoustic transient through a system. The remainder of this chapter will deal with the design and realisation of such a system, starting with an overview of the workings of a semiconductor laser.

3.2 - The semiconductor laser diode

The first semiconductor lasers were developed in 1962 after the discovery that gallium arsenide (GaAs) could be effectively used as a lasing medium within what was later to become the workings of a Light Emitting Diode (LED) [11]. It was nearly a decade later, however, that researchers at Bell Laboratories and also in the Soviet Union were able to manufacture continuous beam semiconductor lasers operating at room temperature. Since then the pace of development of laser diodes and the number of applications have accelerated rapidly, finding uses in the telecommunications industry, compact disc players and laser printers, amongst numerous others.

Semiconductor diode lasers have all the general advantages and conveniences of solid state devices. They are compact, efficient, cost effective, amenable to mass production, modulatable, and in many ways superior to their non solid state counterparts. Currently the smallest diode lasers, mounted complete with heat sink, can measure as little as 50mm³ yet deliver a continuous output intensity of as much as 100mW [12]. Their efficiency far exceeds that of other types of laser, typically 20% of the electrical input power is converted to light, compared to less than 2% for He-Ne or Nd-YAG lasers. Above the lasing threshold far greater efficiencies are achieved in laser diodes, typically 80% of additional input power being converted to laser radiation.

Generally diode lasers are fabricated from the group III-V compounds in the periodic table, the most popular material combinations being the gallium-arsenide family which have lasing transitions at wavelengths from 660nm to 900nm, and also indium-phosphide based compounds which radiate in the 1300nm to 1550nm telecommunications window. Recently visible light semiconductor lasers fabricated out of InGaAlP or InGaP compounds have also become available, however they are not as efficient as those in the near infrared.

3.2.1 - The semiconductor junction diode [13]

It is initially worth considering the operation of a p-n junction diode since this device forms the basis of both LEDs and semiconductor lasers. Most active electronic devices contain junctions between two dissimilar materials, such as metal-metal, metal-semiconductor or semiconductor-semiconductor combinations. A p-n junction is formed between two variants of the same semiconducting material. It is useful here to briefly review the properties of the materials used, before going on to describing the operation of p-n junctions and diodes, LEDs and finally semiconductor lasers.

(i) The doping of semiconductor materials

An *extrinsic* semiconductor is produced from an *intrinsic* semiconducting material by introducing appropriate impurities into its crystal lattice. This has the effect of increasing the number of charge carriers within the material. The process, called *doping*, alters the crystal so that it has a predominance of either *electrons* or *holes* (the latter occur as vacancies in the valence band of the crystal which can be considered as positive charge carriers.) The material can be either *n-type*, where the majority carriers are negative electrons and the minority carriers are positive holes, or *p-type* material where the opposite is found. For example, by doping the tetravalent element silicon with impurities from group V of the periodic table, such as phosphorus or arsenic, the material will become n-type. Whereas by doping with group III elements such as boron or indium, p-type material is produced. In a doped material the impurity atoms are found to occupy atomic sites which normally contain silicon atoms.

When silicon is doped with phosphorus the material becomes n-type, as shown in figure 3.1(a). In this situation only four out of the five valence electrons of the phosphorus atoms are used in forming covalent bonds with the tetravalent silicon, leaving one electron weakly bound to its parent atom which can easily be excited into the conduction band. Such impurities are called *donors*, since they donate electrons to the conduction band from *donor levels*. Typically the difference in energy between the bottom of the conduction band and the donor levels is $\sim 0.04\text{eV}$, so above moderately low temperatures most of the extra electrons are excited into the conduction band. Hence there is a greater number of free electrons in the material resulting in an increase in the conductivity.

If on the other hand silicon is doped with boron to produce p-type material, then there is one electron too few to complete the bonding, as shown in figure 3.1(b). At temperatures above absolute zero an electron from a neighbouring silicon atom can move to the impurity to complete the bonding at that site, but by doing so it leaves a vacant state in the valence band thereby creating a hole. The impurities, which are trivalent for p-type doping of silicon, are called *acceptors* since they accept electrons excited from the valence band of the crystal. It is convenient to regard this situation as a negative ionised acceptor atom with a hole orbiting around it analogous to a positive charge carrier, just as the free electrons in n-type material are negative charge carriers.

The main semiconducting material used in the fabrication of diode lasers is the compound gallium arsenide, which is formed out of the group III element gallium (Ga) and arsenic (As) from group V. This and other compounds such as GaP, InP and AlSb

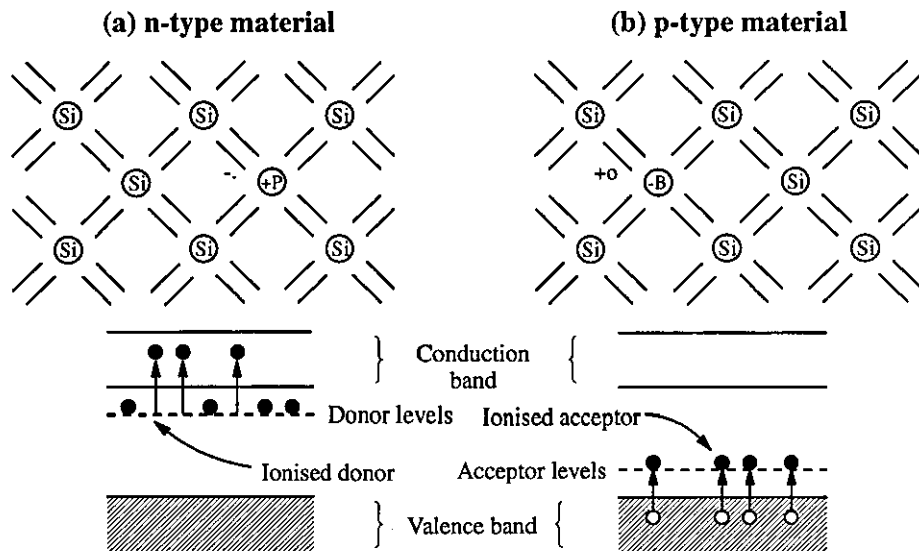


Figure 3.1 - Impurities in Silicon.

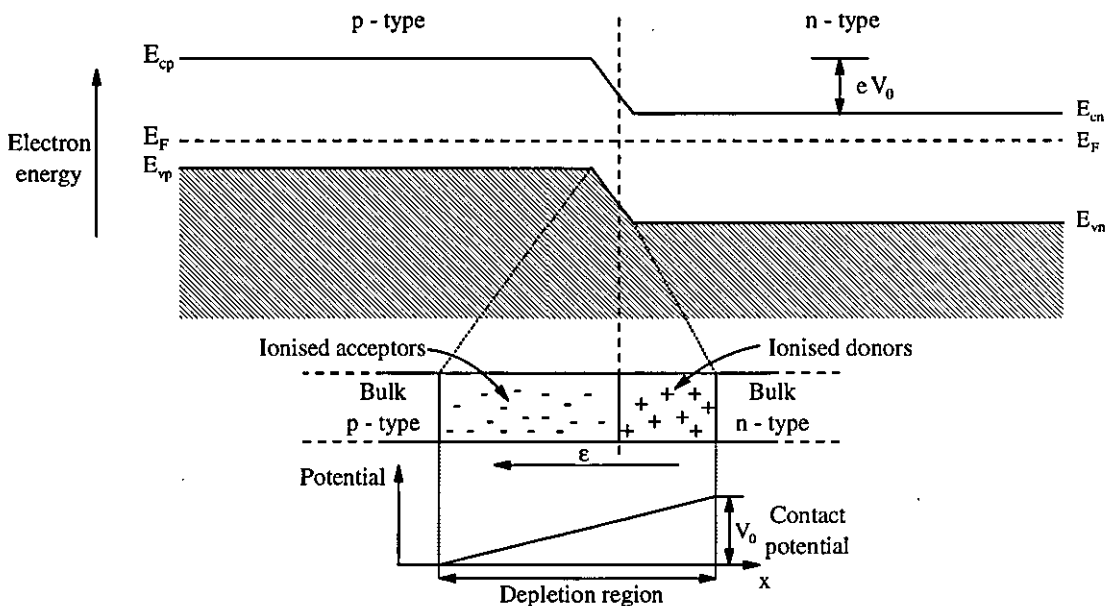


Figure 3.2 - Schematic representation of a p-n junction.

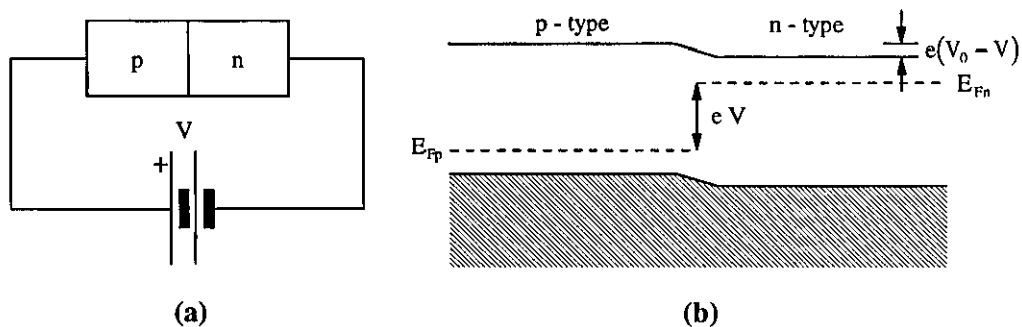


Figure 3.3 - Forward biased p-n junction.

are often referred to as the group III-V compounds, which can be doped to create n- and p-type materials. For example, if a group II element such as zinc replaces a gallium atom then the material becomes p-type; whereas if a group VI element such as tellurium is substituted in place of an arsenic atom then n-type material is formed. It is also possible to dope GaAs with group VI elements such as germanium or silicon, however exactly which type of material (p- or n-type) is produced depends on whether the impurity replaces the arsenic or the gallium atoms (respectively.)

(ii) p-n junctions

A p-n junction is usually constructed out of a single crystal of semiconducting material. The precise fabrication process in which these crystals are transformed into p-n junctions determines the distances over which there is a change between p-type and n-type materials. This distance controls the exact behaviour of the junction, however for convenience it is best to assume here that the junction is abrupt. That is, the junction can be considered to be formed out of two initially isolated pieces of n-type and p-type materials (this is not the case in reality) which are brought together into intimate contact. Since there are many more holes in the p-type material than in the n-type material, holes will diffuse from the p to the n-type regions. The migration will leave behind many ionised acceptors thereby building up a negative space charge layer in the p-type side of the junction. Likewise electrons diffusing to the p-type material will create a positive space charge layer of ionised donors in the n-type semiconductor. This is shown schematically in figure 3.2. The double space layer causes an electric field to be set-up across a narrow region on either side of the junction. Although diffusion is not prevented entirely, this electric field inhibits further migration of the minority carriers (i.e. holes in n-type and electrons in p-type regions.) In other words the electric field sweeps minority carriers across the junction so that there is a drift current of electrons and holes in the reverse direction to that of the diffusion current. Hence the junction potential builds up until equilibrium is reached between both diffusion and drift currents, at which point the *Fermi level* becomes constant across the junction.

The induced electric field establishes a contact or diffusion potential V_0 between the two regions, displacing the energy bands of the p-type material relative those of the n-type. This contact potential depends on the temperature, doping levels and the fabrication of the p-n junction. The space charge region is called the *depletion region* due to the almost total absence of majority carriers, and it is therefore highly resistive.

(iii) The p-n junction diode under forward bias

If an external voltage source is connected across the junction, as shown in figure 3.3(a), then the junction is said to be *forward biased* and the equilibrium situation is disturbed to give a net current flow. Given that the depletion region is extremely resistive, the external voltage V is dropped almost entirely across the junction and has the effect of lowering the height of the barrier potential to $V_0 - V$. This is shown schematically in figure 3.3(b), and it allows majority carriers to overcome the potential barrier more easily thereby allowing the diffusion current to become larger than the drift current. A net current therefore flows from the p region to the n region in the conventional sense, and carriers flow in the external circuit to restore equilibrium in the bulk regions.

It is worth noting that the Fermi levels in the p and n-type materials are altered somewhat in both regions giving an abrupt change across the junction. As majority carriers are "injected" across the junction they instantly become minority carriers. These then diffuse away from the junction and eventually recombine as electron-hole pairs, the probability of an injected electron existing without recombination decreases exponentially with time. When an electron in the conduction band makes a transition into a vacant state in the valence band there is an energy release in the form of either a *phonon* (lattice vibrations) or a *photon* (light) - which is the phenomena utilised in LEDs and semiconductor lasers.

Finally the response to the applied potential V giving rise to current flow I is given by the following relationship known as the *idealised diode equation*:

$$I = I_0 \left(\exp\left(\frac{eV}{kT}\right) - 1 \right) \quad - (3.1)$$

3.2.2 - The light emitting diode [13]

It has already been commented that under forward bias conditions majority carriers from both sides of a p-n junction are injected across the potential barrier, becoming minority carriers on the opposite side of the junction. Close to the junction the local minority carrier population becomes larger than normal which causes them to diffuse away and recombine with majority carriers within a short distance there after. This mechanism which is shown schematically in figure 3.4 forms the basis of a *Light Emitting Diode*, or LED.

Ideally every injected electron and hole in a LED will give rise a radiative recombination emitting a photon. In practice however this does not occur efficiently, so a term known as the *quantum efficiency* is defined, which is the probability that a photon is released during any one electron-hole recombination. The number of radiative recombinations that take place is usually proportional to the carrier injection rate, or rather the current flowing through the LED, as described by equation (3.1).

If a transition takes place directly between states at the bottom of the conduction band and the top of the valence band, then the emitted photon will have wavelength λ_g which can be calculated using Plank's equation:

$$\lambda_g = \frac{hc}{E_c - E_v} \quad - (3.2)$$

For example, an ideal LED fabricated out of GaAs will have a bandgap of $\sim 1.43\text{eV}$ giving rise to emission at $\lambda_g \sim 860\text{nm}$. In reality however thermal excitation of electrons in the conduction band give rise to higher energy differences than assumed above, and therefore the emission of photons occurs over a range of wavelengths slightly shorter than λ_g . A further problem that can occur is *self absorption*, in which an emitted photon might travel a short distance in the material and then be absorbed at another site (the opposite transition to emission,) raising another electron from the valence band to the conduction band.

Radiative recombinations in LEDs do not occur in the simplistic sense that has been described above, but by three different mechanisms which are listed here in order of probability:

- (i) *Interband Transitions* - which have high quantum and luminescent efficiency. Semiconductors can have either a direct (figure 3.5(a)) or an indirect (figure 3.5(b)) bandgap, depending upon the material used. A photon of wavelength λ has a momentum that is proportional its wave vector \underline{k} which has a magnitude of $2\pi/\lambda$. The electron wave vector can be between $-\pi/a$ and π/a , where a is the crystal lattice spacing of the semiconducting material. For emission wavelengths in the visible and infrared the wave vector of the photon will be extremely small compared with that of the electron, that is $2\pi/\lambda \ll \pi/a$. Consequently, since only an electron and a photon are involved, the only transitions allowed by the conservation laws are ones that do not alter the momentum of the electron. That is, it is highly unlikely for radiative transitions to occur in a material with an indirect bandgap, such as silicon, unless a

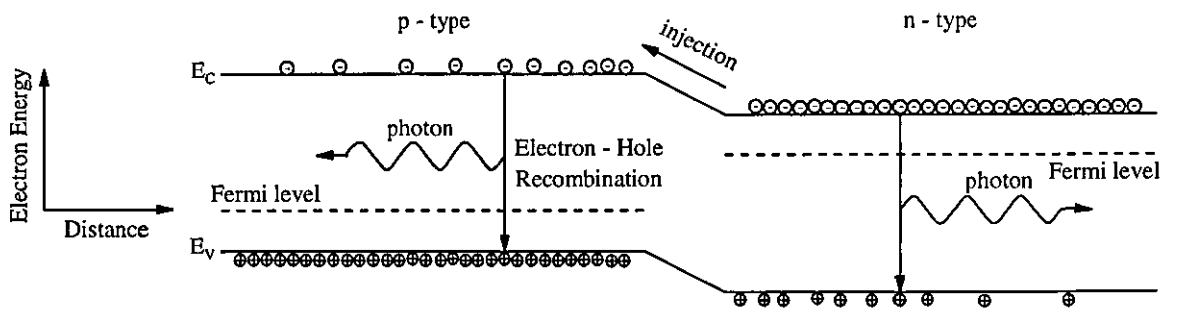


Figure 3.4 - Injection of minority carriers and subsequent recombination with majority carriers in a forward biased p-n junction.

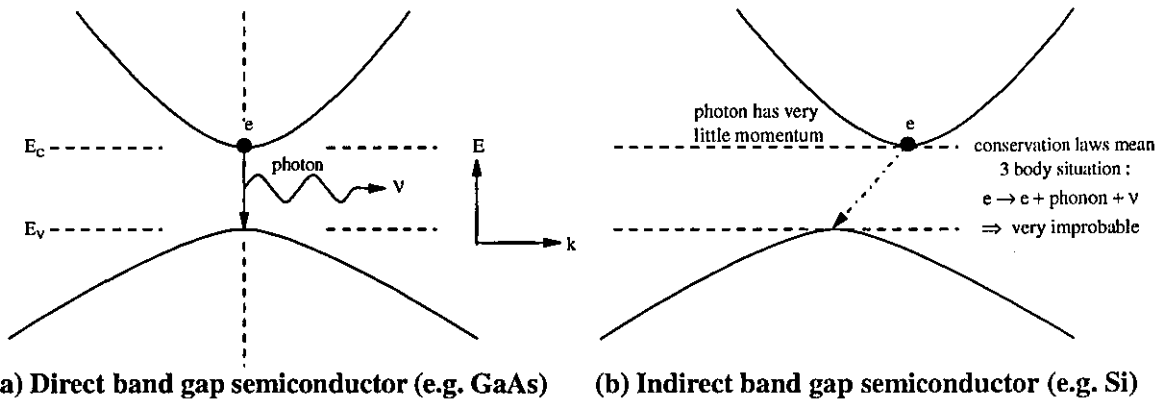


Figure 3.5 - Interband transitions.

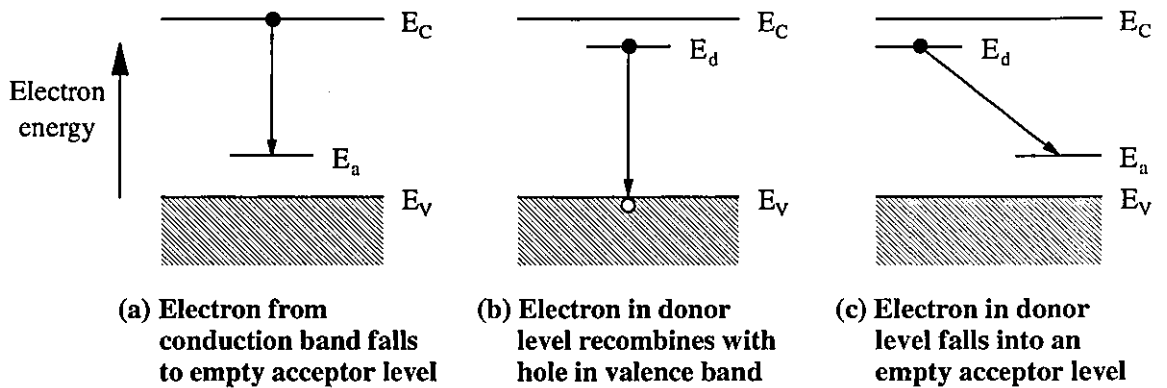
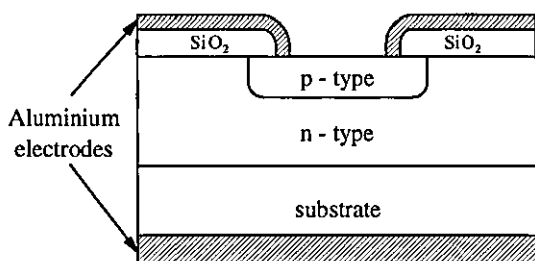
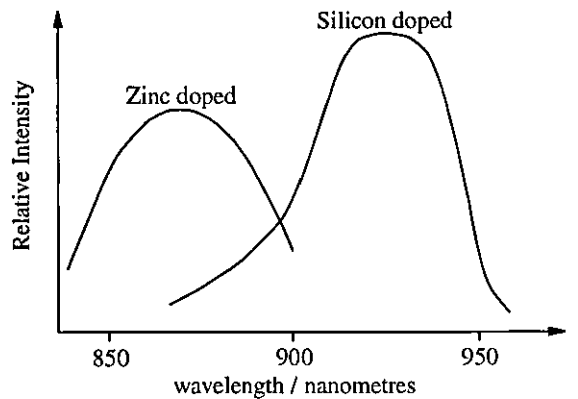


Figure 3.6 - Impurity Centre Recombination.

Figure 3.7 - The Light Emitting Diode.



(a) Typical L.E.D. construction



(b) Typical spectral output of GaAs L.E.D.

third body (i.e. phonon) is involved which is even more improbable. As a result the most efficient LEDs are fabricated out of a direct bandgap materials such as GaAs.

- (ii) *Impurity Centre Recombination* - of which there are three types of transition involving the acceptor and donor levels, as illustrated in figure 3.6. When an electron is in any of these states it will be fixed relatively strongly in its spatial position. *Heisenberg's uncertainty principle* ($\Delta x \Delta p \geq \hbar/2$) therefore implies that the electron will have a range of possible momentum values, thus the wave vector \underline{k} of the electron will also have a range of values given that it is proportional to momentum. These values are sufficiently spread to cover the wave vector range of both the conduction and valence bands ($-\pi/a$ to π/a .) As a result there is a significant number of transitions between the impurity and band extreme states which do not require phonon interactions. It is therefore a mechanism for photon emission not only in materials with direct band-gaps but also in those with indirect band-gaps.
- (iii) *Exciton recombination* - these exist even in pure semiconductors, and can be visualised as Bohr like states where an electron and a hole orbit at relatively large distances round a common centre of gravity. They are weakly bound, the exciton states existing just below the bottom of the conduction band. Exciton states may be sufficiently well localised to allow electron-hole recombination, even in indirect bandgap materials without the need for a phonon.

A typical construction for a light emitting diode is shown in figure 3.7(a). The p-type material is made as thin as possible so that very little of the output radiation is absorbed. Care is taken to ensure that the majority of the radiative recombinations occur close to the output surface. This is done by arranging that most of the current flowing through the device is carried by those carriers which are injected across the surface layer. Even though the internal quantum efficiencies of some LED materials approach 100%, the external efficiencies are substantially lower. This is due to the majority of the radiation being trapped inside the device as it is reflected back at the p-type to air interface, since it strikes the boundary at trajectories greater than the critical angle. Improvements in the design of the output interface can reduce this effect, however this will not be discussed further here.

The output wavelengths and efficiency of LEDs depend primarily upon the radiative processes involved, which in turn is determined by the material used. The most efficient LEDs (~13%) are manufactured out of $\text{Ga}_x\text{Al}_{1-x}\text{As}$ ($1 < x < 0.7$) - a ternary "alloy" which uses impurity centre recombination as the mechanism for light production. As explained

before, very little of the output light is absorbed since the photon energy is less than the bandgap of the material giving rise to high efficiency. The next most efficient devices are fabricated from GaAs (~10%) which is a direct bandgap material, so has high luminescent efficiency but has problems with self absorption. Both these materials produce light in the red to near infra-red range. Mid-visible wavelength LEDs have also been manufactured but are extremely inefficient (~0.1%,) this is because they are generally fabricated from materials with indirect band-gaps and use the exciton recombination process.

3.2.3 - Homojunction semiconductor lasers [8,11-13]

In principle semiconductor lasers operate in a similar manner to LEDs and emit light spontaneously when current flows through the p-n junction. In a diode laser however the p-n junction also operates as the active medium in a laser cavity, where simulated emission may occur under suitable conditions. These conditions are as follows. When the junction is placed under forward bias with a voltage comparable with the energy gap potential V_0 , electrons and holes are injected across the junction in sufficient numbers so as to create *population inversion* in a narrow zone called the *active region*. If the semiconductor material has a direct bandgap then *spontaneous emission* of light will occur as these electrons and holes recombine, just as in a light emitting diode. The radiation released could interact with valence electrons and be absorbed a short distance later, however this is unlikely during population inversion due to there being more electrons in the conduction band than in the valence band. Alternatively the photons could interact with other electrons in the conduction band and cause the *stimulated emission* of more photons. A stimulated photon will have the same energy (and hence wavelength or frequency), phase, polarisation and direction as the photon that caused its release. Grouped together these may then go on to stimulate yet further photon releases in the same way, causing amplification of the total light intensity.

If the active region is placed between two parallel mirrors, then laser oscillations will occur when the round trip losses are exceeded by the gain in intensity over the same distance. In semiconductor lasers the principle losses are due to free carrier absorption and scattering at optical inhomogeneities. Free carrier absorption results when a photon is absorbed by either an electron or a hole, moving these to higher energy states within the conduction band and valence bands respectively. This presents several practical limitations in the choice of semiconducting materials, as well as a few advantages:

- (i) The material must have a direct bandgap so that the electrons and holes can recombine radiatively with high probability. As mentioned before, indirect bandgap materials are unlikely to have radiative transitions since photons have very little momentum and therefore additional phonon interaction is required - which is highly improbable. Furthermore the impurity recombination mechanism can not be used in homojunction lasers due to low quantum efficiency.
- (ii) Stimulated emission requires a region of the device where there is a large number of excited electrons and vacant sites (holes) present together. This is achieved under forward bias conditions only in materials that are heavily doped. In such n⁺-type materials the Fermi level lies within the conduction band, whereas in p⁺-type materials it is in the valence band. When these materials form a p-n junction, the energy bands become as those shown in figure 3.8 for equilibrium and forward bias conditions. Recombination will only occur in a small zone around the junction since the injected charge carriers can only travel a short distance across the junction.
- (iii) A resonant cavity is created by cleaving the semiconductor material along its natural crystal planes, as shown in figure 3.9. The high refractive index of the semiconductor compared with that of air ensures that the reflectivity R at the interfaces are sufficiently large to act as partially reflecting mirrors. For example, GaAs has a refractive index of ~3.6 giving the reflectivity to be approximately:

$$R = \left(\frac{n_{\text{GaAs}} - n_{\text{Air}}}{n_{\text{GaAs}} + n_{\text{Air}}} \right)^2 = \left(\frac{3.6 - 1}{3.6 + 1} \right)^2 \approx 0.32 \quad - (3.3)$$

The simplest *homojunction* semiconductor lasers are fabricated using GaAs. The p⁺-type material is very heavily doped with germanium and the n⁺-type is doped with tellurium. Typically the cavity length and the width are between 200 and 400μm, whereas the depth of the junction or active region is of the order of 2μm.

Finally it is difficult to define exactly what the term *population inversion* means when applied to semiconductor lasers. In other types of lasers the energy level system is as that shown in figure 3.10. That is under equilibrium conditions the energy levels are filled according to Boltzmann statistics; whereas under population inversion more electrons occupy the upper energy levels than the lower states. As a result if a photon interacts with an electron in the lasing medium, then there will be a higher probability of it stimulating emission of another photon (since there are more electrons in the upper states) rather than it being absorbed. In a semiconductor laser however there are two

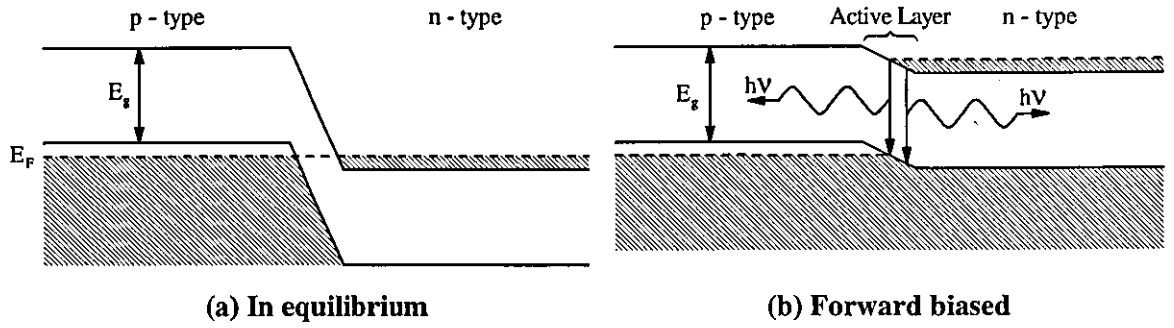


Figure 3.8 - Heavily doped p-n junction diode laser.

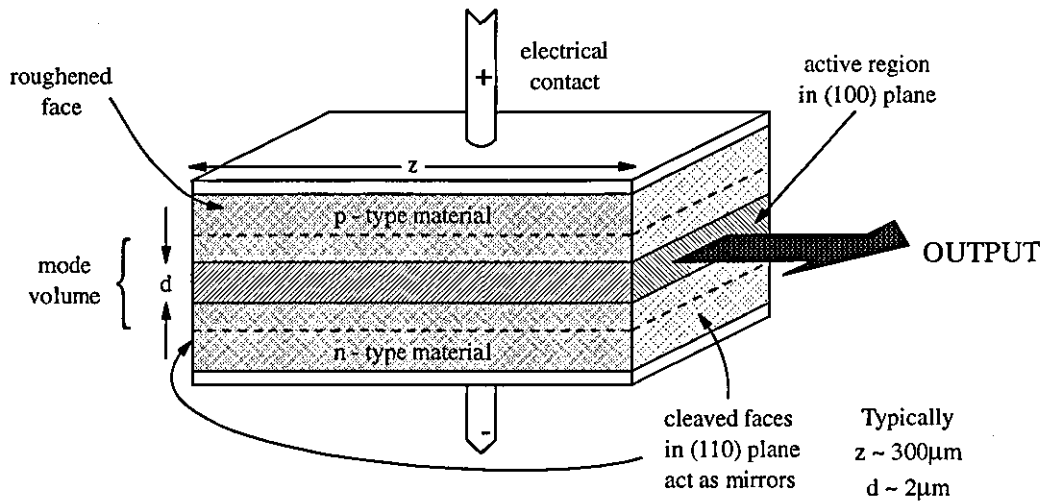


Figure 3.9 - Active region of a Diode Laser and cleaved planes.

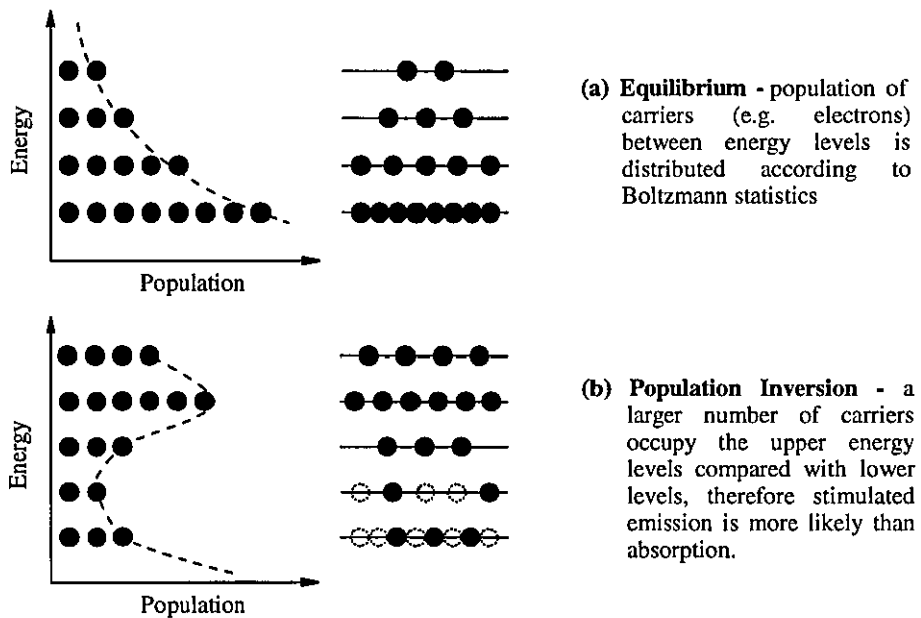


Figure 3.10 - Electron levels in lasers.

distinct energy level bands, and the distribution of electrons is likely to be like that shown in figure 3.11. During population inversion there will be a greater number of electrons that have been injected across the junction into the conduction band compared with that in the valence band. Therefore since laser transitions occur mainly between the bottom of the conduction band and the top of the valence band, population inversion could be visualised as only occurring between these two regions in the energy bands.

3.2.4 - Properties of homojunction lasers

Unfortunately a great deal of the radiation created within the active region of a homojunction laser does not head towards the cleaved plane mirrors, but spreads out into the rest of the surrounding semiconductor and is lost. There is however limited amount of containment of this radiation within a region called the *mode volume*. This is because an increase in carrier concentration causes a slight increase in refractive index around the junction, which in turn forms a rather weak dielectric wave guide. Also in order to operate a homojunction laser as it has been described up to now, very vigorous pumping is required. Typically the current density might be of the order of 400Amm^{-2} at room temperature for a GaAs homojunction laser emitting at 840nm [13]. This means that such a laser could only be used in practice in pulsed mode, otherwise over heating will destroy the delicate device. The conditions under which a device can be safely operated without thermal damage is given by the *duty cycle*, which is defined for specified input current pulses as:

$$\text{duty cycle} = \text{current pulse width} * \text{frequency of pulses} * 100\% \quad - (3.4)$$

So if a device has a duty cycle of 0.025% for pulses of 50ns duration and specified peak current, then it can be safely pulsed at a maximum rate of 5kHz before damage will occur. If the device is overdriven using higher peak current pulses then the duty cycle will decrease accordingly. Also if the device is pulsed only a limited number of times then it is also possible to increase the repetition rate, providing that the overall duty cycle over a long period of time is not exceeded.

The lifetime and reliability of semiconductor lasers are limited by two processes, *catastrophic failure* and *gradual degradation*. The latter depends principally upon the current density, duty cycle and the fabrication of the laser. Generally as damage occurs the threshold current (the minimum current for which lasing occurs) increases and dark lines develop in the emission. Whereas catastrophic failure is generally most evident in

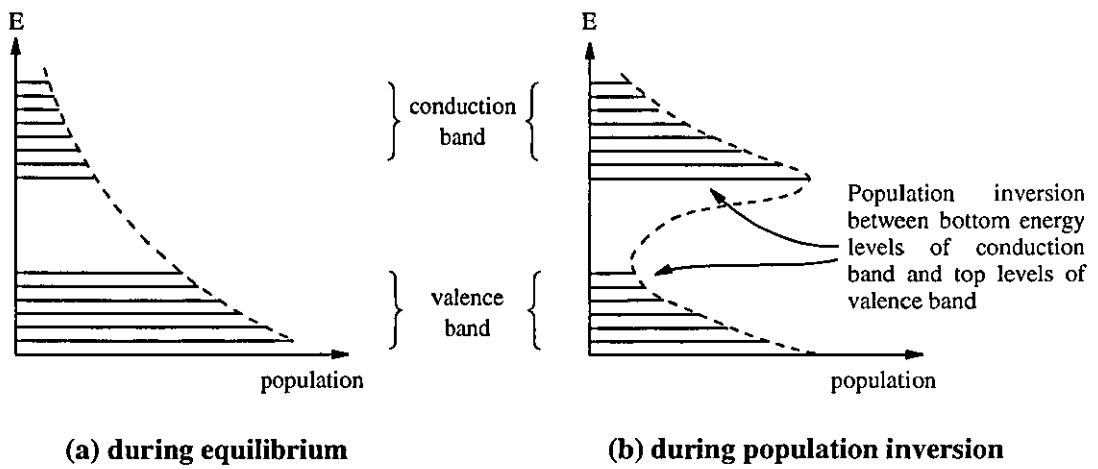


Figure 3.11 - Diode laser band structure at the p-n junction.

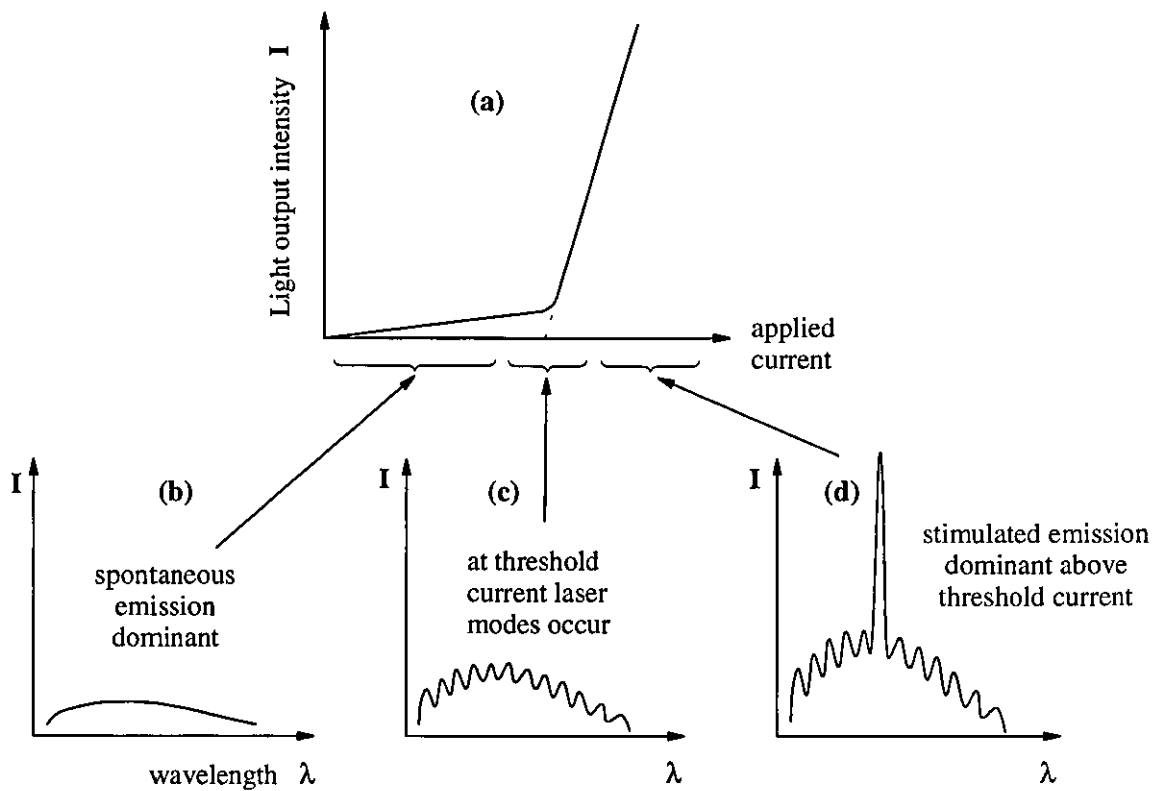
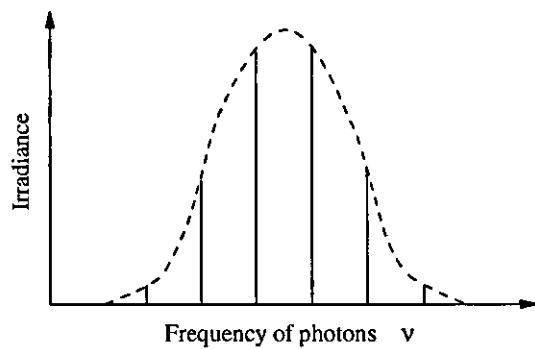


Figure 3.12 - Radiant output intensity for a p-n junction semiconductor laser.

Figure 3.13 - Axial modes in a laser.



pulsed lasers, where mechanical damage to the mirror facets caused by high optical intensities occur. The damage threshold (i.e. the maximum input current before damage) is lowered by faults in the cleaved ends facets, but can be improved by use of half-wave coatings of Al_2O_3 , for example.

The typical output characteristics of semiconductor lasers are shown in figure 3.12. Below the *threshold current* the diode laser behaves like an inefficient LED. Whereas at the threshold current lasing begins to occur causing an abrupt increase in the radiance of the emitting region, and axial modes are set-up in the optical cavity. Finally above threshold the energy is supplied almost entirely into just the most dominant of these modes, significantly narrowing the spectral width of the output as the light intensity increases. The typical threshold current density for a homojunction laser is $\sim 16 \text{Amm}^{-2}$ [13], which corresponds to about 1.5A for a junction with dimensions of $300 \times 300 \mu\text{m}$. This depends however upon several factors:

- (i) *Internal quantum efficiency* - that is the probability that the recombination of an electron-hole pair by either spontaneous or stimulated means will be by a radiative process. Other non-radiative recombinations are also likely to exist.
- (ii) *Dimensions of the junction* - which control the confinement of the carriers and, as noted earlier, affect the wave guide confinement of the radiation.
- (iii) *Refractive index* - this determines the reflectivity of the cleaved end mirrors and hence the optical gain of the laser cavity.
- (iv) *Loss coefficient* - defines the total amount of radiation loss in the laser by undesired means, such as absorption and scattering in the semiconductor and at the mirrors.

A more comprehensive treatment of the threshold characteristics is given in reference [13], together with discussions on how power and efficiencies may be calculated for simple homojunction lasers. In general the output power is proportional to the input current above threshold current.

Another effect within semiconductor lasers is the setting up of *axial modes* within the cleaved mirror resonant cavity. The modes satisfy the standing wave condition:

$$m \lambda = 2 L \quad - (3.5)$$

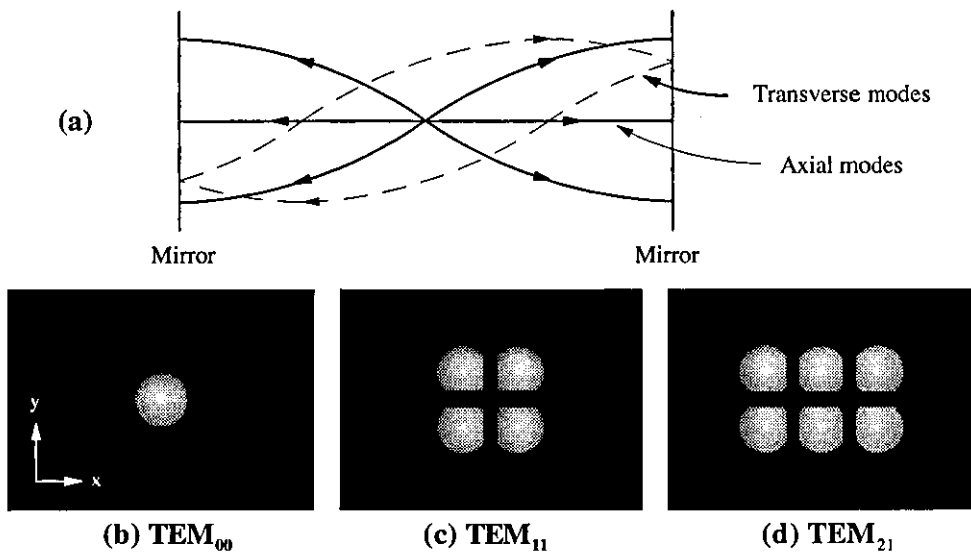
where L is the length of the cavity, λ the wavelength in the cavity and m an integer. The range of energy levels in the band structure of the semiconductor means that the emission or gain curve has quite a large spectral line width, as shown by the dotted line in figure 3.13. However the resonant cavity will only amplify those wavelengths determined by equation (3.5) above, hence giving rise to a spectral output more like that shown by the continuous line in figure 3.13. That is, the output consists of several wavelengths of different intensities, each with very narrow line-width. It is usually the case that as the input current is increased one mode will become dominant over the others, as shown in figure 3.12(d).

Transverse Electromagnetic Modes (TEM) can also be set-up in the laser cavity as shown schematically in figure 3.14(a). Each mode corresponds to waves travelling just off axis that are able to replicate themselves after covering a closed path, giving rise to resonant modes that include the transverse components of their electromagnetic fields. By far the most dominant of these is the TEM_{00} mode which has a Gaussian irradiance distribution, shown in figure 3.14(b). The mirrors act as planes of constant phase and the beam spread varies with distance away from the cavity along the axis.

Higher TEM modes extend further from the cavity axis compared with the TEM_{00} mode, and therefore can only oscillate if the output aperture of the cavity is large enough. It is often the case that only the TEM_{00} mode is wanted and usually the active region is small enough to eliminate all other modes. The TEM_{00} mode is often called the uniphase mode since all parts of the propagating wavefront are in phase, which is not the case for higher transverse mode patterns. Consequently a homojunction semiconductor laser with only the TEM_{00} mode operating will have greater spectral purity and coherence. Furthermore this mode also represents the diffraction limited output of the semiconductor laser. That is since the radiation is emitted through a narrow window, as illustrated in figure 3.15, the far field intensity distribution will conform to Fraunhofer diffraction for a single slit [14]:

$$I(\theta) = I(\theta = 0) \text{sinc}^2 \left\{ \frac{\pi b}{\lambda} \sin \theta \right\} \quad - (3.6)$$

where λ is the output wavelength of the semiconductor laser, b is the slit width $\gg \lambda$ and, θ is the angle from the normal. For example, GaAs lasers typically emit at 904nm with an output window of $2\mu\text{m}$ by $300\mu\text{m}$. This gives rise to first zero intensities at $\theta_{\perp} \approx 27^{\circ}$ and $\theta_{\parallel} \approx 0.2^{\circ}$ in the directions perpendicular and parallel to the junction respectively. The output beam will therefore be elliptical, spreading most in the direction perpendicular to the junction. In practice however the output beam is subject to the



The beam spread of the TEM₀₀ mode at a certain distance from the origin has a gaussian distribution and is dependant upon the beam waist w .

$$\epsilon(x,y) = \epsilon_0 \exp\left\{-\frac{x^2 + y^2}{w^2}\right\}$$

Figure 3.14 - Transverse modes.

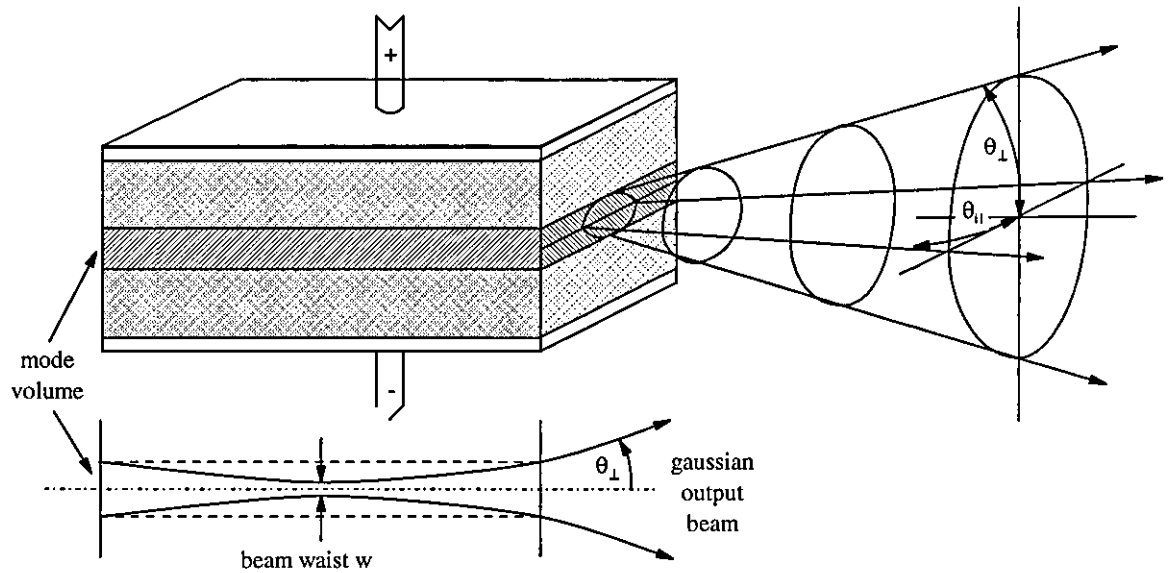
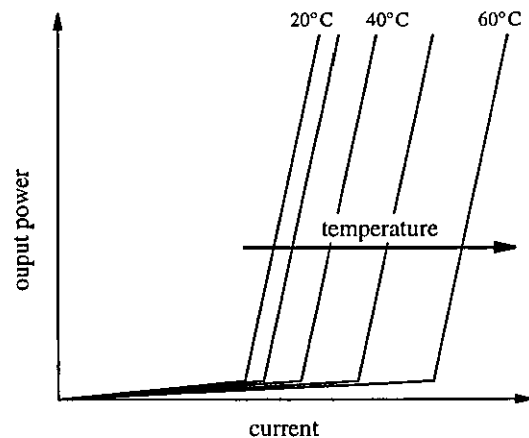


Figure 3.15 - Output beam spread of a diode laser.

Figure 3.16 - The effect of an increase in temperature on the output of a diode laser.



electric current profile within the laser, which dominates over diffraction in the plane parallel to the junction. The output beam will therefore typically have a spread of $\theta_{\perp} \approx 30^\circ$ by $\theta_{\parallel} \approx 15^\circ$.

The output intensity also varies with temperature since the threshold current, which is a function of quantum efficiency and other parameters of the junction, is dependant on temperature. In general an increase in temperature significantly reduces the quantum efficiency thereby increasing the threshold current required for lasing, as indicated in figure 3.16. Finally semiconductor lasers exhibit linear polarisation, usually with the electric field vector parallel to the junction. In practice the polarisation ratio of parallel to perpendicular components is of the order of 100:1.

3.2.5 - Heterojunction semiconductor lasers

In the last section it was mentioned that the threshold current, and therefore the output power, of a homojunction laser depends on both optical and electronic carrier confinement. Homojunction lasers have extremely poor confinement giving a large mode volume in comparison to the active region within it. Dramatic reductions in the threshold current can be made by changing the structure to that of a heterojunction, giving large increases in the output light power.

A typical *single heterostructure* is shown in figure 3.17(a). This structure is fabricated with a thin layer of p-type GaAs sandwiched between P-type GaAlAs compound and n-type GaAs semiconductor. (Note: P- and N- represent very heavily doped forms of p-type and n-type materials respectively.) The P-type GaAlAs has a larger bandgap than GaAs and so the material absorbs less of the radiation that is produced in the p-type region. This arrangement also confines the charge carriers, that is the holes to the P- and p-type materials and the excited electrons to the n- and p-type regions. The result of this is that electron-hole recombination is restricted to the p-type semiconductor. Furthermore the refractive index of the p-type material is substantially higher than in the other two regions therefore giving improvements in optical confinement. Hence less radiation is absorbed by being allowed to stray away from the junction, thereby making the efficiency of the device greater and reducing the threshold current.

Further improvements may be made by using a *double heterostructure*, as shown in figure 3.17(b). As in the single heterostructure, the carriers are confined and radiative recombination is restricted to just the GaAs p-type region. This material is sandwiched

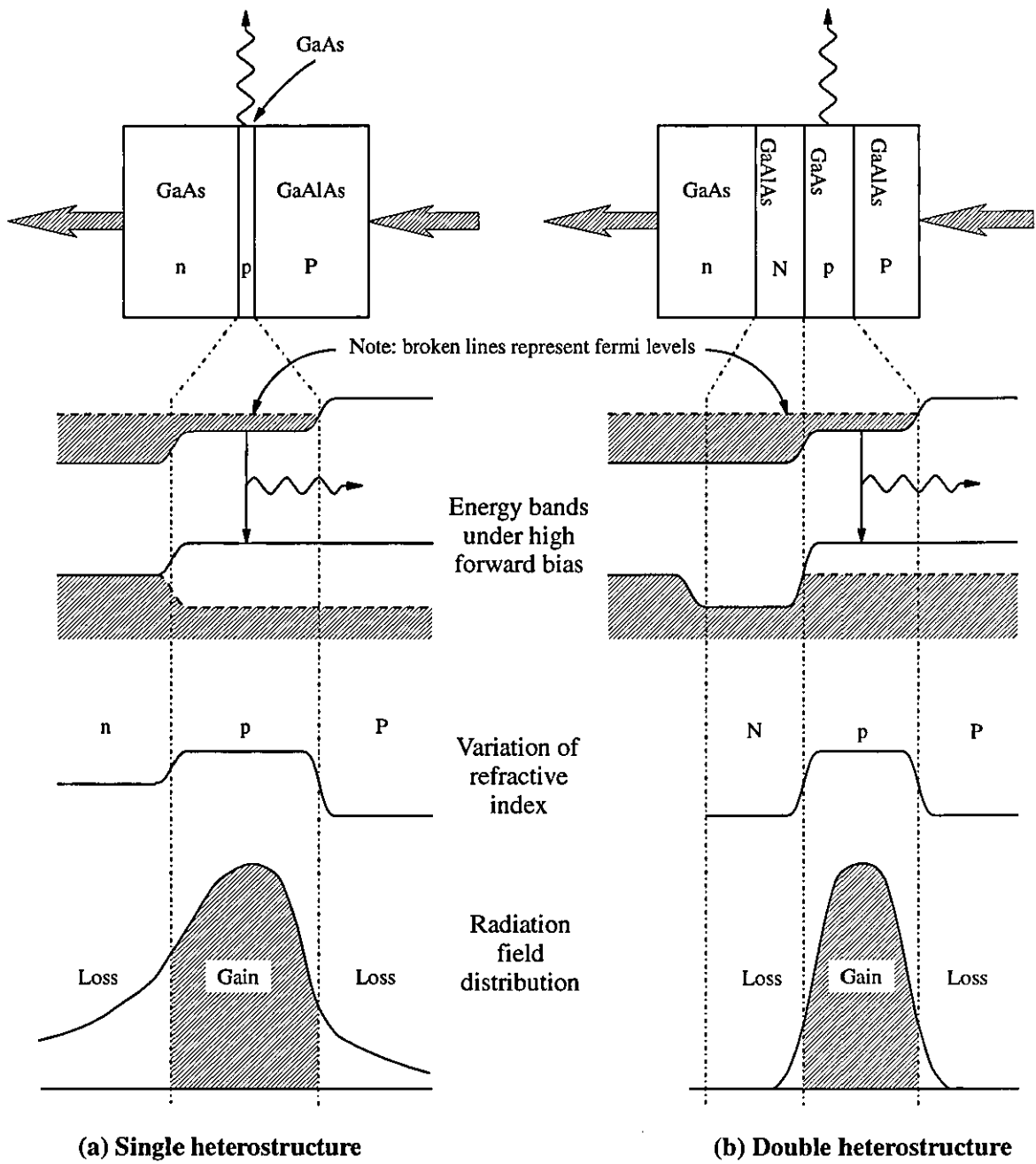
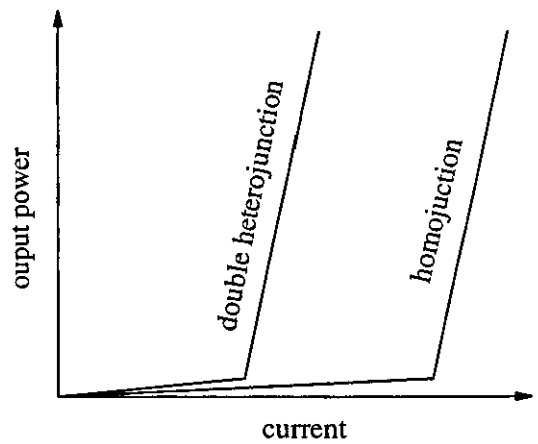


Figure 3.17 - Heterojunction Lasers.

Figure 3.18 - Typical differences in output power between junction types.



between two layers of the ternary compound $\text{Ga}_{1-x}\text{Al}_x\text{As}$, which has a much wider bandgap than the GaAs - so very little of the radiation is absorbed. The P- and N-type $\text{Ga}_{1-x}\text{Al}_x\text{As}$ materials also have smaller refractive indices than the p-type material giving better optical confinement than with the single heterojunction arrangement.

Typically these improvements in efficiency can lower the threshold current density from the 16Amm^{-2} of a homojunction laser to 10Amm^{-2} for a double heterojunction laser. This gives rise to an extremely large improvement in power output - as shown in figure 3.18, allowing such lasers to operate in continuous wave mode since the greater efficiency of the device reduces thermal heating. Further improvements can be made by making the junction structure into a quantum well structure, however this will not be reviewed here and the reader is referred to reference [13] for further information.

3.3 - Semiconductor laser drive circuitry

It has already been commented that a flash light source must have an output pulse duration of less than about 100ns in order to resolve acoustic transients temporally. It was also suggested that pulsed semiconductor lasers have become viable sources given that they offer both sufficiently short output pulse durations and high enough output power. Figure 3.19 shows the operational characteristics of such a light source - the Northern Telecom model LJ30 GaAs/GaAlAs semiconductor laser. This device has been used in all the experiments that will be described during the remainder of this chapter. It was chosen not only because of its large power output (30W), high duty cycle (0.025%) and short pulse duration (50ns), but also because of its robust design and ability to withstand severe environmental conditions with stable output properties.

3.3.1 - Single pulse [15,16]

The design of electronic circuits for driving semiconductor lasers are generally based upon current sources rather than voltage sources, since these devices exhibit extremely low impedance beyond their threshold potential. They are designed with primary consideration given to required pulse duration, energy, shape, amplitude and duty cycle of the laser.

The traditional means of driving a pulsed semiconductor laser is shown schematically in figure 3.21, where the important operational components are shown within the dotted line. The operation is simple, where after an appropriate trigger pulse to the *thyristor* the

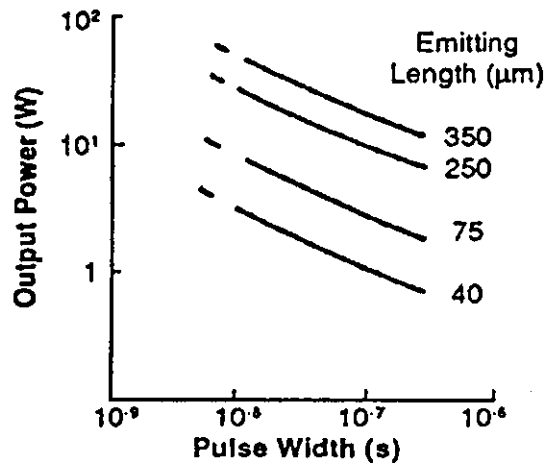
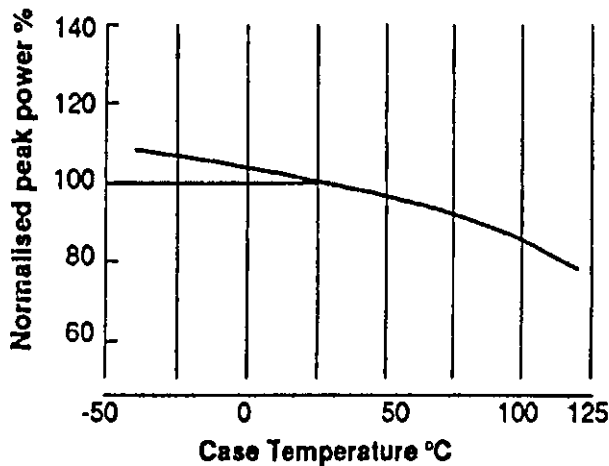
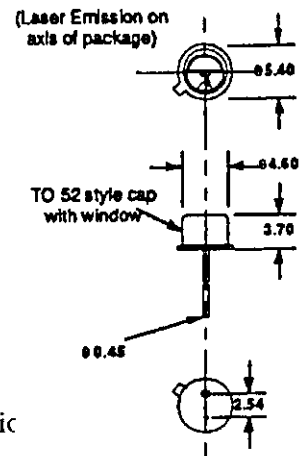
The Northern Telecom LJ30 Semiconductor Laser is a GaAs/GaAlAs Multiple Quantum Well Chip, manufactured using MOCVD (Metal Organic Chemical Vapour Deposition) semiconductor process. It has the following typical device parameters.

| PARAMETERS | min. | typ. | max. | Units |
|-------------------------------|------|-------|------|---------|
| Wavelength at peak intensity | 800 | 860 | 870 | nm |
| Spectral width, 50% intensity | | 5.0 | | nm |
| Beam divergence | | 12x30 | | degrees |

| | | | |
|---|----------|-----|---------------|
| Peak output power | Φ_T | 30 | W |
| Max. forward current (for rated output) | I_F | 40 | A |
| Threshold current (typ.) | | 2 | A |
| Forward voltage (typ.) | | 13 | V |
| Emitting length (typ.) | l | 350 | μm |
| Emitting width (typ.) | d | 2 | μm |

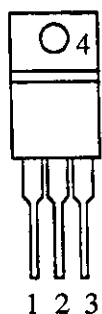
Measurement conditions

| | |
|----------------------|---------|
| Case temperature | 25 degC |
| Pulse duty cycle | 0.025% |
| Pulse width | 50ns |
| Measurement aperture | f/0.75 |



| ABSOLUTE RATINGS | Min. | Max. | Units |
|-----------------------|----------|------|-------|
| Peak output power | Φ_T | 35 | W |
| Forward current | I_F | 45 | A |
| Operating temperature | -50 | +120 | °C |
| Storage temperature | -50 | +120 | °C |
| Pulse width | | 300 | ns |

Figure 3.19 - Typical characteristics and absolute ratings of the LJ30 semiconductor laser.



top view
TO220 package

- (1) Gate
- (2) Drain
- (3) Source
- (4) Drain

Figure 3.20 - SMP60N06-18 M.O.S.F.E.T. specifications.

| | | | |
|-----------------------------|---------------------------|----------------------------------|-----------------------------|
| $I_{max} = 60 \text{ A}$ | $P_{max} = 105 \text{ W}$ | $V_{GS(th)} \approx 4 \text{ V}$ | $t_r = 35 \text{ ns (max)}$ |
| $R_{DS(on)} = 0.018 \Omega$ | $V_{DSS} = 60 \text{ V}$ | $C_{GS} \approx 50 \text{ nF}$ | $t_f = 30 \text{ ns (max)}$ |

"on" resistance gate switching potential gate capacitance "on" switching time

main capacitor C is discharged through the semiconductor laser. Since the circuit has an inductance L (which is the inductance of the wire loop formed by the connection wires between the components) it will attempt to oscillate, however this is prevented by the thyristor switching off as the current drops towards zero. In effect the circuit acts as a high energy current pulse generator where the duration, shape and amplitude of the output light pulse are determined by L and C; the energy released in the laser diode being slightly below that stored in the capacitor ($\frac{1}{2}CV_0^2$.) Typically the capacitor might have a value of $\sim 0.1\mu\text{F}$ and charged to a potential of 30V, storing an energy of approximately $45\mu\text{J}$.

The signal diode D_1 is included to protect the laser diode from a potentially damaging negative voltage. Typically a reverse bias or transient potential above $\sim 1\text{V}$ is capable of irreversibly damaging a semiconductor laser. The high speed thyristor (or *silicon controlled rectifier*, SCR) needs to have a large current rating, so that the device has a low impedance once switched on, as well as a rapid switch on time - that is much faster than the discharge pulse duration. In the case of the GB301A shown, a 0.7V, 2mA abrupt gate pulse trigger is required to switch on the SCR within 20ns. This positive trigger pulse is applied to the gate relative to the cathode through a large bandwidth pulse transformer. Due to the high bandwidth necessary for rapid triggering of the thyristor, the transformer has to be constructed very carefully with few turns and low inductance.

It is also worth noting that the charging of C takes place through R_1 , L_2 and D_3 , all of which serve to protect the semiconductor laser during the charging process. The charging current is limited by R_1 to well below the switching current of the SCR and the threshold current of the diode laser, whereas the inductor prevents the circuit from experiencing quickly varying charging currents and, the diode D_3 protects against any possibility of negative potentials being connected to the circuit. Finally the two signal diodes D_2 and D_4 dampen back-e.m.f.s created by the pulse transformer which could switch off the SCR prematurely.

The main problem with this circuit is that it is difficult to match the pulse transformer to the thyristor. Furthermore such fast SCRs are extremely difficult to fabricate so are therefore both expensive and not widely available. An alternative switching device that can be considered is the *Metal Oxide Semiconductor Field Effect Transistor* (MOSFET). The advantage of thyristors is that once switched on they can pass large currents and have little impedance. Whereas until recently MOSFETs could only deal with small currents (due to their "on" resistance being a few ohms), low voltages (otherwise gate breakdown can occur) and have slow switching speeds (200ns upwards.) The SMP60N06-18 n-

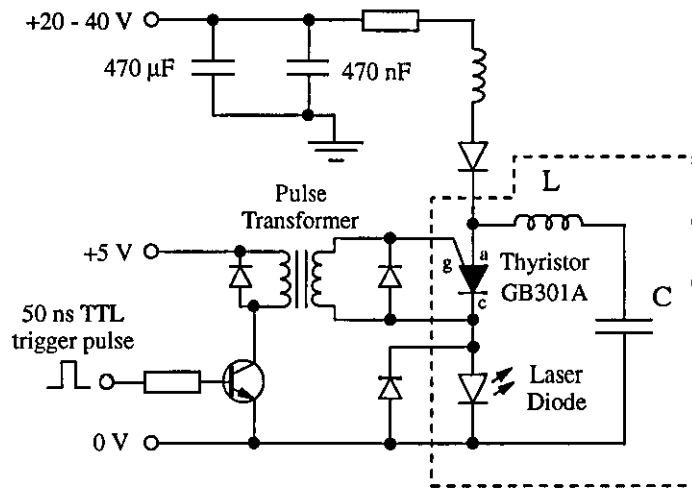


Figure 3.21 - Standard drive circuit for high power pulsed diode laser.

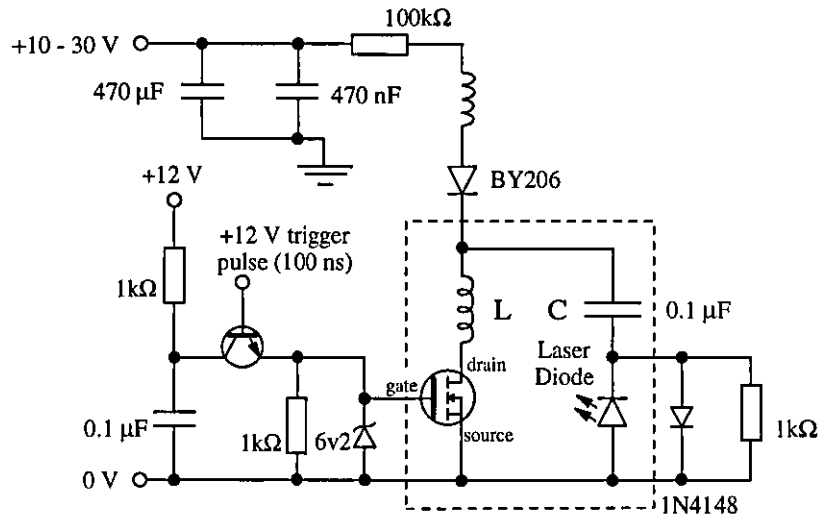


Figure 3.22 - Pulsed laser drive circuit using MOSFET as a fast switch.

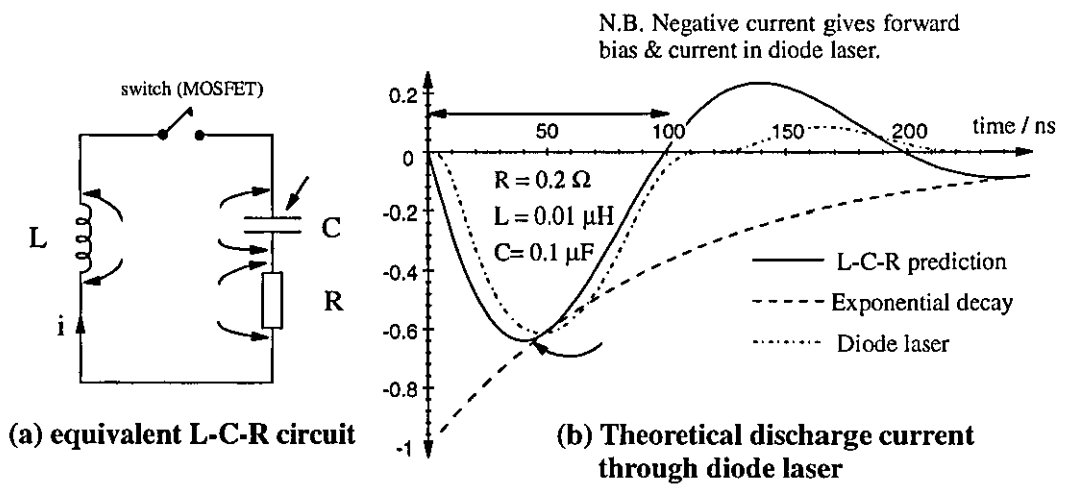


Figure 3.23 - The L-C-R approximation of the MOSFET diode laser driver circuit.

channel MOSFET however has sufficiently good operating characteristics (see figure 3.20 [17],) low cost and availability to warrant its consideration as a replacement for the thyristor. Unfortunately a direct swap cannot be made since the *gate* of the MOSFET has a comparatively high capacitance requiring a considerable quantity of charge to switch the device on.

A suitable replacement drive circuit is shown in figure 3.22, where the critical components within the dotted line have been rearranged so that the *source* of the MOSFET is connected to zero volts. The semiconductor laser is also moved to allow the potential across it to be monitored with respect to zero volts. Initially the capacitor C is charged through the resistors R_1 , R_2 , the inductor L_2 and the signal diode D_2 to a potential appropriate to the output light power required. The diode D_2 is also used to protect the laser from potentially damaging reverse bias conditions, whereas R_2 is included in case D_2 should fail. The value of the resistor R_1 is chosen so that the potential across the laser does not rise above 1V (viz. the maximum safe reverse bias potential for laser diode.) In order to trigger the system a brief 12V pulse is sent to the transistor Q_2 which allows rapid transfer of charge from C_2 into the gate of the MOSFET Q_1 . Within 30ns the MOSFET is switched on and the discharge begins to occur. Note that the inclusion of the 6.2V zener diode prevents the gate potential reaching damaging proportions. After triggering R_3 allows charge to drain away from the gate of Q_1 allowing the MOSFET to switch off a short time after the main capacitor has discharged.

The discharge can be modelled very simply by acknowledging that the laser diode and D_2 exhibit low impedance at potentials greater than their forward bias thresholds. These two components can be approximated as purely resistive, forming along with the connecting wire and MOSFET "on" resistance a total resistance R . The discharge circuit then becomes like the L-C-R circuit shown in figure 3.23(a). The behaviour of this circuit after the MOSFET has switched on can be found by applying Kirchoff's law:

$$V_L + V_R + V_C = 0$$

$$L \frac{d^2q}{dt^2} + R \frac{dq}{dt} + \frac{q}{C} = 0 \quad \text{given that} \quad i = \frac{dq}{dt}$$

which can be solved to give the current in the circuit i with time:

$$i = \frac{-q_0}{LC\omega} \exp\left(\frac{-Rt}{2L}\right) \sin(\omega t) \quad - (3.7)$$

where

$$\omega = \sqrt{\frac{1}{LC} - \frac{R^2}{4L^2}} \quad - (3.8)$$

The inductance of the circuit is roughly that of a wire loop of radius a , which is approximately equal to:

$$L \approx \frac{\mu_0 a}{2} \quad - (3.9)$$

For example, if the discharge occurs in a wire loop of radius of say 2cm, then the self inductance will be approximately 10^{-8} H. Since the resistance is comparatively small then $R^2/4L^2 \ll 1/LC$ making the angular frequency from (3.8):

$$\omega \approx \sqrt{\frac{1}{LC}} \quad - (3.10)$$

The current i through the circuit reduces to:

$$i \approx -V_0 \left(\frac{C}{L}\right)^{1/2} \exp\left(\frac{-R}{2L}t\right) \sin\left(\frac{t}{\sqrt{LC}}\right) \quad - (3.11)$$

given that the capacitor has an initial charge $q_0 = CV_0$, where V_0 is the initial charge potential of the capacitor. The current pulse duration is approximately the time taken for the current to return to zero since D_2 prevents a negative potential building up across the laser. Therefore when $\omega.t = \pi$ equations (3.7) and (3.10) give:

$$t_{\text{discharge}} \approx \pi\sqrt{LC} \quad - (3.12)$$

The solid line in figure 3.23(b) shows the calculated current waveform for a circuit with inductance $L=10^{-8}$ H, capacitance $C=0.1\mu\text{F}$ and resistance $R\sim 0.2\Omega$. It is evident from this that the pulse duration (full width half maximum) and the peak current are approximately equal to:

$$t_{\text{FWHM}} \approx \frac{t_{\text{discharge}}}{2} \approx \frac{\pi}{2}\sqrt{LC} \quad - (3.13)$$

and,

$$I_{\text{peak}} \approx 0.6V_0\sqrt{\frac{C}{L}} \quad - (3.14)$$

The average current I_{av} can also be approximated as the root mean square of the above, so that:

$$I_{av} \approx \frac{0.6V_0}{\sqrt{2}} \sqrt{\frac{C}{L}} \quad - (3.15)$$

Note that the time for the MOSFET to switch on has been ignored here, together with the fact that the diode laser and protection diode have higher impedance at low currents, as indicated by the diode equation (3.1) mentioned earlier. In general the latter will have the effect of damping the oscillations significantly during low current flow, as well as delaying the oscillations slightly - as shown by the dotted and dashed line in figure 3.23(b).

The main capacitor C is chosen to give the appropriate amount of electrical energy to the diode laser. This must account for the efficiency of the semiconductor laser (~20%, say,) pulse length required and, the proportion of energy dissipated by resistive elements of the circuit. The average power dissipated in the circuit during the discharge can then be estimated by assuming that all the energy in the capacitor is discharged within time $t_{discharge}$:

$$P_{av} \approx \frac{\frac{1}{2}CV_0^2}{\pi\sqrt{LC}} \approx \frac{V_0^2}{2\pi} \sqrt{\frac{L}{C}} \quad \text{watts} \quad - (3.16)$$

If the laser has an efficiency of $\epsilon\%$ and the power dissipated in the resistance of the wires, contacts and MOSFET switch accounts for $X\%$, then the peak light power emitted by the semiconductor laser can be found using equation (3.16) and a.c. theory:

$$P_{peak} \approx \sqrt{2} X\% \epsilon\% \frac{V_0^2}{2\pi} \sqrt{\frac{L}{C}} \quad - (3.17)$$

Typically the efficiency of the laser will be ~20%, and it is not unreasonable to assume that approximately 1/2 of the energy is dissipated resistively in the circuit resistance of ~0.1 Ω . The remainder of the energy is converted to light within the semiconductor laser which is also assumed to have an impedance of 0.1 Ω , giving a total resistance of 0.2 Ω . Hence the pulse duration, peak current and light output power can be estimated from equations (3.13), (3.14) and (3.17):

$$t_{discharge} \approx 50\text{ns} \quad I_{peak} \approx 38 \text{ amps} \quad P_{peak} \approx 28.5 \text{ watts}$$

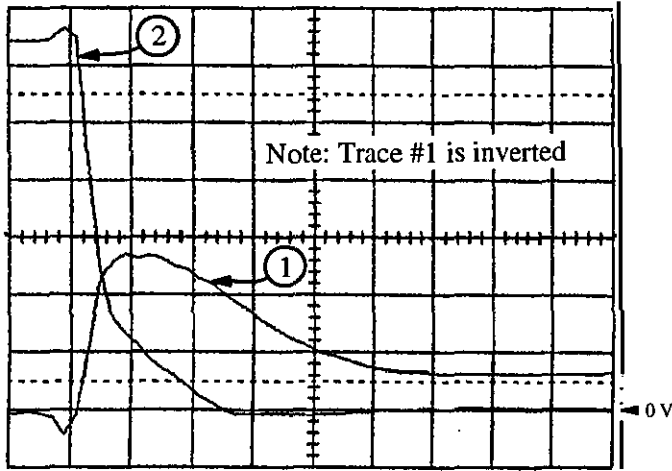
when $L=10^{-8}$ H, $C=0.1\mu\text{F}$ and $R\sim 0.2\Omega$ and the main capacitor is charged to $V_0=20\text{V}$. These values are in agreement with those quoted in the LJ30 semiconductor laser specifications shown in figure 3.19. As a result the circuit shown in figure 3.22 with similar inductance, resistance and capacitance values as in the rough calculations above should drive the LJ30 semiconductor laser adequately.

3.3.2 - Experimental single pulse set-up

Before a semiconductor laser can be incorporated into the single pulse drive circuit described, it is vital that the circuit is tested so as to ensure that the semiconductor laser will not be damaged by either too high or too long a current pulse, or alternatively by negative voltages. This may be done using a *dummy load* which is chosen to have similar electrical characteristics to the laser, for example the diode can be replaced with two 1N4148 signal diodes placed in series, or alternatively a 0.5Ω pure resistor.

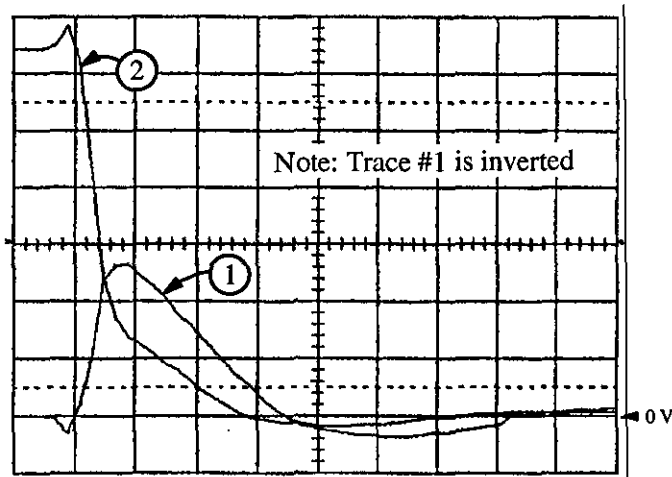
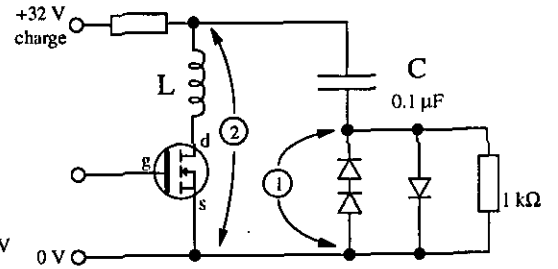
The drive circuit described in the last section (figure 3.22) has been constructed for the Northern Telecom LJ30 semiconductor laser. This was done on a strip board approximately 1 inch square minimising the circuit size to keep the inductance of the discharge loop as low as possible. That is the diameter of the capacitor-MOSFET-laser circuit was approximately 2cm - close to that used in the calculations earlier where the inductance was estimated to be $\sim 10^{-8}$ H. The two suggested dummy loads were inserted in place of the semiconductor laser and the voltage across them measured on an oscilloscope, and the results are shown in figure 3.24:

- (i) *Dummy load of two signal diodes in series* - it is seen in figure 3.24(a) that the potential across this dummy load behaves very similarly to that predicted in the last section (see figure 3.23,) however with two distinct differences. The first is that in order to generate the 13V peak forward voltage quoted for the LJ30 (see specifications in figure 3.19,) the capacitor had to be charged to 35 volts - larger than the charge potential estimated earlier. This implies that the circuit resistance is greater than expected. The other difference is that the potential measured across the diodes does not drop back to zero after discharge (at least not until the MOSFET switches off several hundred microseconds later) or oscillates, but settles to $\sim 3\text{V}$. This is most likely to be due to the diodes having high impedance at low potentials.
- (ii) *0.5Ω Pure resistance dummy load* - this circuit shown in figure 3.24(b) behaves more like that predicted earlier. The resistance used here is higher than that used in



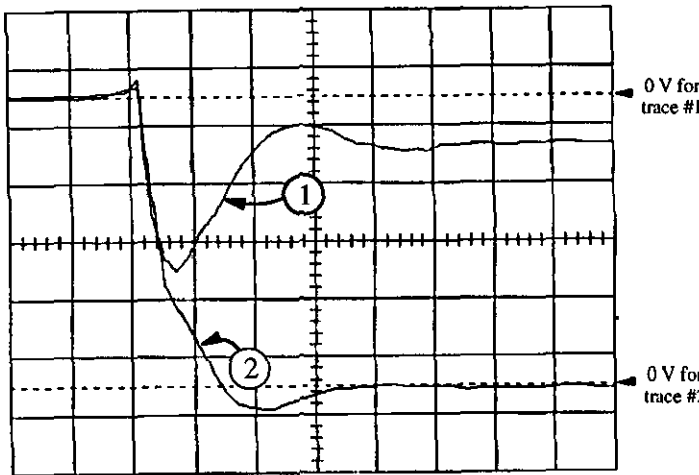
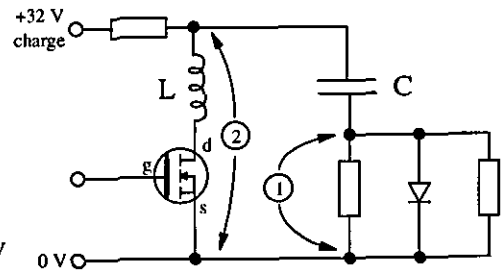
(a) 2 x 1N4148 signal diodes

horizontal timebase : 50ns / div
vertical scale : 5V / div



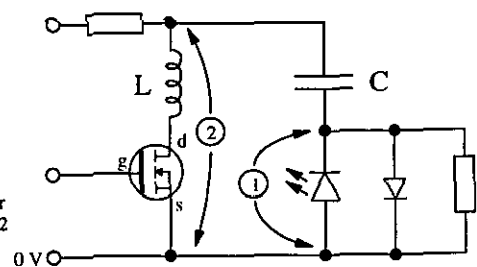
(b) 0.5 Ω pure resistor

horizontal timebase : 50ns / div
vertical scale : 5V / div



(c) LJ30 semiconductor laser

horizontal timebase : 50ns / div
vertical scale : 5V / div



All circuits have a total empirical wire loop of 2cm radius which makes up inductance L, C is a 0.1μF ceramic disc capacitor,

Figure 3.24 - Voltages measured from single pulse diode laser driver.

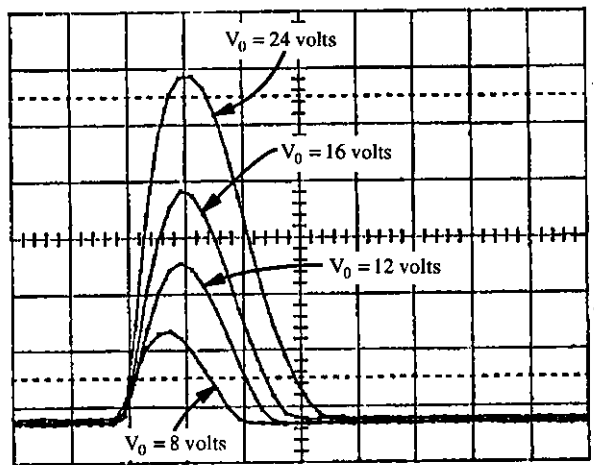
the approximations, however it is not high enough to lengthen the pulse duration significantly. Again, the charge potential V_0 had to be increased to $\sim 32\text{V}$ since the potential measured across the dummy load was lower than expected - due to higher circuit resistance. Since the dummy load is a pure resistor then the peak current flowing through the circuit can be estimated applying Ohm's law:

$$i_{\text{peak}} = \frac{V_{\text{peak}}}{R_{\text{dummy}}} = \frac{13\text{V}}{0.5\Omega} \approx 26 \text{ amps}$$

This is large enough to be beyond the lasing threshold of the laser but also low enough so as not to damage the laser. The slight increase in pulse duration can be explained by there being greater inductance in the circuit than estimated, say about $2 \cdot 10^{-8}\text{H}$.

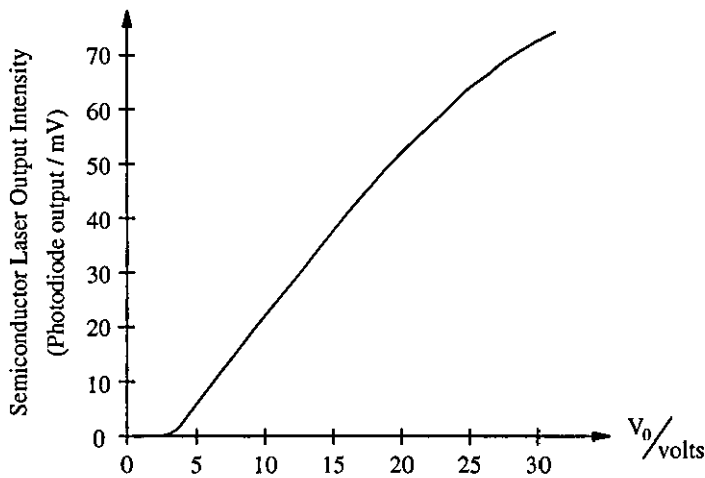
Having determined that the circuit provides a suitable current pulse, the semiconductor laser can now be inserted. The laser diode is not soldered into position since it can easily be damaged by the high temperatures involved, but is attached using screw terminals. Figure 3.24(c) shows the voltage trace measured with respect to time across the laser diode when the capacitor C is charged to 25 volts. It can be seen that the peak voltage is $\sim 15\text{V}$ implying that the impedance of the diode, which is a function of both the applied voltage and current, is significantly lower than that of the test loads. The pulse duration (Full Width Half Maximum) is approximately 60ns, which is marginally longer than expected. Figure 3.25(a) shows the output light intensity with time (arbitrary vertical scale) measured by the fast photodiode circuit shown in figure 3.25(c). It is observed here that the output pulse shape roughly follows that of the input current, however as the charge potential V_0 is increased the pulse duration lengthens. The measured peak output light intensity above the threshold potential ($\sim 3\text{V}$) is essentially linear with V_0 , as seen in figure 3.25(b), however as the charge potential is increased above 20V the peak intensity begins to fall off. Both of these effects are due to saturation of the recombination rate at the junction. There is also the essential requirement for the semiconductor laser to produce enough light to suitably expose a recording medium. This is experimentally verified in section 3.4.2 where it has been found that the laser produces sufficient light to saturate an entire field of a CCD camera. Also calculations involving the amount of light available from the semiconductor laser compared with the sensitivity of the CCD camera have been performed and can be found in section 3.5.3.

One important aspect in the design of the circuit is that the correct type of capacitor is used. The inherent inductance and resistance of real capacitors depend upon their fabrication, that is a capacitor which has plates with a large area is likely to have a higher

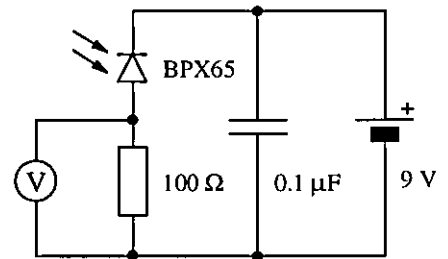


Scale : horizontal 50 ns/div
vertical 10 mV/div

(a) Light output intensity with respect to time



(b) Peak magnitude of output pulse



(c) Photodiode measuring circuit

Figure 3.25 - Light pulse output of diode laser measured by photodiode.

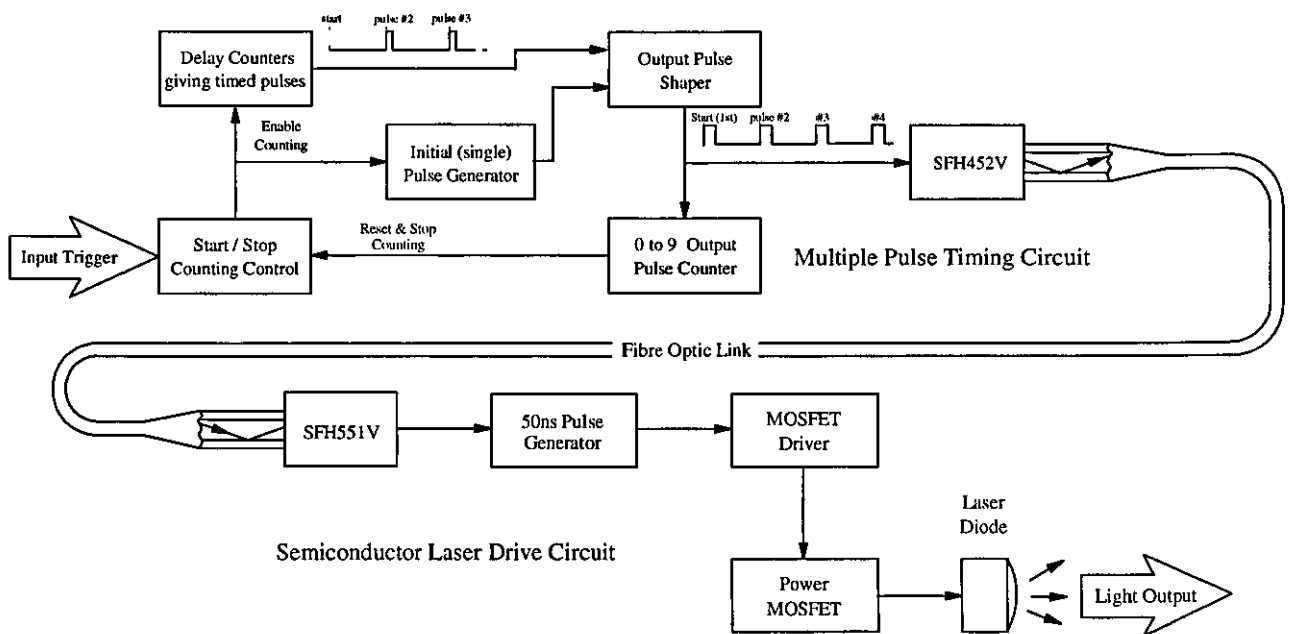


Figure 3.26 - Multipulse timing control circuitry and diode laser controller schematics.

inductance since the charge has to "travel" greater distances during charging and discharging. With this in mind, the capacitor found best experimentally for this application was a 0.1 μ F Ceramic Disc (30V) type.

Another problem is the effect that long wires have on trigger pulses. That is a 50ns square shaped pulse sent from timing circuitry to the trigger of the semiconductor laser drive circuit down a 1 metre cable can deform in shape significantly. This problem is entirely in accordance with transmission line theory and the wire can therefore only be of a limited length before the signal is lost. One solution to this problem is to use a fibre optic cable link in place of the wire.

3.3.3 - Problems with electromagnetic noise

Devices that produce acoustic transients, such as high power lasers and electromagnetic lithotrippers often emit large amounts of electromagnetic noise during the discharge of their large high voltage capacitors. As a result of this, the semiconductor laser drive and timing circuitry is often prone to false triggering. It is therefore advisable that the circuit is protected from external influences by the following:

- (i) *Isolation of power supplies* - often false triggering is caused by electrical transients entering through the power supply. Several techniques are available to reduce this problem though none can completely solve it. These include using noise suppression circuitry, isolating the supply with a toroidal coil transformer and, the use of large inductances and capacitances. An example of how these can be applied can be seen in appendix A1.1 for the protection of digital timing circuitry used later.
- (ii) *Reducing the number and size of current loops in the circuit* - electromagnetic noise can be picked up in any complete conducting loop. In order to reduce this effect the size of the control circuit (i.e. power supply, timing and drive circuitry) should be minimised. Also breaks in large circuits which therefore have large current loops can be made using optical isolators and dual power supplies (e.g. appendix A1.2).
- (iii) *Optical fibre links* - these are especially useful where a signal must be sent over a great distance, for example between timing, event and laser control circuitry. If a cable link is used in these cases then the wire can pickup both electromagnetic noise and transmit transients from the event causing device. Fibre optic cable on the other hand only carries the signal and is not susceptible to pickup, although the emitters

and detectors can be effected. *Opto-isolators* can also be used to stop the passage of noise spreading within control circuitry.

- (iv) *High current circuitry* - electromagnetic noise is rarely capable of generating high currents. Therefore one way of reducing the effects of noise is to use switching devices that require large amounts of current. Alternatively capacitors and resistors can be added to the inputs of each device within the circuit. However this is often disadvantageous since large amounts of power are required and high speeds are harder to achieve.
- (v) *Shielding circuits and cable* - this can reduce the amount of electromagnetic noise picked up. The circuit to be protected could be encapsulated in a conducting shield, sometimes called a *Faraday Cage*. The electromagnetic noise will generate eddy currents in the shield which is then dissipated resistively, the electromagnetic radiation does not penetrate through the shield. Cable can be protected in the same way using a coaxial arrangement of the wire, however with limited effect.

All these techniques were applied, the semiconductor laser was encased in a brass housing, connected to timing and power supply circuitry (both housed in an aluminium die cast box) by earthed coaxial cable.

3.3.4 - Multiple pulse drive circuitry

It was commented earlier in section 3.1 that semiconductor lasers can be pulsed beyond their duty cycle limit for a short amount of time provided that over a much longer period the duty cycle is not exceeded. This property can therefore be exploited to provide a source of short duration light pulses in high speed photography.

Unfortunately the drive circuit shown in figure 3.22, and described in the last three sections, can not be used to drive the laser diode with several pulses in quick succession. This is for two reasons, firstly due to the main capacitor C not being able to recharge quickly enough and, also because the MOSFET switches off slowly in its present configuration. In order to reduce the recharge time of C to say $1\mu\text{s}$, the resistance would have to be lowered to $\sim 10\Omega$. This however causes a problem in that the laser diode will be damaged if it is put in reverse bias above 1V, which will occur with R so small. The present configuration of the MOSFET allows the gate charge to leak away through R_3 , switching it off over a few hundreds of microseconds. Unfortunately only slight

improvements can be made by reducing the size of R_3 . As a result of these problems a completely different circuit design is required.

A more appropriate system for driving the semiconductor laser is shown schematically in figure 3.26. It comprises of two parts: a digital timing circuit providing a pre-set number of trigger pulses at regular intervals in time, and a circuit which drives the semiconductor laser with constant duration current pulses. These are connected by a fibre optic link. The detailed circuit diagram for the timing circuitry can be found in appendix 1, figure A1-8, and operates as follows. A single external triggering pulse (for example from the camera synchronisation and timing circuitry described later in section 3.6) allows counting to start and triggers the first output pulse. At the same time delay counters are triggered. These wait for a pre-set time before triggering a further output pulse, resetting and repeating the same operation. The output pulses are counted until a pre-set number have been sent down the fibre optic link, at which the counters are stopped and reset. The counters can not be started again until a fresh trigger pulse is sent to the system after a further pre-set "safety" period, which is so that the semiconductor laser is not operated beyond its duty cycle limit. The circuit can trigger the semiconductor drive circuit up to 9 times at regular pre-set intervals of between 200ns-2.0 μ s, in 100ns steps, to an accuracy of within a few nanoseconds.

The circuit for driving the semiconductor laser is shown in figure 3.27. Upon receiving a trigger pulse through the fibre optic link, a monostable multivibrator generates a 30ns duration 5V pulse. This is inverted by the 7406 buffer and converted to the 12V logic needed to control the IR2110 MOSFET driver [18]. The IR2110 then briefly switches the power MOSFET on for a few nanoseconds allowing charge from a large capacitor bank (50 μ F) to flow through the laser diode for ~50ns. The increase in pulse duration is due to both the IR2110 and the MOSFET taking longer to switch off than on. The precise pulse length can be controlled by adjusting the potentiometer VR1 controlling the monostable multivibrator, however it is also dependant upon the exact properties of the semiconductor laser.

The power MOSFET is chosen to have fast switching times, very low 'on' resistance and the ability to withstand high currents. Here a RFD16N05 is used since it has an on resistance of 0.08 Ω , switching times of 24ns and 20ns for on and off respectively [19], and can withstand up to 45A when pulsed. A signal diode is also placed across the laser to protect the laser against reverse bias potentials. The drive circuit is kept small (30mm by 25mm) to keep the inductance and the capacitance to a minimum. As before, it is

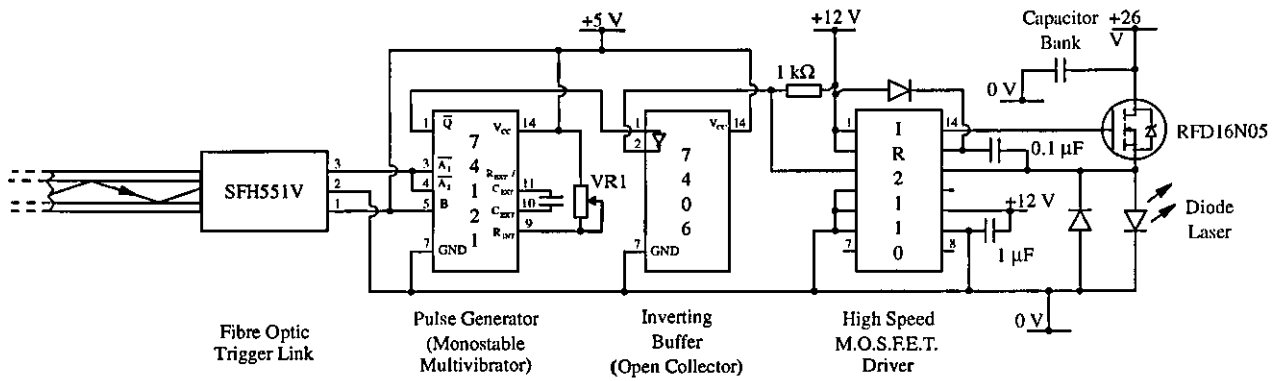
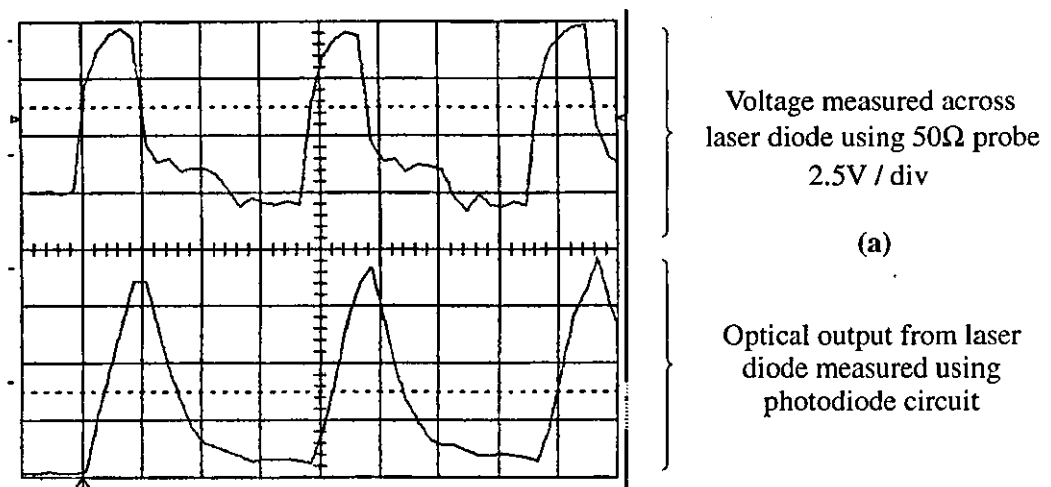
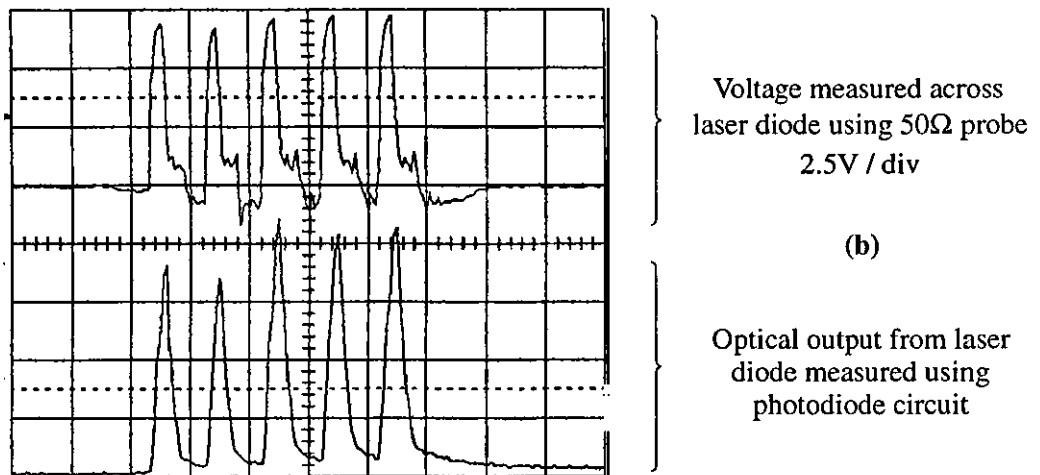


Figure 3.27 - Diode Laser Drive Circuit.



Scale of 50 ns per horizontal division



Scale of 200 ns per horizontal division

Figure 3.28 - The optical output of the multi-pulsed semiconductor laser in comparison to the drive potential.

cased in a brass shell so that the circuit is not triggered falsely by stray electromagnetic noise from the laser used here to create the event.

The fibre optic link used is based upon the Siemens SFH452V infrared transmitter and SFH551V digital receiver [20,21], connected by a 1mm core diameter polymer cable. The system is capable of transmitting 5Mbits/sec over a maximum length of 50m. It was chosen due to the relative ease of connection between the transmitter, fibre and receiver; as well as being extremely inexpensive. As explained earlier, the fibre optic connection is used because of its high immunity to electromagnetic noise.

3.3.5 Experimental multiple pulse drive circuit

The multiple pulse semiconductor laser drive circuit described in the last section was first tested with the same dummy loads described earlier in section 3.3.2, and the circuit was found to be safe for the laser diode to be included. Figure 3.28 shows the voltage measured across the laser with respect to time by an oscilloscope. The timing circuit is set-up so that after triggering there are 5 pulses emitted by the laser with 200ns separation. The oscilloscope was set to have an impedance of 50Ω preventing signal reflections at the oscilloscope end of the measuring cable, which could disrupt the measurements.

It can be seen that the voltage pulses applied to the semiconductor laser have a FWHM duration of about 50ns, the rise and fall times of the pulses being less than 20ns. The voltage does not immediately settle back to zero after each pulse however, probably due to the laser having high impedance at low voltages (or currents.) Also the peak voltage is only about 7V when the capacitor bank of the drive circuit is charged to 26V, which is most likely due to the MOSFET having a comparatively large "on" resistance compared with laser diode. This could be rectified by choosing a MOSFET with lower "on" resistance, however this is usually at the expense of increasing the switching times. Therefore the only alternative is to increase the voltage that the capacitor bank is charged to, but this was unfortunately not possible during these experiments.

The optical output intensity of the laser was measured with a photodiode at the same time as the voltage measurements were made. The photodiode set-up used was similar to that used earlier with the single pulse drive circuit as shown in figure 3.25(c). It can be seen that the output intensity rises and falls much more slowly than the voltage pulses, however the pulse duration (FWHM) is still about 50ns. All the pulses emitted are of

similar shape, however they vary slightly in intensity, but do not fall off with time. This is due to slight fluctuations in the drive voltage pulses and appears to be somewhat random.

3.4 - Collimation techniques

It is essential in any analytic optical system, such as Shadowgraphy or Schlieren imaging, that the output beam of the light source is properly collimated. By this it is meant that the beam appears to originate from a single point in space, which is at an infinite distance away from the observer. To the observer the point source will appear to have a planar wavefront and negligible beam divergence, so that the light will appear to travel in a straight line with the same cross-sectional area everywhere along its path. In section 3.2.4 it was commented that the output beam properties of semiconductor lasers differ between the two planes parallel and perpendicular to the junction. That is in the perpendicular plane the output beam is limited entirely by diffraction, whereas in the parallel plane the characteristics are controlled by the electric current profile across the junction. Typically the output facet of the LJ30 pulsed semiconductor laser is about $2\mu\text{m}$ by $350\mu\text{m}$, giving rise to a far field beam divergence of $\theta_{\perp} \approx 30^{\circ}$ by $\theta_{\parallel} \approx 12^{\circ}$ [8]. Consequently the beam profile in the far field will be elliptical, the diameter of the beam perpendicular to the junction being about 2.5 times that in the parallel direction.

The output beam of a semiconductor laser also suffers from *astigmatism*. Although in the plane perpendicular to the junction the beam originates from the front face of the laser, the beam in the direction parallel to the junction appears to diverge from a point that is up to $50\mu\text{m}$ behind the front face. This occurs because the beam is limited by different physical effects in the two directions, that is by the electric current profile in the parallel plane and diffraction in the plane perpendicular to the junction. Astigmatism of the order of $50\mu\text{m}$ may not seem large, but it becomes very significant when compared with the dimensions of the junction and the beam divergence, and makes good Schlieren imaging difficult.

The current flow across the junction of a semiconductor laser also results in the output beam being *polarised*. Typically the beam polarisation is 100 times greater in the plane parallel to the junction compared with the perpendicular direction. This can cause problems if the beam is reflected off surfaces (e.g. beamsplitters,) or in systems that analyse the polarisation properties of materials. Finally spherical aberration is introduced by the $\sim 0.2\text{mm}$ protective glass window on the semiconductor laser casing.

3.4.1 - Commercial semiconductor laser collimators

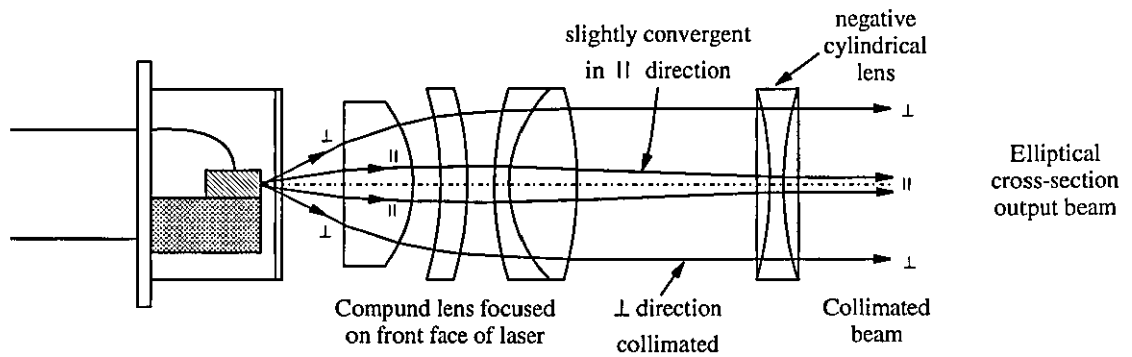
Two typical commercial lens arrangements for the collimation of semiconductor laser beams are shown in figure 3.29 [22,23]. Both consist of a diffraction limited compound lens which collimates the light in one plane, and a weak cylindrical lens corrects the astigmatism in the other plane. The type and power of the cylindrical lens primarily depends upon which point on the semiconductor laser the compound lens is focused on:

(i) *Compound lens focused on the front facet* - as shown in figure 3.29(a) and schematically in figure 3.30(a). In the plane perpendicular to the junction the output beam appears to originate from the front facet of the laser P1, so the light will be collimated by the compound lens in this direction. Whereas, in the perpendicular plane the beam appears to originate from a point P2 several microns behind the front facet. In this plane the beam is imaged by the compound lens to a point P3, distance b beyond the lens. Assuming that the compound lens can be approximated to a single lens focused on the front facet, then b can be calculated using the *Gaussian lens formula* :

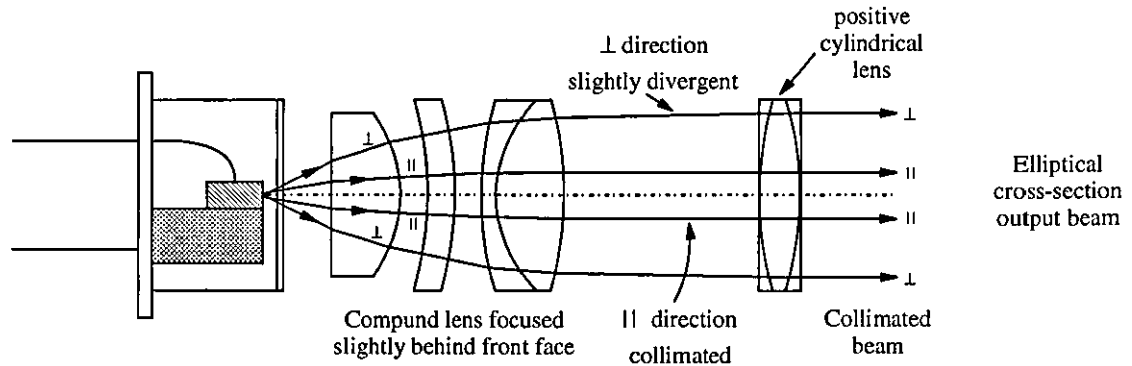
$$\frac{1}{f+a} + \frac{1}{b} = \frac{1}{f} \quad - (3.18)$$

where f is the effective focal length of the compound lens and, a is the distance into the semiconductor laser that the beam appears to originate from in the plane parallel to the junction. For example, if the compound lens has a focal length of 0.4cm and the light appears to originate from a point $50\mu\text{m}$ before the focal point, then the beam will be focused at a point $\sim 32\text{cm}$ beyond the lens. This is then corrected by a negative cylindrical lens with a focal length of 32cm positioned very close to the compound lens, with the curvature in the direction parallel to the junction.

(ii) *Compound lens focused on apparent origin of beam in plane parallel to junction* - as shown in figure 3.29(b). In this case the light in the parallel plane is collimated by the compound lens. This also results in the beam orthogonal to the junction becoming slightly divergent upon leaving the first lens. The divergence can be calculated using equation (3.18) and slightly redefined distances as shown in figure 3.30(b). For example, suppose a $f=0.4\text{cm}$ compound lens is used to collimate the beam in the parallel plane originating from a point P4, distance $a=-50\mu\text{m}$ behind the front facet P6. In the perpendicular plane the beam will appear to originate from a point P4, distance $b=-31.5\text{cm}$ behind the front facet and, this can then be corrected by a positive cylindrical lens with a focal length of 31.5cm placed close to the compound lens.



(a) Using negative cylindrical lens



(b) Using positive cylindrical lens

Figure 3.29 - Standard collimation methods, correcting astigmatism with a weak cylindrical lens.

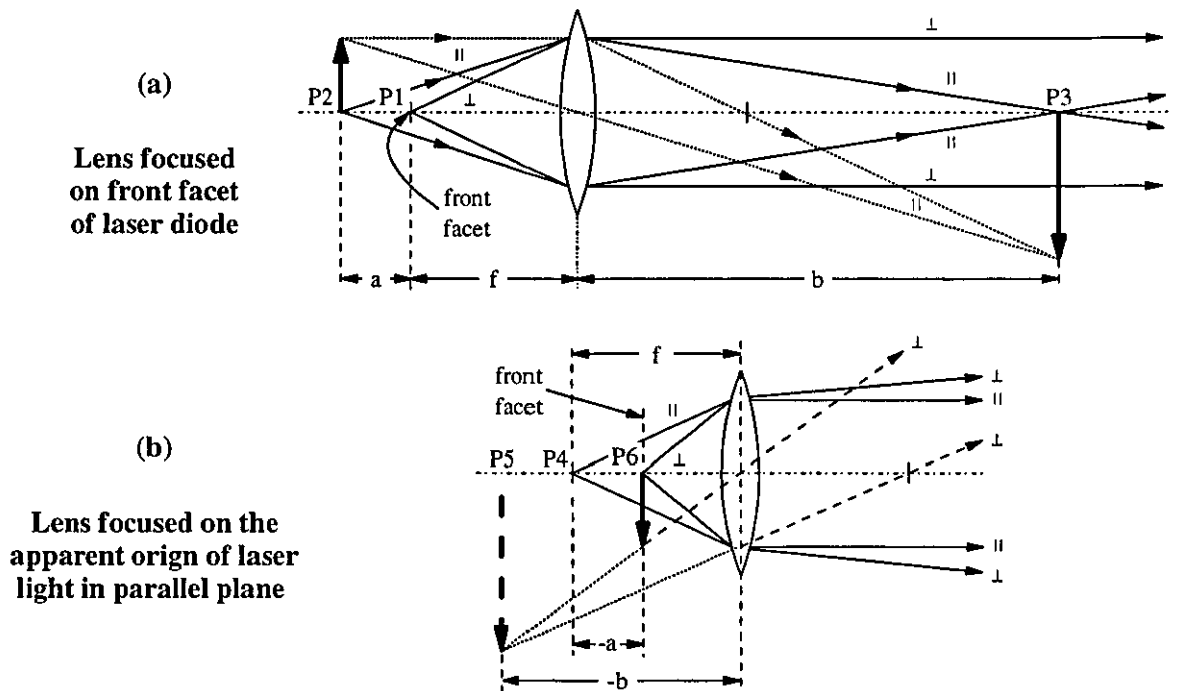


Figure 3.30 - Geometric interpretation of the effects of a lens on the astigmatic output of the diode laser.

In the last section it was commented that the semiconductor laser beam is highly divergent. As a result the compound lens must have a large numerical aperture, which is defined as:

$$\text{N.A.} = n_0 \sin \theta_{\max} \quad - (3.19)$$

where θ_{\max} is the maximum angle of the light entering the lens aperture through refractive index n_0 , which is usually air $n_0 \sim 1$. Alternatively if the lens has an aperture with diameter D and focal length f , the lens can be quoted in terms of its *f-number* [14]:

$$f/\# = \frac{1}{2(\text{N.A.})} = \frac{f}{D} \quad - (3.20)$$

Therefore a beam that has a maximum divergence of 30° , for example, will need a lens having a numerical aperture of at least 0.5, which corresponds to a $f/2$ lens. This obviously causes problems when it comes to selection of the focal length of the compound lens, in this case restricting f to less than about 1cm. It is best to have a large focal length, since this will reduce the effects caused by the astigmatism of the semiconductor laser. Also the compound lens becomes more difficult to accurately align relative to the front facet of the laser with shorter focal lengths. This is due to the tight mechanical tolerances involved in all three directions, for example in the direction of the output beam the positioning error must be very much smaller than the astigmatism (few microns.) Therefore semiconductor laser collimators cannot simply be assembled by eye relying solely on mechanical tolerances. Hence micro translation stages are vital for the alignment of the first collimation lens, whereas the cylindrical lens does not need to be accurately positioned due to its comparatively long focal length. Additionally there is the problem of spherical aberration caused by the output window of the laser; this can be compensated by adjustment of the thickness of the first element of the compound lens.

Collimation of light from a semiconductor laser in the way described above yields an output beam that has an elliptical cross-section, due to the differing divergences in the two planes. This can be corrected using either a cylindrical lens telescope or a pair of *anamorphic prisms*, as shown in figures 3.31(a) & (b) respectively. The second method is preferred commercially since it is both difficult and expensive to manufacture cylindrical lenses with the diffraction limited performance necessary. The anamorphic prism pair consists of two identical prisms mounted in such a way that the incident beam enters both prisms at *Brewster's angle*. At this angle the component of the light polarised with the electric field parallel to the plane of incidence (which is perpendicular to the surface of the prism) is completely transmitted; whereas the component orthogonal to the

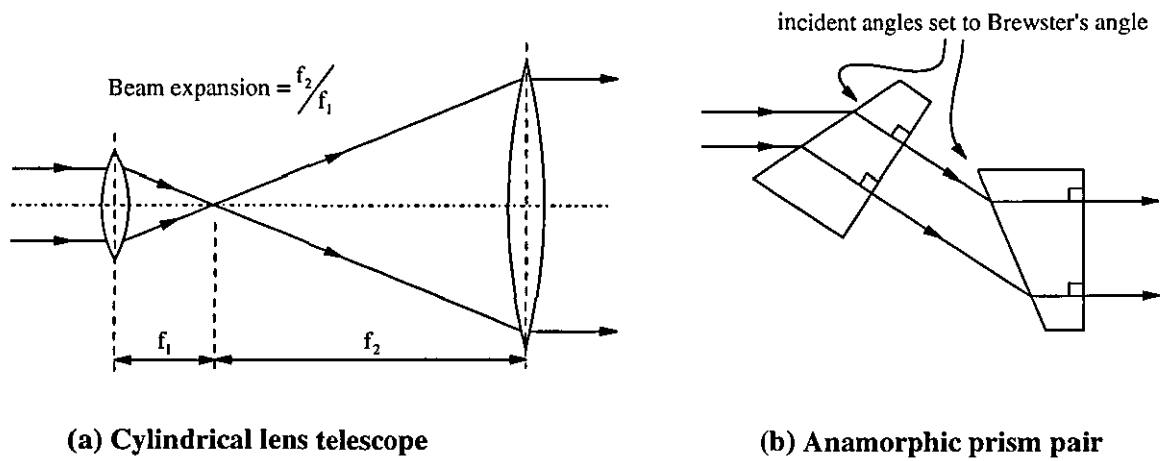


Figure 3.31 - Methods for the correction of the elliptical output from a semiconductor laser, where the correcting optics are placed in the minor plane.

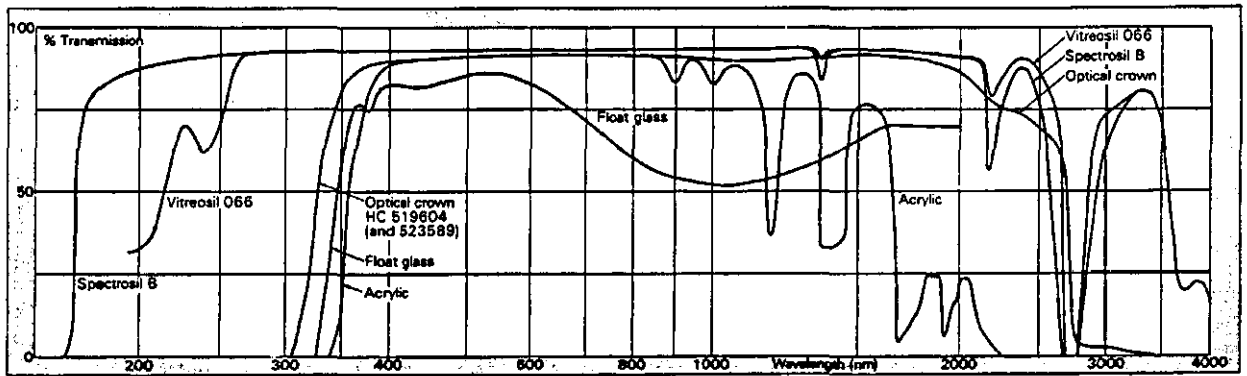


Figure 3.32 - Energy transmission of commercial optical materials for 10 mm thickness window.

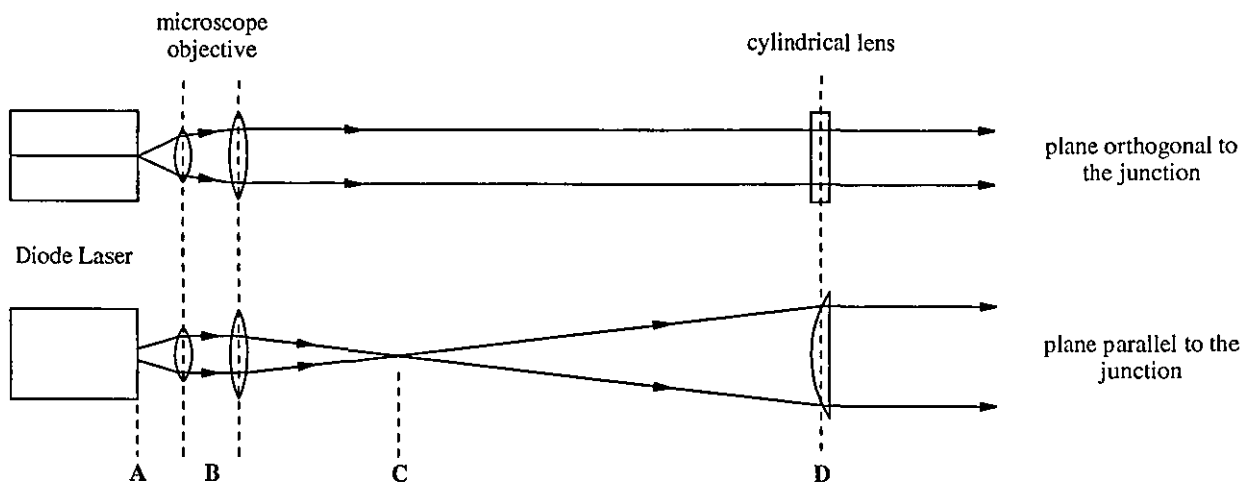


Figure 3.33 - Experimental collimation setup used with the semiconductor laser.

plane of incidence is partially reflected. Since the light emitted from semiconductor lasers is usually polarised with the dominant component of electric field in the plane parallel to the junction, then the prisms are mounted such that the plane of incidence is parallel to the junction. The Brewster angle θ_p and the wedge angle θ_w of the prisms can be calculated using:

$$\tan \theta_p = \frac{n_{\text{prism}}}{n_{\text{air}}} \quad \& \quad \sin \theta_w = \frac{n_{\text{air}}}{n_{\text{prism}}} \sin \theta_p \quad - (3.21)$$

where n_{prism} is the refractive index of the prisms.

3.4.2 - Simplified experimental collimation set-up

One problem with commercial semiconductor laser collimators is that the light has to travel through a considerable number of glass elements. This will not only attenuate the beam, but the light will also be scattered and reflected at the glass-air interfaces. Therefore the lenses used must be anti-reflection coated, otherwise over several lens elements a significant quantity of the beam will be scattered and phantom sources will become visible. Also the right lens material must be selected since few optical materials transmit light efficiently over the entire spectral range of available semiconductor lasers. For example, *float glass* is unsuitable when using the LJ30 diode laser which emits at $\sim 860\text{nm}$, since the intensity transmission coefficient of that material at that wavelength is quite low, as shown in figure 3.32 [24]. Whereas optical *crown glass* transmits 90% of the light over the entire visible and near-infrared range.

A much more simple collimation technique has been developed using fewer elements and is shown schematically in figure 3.33. The light from the semiconductor laser is first collimated in the plane perpendicular to the junction using a microscope objective (B) focused on the front facet of the laser (A). Instead of immediately correcting the astigmatism, the beam in the plane parallel to the junction is allowed to converge to a focus (C). It is then allowed to diverge until it is the same size as the light in the perpendicular plane, where it is collimated using a positive cylindrical lens (D) having a focal length comparable with the distance from C to D. This was achieved practically using a dual element microscope objective with a focal length of 0.4cm and $f/1.4$ aperture, together with a cylindrical lens with 10cm focal length and aperture dimensions of 1cm (in the direction of curvature) by 2cm. The highest power pulsed semiconductor lasers emit in the near infrared, typically at about 860nm for the LJ30, and therefore the light emitted can not be seen by the human eye making adjustment of the collimation

optics difficult. Standard CCD cameras however have a peak response at these wavelengths, so can be used as an aid to the setting up of the optical system as well as being the recording medium during the subsequent high speed photography. Also it is worth noting that the LJ30 semiconductor laser used here is a class IIIb laser, so caution is required in the handling of the output beam to avoid eye injury.

Given that the semiconductor laser beam can only be seen by using a CCD camera connected to a television monitor, a general method for setting up the collimation optics has been developed and is shown schematically in figure 3.34:

Stage I - The microscope objective is first mounted in a micro-translation stage, and is placed in front of the semiconductor laser with the junction aligned horizontally. This is mounted appropriately on an optical rail and the laser is pulsed periodically (e.g. @ 10 Hz) with medium output power. The CCD camera is placed a short distance beyond the microscope objective and is positioned by eye at the same height as both the objective and the laser. The microscope objective is then adjusted until the beam is focused on the camera in the vertical direction, which is shown as a horizontal broad band on the TV monitor, for example as seen in figure 3.35(a). In practice, when the system is not properly focused diffraction lines are seen, as in figure 3.35(b & c). The CCD camera is then progressively moved further away from the laser, re-adjusting the microscope objective so that the beam is focused and centralised on the screen, until the camera is at the opposite end of the optical bench from the laser (i.e. >1m away.) The output beam of the semiconductor laser is now effectively collimated in the plane perpendicular to the junction.

Stage II - The CCD camera is now positioned as close as possible to the microscope objective and the output beam dimensions measured in the horizontal direction. As the camera is moved slowly away it is usually observed that in the horizontal plane the beam comes to a rough focus and then diverges. Beyond this distance the position of the camera is noted first when the width of the beam is approximately half that of its height (position #1) and, then when the width is roughly equal to its height (position #2.) Results obtained experimentally using the LJ30 semiconductor laser are shown in figures 3.34(b) and 3.36. The beam doubles in width over a distance of ~7cm, therefore it can easily be calculated using simple geometry that the cylindrical lens should have a focal length of ~14cm. However the nearest focal length available is 10cm, so this is used instead and is placed at position #2.

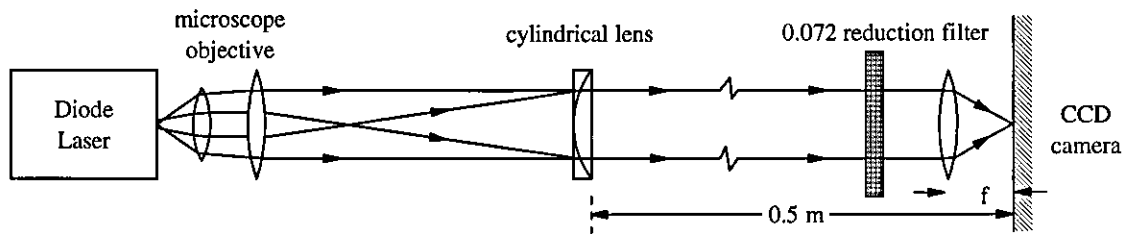
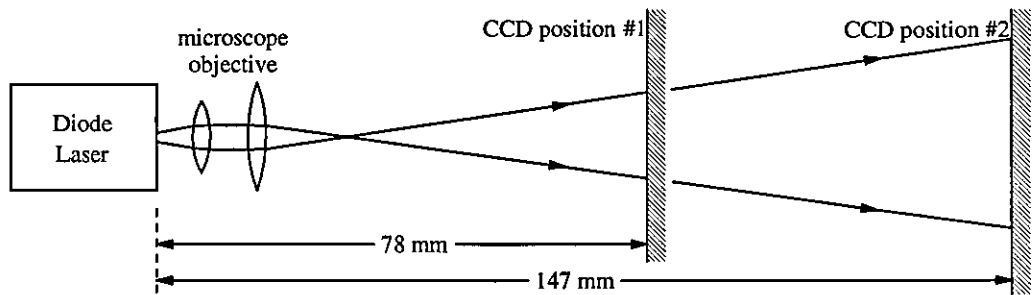
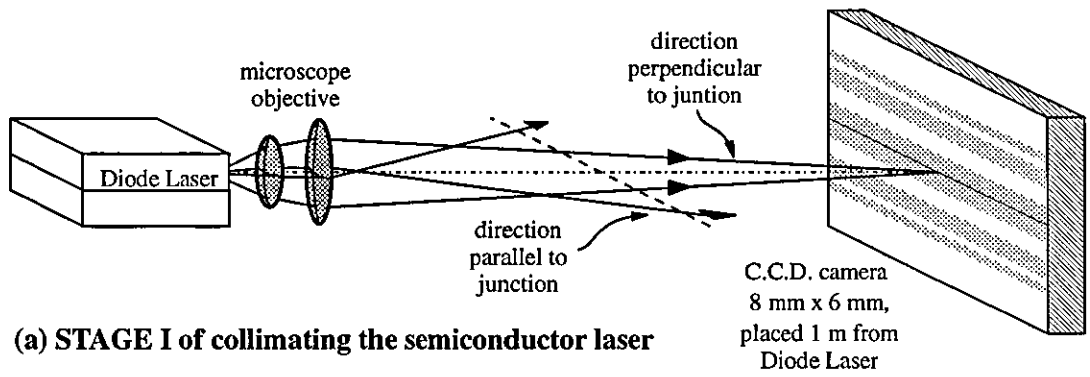


Figure 3.34 - Collimation method.

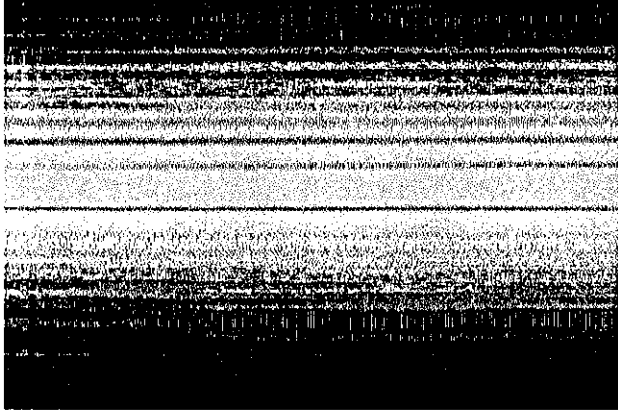
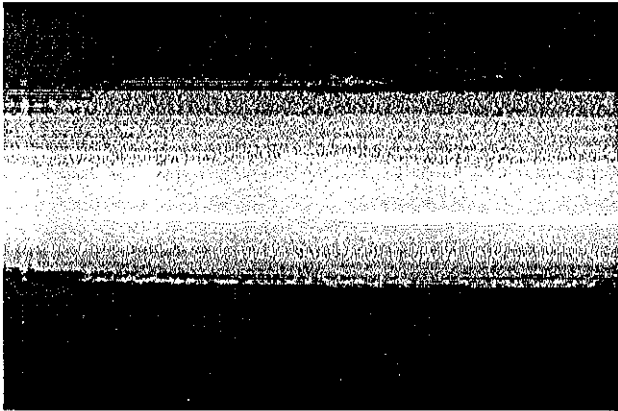
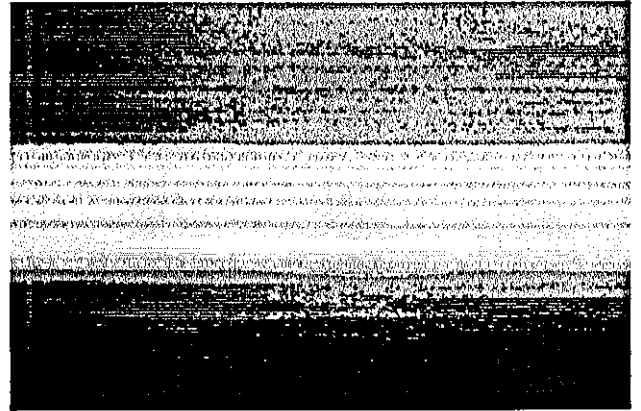


Figure 3.35 - Image seen on CCD camera during STAGE I of semiconductor laser experimental collimation.

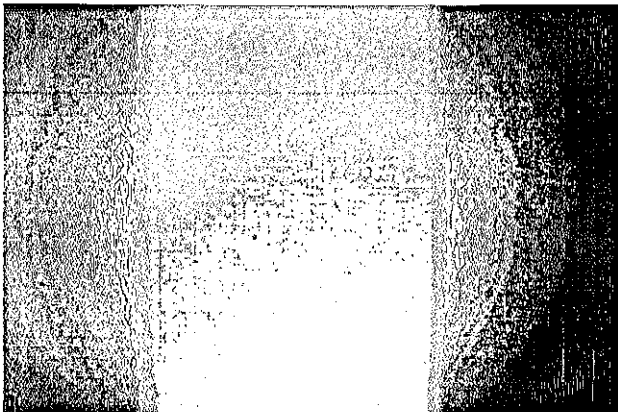
(a) Microscope objective correctly positioned.
 Diffraction lines are clearly resolved and in focus, hence objective is focused on the front facet of the diode laser.



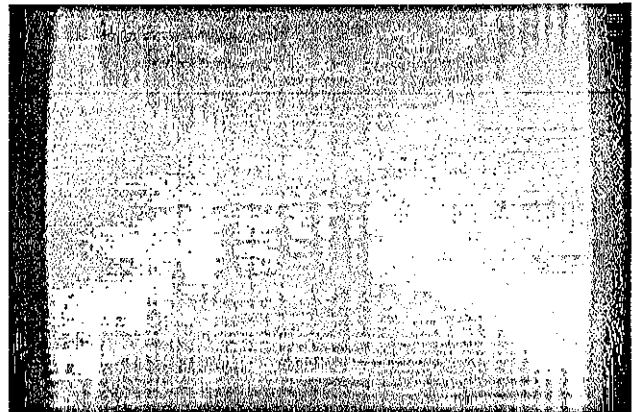
(b) Objective too close to front facet.



(c) Objective too far from laser.



(a) Camera at position #1, 78 mm from diode laser front facet.



(b) Camera at position #2, 147mm from laser.

Figure 3.36 - Image seen by CCD camera during STAGE II of experimental collimation of diode laser. (See also figure 3.36 and text.)

Stage III - A 50mm lens is fitted to the CCD camera and is focused at infinity. The camera is placed at an intermediate distance along the optical rail (e.g. ~1/2m from the laser), as shown in figure 3.34(c). A high attenuation neutral density filter is attached to protect the camera, since the light beam is now focused to a point on the camera. The position of the cylindrical lens is then adjusted until the size of the focal spot is as small as possible, at which point the output beam is completely collimated. The results obtained using the LJ30 semiconductor laser are shown in figure 3.37. Note that the haloes around the very bright central spot represent the uncollimated or diverging parts of the output beam, however the majority of the energy is in the focused spot. The image seen is in fact that of the front facet of the laser, where the central spot is the lasing output and the bright horizontal line is the spontaneously emitted radiation

Finally figure 3.38 shows the output beam obtained experimentally using the LJ30 semiconductor laser and the described optical collimation system, as seen by the CCD camera 1/2m beyond the laser. It is approximately 5mm square in cross-section and has roughly uniform intensity.

3.4.3 - Beam expansion

Unfortunately a working beam of 5mm square is often too small for examining the travel of acoustic transients since, for example, they travel in water at ~1.5mm/ μ s. Therefore the beam must be expanded to a suitable size using the telescope arrangement shown in figure 3.39. The magnification of this system is given by:

$$\text{beam expansion} = \frac{f_2}{f_1} \quad - (3.22)$$

where f_1 and f_2 are the focal lengths of the two lenses. The separation of the two lenses is slightly shorter than shown since the focal lengths are less than quoted as the output of the laser is in near infrared (~860nm) Again to ascertain if the lenses are correctly positioned, a technique similar to stage III in the collimation of the laser is applied. That is a lens is fitted to the CCD camera and focused at infinity, the beam expander lenses are then adjusted until the spot seen on the camera is as small as possible - at which point they are correctly positioned.

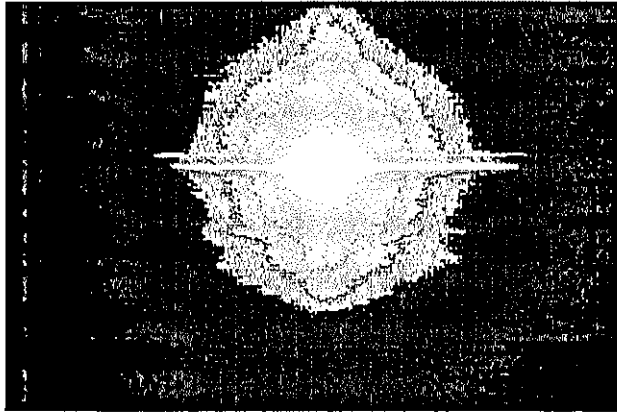


Figure 3.37 - Laser diode collimation STAGE III, CCD camera image taken at the focus of a 50mm f/2.4 camera lens, with 0.072 filter attenuating the beam of light.

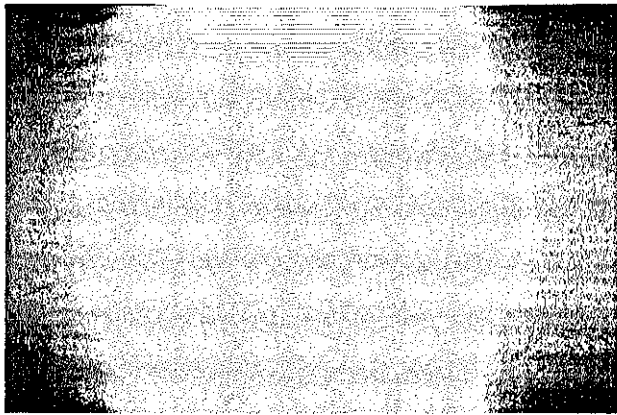


Figure 3.38 - Output beam of collimated diode laser as seen by CCD camera, showing cross-section that is roughly circular approx. 5mm in diameter.

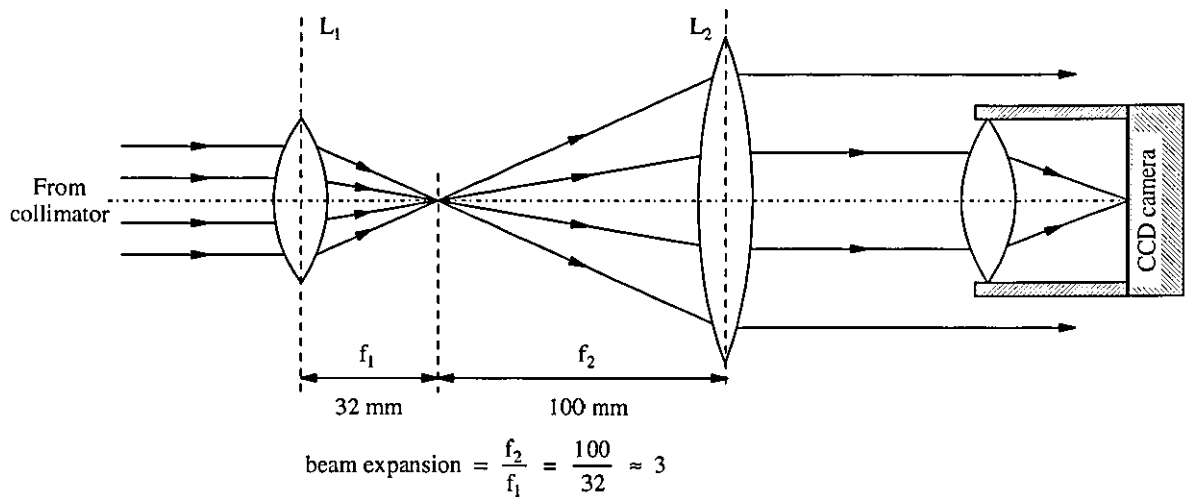


Figure 3.39 - Beam expansion setup.

3.5 - Imaging onto a CCD camera

In chapter two it was commented that there are several techniques which can be used to detect and image scenes illuminated by radiation emitted from a semiconductor laser. Unfortunately the human eye is unsuitable as a detector because the majority of high power pulsed laser diodes emit light in the near infrared, which is outside the spectral range of the eye. Also, these lasers fall into the class IIIb category in terms of their output power, and so the light is intense enough to cause irreparable damage to the eye when viewed directly. It is possible to use a recording medium such as photographic film having the general advantages of high resolution and sensitivity; film however has the considerable draw-back of not being able to give instantaneous results. Alternatively electronic cameras such the *Vidicon* system can be employed to give an instantaneous output, however they are often quite bulky.

A newer development in electronic detectors is the CCD camera. This device has broad spectral sensitivity across all of the visible and near infrared wavelengths, peaking at the output wavelength of the LJ30 semiconductor laser. It is also compact, and gives instantaneous results in terms of a serial signal repeated 50 times per second which can be viewed on a TV monitor. The remainder of this section deals with the operating principles of CCD cameras and, tries to calculate the response of a typical CCD camera to a single light pulse created by the LJ30 semiconductor laser.

3.5.1 - General principles of charge coupled devices

The concept of the *charge coupled device*, or CCD, was proposed in 1970 by Boyle and Smith [25] in an attempt to produce an electrical analogue to magnetic bubble devices. The essential principles of operation of CCD devices are as follows. Potential wells are first created in a semiconducting material by the influence of overlying electrodes which are separated from the semiconductor by a thin insulating layer. The potential wells can then be used to store information in the form of electrical charge packets placed within them. Therefore under the control of external voltages applied to the electrodes, the potential wells and hence the charge packets can be shifted through the semiconductor. By introducing the charge packets at one end and detecting them at the other, a shift register or delay line can be created.

The delay line is not however limited to the storage of digital information only. The potential wells are capable of storing variable amounts of charge and so the CCD is capable of providing an analogue signal delay. Furthermore, the charges may be

introduced into the potential wells by optical means: that is light incident on the semiconductor can be allowed to generate charge carriers by the photoelectric effect. These charges can be collected in the potential wells and subsequently clocked out of the structure thereby enabling the CCD to act as an imaging sensor. Charge coupled devices are a hybrid of both analogue and digital electronics effectively quantising the time variable but not the signal amplitude.

3.5.2 - CCD camera systems

Electron-beam camera tubes such as the *Vidicon* system have been developed over several decades and provide very high performance in terms of resolution and sensitivity. In spite of the huge advances in solid state technology, it has been found extremely difficult to find an equivalent device using the rugged, long life, compactness and low-voltage advantages of semiconductor devices [25]. That is until the recent development of the CCD camera.

The basic structure of a CCD camera is shown in figure 3.40(a). One horizontal line of a camera is made up of p-type semiconductor material coated with 3 sets of metallic electrodes. Several of these horizontal rows can be stacked in parallel to form a 2 dimensional grid of sensing elements called *pixels*. A lens can then be used to focus an image on the front face of the p-type substrate, which is depicted here as a single spot of light on the diagram. Initially input ϕ_1 is held at a positive voltage creating a potential well under each of the respective electrodes, the other electrodes are held at zero volts. Photons entering the silicon substrate generate electron-hole pairs by the photoelectric effect, and the minority carriers (i.e. the electrons) are collected under each ϕ_1 electrode. The number of electrons collected under a given electrode within a given time (called the *integration period*) is proportional to the local light intensity on that electrode. Hence the quantity of charge that collects under each ϕ_1 electrode represents the light intensity across the original image. At the end of the integration period the charge pattern is then read out by clocking the electrodes in a 3-phase manner as shown in figure 3.40(b), until all the charge packets are removed. At the end of the read out cycle the device is switched back to the integration mode and the process repeated.

During the read out period light is still incident on the array. Consequently signal charge packets being transferred through the array will pick up additional spurious charge causing the image to be smeared. This can be eliminated by using alternative CCD arrangements such as the *Frame Transfer* (FT) and the *Inter-Line Transfer* (ITL) methods [26], which are shown in figure 3.41. In both of these, photon generated charge

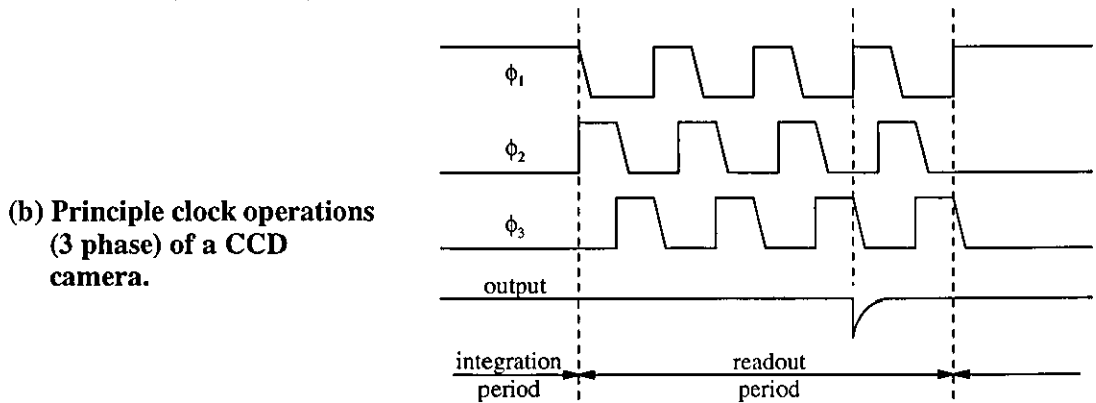
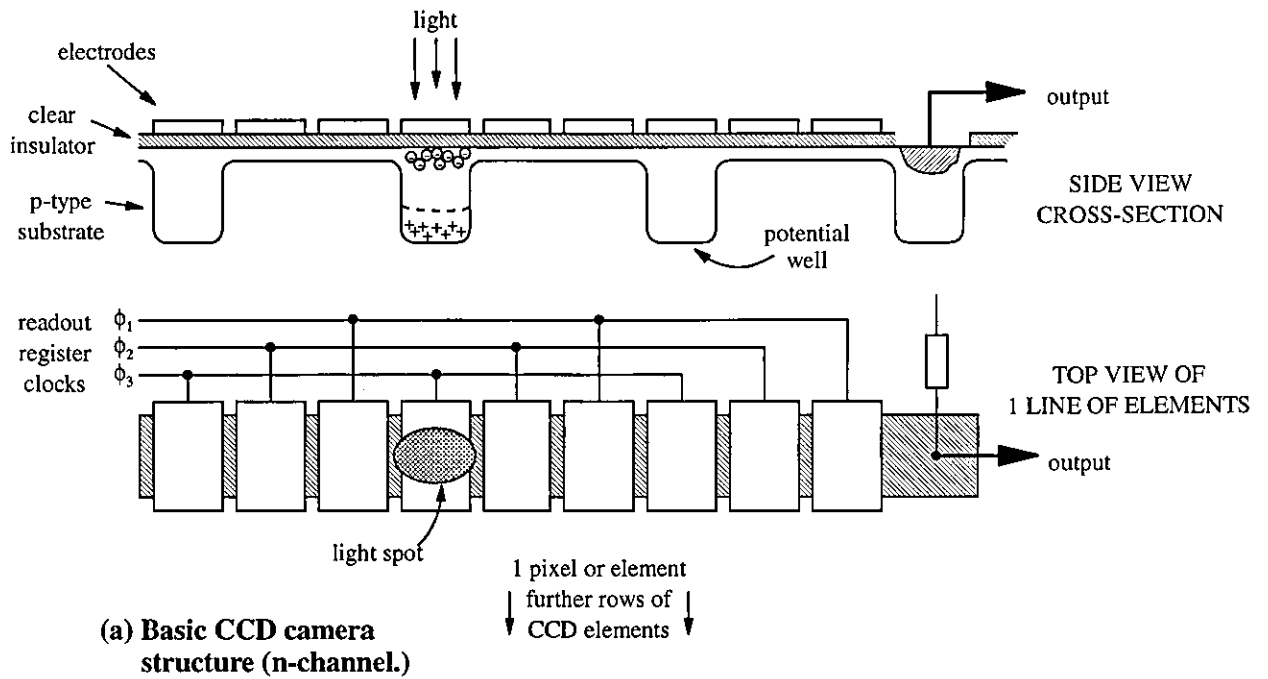


Figure 3.40 - The basic construction and operation of a CCD camera.

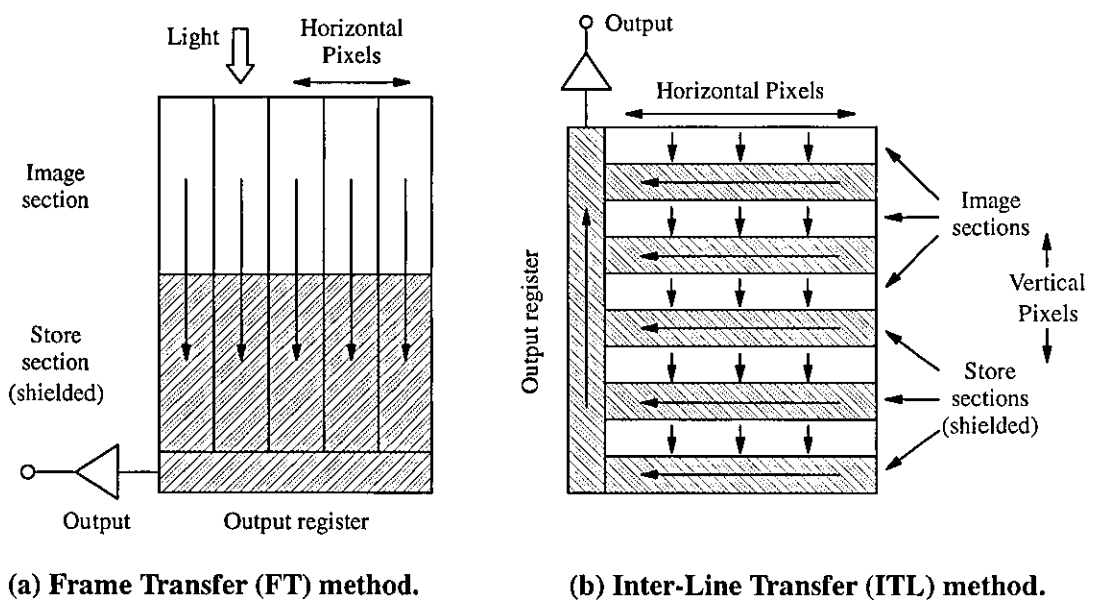


Figure 3.41 - CCD camera arrangements for reducing image smear.

is first collected under the photo-gate for a set integration period, each sensing element or pixel being separated by a channel stop diffuser. The charge is then transferred in parallel within a very short amount of time ($\sim 1\mu\text{s}$) into the CCD shift register using the transfer gate. Each line of charge packets is then read out from the shift register as before, while the next line of information is being collected under the photo gate. Smear is avoided by shielding the shift register from the incident radiation by a metal overlay.

A CCD imaging camera is usually made up of a grid of elements or pixels, whose information is clocked out sequentially in a raster fashion (i.e. top left \rightarrow top right, down a line, left to right, etc. until bottom right pixel is reached.) A typically high resolution black and white CCD camera, such as the Pulnix PE530 (which uses the inter-line transfer method) used later experimentally in this chapter, might have 582 vertical lines each comprising of 752 pixels running horizontally. The analogue electronic output signal is usually amplified and encoded in one of two standards: the CCIR (black & white) and PAL (colour) standards (50Hz) in Europe and, the EIR (b & w) and NTSC (colour) standards in the USA (60Hz.) A typical CCIR/PAL signal [27] is shown in figure 3.42. A complete *frame* of pixels is outputted every 40ms (25Hz) and comprises of two 312.5 line interlaced *fields*, which are labelled as the *odd* and *even* fields. The first 21.5 lines of each field usually only contain timing information, and lines 22 to 312 (or lines 335 to 625 for even field) contain the interlaced image information. In total there are 625 lines for the CCIR and PAL standards and, in addition the PAL standard has a *burst* at the beginning of each line which contains the colour information of the image.

3.5.3 - Brief calculations

It is necessary to calculate the whether the LJ30 semiconductor laser emits enough light to expose a single typical CCD camera frame. When a CCD camera views a scene through a $f/1.4$ lens, the minimum illuminance on the scene needed to give a full white output from the Pulnix PE530 camera used later in this chapter is about 1 lux [28]. In photometry *illuminance* is defined as the *luminous flux* reaching a surface perpendicularly per unit area, and has unit of *lux* which is equivalent to lm m^{-2} . The luminous flux ϕ_v can be defined using the human eyes normalised response curve $V(\lambda)$ with respect to wavelength λ (shown in figure 3.44), together with the spectral power distribution $\phi_e(\lambda)$ of the incident light in watts, as follows [29]:

$$\phi_v = 680 \int_0^{\infty} \phi_e(\lambda) V(\lambda) d\lambda \quad \text{in lumens (lm) or cdsr (1cd=1msr}^{-1}\text{)} \quad - (3.23)$$

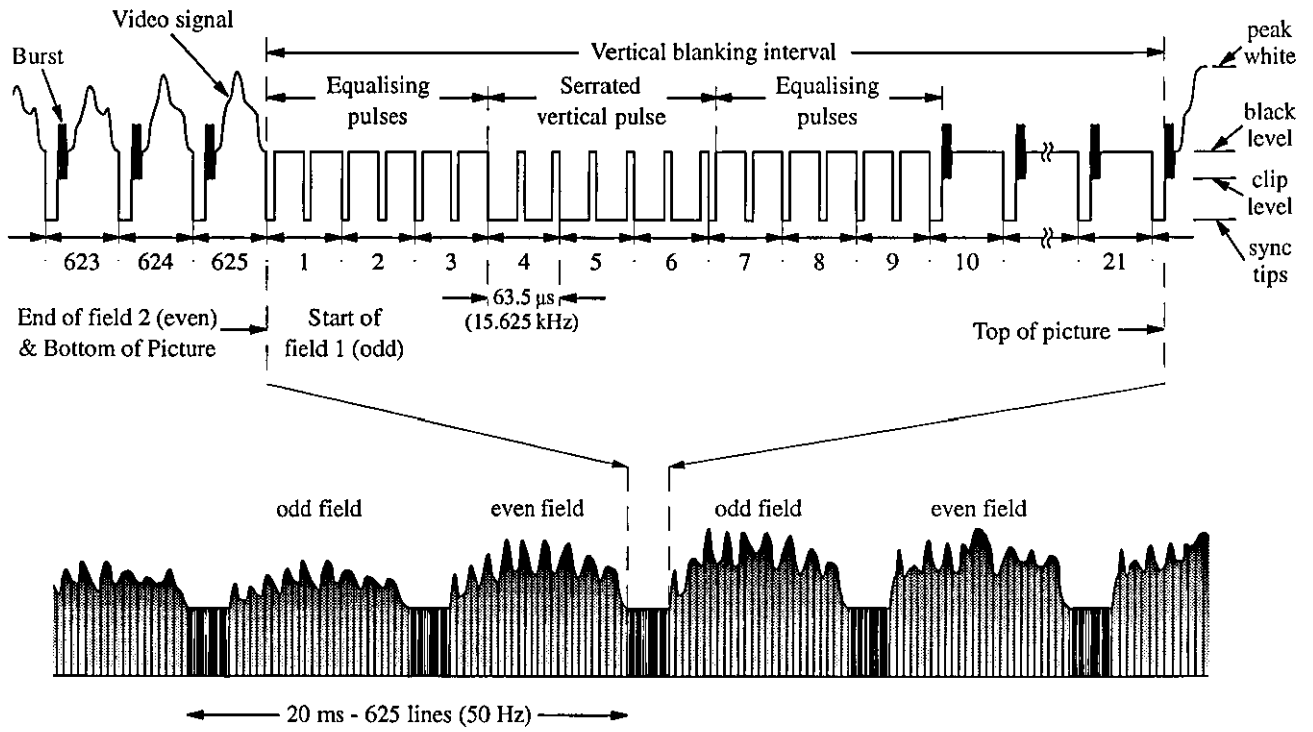


Figure 3.42 - C.C.I.R. standard composite video signal.

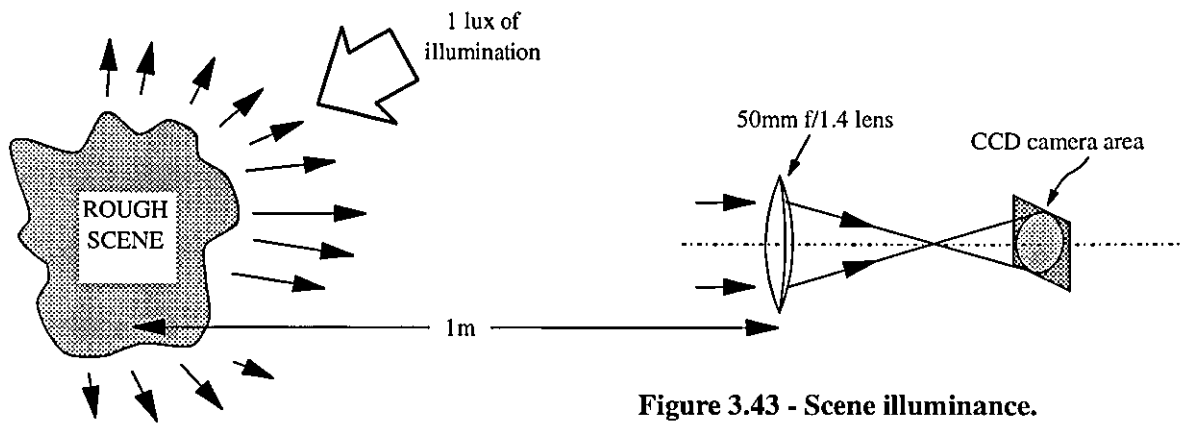


Figure 3.43 - Scene illuminance.

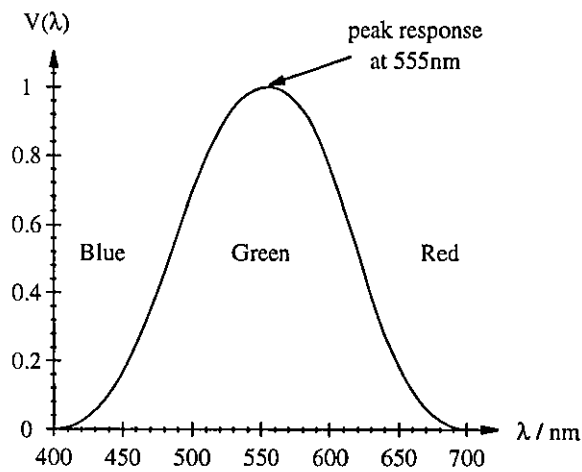


Figure 3.44 - Response of the human eye.

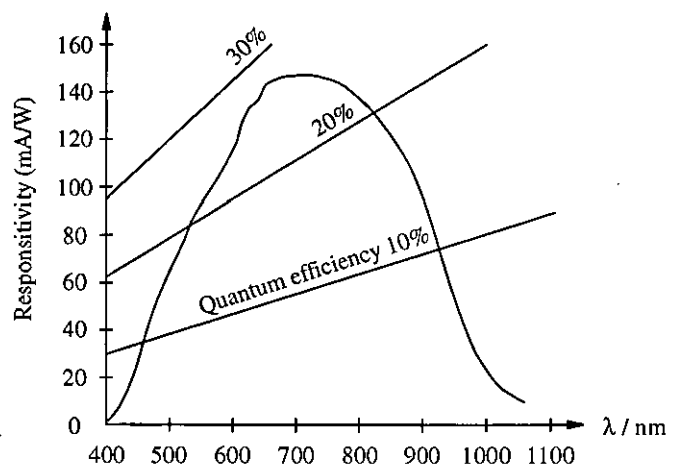


Figure 3.45 - Typical response of CCD camera.

Suppose a scene having an area of 1m^2 is illuminated with 1 lux of monochromatic light of wavelength $\lambda=555\text{nm}$. At this wavelength $V(\lambda) = 1$, so the light power incident on the scene can then be calculated as:

$$\phi_e(\lambda=555\text{nm}) = \frac{1\text{lux} \times 1\text{m}^2}{680\text{lm/W}} \approx 0.0015\text{ W} \quad - (3.24)$$

If the camera is placed at a distance of 1m away from the scene and fitted with a $f=50\text{mm}$ $f/1.4$ lens, as shown in figure 3.43, then the scene will be imaged on to an area of 1cm^2 on the CCD chip. The light power ϕ_L that reaches the lens aperture and is therefore imaged on to the CCD camera chip, assuming that there are no losses in the system, will approximately be equal to:

$$\phi_L = \frac{\text{cross sectional area of lens}}{2\pi(\text{distance from scene})^2} \times 0.0015\text{ W} \approx 0.24\mu\text{W} \quad - (3.25)$$

Figure 3.45 shows the typical response characteristics of a standard CCD camera [26]. With light of wavelength 555nm the responsivity of the CCD chip will be $\sim 100\text{mA}$ per watt of incident radiation. Therefore a full white output from the camera will produce $\sim 24\text{nA}$ of current in the CCD chip. The same current will be required to produce a full white output at any other wavelength.

At the output wavelength of the LJ30 semiconductor laser (860nm) the responsivity of the CCD camera chip is $\sim 120\text{mA/W}$. The minimum light power needed to give a full white output will then be $\sim 0.2\mu\text{W}$, or alternatively an energy of $\sim 4\text{nJ}$ per 1/50sec frame. Given that the laser diode emits 30W over a period of 50ns, or $\sim 1.5\mu\text{J}$ per pulse, then the laser will therefore emit about 500 times the amount needed to fully expose one CCD camera frame.

3.5.4 - Shadowgraphy and schlieren imaging

It is extremely difficult to observe directly changes in systems that are colourless or transparent. This particularly applies to acoustic transients travelling in air or liquids, and also to other examples such as the passage of air past aeroplane wings and compressor blades, convection currents and faults in glass windows. In these cases only the refractive index of the medium involved changes locally with small perturbations in density, which is caused by changes in pressure and temperature. Light incident upon the disturbances in refractive index is not attenuated, but is deflected away from its normal

path. This effect, as it has been seen in chapter 2, can be exploited to see the changes in density in the system using either *Interferometry*, *focused Shadowgraphy* or *Schlieren imaging* [30]. The latter two techniques will be considered here experimentally using the Northern Telecom LJ30 semiconductor laser and a Pulnix PE530 CCD camera.

The experimental set-up for both focused Shadowgraphy and Schlieren imaging is shown in figure 3.46. In both techniques the CCD camera is focused on the region of interest which is directly illuminated by collimated light from the semiconductor laser; the results are then displayed on a television monitor. The only difference between the two methods is that in Schlieren an opaque stop, such as a razor blade, is placed at the focal point of the imaging lens L_2 which filters out the lowest spatial frequencies from the image information, that is removing the unrefracted light. In chapter two it was deduced that the intensity distribution of the image recorded by the CCD camera represents the first order changes in refractive index of the test region, in the plane perpendicular to the incident light. Whereas in focused Shadowgraphy refractive index changes in the object plane of the camera lens do not give rise to alterations in the image, but are just imaged as undisturbed "background" light on the CCD camera. Any increases in the local intensity of the image are a result of refractive index changes that are not in the object plane. These are superimposed on top of the background light and are either magnified or reduced on the image according to their relative position to the lens. Decreases in local intensity are due to light either being absorbed or scattered beyond the aperture of the imaging lens.

Unfortunately the region of interest is transparent, therefore a well defined object such as a knife blade is temporarily placed in the test area to aid the positioning of L_2 experimentally. If the output from the CCD camera is viewed on a television monitor and the semiconductor laser pulsed frequently, then the imaging lens will be correctly positioned when the object comes into focus on the screen. The position of the lens with respect to the test area and the CCD camera will then conform to the Gaussian lens formula [14]:

$$\frac{1}{f} = \frac{1}{u} + \frac{1}{v} \quad - (3.26)$$

where f is the focal length of the imaging lens and, the distances from the lens to the region of interest and the CCD camera u and v respectively. The position of L_2 determines not only which parts of the working region are in focus on the screen, but also the magnification M of the image on the screen:

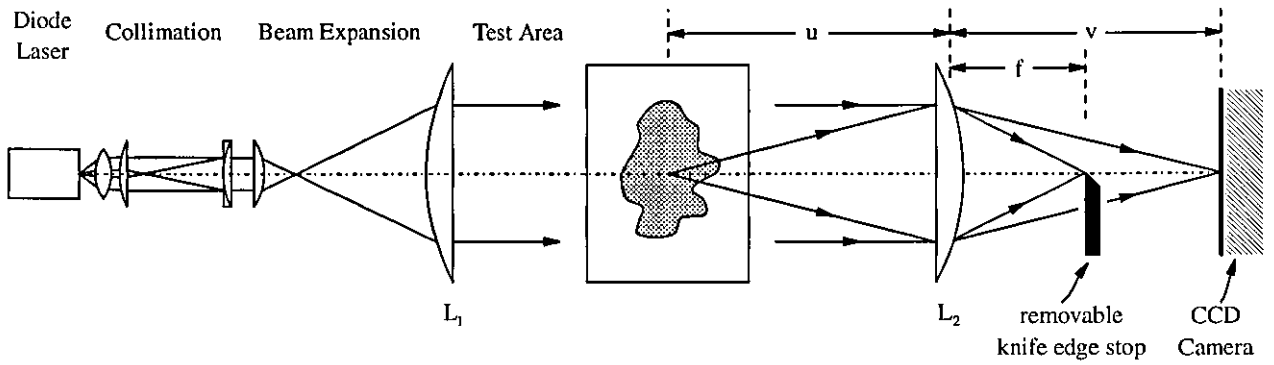


Figure 3.46 - Experimental Schlieren and Shadowgraphy set-up.

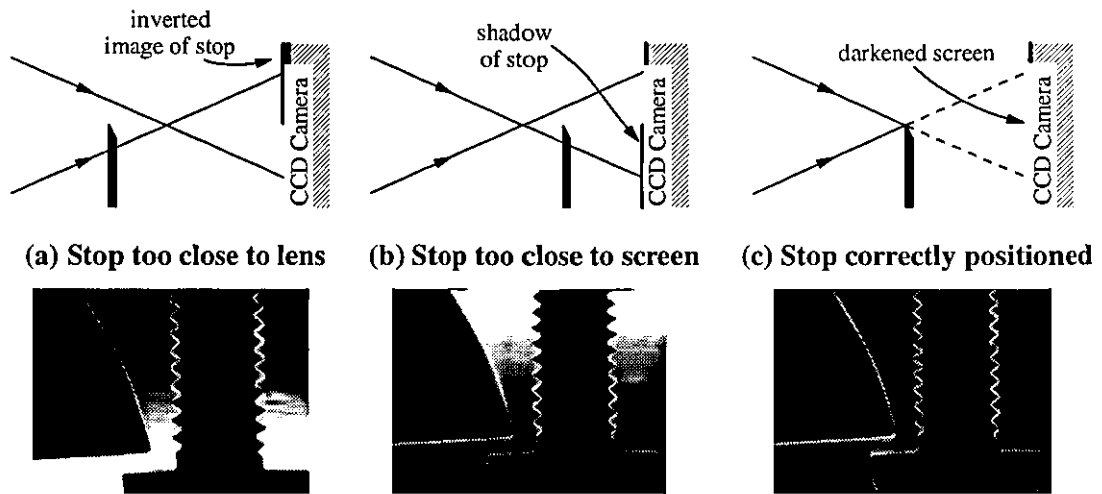


Figure 3.47 - Positioning of the Schlieren knife edge.

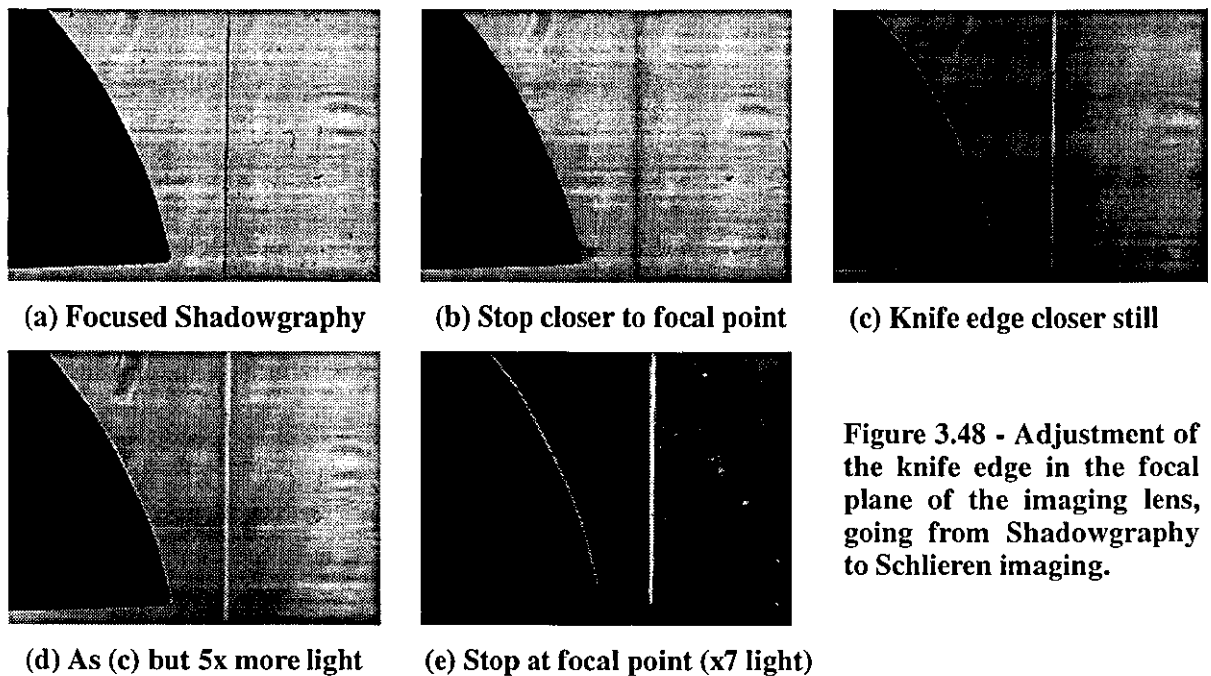


Figure 3.48 - Adjustment of the knife edge in the focal plane of the imaging lens, going from Shadowgraphy to Schlieren imaging.

$$M = \frac{v}{f} - 1 \quad - (3.27)$$

Obviously the magnification is set as desired for the size of the imaging device and test area being used. In order to image the area of interest on to the CCD camera with no magnification the distances are set so that $u = v = 2f$.

The positioning of the opaque stop at the focus of L_2 for Schlieren imaging is illustrated in figures 3.47 and 3.48 experimentally using a razor blade as the stop. It is moved into position using a micro transition stage since the diameter of the semiconductor laser beam at the focal point of the imaging lens is very small in comparison to the dimensions of the rest of the system. Here the test area is illuminated by the semiconductor laser with medium power and a beam diameter of 15mm before being imaged onto the CCD camera using a 135mm (f/1.4) camera lens, giving a focal spot diameter of about 50 μ m (full width half maximum intensity.)

Initially the stop is placed close to the focal point and is moved in towards the axis, that is in the plane parallel to the CCD camera, so that the stop just enters the light beam. If an inverted image of the stop is produced on the CCD camera, such as in figure 3.47(a) then the stop is positioned too close to the imaging lens and it is moved towards the camera. Whereas if a non-inverted image occurs the stop is moved away from the camera and towards L_2 , as in figure 3.47(b). The stop is then moved closer to the axes and the process repeated until the background of the image is seen to go evenly dark, as in figure 3.47(c). At this point the stop is correctly positioned in the focal plane of L_2 and only light diffracted by the edges of the test objects can be seen, here a knife blade and a screw, since the direct light from the semiconductor is spatially filtered out.

The transformation from Shadowgraphy to Schlieren imaging as the knife edge stop is moved in towards the axis in the focal plane can be seen in figure 3.48. Initially when the system is in Shadowgraphy mode the knife edge is imaged as a shadow on the CCD camera and, a glass microscope slip appears to be invisible except at its edge where the light is scattered and lost outside the lens aperture - thereby casting a shadow on the image. As the edge of the razor blade is moved closer to the focal point, say 200 μ m from the axis as shown in figure 3.48(b), the boundaries of the objects begin to blur since the stop removes some of the middle spatial frequencies from the image but still allows the direct light through. When the stop is moved into the focal point the background intensity drops and, light refracted at the edge of the microscope slip and diffracted at the edge of the knife blade also becomes visible, as figures 3.48(c)&(d) show. Since the

direct light from the semiconductor laser is not focused to a precise point but to a spot $\sim 50\mu\text{m}$ in diameter, the stop has to be moved about $25\mu\text{m}$ further through the focal point to cut off all of the undeflected light. When this is done the contrast between the deflected and the background light is improved, as seen in figure 3.48(e). However the intensity of the semiconductor laser light pulses has to be increased somewhat since most of the power exists in the undeflected beam which has been filtered out.

In Schlieren imaging the best sensitivity is achieved when the focal length of the imaging lens is large and the stop is made as small as possible. In the above example the razor blade removes not only the direct light from the semiconductor laser but also the light deflected downwards towards the stop. In figure 3.48(e) this can be seen as an absence of light diffracted by the bottom edge of the knife blade. Therefore the razor blade is replaced by a thin wire to improve the sensitivity. The minimum thickness of the wire is limited by the size of the spot that the semiconductor laser light is focused down to, since the wire is required to remove all of the direct light but allow through as much of the higher spatial frequencies in the image as possible. It was found that using the diode laser set-up described the diameter of the wire schlieren stop could be made as small as $100\mu\text{m}$ to give good results.

3.6 - Synchronisation and timing of the semiconductor laser

In water, acoustic transients travel at speeds approaching $1.5\text{mm}/\mu\text{s}$ and have a typical duration of about 200ns. If a shock is imaged 1:1 onto a typical CCD camera chip having dimensions of say 8mm by 6mm, then the shock will traverse the picture in less than $6\mu\text{s}$ and will be imaged with a thickness of $\sim 1/3\text{mm}$. It is therefore necessary to synchronise the light pulses from the semiconductor laser with the creation of the acoustic transients to a greater accuracy than this. This could be done by placing a detector somewhere in the field of view to detect the shock and then immediately trigger the pulse from laser diode to expose the CCD camera. This is advantageous when the creation of the acoustic transients are not predictable, however the detector can obstruct either the path of the shock or the image on the camera. Alternatively if the creation of the acoustic transient is able to be triggered externally and its path can be predicted accurately, then the semiconductor laser can be synchronised with the external trigger and fired after a pre-set delay. The latter of these two methods will be employed here since both the acoustic transient sources described later in this chapter are externally triggerable with good accuracy.

Unfortunately the output of the CCD camera is continuous and is difficult to synchronise to an external trigger. Consequently both the event and semiconductor laser have to be synchronised to the output of the camera, as shown schematically in figure 3.49. If the event and laser diode are triggered during the middle of one frame that is being outputted serially by the CCD camera, then the image of the shock will be appear on the following frame. Since the shock appears on just one of the output frames, a frame grabber is required to store the image information on this frame, and this is triggered at the same time as the acoustic transient is created.

3.6.1 - Analogue delay system

A complete analogue delay system is shown schematically in figure 3.50. The system is synchronised to the output of the CCD camera using a video sync separator, such as the LM1881 in the circuit shown in figure 3.51 which detects the start of each output field. In practise it is found that the pulse from the semiconductor laser has to occur after the frame sync information (such as the equalising and serrated vertical pulses shown in figure 3.42) otherwise the image is lost. This is because during this period the image on the CCD chip is transferred to the output shift registers and the light sensitive regions are flushed. Therefore the synchronisation pulse from the LM1881 is pre-delayed by about 3ms using a 74LS123 monostable multivibrator.

The output from the vertical sync circuit gives out a positive going pulse every 22.5ms, or 50 times per second, with every new field from the camera. Unfortunately sources of acoustic transients may not be able to be triggered at this rate, perhaps needing several seconds to recharge after causing a single event. Thus a manual push button trigger is incorporated into the system using a S-R flip-flop (see appendix 1, figure A1-3), which allows just one synchronisation pulse through every time a single-pole-double-throw switch is operated. This pulse is then shaped by a monostable multivibrator before triggering both the source of the acoustic transients and the frame grabber.

The synchronised trigger pulse also starts another monostable multivibrator, shown in figure 3.52, which acts as a pre-set delay. The delay is controlled by the variable resistor VR_1 , and the negative going output pulse is then shaped before goes on to trigger the semiconductor laser. Note that the 74LS123 shown here contains two monostable multivibrators. Often when an acoustic transient source is triggered there is a time lag before the creation of the event, perhaps by a few hundred microseconds. Consequently the delay between the triggering of the event and the pulsing of the semiconductor laser must take account for this.

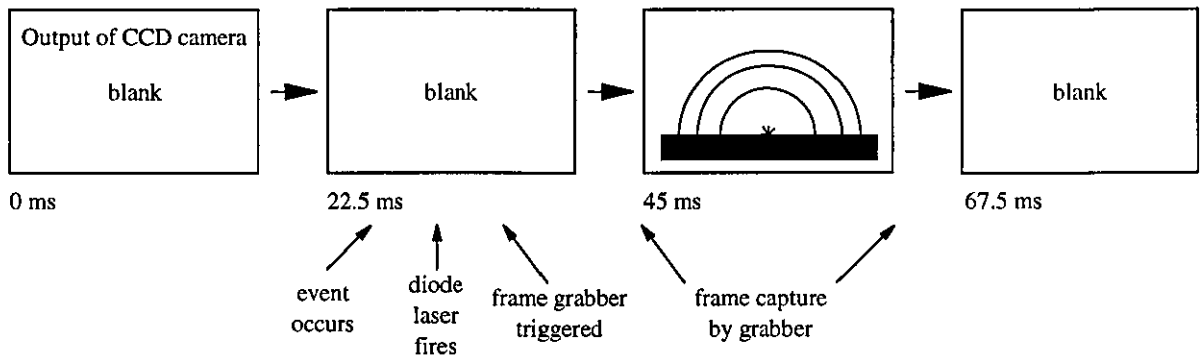


Figure 3.49 - Synchronisation between CCD camera, event, diode laser and frame grabber.

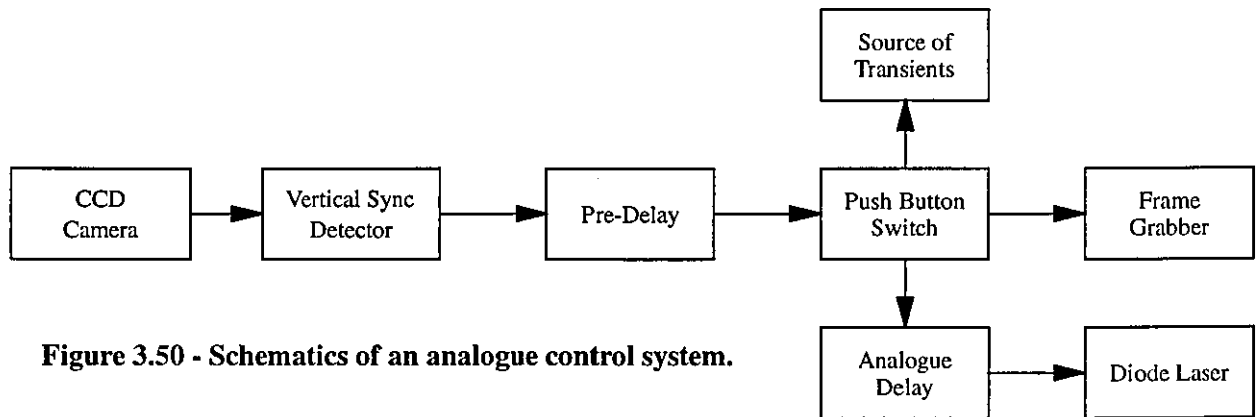


Figure 3.50 - Schematics of an analogue control system.

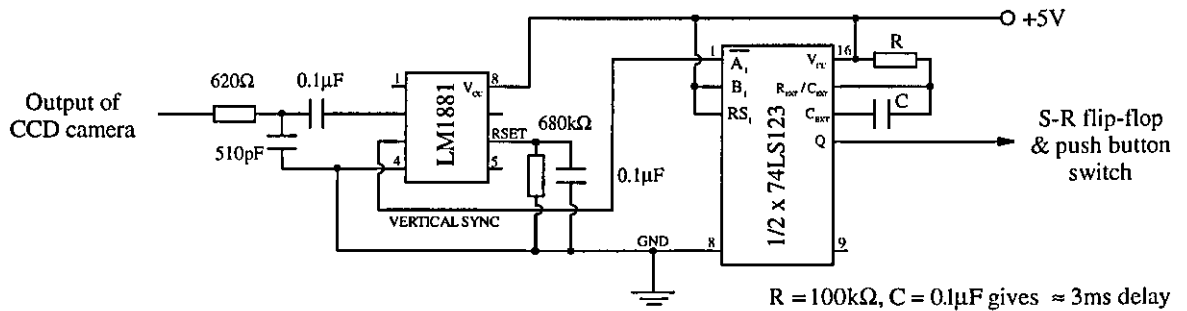


Figure 3.51 - Pre-delay after CCD camera synchronization pulse.

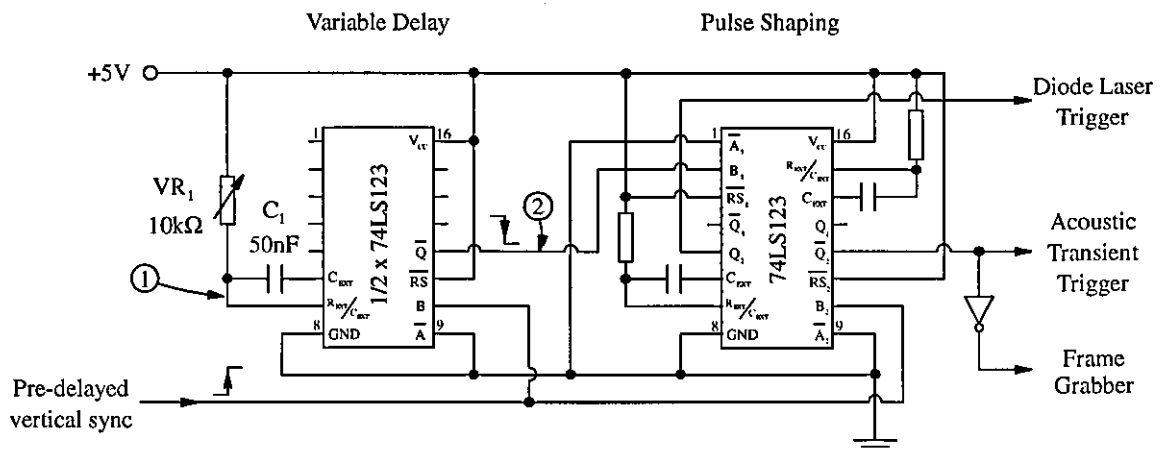


Figure 3.52 - Analogue delay circuitry.

3.6.2 - Problems with analogue delays

Many sources of acoustic transients, such as high power lasers and spark-gaps, generate large quantities of *electromagnetic noise* during the fast discharge of the large high tension capacitors that they use. Unfortunately this can interrupt the timing of the analogue variable delay causing premature and false triggering of the semiconductor laser. This problem arises from the method used to time the delay in the monostable multivibrators. The capacitor C_1 is charged through variable resistor VR_1 until the voltage across it (measured at point 1 in figure 3.52) exceeds a certain level switching a Schmitt trigger, where the charge time and hence the delay is proportional to $VR_1 * C_1$. As commented earlier, there may well be a time lag of a few hundred microseconds between the triggering of the source and the creation of acoustic transients. Given also that the pre-set delay may only last perhaps $3\mu s$ longer than this, that is the time for the transient to traverse perhaps half the CCD frame for example; then the capacitor will be charged to beyond 90% of its final voltage. It is very easy for just a small amount of electromagnetic-magnetic noise to raise the potential across the capacitor above that needed to switch the Schmitt output, as illustrated in figure 3.53, thereby prematurely triggering the semiconductor laser.

Several ways of reducing the effects of electromagnetic noise picked up in a circuit have been discussed earlier in section 3.3.3. These include stopping noise entering the circuit by isolating the power supply and using either opto-isolators or fibre optic links on the signal inputs, reducing the number and physical size of the current loops in the circuit, adding capacitance to the circuit and also shielding the circuit. In practice however, very little can be done to prevent electromagnetic noise from affecting the timing of monostable multivibrators, since only a very small amount of noise is required to cause false triggering. Hence an alternative method must be used to provide the variable delay in the control system.

3.6.3 - Digital delays

One solution to the problem of accurate timing in an environment with a large amount of electromagnetic noise is the use of a digital delay. Although not being totally immune, such devices do not suffer as much from the effects of electromagnetic noise pickup. The only drawback with digital circuits is that they are substantially more complicated and therefore use more power.

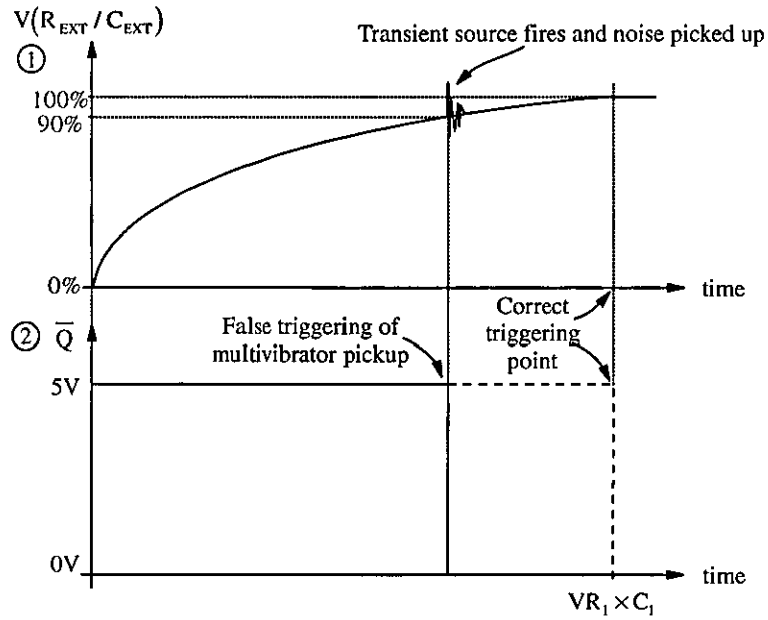


Figure 3.53 - Problems with E-M noise and analogue delays.

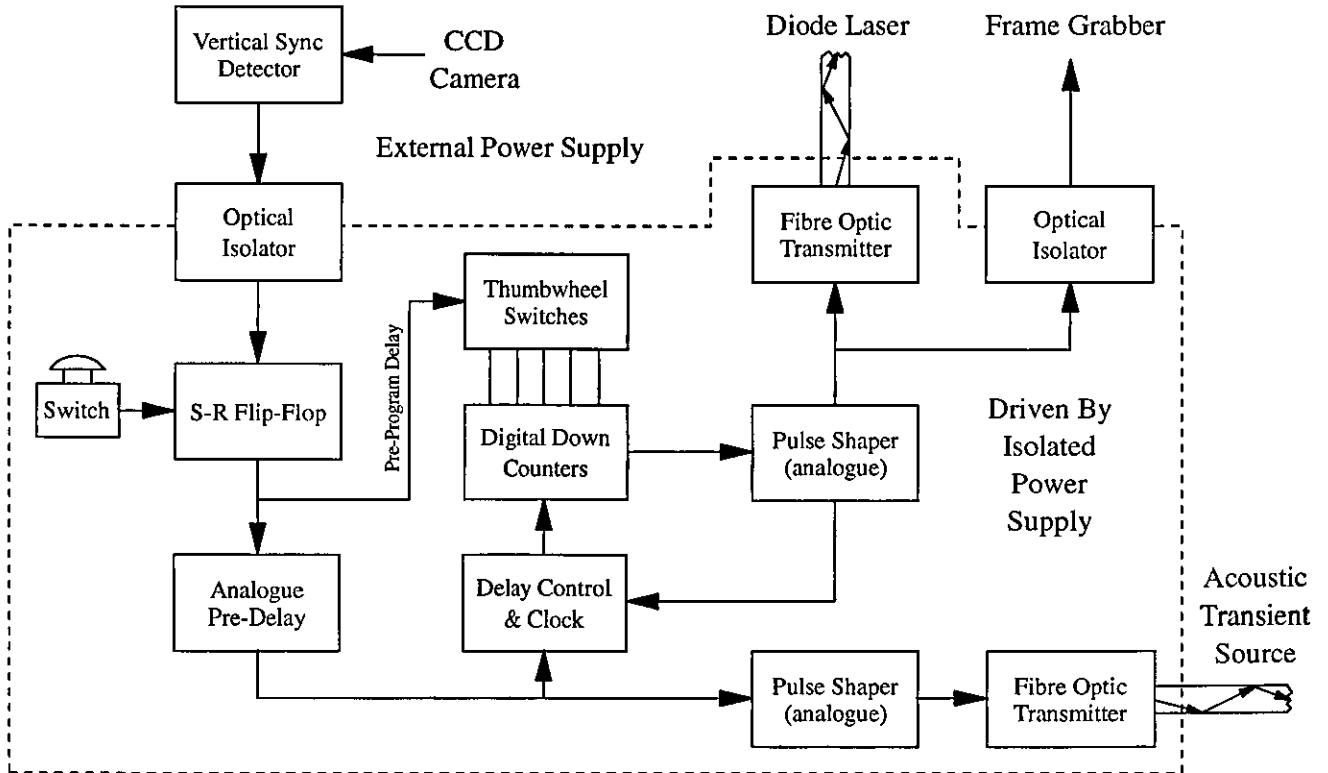


Figure 3.54 - Schematic representation of a digital delay system.

A digital control system for the control of the acoustic transient source, semiconductor laser and, the frame grabber is shown schematically in figure 3.54. More detailed circuit diagrams can be found in Appendix 1. The elements of the system are very similar those in the analogue delay and, some of the monostable multivibrators are retained due to their relative simplicity and because they are not in operation when the acoustic transient source triggers. As before the system is synchronised to the start of each frame given out by the CCD camera, however instead of directly operating the S-R flip-flop the chain of pulses is first passed through an optical isolator (see figure A1.2). This is used to transfer the synchronisation pulses into the main timing circuit which is driven by an isolated and conditioned power supply, this avoids the transmission of noise picked up by the coaxial lead from the camera. The isolated power supply is heavily filtered against high frequency noise picked up through the 'mains' input leads by large inductors, capacitors and transient suppressors (see figure A1.1).

When the push button switch is operated (figure A1.3) the next frame synchronisation pulse triggers the pre-delay (figure A1.4) and, also programs several digital down counters (figure A1.6) with values pre-set on thumbwheel switches (figure A1.7). Again the pre-delay of $\sim 3\text{ms}$ is required so that the semiconductor laser light pulses do not occur during the CCD camera refresh cycle. After this the source of the acoustic transients is triggered and, the counters are allowed to count down according to a clock operating at a rate of 10MHz. When the counters reach zero a monostable multivibrator produces a pulse which stops the clock and triggers both the semiconductor laser and the frame grabber. Therefore the down counters programmed with values set on the thumbwheel switches act as a variable delay between the triggering of the acoustic transient source and the semiconductor laser. With 4 down counters and their respective thumbwheel switches, a variable delay of between $0.1\mu\text{s}$ to $999.9\mu\text{s}$ can be achieved with steps of 100ns and an accuracy of better than $\sim 5\text{ns}$.

Both the semiconductor laser and the source of the acoustic transients are triggered via a fibre optic link. The control line for the frame grabber is also separated from the timing circuit by an opto-isolator. Finally the effects of electromagnetic noise pickup within the timing circuit can be reduced further by encasing the system in a metal box.

3.7 - Experimental single exposure imaging of laser ablation

A complete high speed photographic system for imaging acoustic transients or other high velocity phenomena can be created using the semiconductor laser, its single pulse drive circuitry, a CCD camera, frame grabber and the timing circuitry as described in the previous sections. Such a system is shown schematically in figure 3.55, where acoustic transients generated by dye laser ablation are photographed using the Shadowgraph and Schlieren imaging techniques described in section 3.5.4. The system is set into operation by pressing a manual trigger button, at which it is first synchronised to the beginning of the next frame from the free running CCD camera output. After a pre-delay of about 3ms to wait for the CCD camera refresh cycle to end, a Rhodamine 6G dye laser is triggered together with the pre-set digital variable delay described in section 3.6.3 (and appendix 1). Approximately 100 μ s after triggering, the dye laser emits a 0.13J, 2 μ s (FWHM) pulse of light at 589nm which is focused using a 50mm, f/2 camera lens onto a highly absorbing surface, in this case black PVC sleeving. The rapid heating of the PVC material gives rise to ionisation of the surrounding air, resulting in a small explosion and a shock wave being generated. A short time later (typically \sim few μ s) the pre-set digital delay triggers the single pulse semiconductor laser drive circuitry as described in section 3.3.2. The diode laser then emits a single 100ns duration, 30W, 860nm pulse of light which is collimated and expanded (section 3.4) before it is allowed to illuminate the acoustic transient. A 135mm SLR camera lens then images this scene onto a Pulnix PE530 CCD camera [28] using either the Schlieren or Shadowgraphy (with the stop removed) techniques. Stray dye laser radiation scattered by the plasma is removed using a 780nm (high pass) cut-off filter placed in front of the imaging lens. The CCD camera has horizontal and vertical resolutions of 752 by 582 pixels respectively, and outputs the recorded image information as a CCIR analogue video signal on the subsequent frame as described in section 3.5. This is stored digitally on an Eltime frame grabber which is set to acquire mode when the semiconductor laser is triggered, and has a resolution of 512 horizontal by 256 vertical pixels with 64 grey levels [31]. Finally the high speed photograph of the acoustic transient is viewed on a television monitor and a hard copy made on a thermal printer. Note that eye protection is worn continually during the experiment since the dye laser radiation is extremely intense.

The set-up shown in figure 3.56(a) is used to aid the setting of the pre-set variable digital delay. A SFH250V photodiode [32] placed in reverse bias mode is used to sample light from the test area via a fibre optic cable and, the current generated by the diode is measured using a digital storage oscilloscope. The oscilloscope is triggered here using the electromagnetic noise generated by the dye laser flash tube discharge as shown

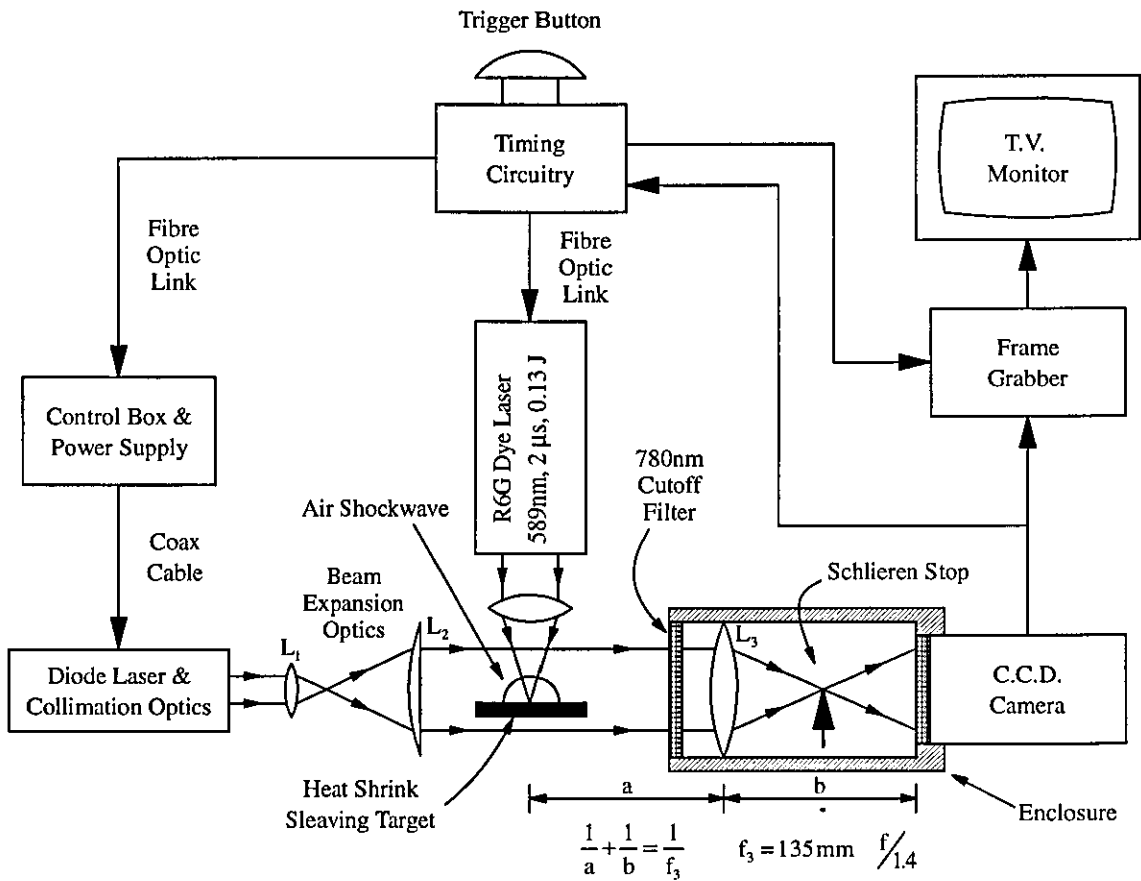
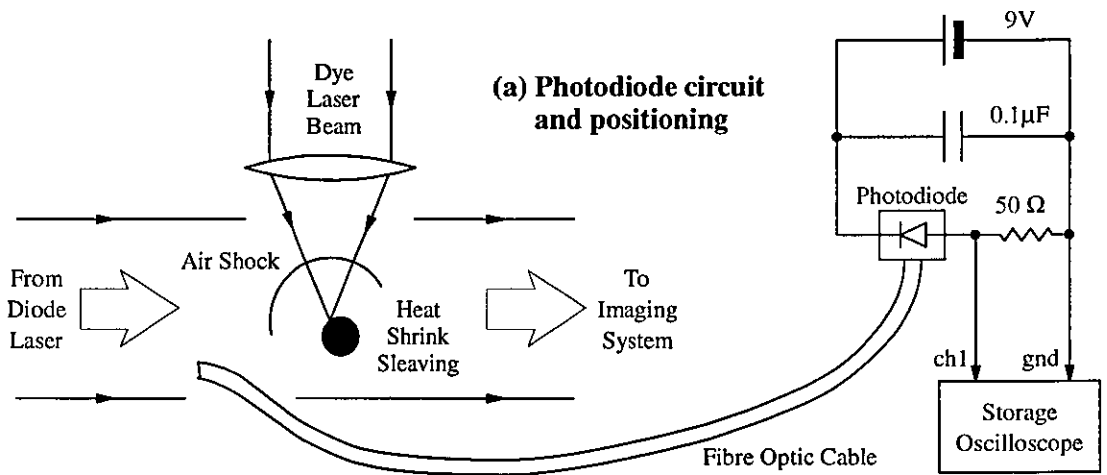


Figure 3.55 - The diode laser Schlieren imaging system.



(b) Optical measurements made using photodiode

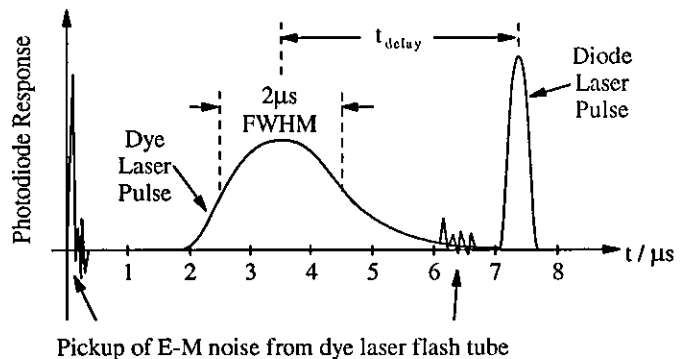


Figure 3.56 - Use of a fibre optic photodetector for timing of output light pulses.

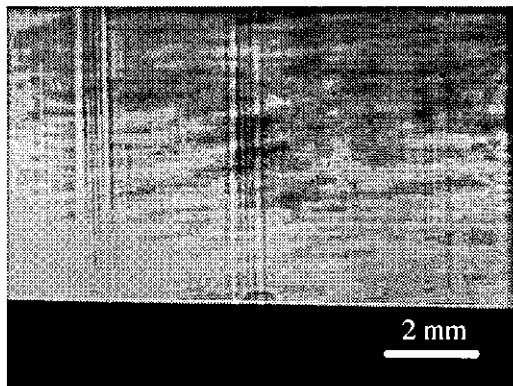
schematically in figure 3.56(b). In this case the dye laser output pulse is generated about $2\mu\text{s}$ later and it lasts for about $2\mu\text{s}$. It is picked up by the detector here by virtue of reflections and scattering around the system since it is extremely intense. The pre-set digital delay is adjusted appropriately so that the output pulse of the semiconductor laser is viewed on the oscilloscope trace after that of the dye laser. In the following experiments this was typically found to be up to $10\mu\text{s}$ after detection of the dye laser flash tube noise and, about $100\mu\text{s}$ after the initial triggering of the dye laser.

3.7.1 - Shadowgraphy results

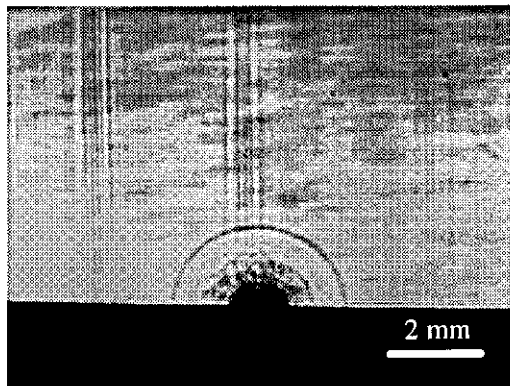
The set-up described in the last section has been used to photograph the development of several air born acoustic transients generated by dye laser ablation. Single exposing pulses from the semiconductor laser are used here and the transients are imaged using the Shadowgraphy technique, as described in section 3.5.4, with the 135mm imaging lens focused on the PVC target. The results are shown in figure 3.57, where several similar acoustic transients at various times after the peak of the dye laser pulse have been photographed. Unfortunately vertical lines can be seen here across all the images, and this is due to local variations in the semiconductor laser beam.

The initiation of a single acoustic transient is shown in figure 3.57(a). The target is seen as a dark horizontal shadow across the bottom of the picture. Further development of similar acoustic transients is seen in figures 3.57(b)→(e). Each hemispherical transient is clearly resolved together with a plume of debris and plasma behind it, seen as the dark turbulent disturbances attached centrally to the target. As commented before, light refracted by the acoustic transient in the plane of the target is imaged onto the CCD camera undisturbed from its normal unrefracted position. The dark semicircular band seen here is partly due to this light being refracted outside of the aperture of the imaging lens and lost. Light that is refracted before it reaches the object plane is imaged out of focus on the CCD camera and is also demagnified, this is seen here as the bright band on the inside of the of the dark band. Also since this light is imaged to a different position on the CCD camera the dark band is enlarged. Only a very small band of light can be identified on the outside of the dark band. This is due to light refracted from positions closer to the imaging lens, but this effect is weak since almost all of the semiconductor laser light is refracted before it reaches the plane of the target.

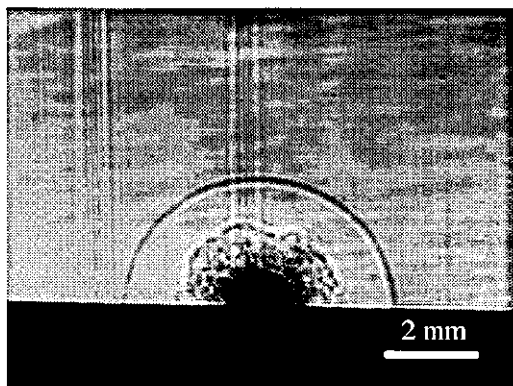
By measuring the average radius of the transients with time after creation the speed of the shock front can be assessed, as in figure 3.58(a). Here it can be seen that initially the



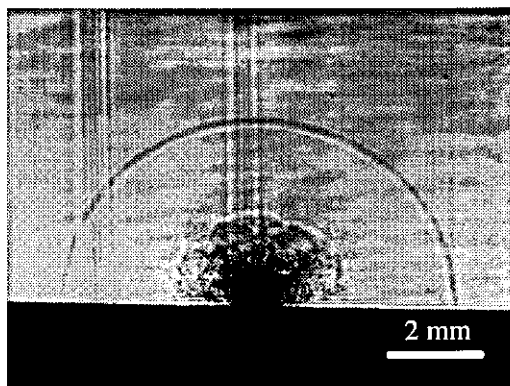
(a) 0.5 μ s after dye laser fires



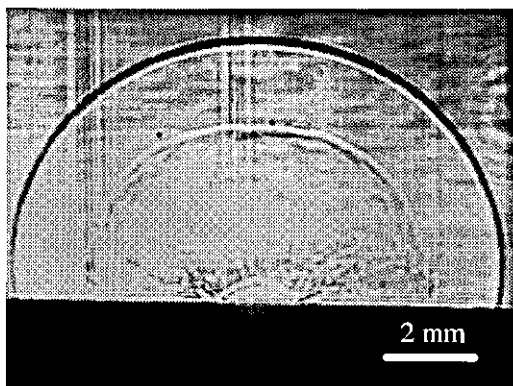
(b) 2.4 μ s after dye laser fires



(c) 4.2 μ s after dye laser fires



(d) 7.5 μ s after dye laser fires



(e) 11 μ s after dye laser fires

Figure 3.57 - Shadowgraphs taken of air born acoustic transients created by dye laser ablation, using single shot semiconductor laser imaging system.

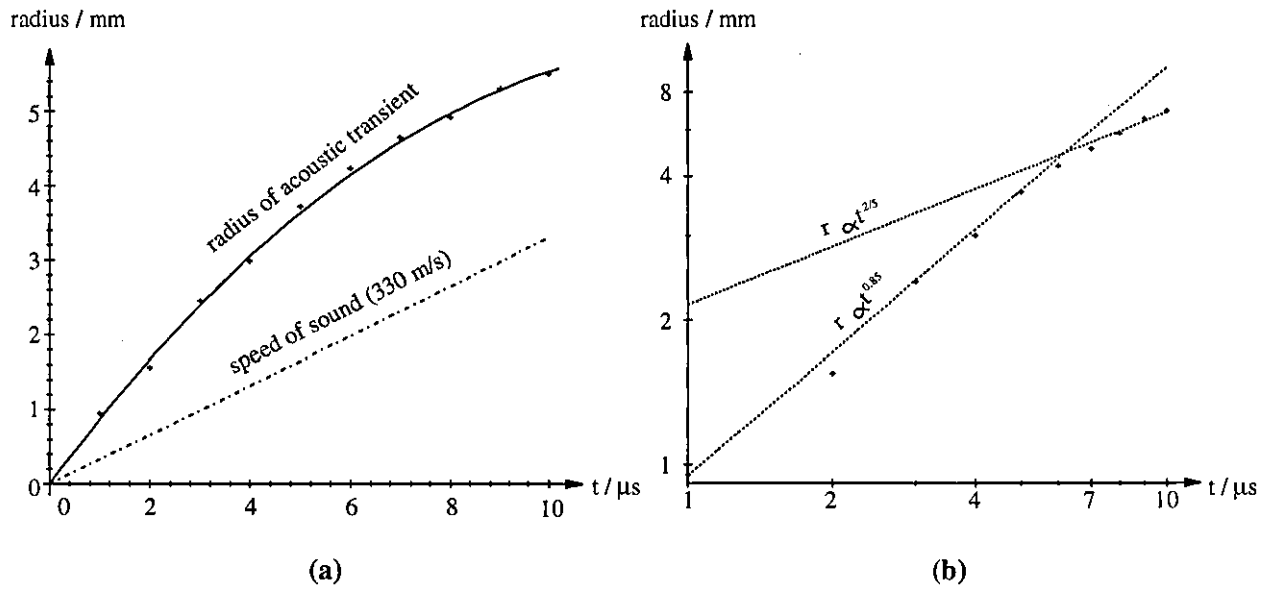


Figure 3.58 - Average radius of air born acoustic transient generated by laser ablation.

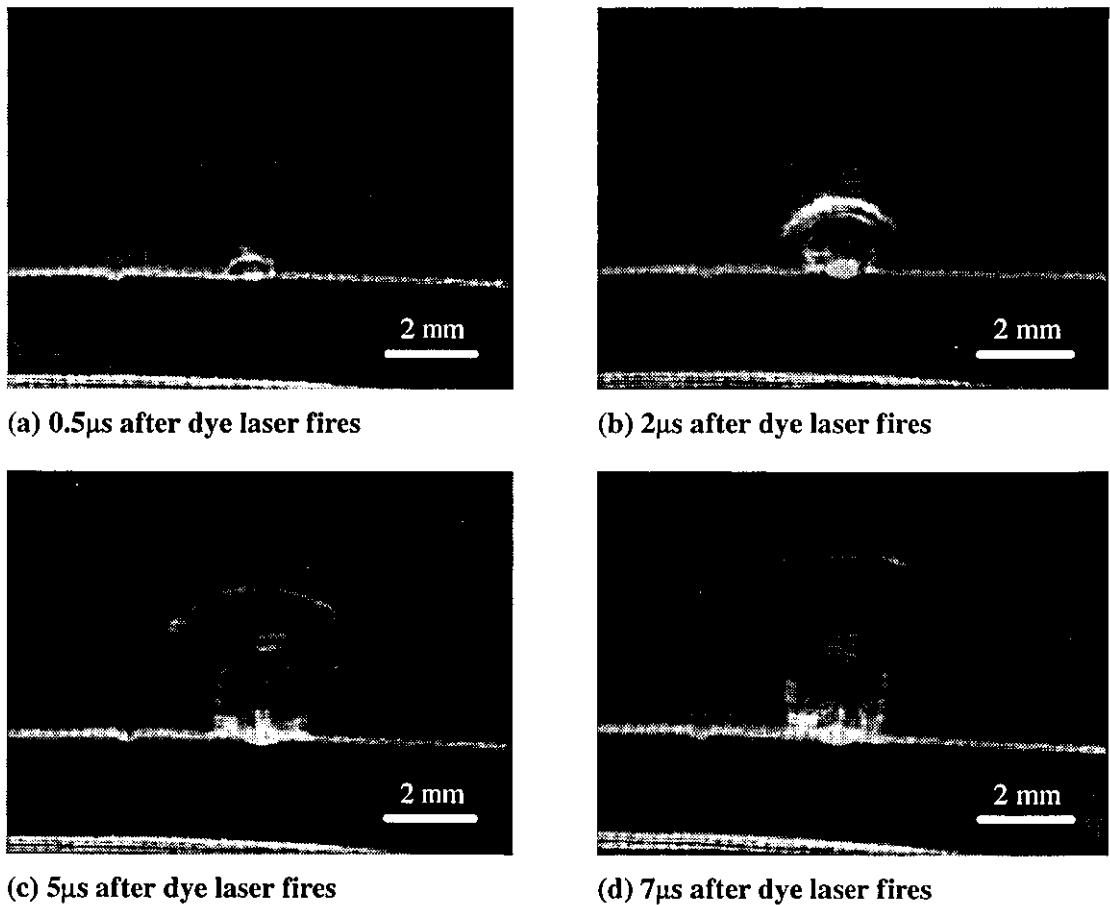


Figure 3.59 - Schlieren imaging of air shocks using single pulse laser diode illumination.

(Note : Vertical bars are due to Moire effect between scanner and pixels on hard copy printer.)

transients travel in excess of Mach 2, but slow to the sound speed (Mach 1, 330ms⁻¹) after about 8μs, or 5mm of travel. This can also be done for the plume of debris which is seen here to disperse at a velocity slightly below the speed of sound. The results can also be plotted on a log-log scale as in figure 3.58(b). It can be seen that for the first 5μs of travel the radius appears to conform to a t^{0.85} power law. This agrees broadly with results obtained by Daiber and Thompson [33] (see section 2.2.3,) who found that the radius of similar acoustic transients follow a t^N relationship during the duration of the generating laser pulse. The time exponent N varies between 0.6 and 0.9, this is determined by the initial state of the gas, the geometry of the laser beam, the shape of the laser pulse with time and whether the gas breakdown occurs at peak laser power or before. It appears that the 5μs of agreement here occurs during the complete duration of the dye laser pulse when energy is still being added to the transient. That is, although the dye laser pulse has a full width half maximum duration of 2μs, the complete duration is in fact of the order of 6μs due to the exponential fall off of the pulse with time.

It can be seen from figure 3.58(b) that as the dye laser pulse dies away 6μs after initiating the acoustic transient, the time-radius relationship of the transient appears to change to a t^{2/5} dependence. This conflicts with Daiber and Thompson results but does agree with the earlier findings of Ramsden and Savic [34] (see section 2.2.3), who considered that acoustic transients under these conditions follow Taylor's blast wave theory [35] (see section 2.2.2). According to Taylor [35], the radius of a spherical blast wave in a gas as a function of the time t after creation, the energy Q in the blast wave, and the initial gas density ρ₀ is:

$$r \approx S(\gamma) \left(\frac{Q}{\rho_0} \right)^{1/5} t^{2/5} \quad - (3.28)$$

For air at atmospheric pressure the constant S(γ) is approximately 1 and ρ₀=1.293kg/m³, which gives a value for the energy of the acoustic transient of about 60mJ. This is approximately a half of the energy of the dye laser pulse. These results broadly agree with those taken by Emmony and Irving [36] who investigated Nd-Glass laser (40ns, 0.35J) induced shock waves generated at a carbon target in several gases over a range of pressures.

The resolution of the shock front on the CCD camera frame is limited by both the distance travelled by the acoustic transient during the single exposure and the density of pixels on the CCD camera. That is the transient travels at up to 660ms⁻¹, giving rise to a travel of ~66μm during the 100ns semiconductor laser pulse. Whereas the maximum

achievable resolution on the PE530 CCD camera is in the horizontal direction, here 752 pixels over a distance of 6.4mm giving a pixel spacing of 8.6 μ m. Hence the resolution of the system is limited primarily by the duration of the semiconductor laser pulse. These figures can also be compared with the thickness of the dark hemispherical band, which is estimated from figure 3.57(b) to be about 130 μ m (\pm 20 μ m). It can therefore be seen that initially the acoustic transient is just resolved to within 8 pixels on the CCD camera; the Shadowgraphs in figures 3.57(a)&(b) are smeared slightly by, say, about half the thickness of the dark band. The resolution does improve however with time as the transient slows to the sound speed, to within about 4 pixels on the CCD camera (1/4 of the thickness of the dark band) for figures 3.57(d)&(e).

3.7.2 - Schlieren imaging results

The same apparatus described above can also be used to take high speed photographs of dye laser ablation using the Schlieren imaging technique. Here a simple Schlieren stop consisting of a 100 μ m diameter steel wire is used. This is manoeuvred into position at the focal point of the imaging lens using the techniques described earlier in section 3.5.4, and it is sufficient to block about 90% of the undeflected semiconductor laser light. Several similar acoustic transients are generated by the pulsed dye laser light which is focused onto a PVC target, as before. These are photographed using single exposures from the semiconductor laser at different times after the peak of the dye laser pulse, and the results are shown in figure 3.59. Unfortunately vertical Moiré fringes have been introduced into these pictures which result from the reproduction method used.

The interpretation of the Schlieren images is complicated since the photographs are dependant upon the geometry of the Schlieren stop. In the classic case where a scene is illuminated by a point source and filtered by a knife edge stop [30] this is relatively straight forward: the local image intensity recorded on the CCD camera would represent, say, the 'positive' first order changes in refractive index with distance, in the direction perpendicular to the knife edge and in the plane of the target. Both the 'negative' changes and the d.c. would be filtered out by the knife edge stop. In this experiment where a wire stop is used, the situation is slightly different. The local image intensity is proportional to the magnitude of the first order changes in refractive index, in the plane of the event and in the direction perpendicular to the wire. The refractive index changes in the direction parallel to the wire are not visible. According to the Gladstone-Dale relation [37,38] (see chapter 2), changes in refractive index are roughly proportional to the changes in pressure for air pressures of up to 100bar [39].

Figure 3.59(a) shows a clearly resolved Schlieren image of the early stage of a dye laser generated acoustic transient propagating in air. It is at approximately the same stage of development as the transient in the Shadowgraph shown earlier in figure 3.57(a). The shock front in the Schlieren image is seen here as the bright hemispherical band just above a bright horizontal line. This line and the other at the bottom of the picture show the position of the PVC target. These are due to semiconductor laser light being diffracted and scattered round the edges of the target. Schlieren images of similar acoustic transients are shown in figures 3.59(b)→(e) for increasing time intervals after the dye laser pulse. The hemispherical transients are clearly resolved with a crown shaped region just above the target which is due to the debris and plasma. In figure 3.59(b) the acoustic transient appears to have two distinct semicircular bands. Given that the image intensity is related to the first order derivative of pressure with respect to distance, the bright outer band is probably due to the shock front and, the weaker inner band is most likely the subsequent fall off in pressure. As commented in the last section, the semiconductor laser pulse lasts for 100ns and the transient travels initially at about 660ms^{-1} . This corresponds to a spatial resolution of about $66\mu\text{m}$, which is approximately a third of the thickness of the outer bright band of the transient photographed in figure 3.59(b).

In contrast to the Shadowgraphs shown earlier, the Schlieren images of the shock fronts do not appear to be hemispherical. This is entirely due to the geometry of the Schlieren stop - light which is deflected by changes in refractive index in the horizontal direction being filtered out by the stop. Finally it can be seen that the intensity of each shock front falls off with distance travelled into the undisturbed air. This is due to the peak pressure of the acoustic transients falling off inversely with radius (see chapter 5.)

3.8 - Multiple pulse imaging of acoustic transients [40]

An experimental layout for high speed multiple exposure photography of acoustic transients generated by Nd-YAG laser assisted breakdown in either air or water is shown schematically in figure 3.60. The system is very similar to the single exposure system described in the last section, and the order of events is as follows. Initially a manual push button switch triggers the system which synchronises itself first to the output of the free running Pulnix PE530 CCD camera [28], as before. A Nd-YAG laser is triggered 3ms later which delivers a 55mJ, 30ns, 1060nm pulse of light into a test area containing either air or water. This is focused by a 25mm, $f/1.56$ lens and results in dielectric breakdown at the focal point giving rise to an acoustic transient. After a further pre-set variable

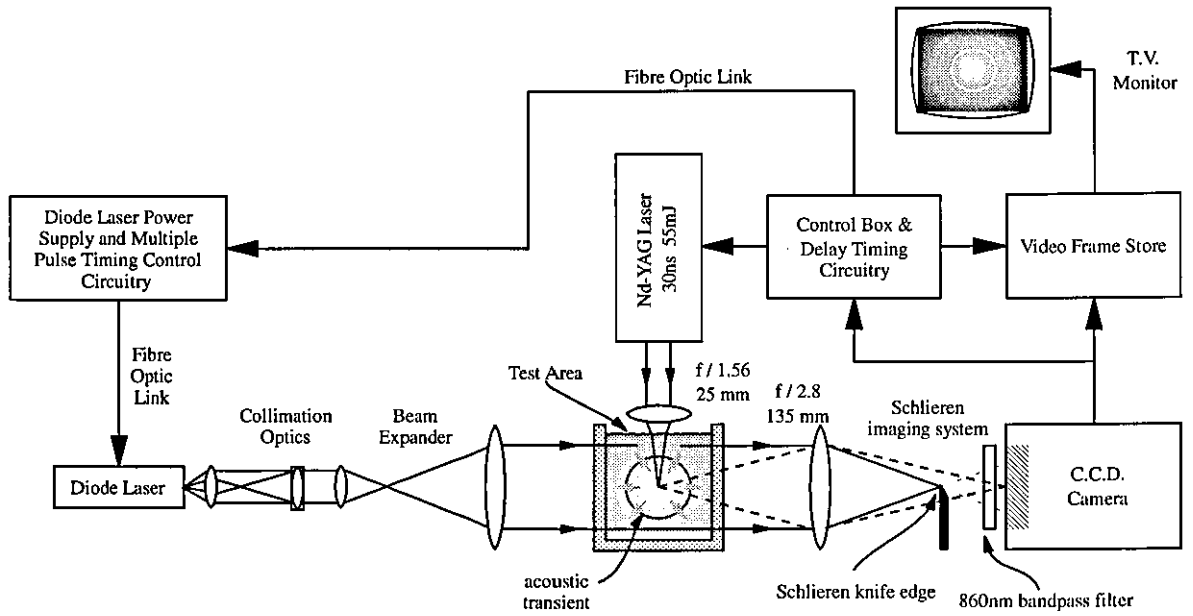
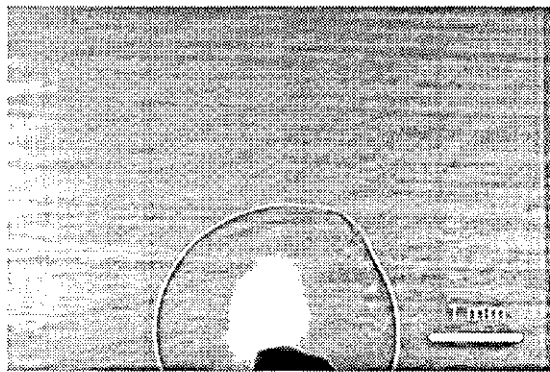


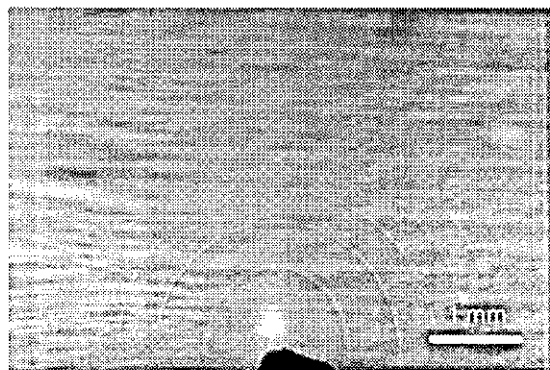
Figure 3.60 - Experimental setup for multiple pulse semiconductor laser high speed photography.



(a) Single 50ns pulse 1.4µs after event



(b) 3 diode laser pulses with 2µs separation, 1st pulse 0.8µs after event



(c) 6 diode laser pulses 1µs apart, 1st pulse 0.5µs after event

Figure 3.61 - Semiconductor laser shadowgraphy in air.

delay of between 1 to 10 μ s the multiple pulse timing control circuitry described in section 3.3.5 is triggered. This pulses the semiconductor laser (Northern Telecom LJ30 [8]) up to 9 times at pre-set intervals of between 100ns and 9.9 μ s, to an accuracy of about \sim 5ns. Each output pulse from the laser diode has a duration of 50ns (FWHM), wavelength of 860nm and peak power of 30W. These are used to illuminate the test area through the collimation and beam expansion optics, and the acoustic event is imaged using a 135mm, f/2.8 SLR camera lens onto the CCD camera utilising either the Shadowgraphy or Schlieren techniques described earlier. This results in the same acoustic transient being photographed at several points in time, each image being overlaid on the previous image. Daylight and plasma scattered Nd-YAG laser radiation are removed from the image by an 860nm bandpass (\pm 40nm FWHM) interference filter and, neutral density filters are used to control the exposure of the CCD camera. The image information recorded by the CCD camera is then stored on an Eltime frame grabber [34], as before, which has a resolution of 512 horizontal by 256 vertical pixels with 64 grey levels. Finally the picture is viewed on a T.V. monitor and a hard copy made when needed. The results presented in the next three sections have been published and can be found in reference [40].

3.8.1 - Shadowgraphic imaging of air born transients [40]

The results obtained using the experimental apparatus described in the last section in Shadowgraphy mode are shown in figure 3.61. Here each pulse of Nd-YAG laser light is focused onto a PVC target and generates a single air born acoustic transient. Figure 3.61(a) shows a transient that is clearly resolved using just a single pulse from the semiconductor laser. The bright circular band is the result of light being deflected away from its normal position, the inner dark band, by the shock front. As commented earlier, this is only due to refractive index changes which are out of the object plane of the imaging lens and, are therefore imaged out of focus. It can also be seen that the transient has spherical symmetry, except in one place on its locus where it has travelled to a slightly greater radius. This anomaly is a result of the uneven target causing non-uniform plasma generation during the dielectric breakdown. Finally the plasma can be seen here as the very bright (saturated) elongated region above the shadow of the target.

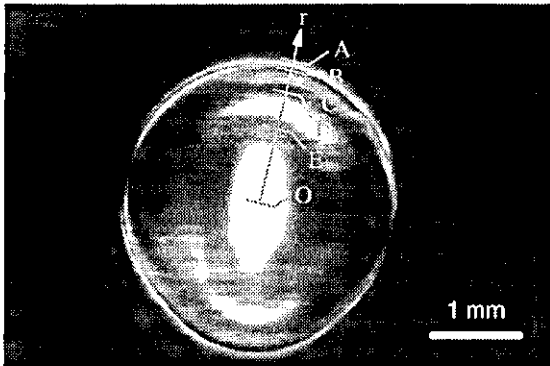
By increasing the number of semiconductor laser pulses the development of an acoustic transient can be seen with time. This has been done in figure 3.61(b) with 3 semiconductor laser 50ns (FWHM) duration pulses separated by 2 μ s and, 6 pulses 1 μ s apart in figure 3.61(c). The timing accuracy of the pulse separations here is to within

5ns. As the number of exposures is increased the unrefracted semiconductor laser light is added to the previous image recorded on the CCD camera. To prevent image saturation appropriate neutral density filters are placed in front of the camera lens. It can be seen here that as a result of this additional "background" light, there is unfortunately a substantial reduction in the contrast of the recorded images of the transients as more exposures are made. These pictures could possibly be improved by subtracting off an appropriately intensity scaled image of the scene, illuminated by the semiconductor laser once, but without a transient. This might not give a great deal of improvement, however, since the frame store has a limited dynamic range of just 64 grey levels.

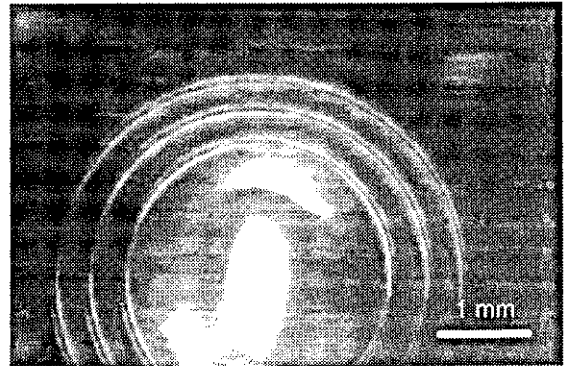
Although the shock fronts are only just resolvable above the unrefracted background light, the velocity-time relationship of a single transient can be examined easily by interpreting the differences in radii between each exposure. For example, in figure 3.61(c) it can be seen that the acoustic transient initially travels at about twice the speed of sound, however it slows extremely quickly to the speed of sound (330ms^{-1}) after just $2.5\mu\text{s}$. Given that the temporal resolution of the photographs is 50ns, that is the duration of the semiconductor laser pulse, this results in a spatial resolution of about $17\mu\text{m}$ for a transient that has slowed to the sound speed. Finally using equation (3.27) Taylor's blast wave theory predicts that the initial energy of the transient is about 3.5mJ. This is substantially less than the energy supplied by the Nd-YAG laser pulse ($\sim 55\text{mJ}$).

3.8.2 - Schlieren imaging of air born transients [40]

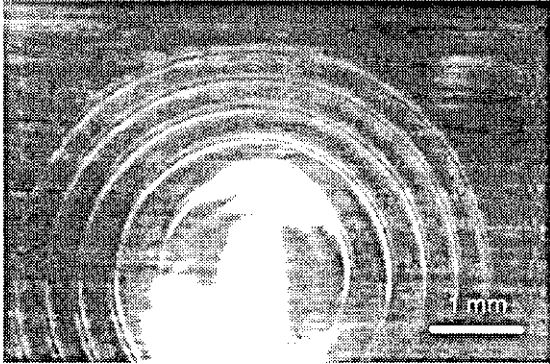
Several multiple exposure Schlieren images of air born acoustic transients are shown in figure 3.62. The set-up used here is identical to that described in the last section for the Shadowgraphs (figure 3.60) with two exceptions. Firstly the dielectric breakdown is caused by a focused 30ns, 55mJ pulse of Nd-YAG laser light as before, but this time the PVC target has been removed. Secondly a $100\mu\text{m}$ diameter wire is moved into position at the focus of the imaging lens using the procedures described in section 3.5.4. This forms a Schlieren stop which filters out approximately 90% of the semiconductor laser light that passes through the test cell undeflected. As commented before in section 3.7.2 the interpretation of the Schlieren images is quite complicated and is entirely dependant upon the geometry of the Schlieren stop. In this experiment the wire is positioned at about 10 degrees to the horizontal. The local image intensity is proportional to the first derivative of refractive index with respect to distance perpendicular to the wire, and in the plane of the event. As commented earlier, in air the changes in refractive index are approximately proportional to changes in pressure up to 100bar [37-39]. Semiconductor



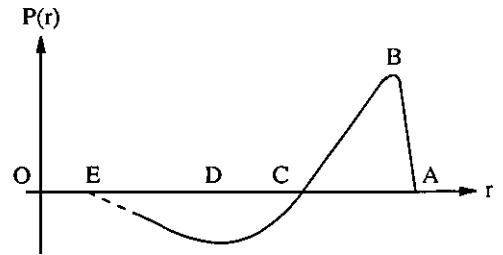
(a) Single diode laser pulse $1.9\mu\text{s}$ after event



(b) 3 semiconductor laser pulses $1\mu\text{s}$ apart, initial pulse $2\mu\text{s}$ after event

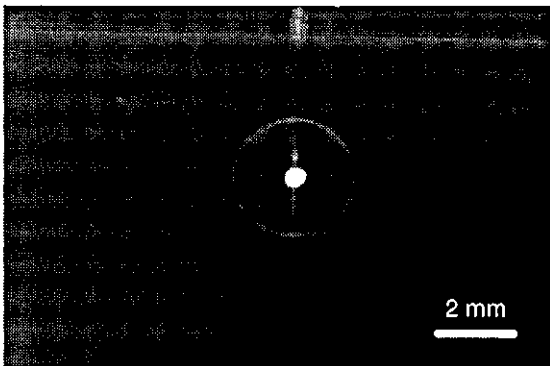


(c) 5 pulses $1\mu\text{s}$ apart, 1st laser pulse $1.2\mu\text{s}$ after event

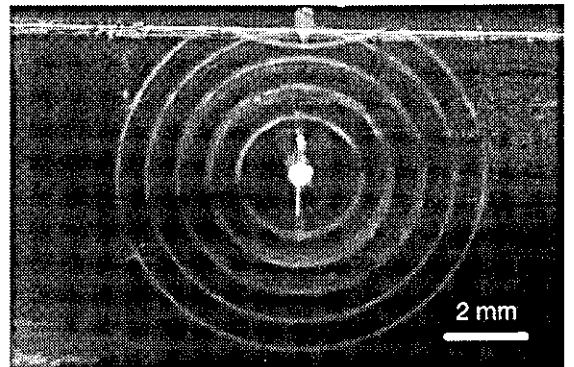


(d) Pressure profile of acoustic transient

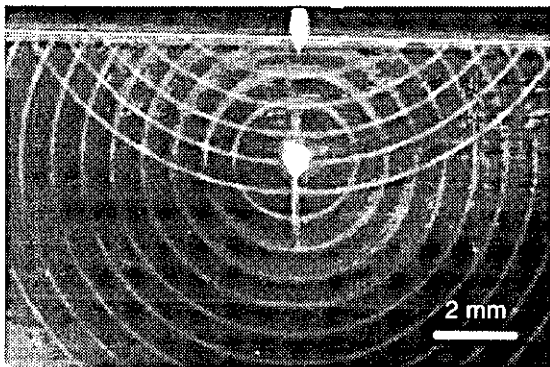
Figure 3.62 - Schlieren imaging of air shocks with multiple semiconductor laser pulses.



(a) Single exposure $0.7\mu\text{s}$ after event



(b) 5 diode laser illuminations $0.5\mu\text{s}$ apart, initial pulse $0.8\mu\text{s}$ after event



(c) 9 diode laser pulses $0.5\mu\text{s}$ apart, initial pulse $0.8\mu\text{s}$ after event

Figure 3.63 - Schlieren imaging of water shocks.

laser light deflected by refractive index changes in the direction parallel to wire and undeflected light are filtered out. This explains both the apparent asymmetry of the acoustic transients in figure 3.62, as well as the dark band 10 degrees to the horizontal; the wire Schlieren stop filters out light deflected along this direction.

Figure 3.62(a) shows an acoustic transient that has been clearly resolved using just a single 50ns exposure. The transient has slowed to the speed of sound and as a result it is imaged with a spatial resolution of about $17\mu\text{m}$. The Schlieren image can be interpreted as follows with the aid of the typical pressure profile of such a shock wave shown in figure 3.62(d). The narrow outer bright band seen between points A and B on figure 3.62(a) is caused by the rapid positive going pressure gradient of the shock front. The thickness of this region measured from the figure is about $35\mu\text{m}$ and, comparing this with the spatial resolution ($\sim 17\mu\text{m}$) this suggests that the shock front has a thickness of less than $20\mu\text{m}$.

Immediately behind the shock front, at B, is a very thin dark band. This band follows where the pressure reaches a maximum, giving a zero first order refractive index derivative, and hence zero local image intensity. Following this is a grey region which can be seen at smaller radii between points B and D. Since this region is quite broad, it occurs over a much greater time span than the shock front. Therefore this region is the gradual fall off in pressure, that is with a negative gradient, and is likely to pass through zero excess pressure at point C. Also since this region is not identifiable in the Shadowgraphs described in the last section (figure 3.61), the Schlieren imaging technique appears to be more sensitive. Finally a bright broad band can be seen between points D and E. This is most likely to be the tail of the shock, and the large dimensions indicate that it occurs over a relatively long time. It is uncertain as to why this region appears intense, the CCD camera is saturated here so the relative intensities between it, the shock front and the fall off region B-D, are misleading. This underlines the fact that it is difficult to gain quantitative results using the Schlieren technique.

The plasma can be seen in figure 3.62(a) as the saturated oval region in the centre of the photograph, and there are two possible reasons for its elongated shape. The first is that the focusing lens causes elliptical growth of the plasma biased towards the lens, as described in section 2.2.3. Since the plasma is extremely hot it will emit very intense light over a broad band during its growth, and the interference filter will allow through some of this light resulting in the elliptical luminous profile being imaged on the CCD camera. A second possible explanation is that the Schlieren stop filters out semiconductor laser light deflected by the plasma that has a component parallel to the

wire. This is seen in figures 3.62(b) and (c), where it can be observed that multiple illuminations of the event appears to increase the general size and intensity of the plasma's image.

Figures 3.62(b) & (c) show results obtained by increasing the number of illuminations by the semiconductor laser to 3 and 5 exposures respectively, both with pulse separations of $1\mu\text{s}$. Perhaps the most striking improvement over the high speed photographs obtained using the Shadowgraphic technique is that there is a substantial improvement in the contrast of the acoustic transients imaged on the CCD camera. This is a direct consequence of the undisturbed semiconductor laser light being filtered out by the Schlieren stop, giving rise to a dark background image. When integrated on the CCD camera chip with images of the transient from previous exposures, the dark background has little effect upon the overall contrast of the resulting image. As a consequence, this technique allows the propagation of individual acoustic transients to be investigated clearly. For example, by considering the radii of the transient photographed in figure 3.62(c), it can be seen that during the first two exposures the transient travels faster than the speed of sound, however slows by the third exposure to the sound speed. It can also clearly be seen in figure 3.62(b) that the negative tail of the acoustic transient (points D to E in figure 3.62(d)) travels very slowly in comparison to the shock front. It can therefore be said that the profile of the transient appears to stretch with time. Finally it can be seen that there is a decrease in the intensity of the images as the transient propagates further. This is due to the energy of the transient being spread over a greater area as it propagates to a larger radius, the acoustic pressure decreasing inversely with distance travelled (see chapter 5.)

3.8.3 - Schlieren imaging of optical cavitation [43]

The set-up described in the last three sections has also been used to photograph acoustic transients generated in water by Nd-YAG laser dielectric breakdown. Multiple exposure photographs of such optical cavitation events in water are shown in figure 3.63, and these have been imaged using the Schlieren technique. Figure 3.63(a) shows the initial acoustic transient given off by such an optical cavitation event in water illuminated by a single pulse from the semiconductor laser. The spherically symmetric shock front is clearly seen together with the bright plasma in the centre of the picture, which later grows into a cavitation bubble. The water air surface is seen at the top of the picture as a horizontal band. Just above this in the centre is an elongated white blob which is the out

of focus image of the plasma reflected off of the cell rear window and the water air boundary.

Figure 3.63(b) shows a multiple exposure photograph of a single acoustic transient. The semiconductor laser is pulsed to give 5 exposures at intervals of 500ns, accurate to within 5ns. By measuring the radii of the photographed acoustic transient at these known time intervals, it can be seen that shock front appears to propagate at a constant velocity which is slightly above that of sound in water (1500ms^{-1}). As a result it can be said that each 50ns semiconductor laser pulse resolves the transient to a spatial resolution of about $75\mu\text{m}$. The thickness of the shock measured in figure 3.63(b) is approximately $120\mu\text{m}$, or 80ns duration. This can be compared with the typical thickness of similar water born shock fronts of about $15\mu\text{m}$ (or alternately a rise time of $\sim 10\text{ns}$), which has been measured using the optical and piezoelectric techniques described in chapters 4 and 5. As a result it can be said that the transient is not fully resolved by the 50ns exposures and therefore appears smeared in the photographs.

Finally a further multiple exposure Schlieren photograph of a single water-born acoustic transient is shown in figure 3.63(c), in which 9 exposures of 50ns duration are made 500ns ($\pm 5\text{ns}$) apart. At the top of the picture the transient is seen to reflect off the water-air interface. Here a phase change occurs in the pressure wave, since Rayleigh's equations (see section 2.1.3, equations (2.20)) give a negative reflection coefficient:

$$R_0 = \frac{P_r}{P_i} = \frac{Z_{\text{air}} - Z_{\text{water}}}{Z_{\text{air}} + Z_{\text{water}}} \approx -0.999 \quad - (3.29)$$

where $Z_{\text{air}} \sim 425 \text{ kgm}^{-2}\text{s}^{-1}$ and $Z_{\text{water}} \sim 1.5 \times 10^6 \text{ kgm}^{-2}\text{s}^{-1}$. This results in the shock front becoming a negative going rarefaction wave, however a change in velocity is not observed in figure 3.63(c) for the reflected wave. This is probably because the rate of change of velocity with pressure (dc/dp) is quite small for water (see sections 2.1.4 & 2.1.5). An apparent change in velocity is however observed as the shock front passes through the plasma region (after it has been reflected at the water-air boundary.) That is, there appears to be a delay of about $100\mu\text{m}$, or 70ns. Given that the plasma has at this stage developed into a microscopic cavitation bubble and therefore has a very different acoustic impedance, equation (3.29) also implies that the transient is unlikely to be transmitted through the plasma. It is therefore likely that the apparent delay is caused by the transient being diffracted around the plasma, before joining up shortly afterwards into a continuous wave front. That is, the resulting increase in path length will give rise to the apparent change in velocity.

Conclusions

In this chapter it has been seen that a pulsed semiconductor laser can be used effectively in high speed photography as a flash light source capable of resolving fast moving events, such as acoustic transients. One such a device, the Northern Telecom LJ30, has been demonstrated providing up to 10 pulses of light at a maximum repetition rate of 5MHz with a timing accuracy of $\sim 5\text{ns}$. Each light pulse emitted by the diode laser has a peak power of 30W, full width half maximum duration of 50ns and wavelength of 860nm. A multiple exposure system incorporating the LJ30 has been demonstrated photographing transients initiated by Rhodamine 6G Dye laser ablation in air, Nd-YAG laser assisted dielectric breakdown in air and optical cavitation in water. When configured to give multiple exposures the system utilises a CCD camera to integrate the successive 'dark field' Schlieren images, the propagation of single acoustic transients subsequently being displayed on the same output picture. As a result the system has proved very useful for investigating the development of single acoustic transients with time, and therefore allows the study of events which are non-repetitive or are not repeatable.

It has been seen that each photograph involves a convolution between the light output of the laser with time, the temporal and spatial profiles of the acoustic transient, the spatial response of the optical imaging system, and the sensitivity of the CCD camera to the laser light. As a result the temporal and spatial resolution of each exposure is limited by both the duration of the semiconductor laser pulse and the velocity of the transient. The system demonstrated in section 3.8 is capable of temporally resolving acoustic transients to 50ns (the duration of the laser pulse.) This translates to spatial resolutions of about $17\mu\text{m}$ for air, and $75\mu\text{m}$ for water which have sound speeds of 330ms^{-1} and 1500ms^{-1} respectively. It has been shown that such a system is capable of clearly resolving acoustic transients propagating in air, however the resulting images of water born transients are not completely resolved due to the relatively small thickness of the shock (typically $\sim 15\mu\text{m}$.) Improvements in spatial and temporal resolution can only be made with shorter laser pulse durations, and this should be possible in the near future with further developments in semiconductor laser technology.

In conclusion it can be said that the high speed multiple exposure imaging system demonstrated has shown the LJ30 semiconductor laser to be an excellent source for Schlieren photography. It is compact, relatively cheap, very reliable and has relatively simple low voltage electronic drive circuitry. Provided that a dark field imaging technique such as Schlieren is used the development of single event acoustic transients can be followed. Finally the system has the potential to be applied in other high speed

photographic diagnostic techniques including Interferometry [42], Electronic Speckle Pattern Interferometry (ESPI) [43], and Particle Image Velocimetry (PIV) [44,45]. This not only allows the study of acoustic transients but also other fast moving mechanical phenomena such as cavitation, fluid flow in engines, ballistics and surface vibrations.

References

- [1] Carnell, M. T., Alcock, R. D. and Emmony, D. C. (1993) - *Optical Imaging of Shock Waves Produced by a High-Energy Electromagnetic Transducer*, Phys. Med. Biol. **38**, 1575-1588.
- [2] Suaidi, M. K. B., Jin, Y. H., Ward, B. and Emmony, D. C. (1992) - *Dynamic Photoelastic Studies of Laser Interaction with Water at a Solid Boundary*, J. Photog. Sci. **40**, pp23-28.
- [3] Stasicki, B., Hiller, W. J. and Meier, G. E. A. (1990) - *Light Pulse Generator for High Speed Photography Using Semiconductor Devices as a Light Source*, Optical Engineering **29**, No.7, pp821-827.
- [4] Asundi, A. and Sajan, M. R. (1995) - *Multiple LED Camera for Dynamic Photoelasticity*, Applied Optics **34**, No. 13, pp2236-2240.
- [5] Bretthauer, B., Meier, G. E. A. and Stasicki, B. (1991) - *An Electronic Cranz-Schardin Camera*, Rev. Sci. Instrum. **62**, No. 2, pp354-368.
- [6] Cranz, C. and Schardin, H. (1929) - *Kinematographie auf ruhendem Film und mit extrem hoher Bildfrequenz*, Zeitschrift für Physik **56**, pp147-183.
- [7] Pawliszyn, J. (1987) - *LEDs and Laser Diodes in Schlieren Optics Methods*, Rev. Sci. Instrum. **58**, No. 2, pp245-248.
- [8] *Pulsed Laser Diodes - LJ/LK Series*, S.T.C. Optical Devices Data sheet No. LJKWA070A.EH, Issue H, March 1991.
- [9] Cross, L. A. (1988) - *Photographic Applications of Pulsed Semiconductor Lasers*, Proc. SPIE **981**, High Speed Photography, Videography, and Photonics VI, pp272-280.
- [10] Haley, R. and Smy, P. R. (1988) - *An Inexpensive Light Source for High Speed Schlieren Photography*, Journal of Physics E: Scientific Instruments **21**, pp1172-1174.
- [11] Hecht, J. (1992) - *The Laser Guidebook*, 2nd Ed., Published by McGraw-Hill Inc., pp108,136,151,297-386.
- [12] *Optics Guide 5*, Melles Griot.
- [13] Wilson and Hawkes (1989) - *Optoelectronics, An Introduction*, 2nd Edition, Published by Prentice Hall International Ltd., pp187-201.

- [14] Hecht, E. and Zajac, A. (1974) - *Optics*, Published by Addison-Wesley, pp336-340.
- [15] *Semiconductor Lasers - Drive Circuits*, Guidance Notes - S.T.C. Microwave & Optical Systems, Data Sheet No. 6380 2686E Ed1, October 1984.
- [16] Fabian, M. E. (1981) - *Semiconductor Laser Diodes - A Users Handbook*, Electrochemical Publications Ltd., pp49-59.
- [17] *SMP60N06/05, SMP50N06/05 N-Channel Enhancement Mode Transistors*, Data Sheet, Siliconix Inc.
- [18] *IR2110 High Voltage MOS Gate Driver*, Data Sheet No. PD-6.011B, International Rectifier.
- [19] *Power MOSFETs - RFD16N10, RFD16N10SM, N-Channel Enhancement-Mode Power Field-Effect Transistors (MegaFETs)*, File No. 2386, Harris Semiconductor.
- [20] *SFH450V/451V/452V, SFH750V/752V Plastic Fibre Optic Transmitter Diode*, Preliminary Data Sheet, Siemens.
- [21] *SFH551 / Right Angle Housing SFH551V Photodetector For Plastic Fiber*, Advance Data Sheet, Siemens.
- [22] Forkner, J. F. and Kuntz, D. W. (1987) - *Characteristics of Efficient Laser Diode Collimators*, Proc. SPIE, **740**, Laser Diode Optics, pp27-35.
- [23] Kuntz, D. (1984) - *Specifying Laser Diode Optics*, Laser Focus/Electro-Optics **20**, No. 3, pp44-55.
- [24] Optics Catalogue, Comar Instruments, 70 Hartington Grove, Cambridge, CB1 4UH.
- [25] Beynon, J. D. E. and Lamb, D. R. (1980) - *Charge-Coupled Devices and their Applications*, Published by McGraw-Hill Book Company Ltd.
- [26] *EEV CCD Cameras*, Brochure, EEV Solid State Devices, Essex.
- [27] *LM1881 Video Sync Separator*, Preliminary Data Sheet, National Semiconductor.
- [28] *PE530 Data Sheet*, Pulnix Europe Ltd., U. K.
- [29] Kaye, G. W. C. and Laby, T. H. (1995) - *Tables of Physical and Chemical Constants*, 16th Edition, Published by Longman, pp116-118.
- [30] Holder, D. W. and North, R. J. (1963), *Schlieren Methods*, National Physics Laboratory Notes on Applied Science No. 31, Published by Her Majesty's Stationary Office.
- [31] *T.V. Picture Frame Store, User Manual*, Eltime Ltd. / British Telecom.
- [32] *SFH250V Plastic Fiber Optic Photodiode Detector*, Preliminary Data Sheet, Siemens.
- [33] Daiber, J. W. and Thompson, H. M. (1967) - *Laser-Driven Detonation Waves in Gases*, The Physics of Fluids **10**, pp1162-1169.
- [34] Ramsden, S. A. and Savic, P. (1964) - *A Radiative Detonation Model for the Development of a Laser-Induced Spark in Air*, Nature **203**, pp1217-1219.

- [35] Taylor, G. I. (1950) - *The Formation of a Blast Wave by a Very Intense Explosion, I. Theoretical Discussion, and, II. The Atomic Explosion of 1945*, Proc. Roy. Soc. A201, pp159-174 and pp175-186. Reprinted in *The Scientific Papers of Sir Geoffrey Ingram Taylor, Volume III, Aerodynamics and the Mechanics of Projectiles and Explosions*, Published by Cambridge University Press, pp493-509 and pp510-521.
- [36] Emmony, D. C. and Irving, J. (1969) - *Strong Shock Wave Generation by the Interaction of a Giant Laser Pulse with a Solid Target*, Brit. J. Appl. Phys. (J. Phys. D) 2, pp1186-1188.
- [37] Dale, T. P. and Gladstone, J. H. (1858) - *On the Influence of Temperature on the Refraction of Light*, Phil. Trans. Roy. Soc. London 148, pp887-894.
- [38] Gladstone, J. H. and Dale, T. P. (1863) - *Researches on the Refraction, Dispersion, and Sensitiveness of Liquids*, Phil. Trans. Roy. Soc. London 153, pp317-343.
- [39] Partington, J. R. (1953) - *An Advanced Treatise on Physical Chemistry, Volume Four: Physico-Chemical Optics*, Published by Longmans, pp6-21.
- [40] Alcock, R. D. and Emmony, D. C. (1995) - *Nanosecond Laser Diode Schlieren Photography*, Proceedings of the 1995 World Congress on Ultrasonics, pp647-650.
- [41] Ward, B. (1991) - *Generation of Acoustic Waves by Focused Infrared Neodymium-Laser Radiation*, PhD Thesis, Loughborough University.
- [42] Ward, B. and Emmony, D. C. (1990) - *Interactions of Laser-Induced Cavitation Bubbles with a Rigid Boundary*, Proc. SPIE 1358, 19th International Congress on High Speed Photography and Photonics, pp1035-1045.
- [43] Jones, R. and Wykes, C. (1989) - *Holographic and Speckle Interferometry: A Discussion of the Theory, Practice and Application of the Techniques*, 2nd Edition, Published by Cambridge University Press.
- [44] Pickering, J. D. and Halliwell, N. A. (1984) - *Speckle Photography in Fluid Flows: Signal Recovery with Two-Step Processing*, Applied Optics 23, pp1128-1129.
- [45] Adrian, R. (1984) - *Scattering Particle Characteristics and their Effect on Pulsed Laser Measurements of Fluid Flow: Speckle Velocimetry vs Particle Image Velocimetry*, Applied Optics 23, pp1690-1691.

Chapter Four

An Optical Transducer

Introduction

In this chapter the design and development of a high speed optical transducer for measuring acoustic transients propagating in water is discussed. The device is based upon the measurement of reflectance at a water-solid interface, which changes with the variations in pressure arising from an acoustic transient traversing the boundary. This chapter begins with a brief review of the techniques used to characterise acoustic transients. In section 4.2 the theory behind the design of the optical transducer is outlined in some detail, and this is followed by consideration of changes in refractive index with pressure in section 4.3. The design and calibration of a prototype transducer fabricated out of perspex is discussed in sections 4.4 and 4.5, and initial experimental results measuring acoustic transients associated with laser cavitation are described in section 4.6. A glass transducer with improved sensitivity is demonstrated practically in section 4.7, where it is shown that the transducer is also useful for studying cavitation phenomena and rarefaction waves. Finally in section 4.8 a commercial design of transducer is proposed as further work.

4.1 - Refractive index transducers

The quantitative measurement of shock waves and acoustic fields in water is usually undertaken using either piezoelectric hydrophones [1,2], optical interferometry [3-5], or quantitative Schlieren methods [6]. In general all of these techniques require measurements to be made with high spatial and temporal resolution. In the case of cavitation phenomena, in which the growth and subsequent collapse of bubbles in liquids is studied, the individual events are usually small ($< 1\text{mm}$) and spherical, so that any form of conventional transducer must have equally small dimensions compared with the cavitation event itself. Needle hydrophones [7] may be used, but these require careful calibration and are relatively delicate. Alternatively high speed photographic techniques can be utilised, however in these cases some form of time resolution such as strobe illumination must be employed because virtually all water born shock phenomena propagate at, or slightly above, the speed of sound (1480ms^{-1}).

A transducer based upon changes in the reflection of light at the end of a glass fibre submerged in water has been built by Eisenmenger [8]. The reflectance at the fibre tip is altered by the changes in refractive index in the water arising from the impact of an intense sound wave, and a probe beam is then used to measure this effect. The spatial resolution of the device is determined by the diameter of the glass fibre, which can be very small. The sensitivity of the transducer to acoustic waves is dependant upon the reflectance at the glass-water interface, however this is not strongly dependant on the refractive index of the water. Furthermore, the change in refractive index of the water with pressure, which is given by the Gladstone-Dale relationship [9,10] is rather small ($\Delta n/\Delta p \sim 1.4 \times 10^{-5} \text{ bar}^{-1}$ for water [11]) and the overall sensitivity of the device is therefore small. As a result a high powered laser is required as the sensing light source for the fibre optic transducer, and the measurement requires the detection of a small decrease in reflected light intensity against a relatively large background.

Phillips [12] suggested a reflection transducer with high sensitivity which was based upon a single mode fibre which is cleaved close to the critical angle. This idea was however never demonstrated practically, and it is believed that this was because the cleaved fibre end disrupted the single mode properties of the fibre giving rise to high beam divergence, thus reducing the sensitivity of the device. In theory the reflectance of the water-to-fibre interface is defined by the Fresnel equations. The greatest sensitivity to small changes in the refractive index is found at, or just below, the critical angle and this is the basis of the transducer described in this chapter. The ideal transducer would have high spatial resolution, as would be the case of the fibre tip, with some parameter which is a rapidly changing and preferably linear function of pressure of the fluid in which it is immersed.

In the transducer described here the changes in reflectance at a flat solid/water interface for light incident from the more dense medium was measured using a probe beam from a semiconductor laser together with a fast photodiode. High spatial resolution and sensitivity were achieved by focusing the probe beam onto the interface at an angle which was slightly smaller than the critical angle. It was found theoretically that some probe beam divergence reduced the sensitivity of the device, resulting in a trade off between the spatial resolution and sensitivity of the device. The prototype transducer was practically demonstrated by measuring the acoustic transients associated with laser generated cavitation events in water. It was fabricated using a semicircular polymer (poly-methyl-meth-acrylate, PMMA) block with the ability to change the angle of incidence of the probe beam on the flat face. The front face of the transducer was later machined back and replaced with glass in order to achieve a high sensitivity. Finally a more practical

transducer is proposed consisting of a ground and polished glass prism with fixed angle of incidence which leads to a more compact device.

4.2 - Theory

The basis of the optical transducer described in this chapter is as follows. The proportion of a probe beam reflected at an interface between two media is a function of angle of incidence of the beam, the polarisation, and the ratio of the refractive indices of the two materials involved. As will be seen in section 4.3, the refractive index of many materials is dependant on the density of the medium, which is in turn a function on the pressure experienced by the material. Therefore by detecting changes in the reflectance at an interface, it is possible to detect the changes in pressure at the interface due to an acoustic transient propagating through it.

4.2.1 - Basic optics

Consider a collimated beam of monochromatic light travelling through a dielectric medium with a refractive index n_I incident upon a boundary with a second such medium having a smaller refractive index n_T . If this beam is incident at an angle θ_I to the normal, then a proportion of this will be reflected at the boundary at the same angle and, the remainder will be transmitted into the second medium and refracted at an angle θ_T to the normal defined by Snell's law [13]:

$$n \sin \theta_I = \sin \theta_T \quad - (4.1)$$

where $n = \frac{n_I}{n_T}$. The proportion of the light energy reflected at the boundary is called the reflectance and is defined by the *Fresnel equations* [13]. The reflectance is dependant not only upon of the angle of incidence and refractive indices of the media, but also on the polarisation of the incident light. That is the reflectance R for light polarised with the electric field perpendicular and parallel to the plane of incidence respectively are [13]:

$$R_{\perp} = \left(\frac{n \cos \theta_I - \sqrt{1 - n^2 \sin^2 \theta_I}}{n \cos \theta_I + \sqrt{1 - n^2 \sin^2 \theta_I}} \right)^2 \quad \text{and} \quad R_{\parallel} = \left(\frac{n \sqrt{1 - n^2 \sin^2 \theta_I} - \cos \theta_I}{n \sqrt{1 - n^2 \sin^2 \theta_I} + \cos \theta_I} \right)^2 \quad - (4.2)$$

These functions are plotted in figure 4.1 for a perspex ($n_i=1.495$) to water ($n_t=1.333$) interface. It can be seen that at small incident angles both of the reflectances tend to the same value defined by:

$$R_{\perp}(\theta_i \rightarrow 0) = R_{\parallel}(\theta_i \rightarrow 0) = \left(\frac{n-1}{n+1} \right)^2 \quad - (4.3)$$

Typically this value is about 0.37% for a perspex to water interface. As the incidence angle is increased the proportion of light reflected differs for the two polarisations. For components of the beam polarised with the electric field perpendicular to the plane of incidence, R_{\perp} increases non-linearly with θ_i until it reaches unity at the *critical angle* θ_c , defined by [13]:

$$\sin \theta_c = n_t / n_i \quad - (4.4)$$

The critical angle for a perspex to water interface is about 63.0° , and at this angle the transmitted light is refracted along the boundary. Whereas for light which is polarised parallel to the interface the reflectance R_{\parallel} does not increase initially with θ_i , but falls to zero at *Brewster's angle* θ_p [13]:

$$\tan \theta_p = n_t / n_i \quad - (4.5)$$

There is also a phase shift between the incident and reflected beams of π radians for incident angles less than θ_p . Beyond the Brewster angle there is no phase shift and the reflectance rises to unity at the critical angle. For a perspex to water interface θ_p is about 41.5° .

For incident angles greater than θ_c all the light is reflected, and there is also a phase shift in the reflected light [12]:

$$\delta_{\perp} = 2 \tan^{-1} \left(\frac{\sqrt{n^2 \sin^2 \theta_i - 1}}{n \cos \theta_i} \right) \quad \text{and} \quad \delta_{\parallel} = 2 \tan^{-1} \left(\frac{n \sqrt{n^2 \sin^2 \theta_i - 1}}{\cos \theta_i} \right) \quad - (4.6)$$

This phase shift rises from zero for light incident at the critical angle, to π at 90° incidence.

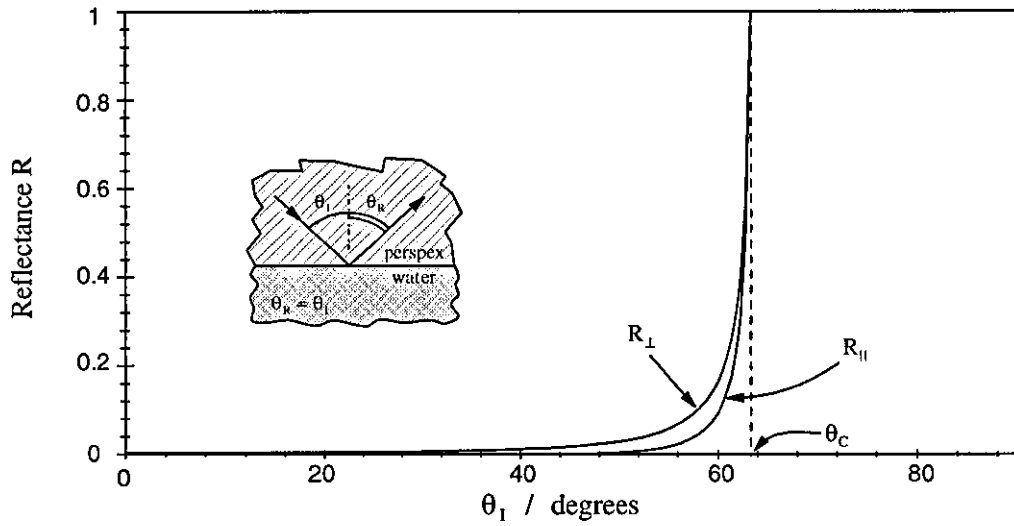


Figure 4.1(a) - Fresnel reflectance with incidence angle for Perspex-Water interface.

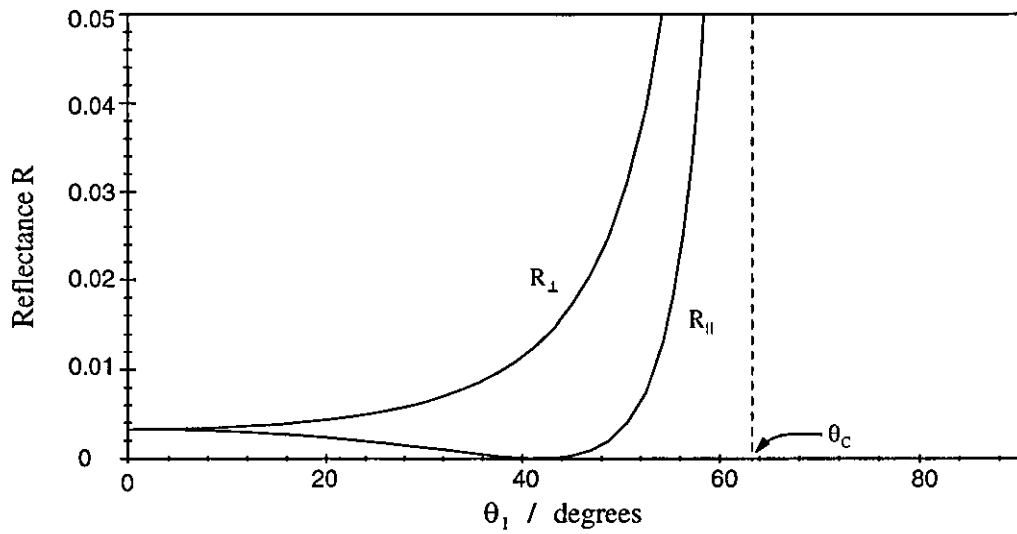


Figure 4.1(b) - Expansion along reflectance axis from (a).

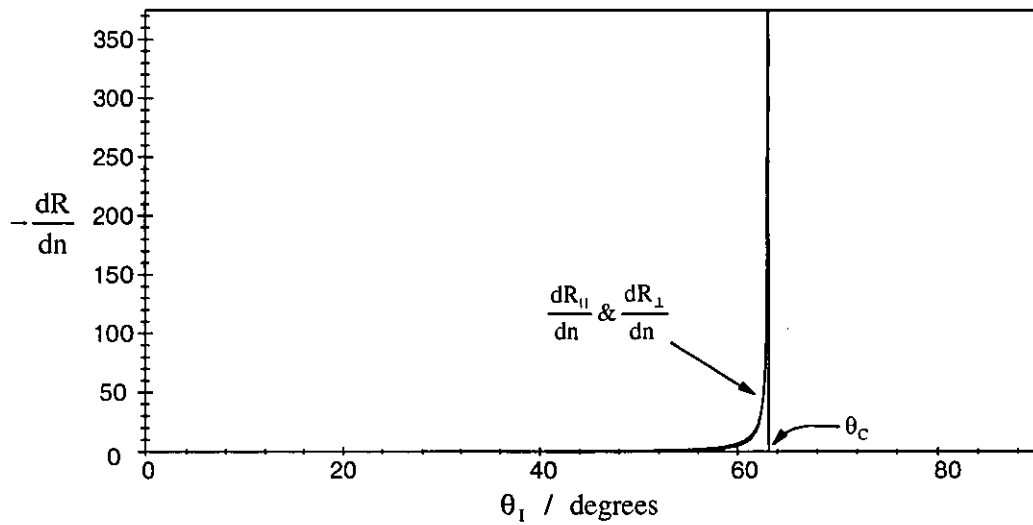


Figure 4.2 - Sensitivity of reflectance to changes in n for Perspex-Water interface.

4.2.2 - Sensitivity of the reflectance

It can be seen from equation (4.4) that when the refractive index of the second medium increases relative to the first medium the critical angle θ_c also increases. The effect of this upon the reflectance is an expansion of the curves shown in figure 4.1 about the zero incident angle. As a result there is a decrease in the reflectance at all angles below the critical angle, for both polarisations.

The sensitivity of the reflectance to small changes in the ratio of the refractive index can be found by differentiating the reflectance equations (4.2):

$$\frac{\partial R_{\parallel}}{\partial n} = 4 \frac{(\cos \theta_1 - n\zeta)(2n^2 \sin^2 \theta_1 - 1)\cos \theta_1}{\zeta (\cos \theta_1 + n\zeta)^3} \quad \text{and} \quad \frac{\partial R_{\perp}}{\partial n} = 4 \frac{(n\cos \theta_1 - \zeta)\cos \theta_1}{\zeta (n\cos \theta_1 + \zeta)^3} \quad - (4.7)$$

where $\zeta = \sqrt{1 - n^2 \sin^2 \theta_1}$.

These functions are plotted in figure 4.2 against incident angle for a perspex to water interface. It can clearly be seen that the peak sensitivity to changes in the refractive index ratio is at or just below the critical angle θ_c , defined in equation (4.4). In fact at the critical angle the reflectance is infinitely sensitive to changes in refractive index. It can therefore be said that a transducer based upon the measurement of small changes in reflectance will have greatest sensitivity when the probe beam is incident at the critical angle.

Such a reflection transducer was suggested by Phillips [12]. This was based upon light propagating in a glass fibre which is incident on an interface with water at the critical angle. The transducer would measure changes in refractive index at the solid-liquid boundary with very high sensitivity, however this device was never practically realised. Later Eisenmenger [8] demonstrated a fibre optic transducer which operated by simply measuring the amount of light reflected at a normal polished fibre end, however in this case the measurements of pressure were made for zero degree incidence. At zero degrees incidence the above equations tend to:

$$\left. \frac{\partial R_{\parallel}}{\partial n} \right|_{\theta_1=0} = \left. \frac{\partial R_{\perp}}{\partial n} \right|_{\theta_1=0} = 4 \frac{n-1}{(n+1)^3} \quad - (4.8)$$

For a glass to water boundary the change in reflectance (ΔR) is numerically just 5% of the change in the ratio of the refractive indices (Δn). This can be compared with the sensitivity achieved at the critical angle which is infinite for small changes in the refractive index ratio. Furthermore only 0.35% of the incident light is reflected back to the detector from the glass fibre-water interface used in Eisenmenger's transducer, the remainder being transmitted into the water. As a result a very large CW laser source was required for Eisenmenger's transducer in order to detect the high speed variations in reflectance above the noise background.

Finally beyond the critical angle the sensitivity for small changes in the refractive index ratio is zero. The consequence of this is that in order to detect a decrease in the refractive index ratio, perhaps arising from a (negative) rarefaction wave, the probe beam would need to be incident at an angle below the critical angle.

4.2.3 - Divergent input beams and spatial resolution

The sensitivity of the reflectance to changes in refractive index is reduced somewhat when the incident beam is uncollimated. This has been simulated for several incident beams having Gaussian shaped angular spreads, as defined in figure 4.3. The resulting reflectances are shown in figure 4.4 for light polarised parallel to a perspex to water boundary. It can clearly be seen that for beams with greater incident beam divergence, the steep gradient of the reflectance close to the critical angle becomes much more gentle.

The sensitivity of the reflectance to changes in the refractive index at a perspex to water boundary has also been calculated for several beam divergences and is shown in figure 4.5. It can clearly be seen that the sensitivity at the critical angle is reduced considerably with greater beam divergence. Additionally the incident angle θ_i at which the sensitivity is greatest decreases with increasing divergence. As a result in the design of a transducer it is desirable to have a collimated incident beam to gain maximum sensitivity to small changes in the refractive index of the water.

It is also beneficial in transducer design to have as small an active area as possible to maximise the spatial resolution. This is practically achieved by focusing the input probe beam down using a lens to the diffraction limit, the active area of the transducer being just that defined by the locus of the beam at the solid-water interface, which is defined by the Rayleigh criterion:

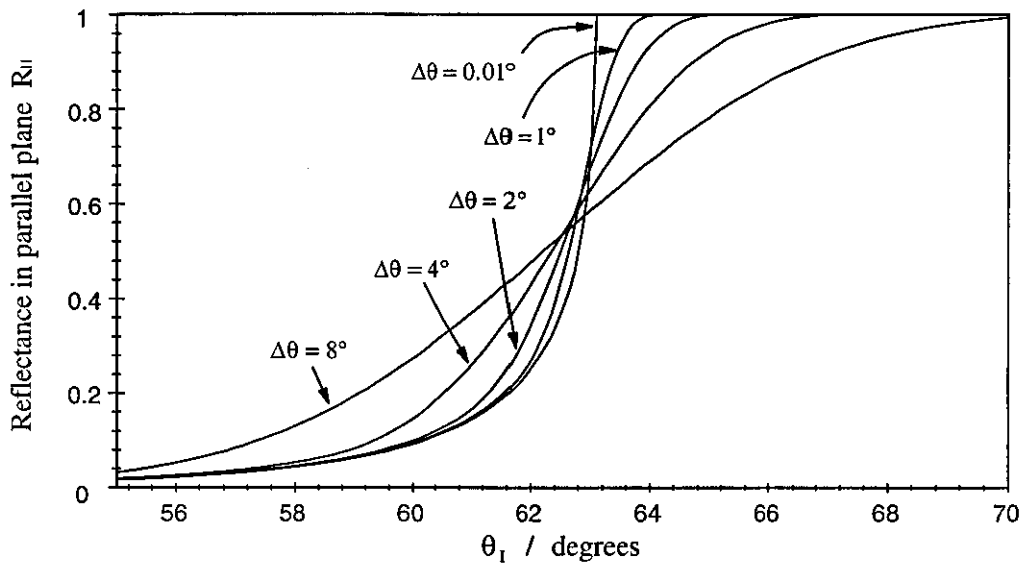
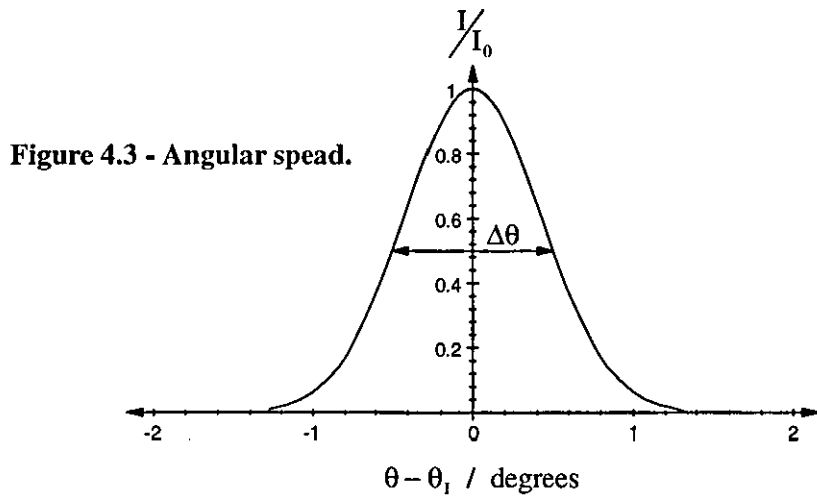


Figure 4.4 - Reflectance for Perspex-Water interface varying with angular spread.

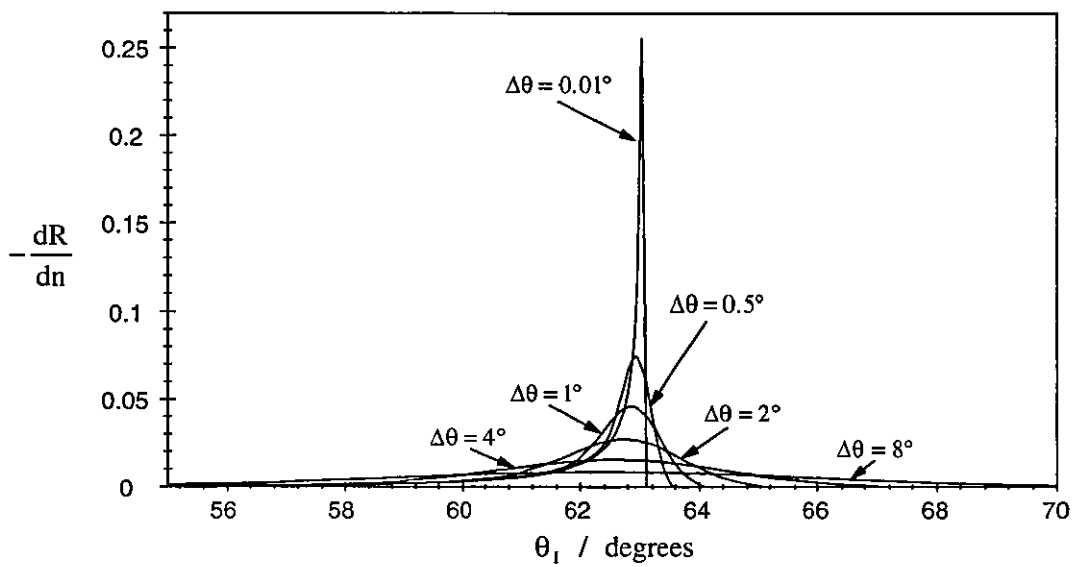


Figure 4.5 - Sensitivity of reflectance to angular spread for Perspex-Water interface.

$$\Delta s = 1.22 \frac{f \lambda}{d} \quad - (4.9)$$

where Δs is the diameter of the active area, λ the wavelength of the probe beam, f the focal length and d the aperture of the lens.

In doing so however beam divergence will be added to the system and the peak sensitivity of the transducer will therefore be reduced. The resulting beam divergence $\Delta\theta$ can be estimated using:

$$\Delta\theta \approx 2 \arctan\left(\frac{d}{2f}\right) \quad - (4.10)$$

It can be said that in the design of such a transducer there is a trade off between the sensitivity and spatial resolution. It is therefore evident that the best transducer would be a compromise between the two, the spot size appropriately chosen to give the required sensitivity.

As commented in the last section, Phillips [12] suggested the use of a single mode fibre optic cable. The prime advantage of this is that the light is confined within the fibre giving rise to a very small sensitive area, thereby resulting in very high spatial resolution. Additionally such fibres exhibit planar wave front propagation giving in theory zero probe beam divergence. In practice however by cleaving the end of a single mode fibre at the critical angle, as suggested by Phillips to gain maximum sensitivity, the single mode properties of the fibre are disrupted at the fibre tip and the beam becomes divergent through diffraction. As commented above this divergence will reduce the sensitivity of the transducer somewhat. Even if this increases the input beam divergence to just a few degrees the sensitivity is reduced hugely, and it is for this reason that it is thought Phillips transducer was not able to be demonstrated practically.

4.3 - The variation of refractive index with temperature and pressure

When a beam of light propagates through a dielectric medium it induces oscillations in the charged particles within the material, giving rise to the emission of secondary waves through scattering. These secondary wavelets have different phases to the original beam and interfere with the original beam resulting in a beam which has a slower propagation velocity than the original beam. This reduction in the speed of light c is defined physically for any given material using the refractive index n :

$$n = \frac{c_0}{c} \quad - (4.11)$$

where c_0 is the speed of light within free space.

The speed of light within the medium is strongly dependant on the density of the medium, which varies with temperature and pressure. When compressive pressure (isothermal) is applied the density of the medium increases giving rise to a greater concentration of charged particles. In turn this gives rise to in a higher scattered wave intensity, a slower wave propagation velocity of the resulting beam, resulting in an increase in the refractive index of the material. Whereas an increase in temperature (constant pressure) usually results in expansion of the medium, a reduction in density, and hence a fall in the refractive index of the material.

As an acoustic transient propagates through a dielectric medium the density of the material is altered, and the electric field arising from the interaction of neighbouring molecules is modified. This gives rise to a change in the refractive index of the medium on a macroscopic scale, which is defined generally by the spatial distribution and intensity of the acoustic wave.

Gladstone and Dale [9,10] studied the properties of several liquids under different pressures and found the following experimental relationship between the refractive index and density:

$$\frac{n-1}{\rho} = \text{constant} \quad - (4.12)$$

A wide range of experimental work has shown the Gladstone-Dale relationship to be accurate for pressures of up to about 100bars ($\sim 10^7$ Pa) for a large number materials [14]. In particular experiments have shown the linear relationship to be valid for water up to 1kbar [11], and also for PMMA [15,16] and glass. Several other relationships have been found including the Newton [17], the Eykman [18] and the Lorentz-Lorentz [19,20]. The latter is also known as the Clausius-Mossotti equation, which describes the dielectric behaviour of gases and liquids at very elevated temperatures and pressures.

All of these relationships require knowledge of the equation of state, that is the pressure-temperature-density relationship of the materials involved. Several have been calculated for water from experimental results, and are called steam tables. To date the most comprehensive one is the NBS/NRC steam tables [21], however the one developed by

Chen, Fine and Millero [22] is used here because of its relative simplicity, being extremely accurate over the range 0–100°C and up to 1kbar. Less detailed relationships have been determined for other materials. In these cases it has been found best to use the *Tait equation* [23] which gives a first order approximation assuming constant temperature:

$$K = \frac{1}{\kappa} = \frac{-\Delta P}{\Delta V/V_0} \quad - (4.13)$$

where K is the bulk modulus, κ is the compressibility, ΔV the change in volume V under applied pressure ΔP . The Tait equation has been found to be valid for solids up to a few gigapascals of pressure [23], and up to about 150MPa for most liquids [23].

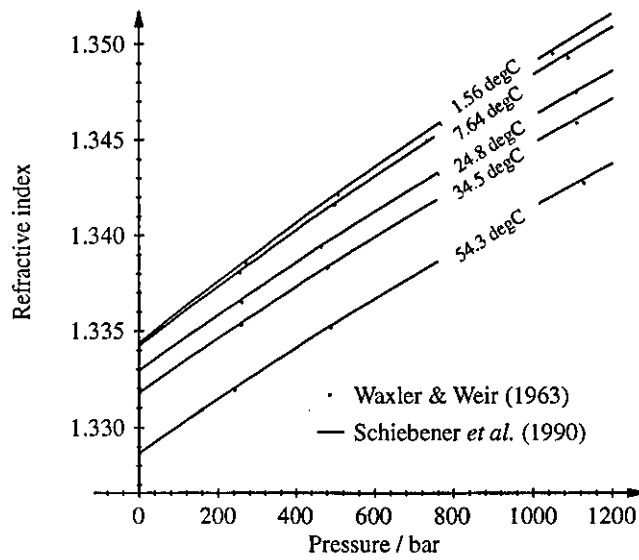
4.3.1 - Refractive index relationships of water, perspex and glass

The variations in the refractive index of water with pressure and temperature are shown in figure 4.6. This has been plotted using theoretical predictions made by Schiebener *et al.* [24], experimental data collected by Waxler and Weir [11], and density data calculated from the equation of state developed by Chen, Fine and Millero [22]. It can clearly be seen from figure 4.6(a) that the refractive index increases linearly with pressure over the range 0 to 1000 bar, provided that there is constant temperature. An increase in temperature at constant pressure on the other hand results in a non-linear decrease in the refractive index, which is shown in figure 4.6(b).

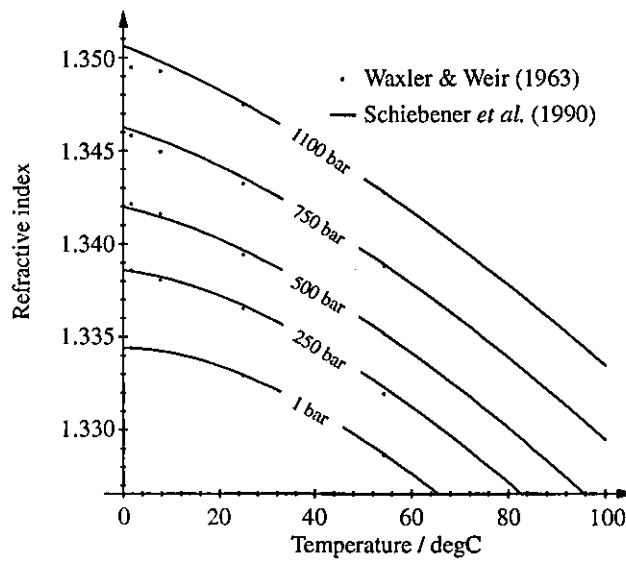
Figure 4.7 shows the variation of refractive index for perspex (also known as PMMA, Lucite, or Plexiglas) [15-16,25-26] and glass (hard crown HC519604) [8,12,27] with pressure at room temperature (20°C, $\lambda=578\text{nm}$). It can clearly be seen that although both solids exhibit a linear increase in refractive index with pressure in the range 0 to 1kbar, glass is significantly less susceptible to changes in refractive index than perspex.

Table 4.1 shows a summary of the first order refractive index properties of the three materials with varying pressure and temperature, which were obtained from data presented in references [22,24-31]. The rate of change of refractive index with pressure was calculated using:

$$\frac{dn}{dP} = \frac{dn}{d\rho} \frac{d\rho}{dV} \frac{dV}{dP} \quad - (4.14)$$



(a) Pressure



(b) Temperature

Figure 4.6 - Refractive index variation with temperature and pressure for water. ($\lambda=587 \text{ nm}$)

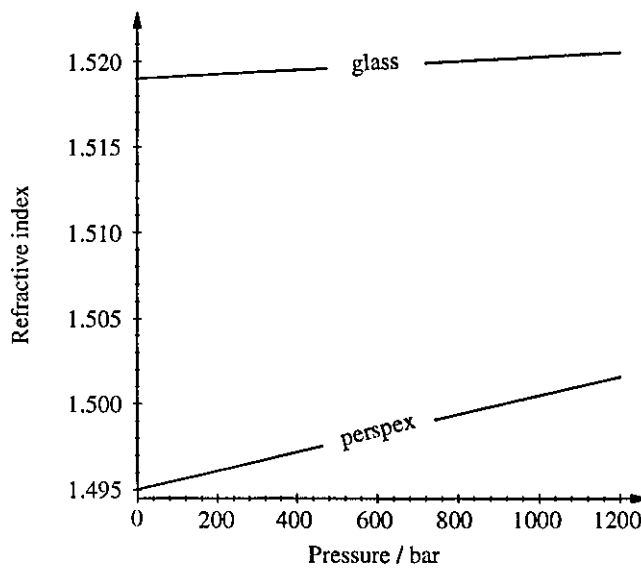


Figure 4.7 - Refractive index variation with pressure for Perspex and Glass. ($\lambda=670 \text{ nm}$)

| Material \ Property | ρ_0 [kg m ⁻³] | n_0 | $\frac{dn}{dP}$ [bar ⁻¹] | $\frac{dn}{dT}$ [C ⁻¹] | K [GNm ⁻²] |
|---------------------|-----------------------------------|-------|--------------------------------------|---------------------------------------|---------------------------|
| Water | 0.998 | 1.333 | ⁽¹⁾ 1.49×10^{-5} | ⁽¹⁾ -8.96×10^{-5} | 2.05 |
| P.M.M.A.(Perspex) | 1.18 | 1.495 | ⁽²⁾ 0.55×10^{-5} | ⁽³⁾ -1.25×10^{-4} | ⁽⁴⁾ 9.0 |
| Glass (HC 519604) | 2.53 | 1.519 | ⁽²⁾ 0.13×10^{-5} | - | 41.2 |

Notes: All data for measurements at T = 20 degC, P = 1 bar, $\lambda = 670\text{nm}$.
 (1) Obtained from Schiebener *et al.* (1990) and Chen-Tung Chen *et al.* (1977).
 (2) Calculated using Tait equation and Gladstone-Dale formula.
 (3) Derived from Michel, Dugas, Cariou and Martin (1986).
 (4) Obtained from Bridgman (1948)
 Other sources: Kaye & Laby (1972); ICI Acrylic Technical Setvice Note PX127.

Table 4.1 - Refractive index properties of Water, Perspex and Glass.

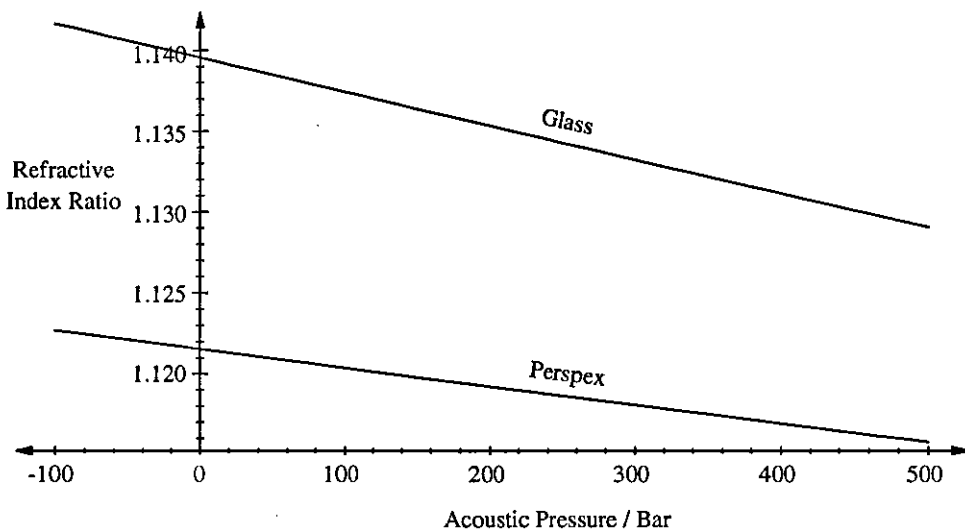


Figure 4.8 - Calculated refractive index ratio as a function of acoustic pressure.

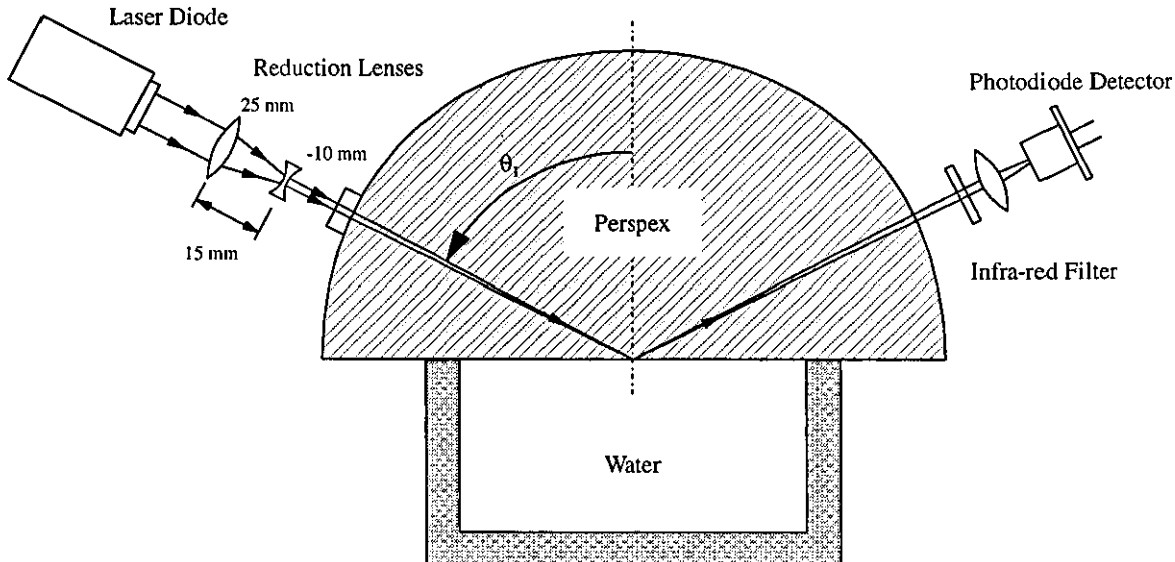


Figure 4.9 - Experimental set-up of Fresnel reflection transducer.

where the term $dn/d\rho$ is found using the Gladstone-Dale equation (4.12) for refractive index n_0 and density ρ_0 at zero pressure, $d\rho/dV$ is calculated from the density definition, and dV/dP is found from the Tait equation (4.13). That is:

$$\frac{dn}{d\rho} = \frac{n_0 - 1}{\rho_0} \quad \frac{d\rho}{dV} = -\frac{\rho_0}{V_0} \quad \frac{dV}{dP} = -\frac{V_0}{K}$$

Combining these in equation (4.14), dn/dP can then be calculated very simply using:

$$\frac{dn}{dP} = \frac{n_0 - 1}{K} \quad - (4.15)$$

The value for the bulk modulus of Hard Crown glass was obtained from Kaye and Laby [28], but can also be calculated from data presented in references [29-31]. For perspex the bulk modulus was calculated from compressibility data presented in references [29,31]. These values were found to be experimentally verified for high dynamic pressures in reference [32]. Finally the rate of change of refractive index with pressure of water was calculated using the data presented by Chen *et al* [22] and Schiebener *et al* [24].

4.3.2 - The refractive index ratio

The effect of changes in pressure on the refractive index ratio n can be modelled as follows to first order accuracy:

$$n = \frac{n_{T_0} + \left(\frac{dn_T}{dP}\right)\Delta P_T}{n_{W_0} + \left(\frac{dn_W}{dP}\right)\Delta P_W} \quad - (4.16)$$

where n_{T_0} and n_{W_0} are the ambient refractive indices of the transducer material and water respectively. The excess pressures on the transducer side of the boundary ΔP_T , and in the water ΔP_W are in fact equal since there must always be an equilibrium of pressure across the interface, as seen in chapter 2, section 2.1.3. Using the values quoted in table 4.1, the above equation is valid for pressures up to about 1kbar.

4.3.3 - Acoustic reflection at the interface

When an acoustic wave is incident at the water-transducer boundary the pressure exerted at the interface will in general be larger than the pressure of the wave during free propagation. This is because the incident wave is partially reflected at the transducer boundary, the reflected amplitude being added to the incident wave amplitude. Assuming that the acoustic transient being measured is normally incident, the pressure exerted at the boundary can be calculated using equation (2.20):

$$\Delta P_W = \Delta P_{IN} \left(1 + \frac{\rho_T c_T - \rho_W c_W}{\rho_T c_T + \rho_W c_W} \right) = \Delta P_{IN} \left(\frac{2\rho_T c_T}{\rho_T c_T + \rho_W c_W} \right) = \Delta P_T \quad - (4.17)$$

or more simply:
$$\Delta P_W = \Delta P_T = k \Delta P_{IN} \quad - (4.18)$$

where ρ_T and ρ_W are the ambient densities of the transducer material and water respectively, and c_T and c_W are the sound speeds in the two media. The input excess pressure ΔP_{IN} here is the time dependant pressure profile of the incident acoustic transient. The above equations are only valid for non-static pressures inputs, which is true for acoustic transients. Typically the constant k is about 1.38 for a perspex-water boundary transducer ($c_W=1500\text{ms}^{-1}$, $\rho_W=998\text{kgm}^{-3}$, $c_T=2700\text{ms}^{-1}$, $\rho_T=1260\text{kgm}^{-3}$), and $k\sim 1.8$ for a glass-water sensor ($c_T=5660\text{ms}^{-1}$, $\rho_T=2500\text{kgm}^{-3}$).

Using equations (4.16) & (4.18), the refractive index ratio has been calculated for an acoustic wave with peak pressures ranging between -100bar to +500bar. This is shown for a normally incident wave at both perspex-water and glass-water boundaries in figure 4.8. It can clearly be seen that both relationships are essentially linear with pressure within the calculated range, however the glass-water boundary exhibits a greater change in the refractive index ratio with pressure. As a result a reflection transducer fabricated out of glass would be expected to have far greater sensitivity than one made out of perspex. One reason for this is that the refractive index of glass does not vary much with pressure, and therefore the bottom half of equation (4.16) becomes almost constant. Whereas perspex has more considerable refractive index variation with applied pressure, which in equation (4.16) counter acts the changes in refractive index in the water. An other reason for choosing glass as the transducer material arises from the fact that the acoustic impedance of glass (i.e. the product $\rho_T c_T$) is much greater than that of perspex. This results in far higher acoustic reflection at the boundary, thereby giving a higher pressure at the transducer interface.

4.4 - Prototype experimental transducer

A prototype reflection transducer for measuring acoustic transients has been constructed, the design of which is shown schematically in figure 4.9. The transducer utilised a semicircular perspex (PMMA) block in which a probe beam was reflected from the flat front surface of the block. The front face formed one wall of a cell in which water was placed and acoustic transients were generated within. At the perspex-water interface light was reflected back into the transducer according to the acoustically modified refractive index properties of the media close to the interface, as has been discussed in the last few sections. The reflected light was subsequently detected by a photodiode and recorded on a digital oscilloscope. A photograph of the prototype transducer can be found in appendix three.

The probe beam was generated using a Melles Griot 06DLB102 diode laser, emitting 5mW of light power at a wavelength of 675nm. A reverse telescope arrangement was used to reduce the 3.3x1.0mm output beam and focus it over a distance of 50mm onto the front face of the perspex block. This produced an active sensing area at the perspex-water interface of just 20 μ m by 80 μ m, with a beam divergence of 1.5°x0.45° respectively calculated using equation (4.10). The probe beam arrangement was rotated to give the smallest divergence in the plane perpendicular to the transducer-water interface (that is flat on the page in figure 4.9.) Furthermore the diode laser was also polarised in this direction, and as a result the transducer was designed to follow the reflectance curve for light incident perpendicular to the front face.

Perspex was initially chosen for the semicircular block material because of its transparent optical qualities and its ability to be easily machined. At a later stage the front face of the semicircular block was machined back 1/4 inch and replaced with a glass (HC519604) plate affixed using a PMMA based optical cement. As was suggested in the last section, in order to gain greater sensitivity.

The shape of the perspex block was chosen to allow accurate adjustment of the incident probe beam angle by simultaneous movement of the laser diode and photodiode along the circumference of the block. The angle of the probe beam was adjusted until the reflectance was about 80% of its maximum value, as measured using the photodiode. This was to allow for the possibility of measuring negative pressures or rarefaction waves. The incident angle of the probe beam was about 63.0° when the transducer boundary was fabricated out of perspex ($n_r \sim 1.495$), and 61.3° when the glass ($n_r \sim 1.519$) formed the front face of the transducer.

The electronic drive circuit for the diode laser and the fast photodiode circuit is shown in figure 4.10. The top portion of the circuit on the left was used to drive the semiconductor laser with a constant pre-set current, the optical output of which was constantly monitored on an oscilloscope using the lower circuit which is a photodiode circuit. The circuit on the right of the figure is the high-speed detection circuit which utilised a AEPX65 photodiode [33]. This photodiode was chosen because of its very fast (1ns) response time, low dark current of $\sim 2\text{nA}$, low noise characteristics and high responsivity of $\sim 0.45\text{A/W}$ at 675nm. A 5mm focal length $f/1.6$ lens was fitted in front of the photodiode to reduce the need for positioning accuracy, together with an infrared absorbing filter to remove some of scattered light from the Nd-YAG laser light cavitation source used in the following experiments. The resulting voltage across the 50Ω resistor was typically around 35mV and was recorded on a Tektronix 5200 oscilloscope set to 50mV range, with a sampling time of 2ns.

4.5 - Calibration

The perspex transducer was calibrated with a variety of input refractive indices using several concentrations of Sodium Chloride solution from pure (de-ionised) water up to 3.5 grams NaCl per litre of water. Figure 4.11 shows the measured reflectances plotted against the refractive index for the different solutions, as calculated using values quoted in reference [34]. These are also plotted with reflectance curves calculated for several incident beam divergences. Note that these graphs have been plotted for static pressure conditions and do not include the effects of acoustic transmission and reflection at the transducer boundary.

It is clear from figure 4.11 that within the limitations of experimental error the transducer behaves in a very similar manner to that predicted for a probe beam divergence $\Delta\theta$ of 0.5° . This compares rather well with the calculated beam divergence of 0.45° , and any small deviations are probably due to probe beam aberrations since the diode laser light is not spatially filtered. By including the effects of acoustic reflection discussed in section 4.3.3, calibration curves have been calculated for the perspex and the glass fronted prototype transducers. These are shown in figure 4.12 and have been calculated as a function of the peak acoustic pressure of an incident acoustic transient. It was assumed here that the probe beam divergence of the glass fronted transducer remained unchanged at 0.5° . It can clearly be seen that glass fronted transducer is much more sensitive than the perspex transducer. The perspex transducer however exhibits a much more linear response over the -100 to 300bar range, whereas the glass transducer has an

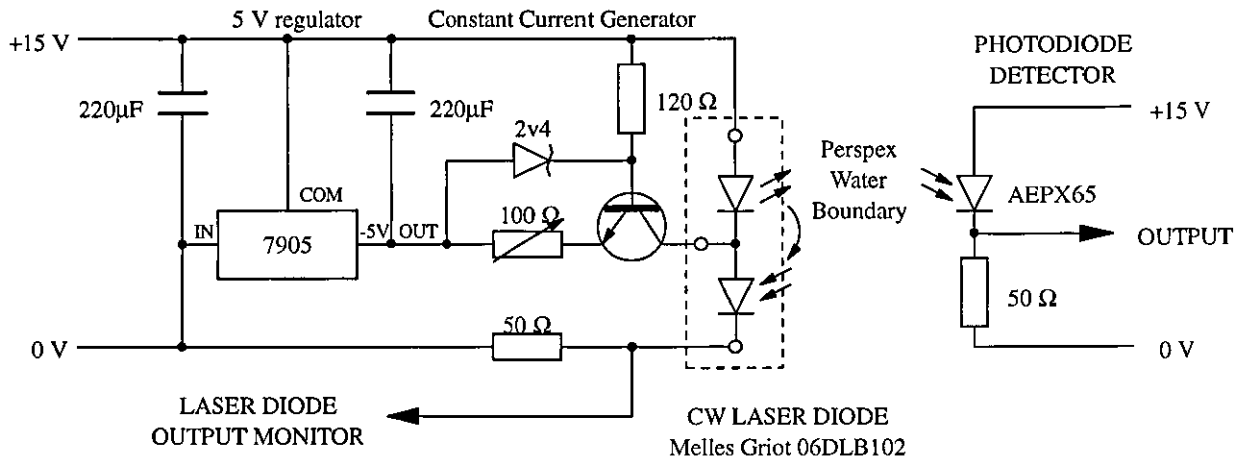


Figure 4.10 - CW laser diode driver, monitor and detector photodiodes.

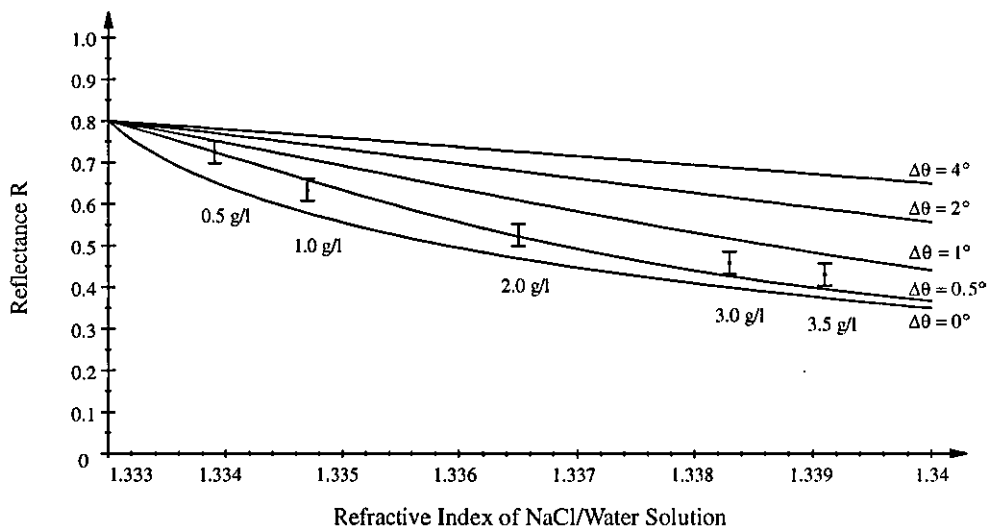


Figure 4.11 - Calibration using measured reflectance with NaCl solution concentration.

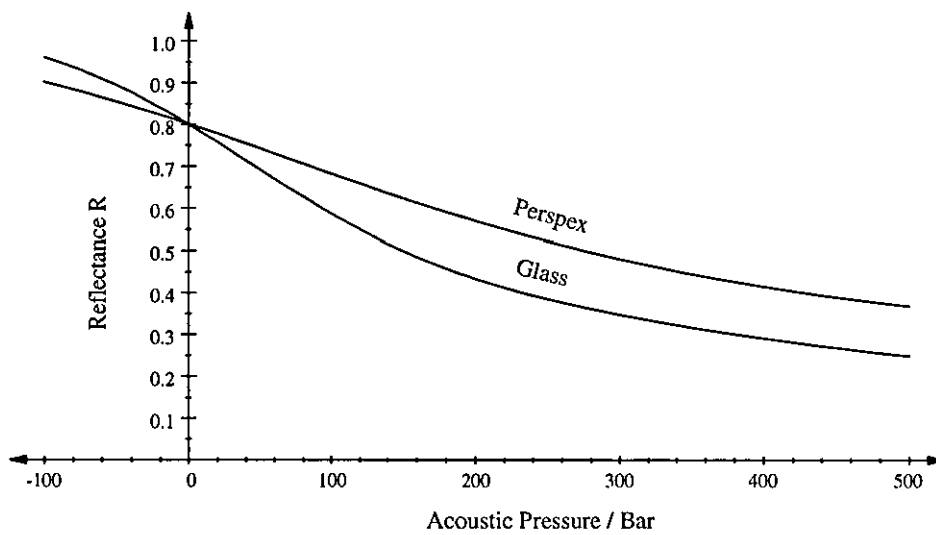


Figure 4.12 - Calculated reflectance as a function of acoustic pressure.

approximately linear response only in the range 0-100bar, after which the response is non-linear and begins to fall off.

4.6 - Experiments with the perspex transducer

To test the capabilities of the prototype transducer fabricated out of perspex, an experiment was performed to detect acoustic transients originating from optical cavitation. Laser cavitation was created in the water cell using radiation pulses from a Nd-YAG laser at an energy of 55mJ, pulse duration of 30ns, and wavelength of 1060nm. The light was focused in the water down to a spot 25 μ m in diameter using a 25mm f/1.5 lens, and during each event dielectric breakdown occurred in the focal region resulting in a high temperature plasma being formed. The plasma would then expand rapidly producing an initial acoustic transient together with a cavitation bubble, both of which are spherically symmetric about the focal point. The bubble then undergoes one or more large amplitude radial oscillations lasting for up to about 0.5ms before finally breaking up, and further acoustic transients are emitted during every collapse of the cavitation bubble. The optical cavitation source was chosen because of its good repeatability and because similar sources have been quantitatively characterised using other techniques such as Mach-Zehnder interferometry [3-5,35].

The optical cavitation events were generated in the water cell at varying distances of between 0.9mm and 12.7mm away from the front face of the transducer. Figure 4.13 shows twelve superimposed output signals from the transducer recorded for the initial acoustic transients generated by the dielectric breakdown at different distances away from the perspex-water interface, which are noted below the respective peaks together with the peak pressures which are deduced from the calibration curve in figure 4.12. The reflectances were recorded by measuring the voltage output from the photodiode circuit on a Tektronix TDS520 oscilloscope, at a sampling rate of 500 megasamples per second. These traces were then simply rescaled to give reflectance, using the nominal reflectance value which was pre-set earlier to 80% by adjusting the probe beam angle of incidence. The minimum resolvable pressure above the r.m.s. noise limit of ~1% (reflectance) was found to be approximately 8bar.

It can clearly be seen that initially the measured reflectance rises well above the 100% mark and saturates the photodiode. This is infact due to Nd-YAG laser light which is scattered from the plasma and is not entirely removed by the heat reflecting filter placed in front of the photodiode. It is not due to any changes in reflectance caused by acoustic

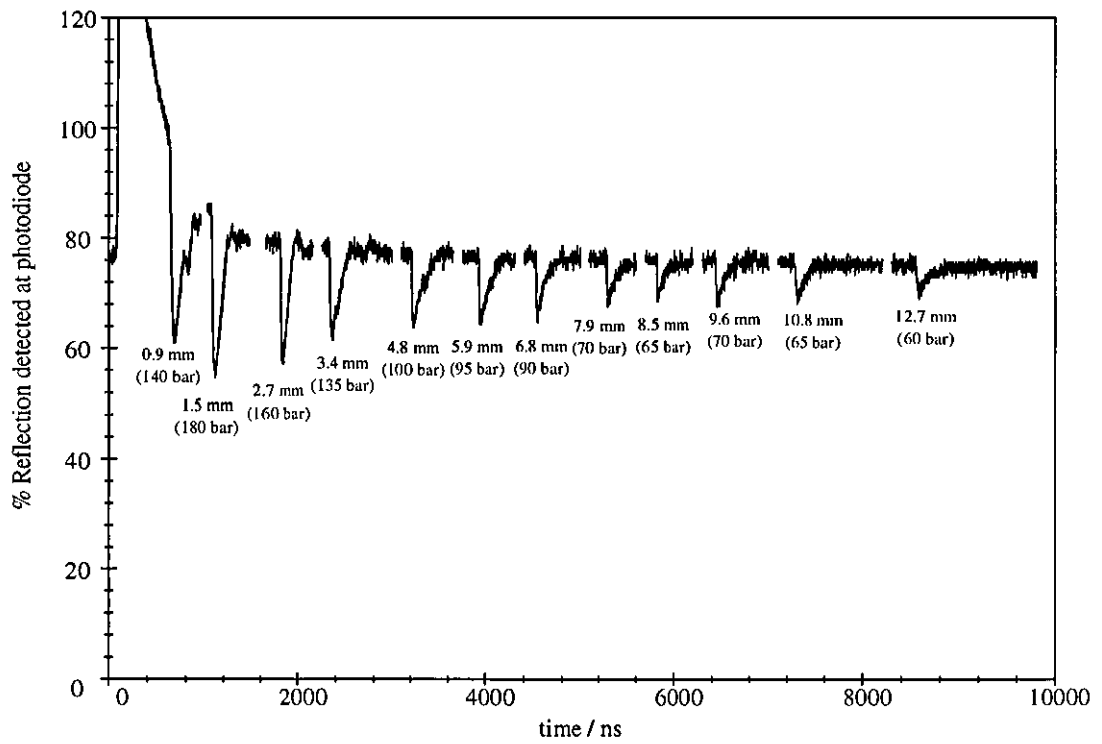


Figure 4.13 - Perspex opto-transducer varying distance from event

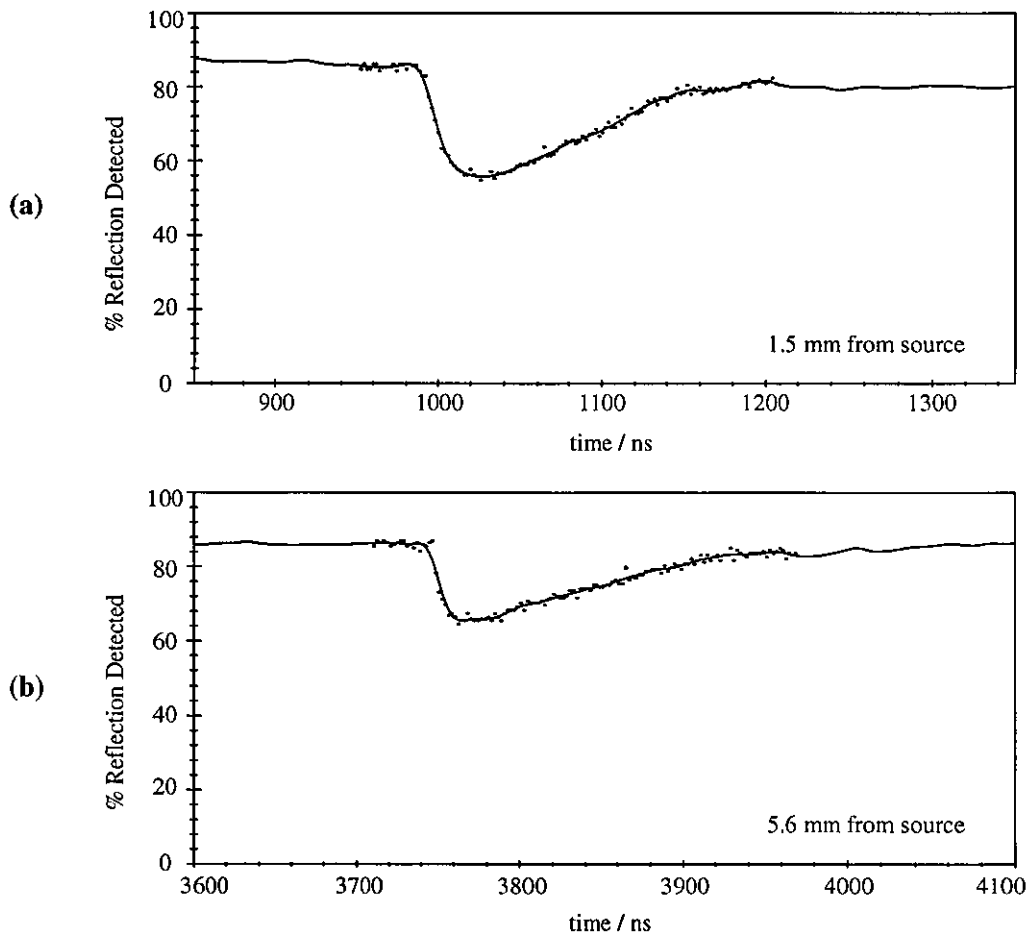


Figure 4.14 - Expansion of figure 4.13 showing fast shock rise times.

transient phenomena. Even though the Nd-YAG laser pulse has a duration of 30ns, the measured positive going "reflectance" pulse lasts for about 600ns and affects the first few measurements of acoustic transients made thereafter. This is because the Nd-YAG laser pulse saturates the photodiode which then requires several hundred nanoseconds to recover.

The measured acoustic transients are shown to the right of Nd-YAG pulse as a number of negative going peaks which are superimposed upon the graph together for convenience of presentation. Normally any one of the recorded reflectance traces would consist of the Nd-YAG pulse followed a short time later by a single negative going pulse, and at all other times the reflectance would remain at about 80%. The distance of the source from the transducer shown below each peak was calculated using the time delay between the initial rise of the Nd-YAG laser pulse and the arrival of the acoustic transient. It was assumed here that the acoustic transients travelled at a velocity very close to that of the speed of sound, which is 1500ms^{-1} for water.

From figure 4.13 it can clearly be seen that the peak pressures measured with the aid of the calibration curves calculated earlier (figure 4.12) diminishes with the distance of the transducer from the source. Experimentally it was observed that for any one source distance successive peak pressures measured could vary by as much as 20% from those shown here. Upon plotting the peak pressures on a log scale, as in figure 4.15, it can be seen that within the limits of experimental error the peak pressure broadly agrees with the inverse distance relationship observed by Ward [3,5] using high speed Mach-Zehnder interferometry. Departures from this relationship can be seen for small transducer to source distances. It is thought that this can be explained entirely by misalignment of the transducer's sensitive area with the acoustic source, so that the spherical acoustic transient is incident obliquely upon the transducer.

Figure 4.14 shows trace expansions of two of the measured acoustic transients in figure 4.13, one generated at a distance of 1.5mm from the transducer, and the other at 5.6mm. Each point plotted represents a sample made every 2ns, and the superimposed solid line has been fitted using the least squares method to remove some of the noise. Clearly the two transients shown are completely resolved and are about 200ns in duration. The temporal profile of the transients agrees with results obtained by Vogel using piezoelectric and optical transducers [35], and also by Ward using high speed Mach-Zehnder interferometry [3,5]. Furthermore the initial shock front appears to have been completely resolved for both acoustic transients measurements. The rise times calculated as a 10% to 80% fall in the signal are $\sim 12\text{ns}$ and $\sim 6\text{ns}$ for the transients shown in figure

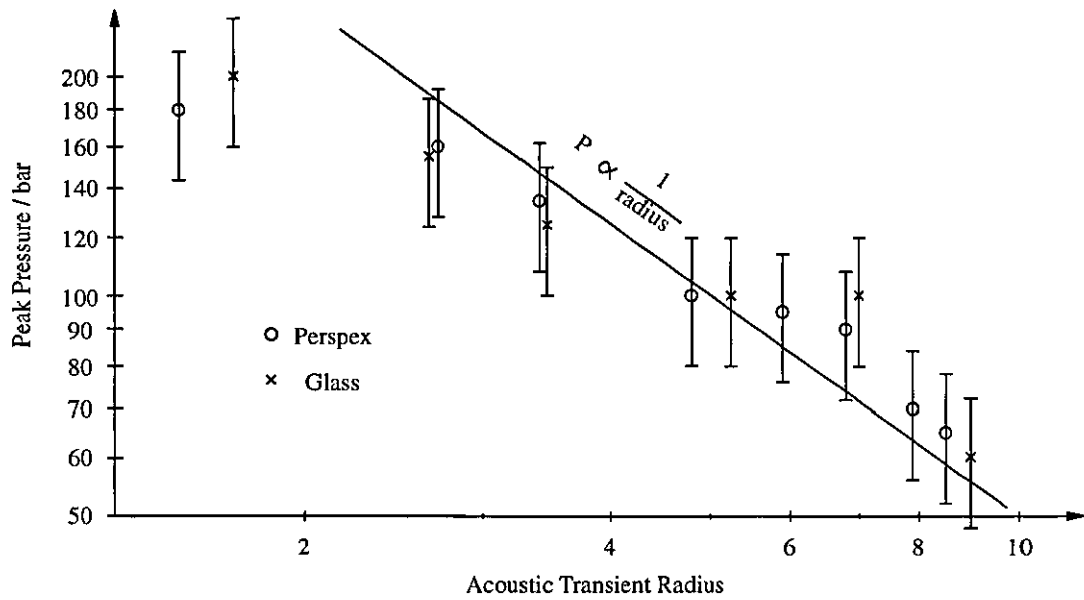


Figure 4.15 - Log scale plot of peak pressure recorded with acoustic transient radius.

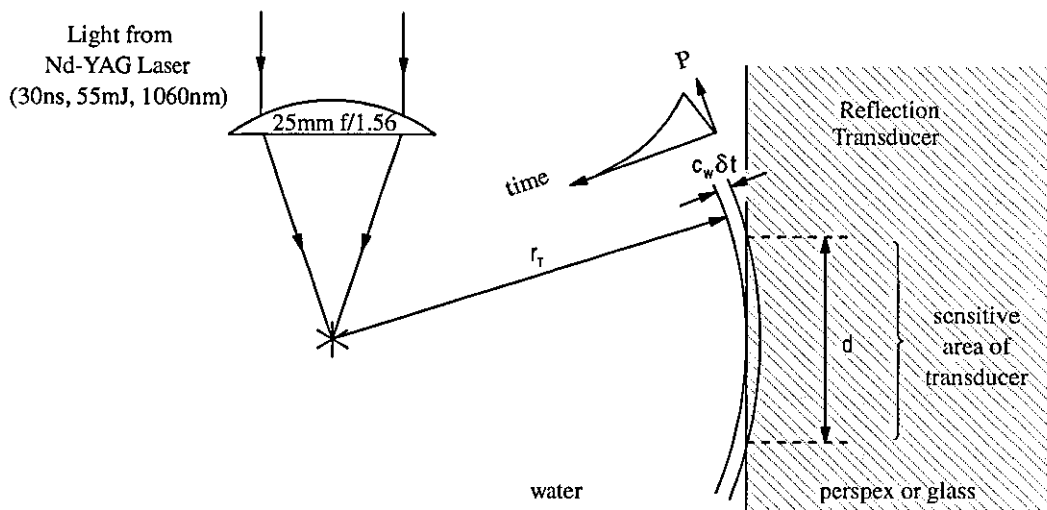


Figure 4.16 - The effect of acoustic wavefront curvature on the transducer time response.

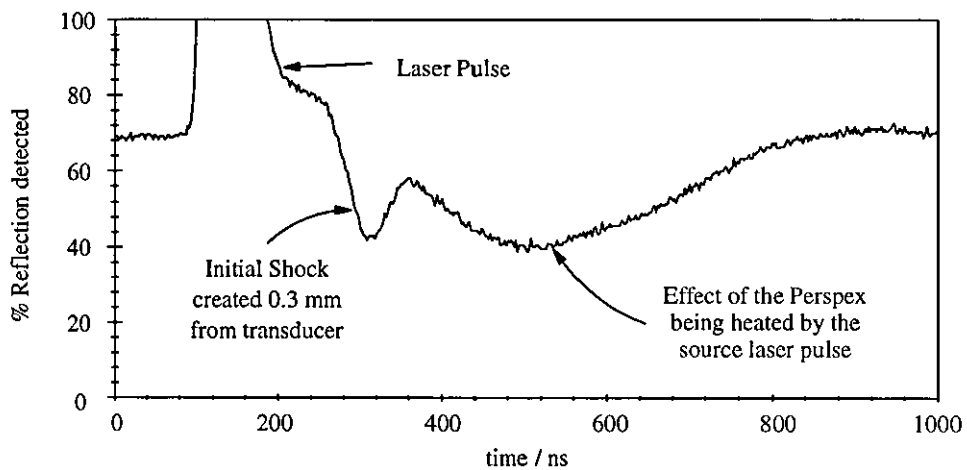


Figure 4.17 - Effects observed when source laser light strikes perspex transducer.

4.14(a) and (b) respectively. From this it can be deduced that the marginally slower rise time of the transient in figure 4.14(a) means that this transient is less developed than the one measured in figure 4.14(b), which has travelled a greater distance.

Clearly the large wavefront curvature on the spherical acoustic transient should have an effect upon the rise time of the transducer. From figure 4.16 it can be seen that this is influenced by two factors, firstly by the radius of the incident transient and secondly by the size of the active area of the transducer. The rise time can be calculated by simply finding the time difference δt between when the transient initially reaches the transducer face, and when the last part of the transient at the same radius r_t leaves the sensitive region of the transducer. That is:

$$\delta t = \frac{\left(r_t^2 + d^2/4\right)^{1/2} - r_t}{c_w} \approx \frac{d^2}{8 r_t c_w} \quad - (4.19)$$

Given that maximum dimension of the transducer sensitive area is about $d=80\mu\text{m}$, then for transients propagating close to the speed of sound ($c_w=1500\text{ms}^{-1}$) generated at the closest distance of $r_t=0.9\text{mm}$ from the front face the rise time is extended by just 0.6ns. Clearly given the 200ns duration of the transients, and minimum 10ns duration of the shock fronts, the wavefront curvature has very little effect upon the temporal pressure profiles which have been measured. Furthermore the temporal resolution is also limited by the reflectance properties across the interface, which are controlled by the refractive index within approximately a wavelength either side of the boundary. The probe beam has a wavelength of 670nm, and the sound speeds either side of the water-perspex boundary are 1500ms^{-1} and 2700ms^{-1} respectively. For an acoustic transient propagating across the interface this gives rise to an increase in the rise time of the transducer of about 0.7ns. Combining the effects of wavefront curvature, reflectance properties across the interface, and the response time of the photodiode, the transducer has a temporal resolution of approximately 2ns.

Finally the effects of heating in the perspex can be seen in figure 4.17, where the Nd-YAG beam has been focused obliquely onto the surface of the transducer close to the sensitive area. Clearly the thermal pulse is relatively long in duration compared with the acoustic transient seen 200ns after the Nd-YAG pulse.

4.7 - Measurements made by glass fronted transducer

As explained in section 4.4, the front face of the semicircular perspex block was machined back 1/4 inch and replaced with a glass (HC519604) plate which was affixed using a PMMA based optical cement. This theoretically provides an improved reflectance sensitivity to incident acoustic transients, firstly because glass has an almost negligible change in refractive index due to pressure giving rise to a greater response in equation (4.16), and secondly because glass has a higher acoustic impedance than perspex giving rise to larger pressures at the water-transducer interface (section 4.3.3, equation (4.18)). The change in material does not however affect the temporal resolution of the device, which remains limited primarily by the ~ 1 ns rise time of the photodiode detector. Furthermore it does not change the spatial resolution of the device, the active area of the transducer remains at $20\mu\text{m}$ by $80\mu\text{m}$.

4.7.1 - Acoustic transients

In order to assess the performance of the glass fronted transducer experimentally, spherically symmetric acoustic transients generated by the same Nd-YAG laser set-up described in section 4.6 have been measured. The results obtained are shown in figure 4.18. As before the reflectance traces for 7 different acoustic transients measured using the device have been edited and are superimposed together here on one graph. Again the distances between the point source and the front face of the transducer are shown below the respective negative going reflectance peaks. In addition the peak pressures for these peaks using the calibration curve in figure 4.12 are also shown. Furthermore a 20% fluctuation in peak pressure was observed for several successive acoustic transients measured at any one distance.

It can clearly be seen in figure 4.18 that for a transient measured at any one distance, the fall in reflectivity is substantially greater than that measured earlier using the perspex fronted transducer. Upon plotting the peak pressures on a log scale with those measured by the perspex transducer, as in figure 4.15, it clear that the recorded pressures from both transducers have good agreement over a range of source distances. In the case of the glass fronted transducer however, the smallest resolvable pressure above the r.m.s. noise limit of $\sim 1\%$ (reflectance) is about 4.5bar, which is 75% better that achieved by the perspex transducer and is entirely due to the improvements in sensitivity made using the glass interface.

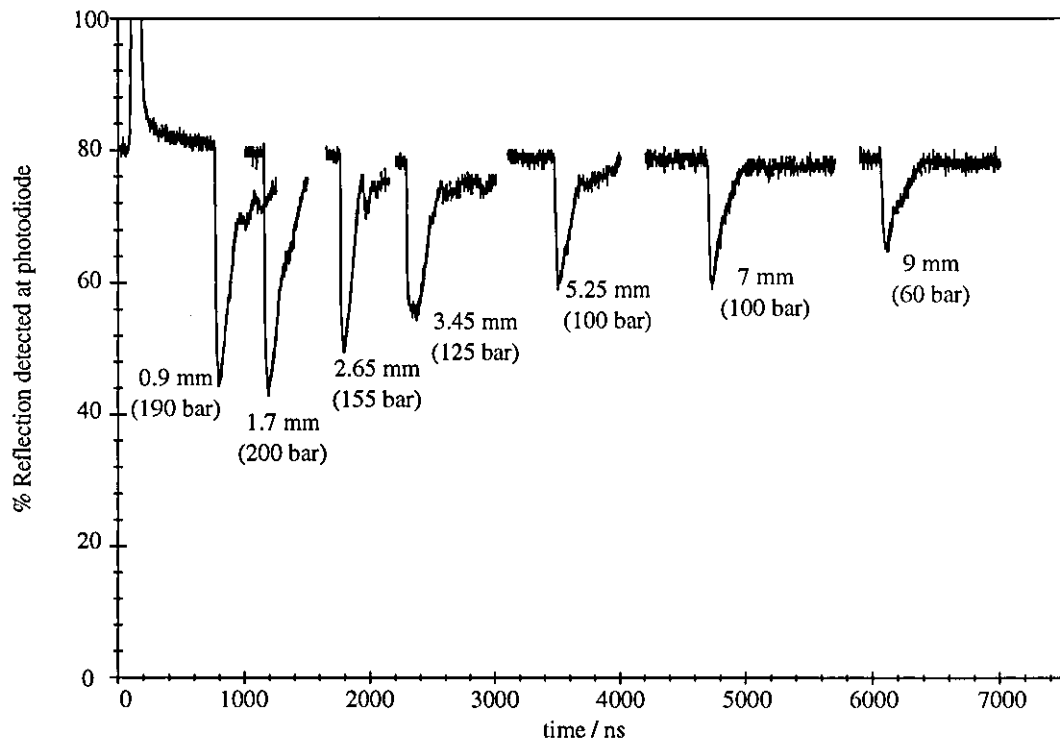


Figure 4.18 - Glass opto-transducer varying distance from event.

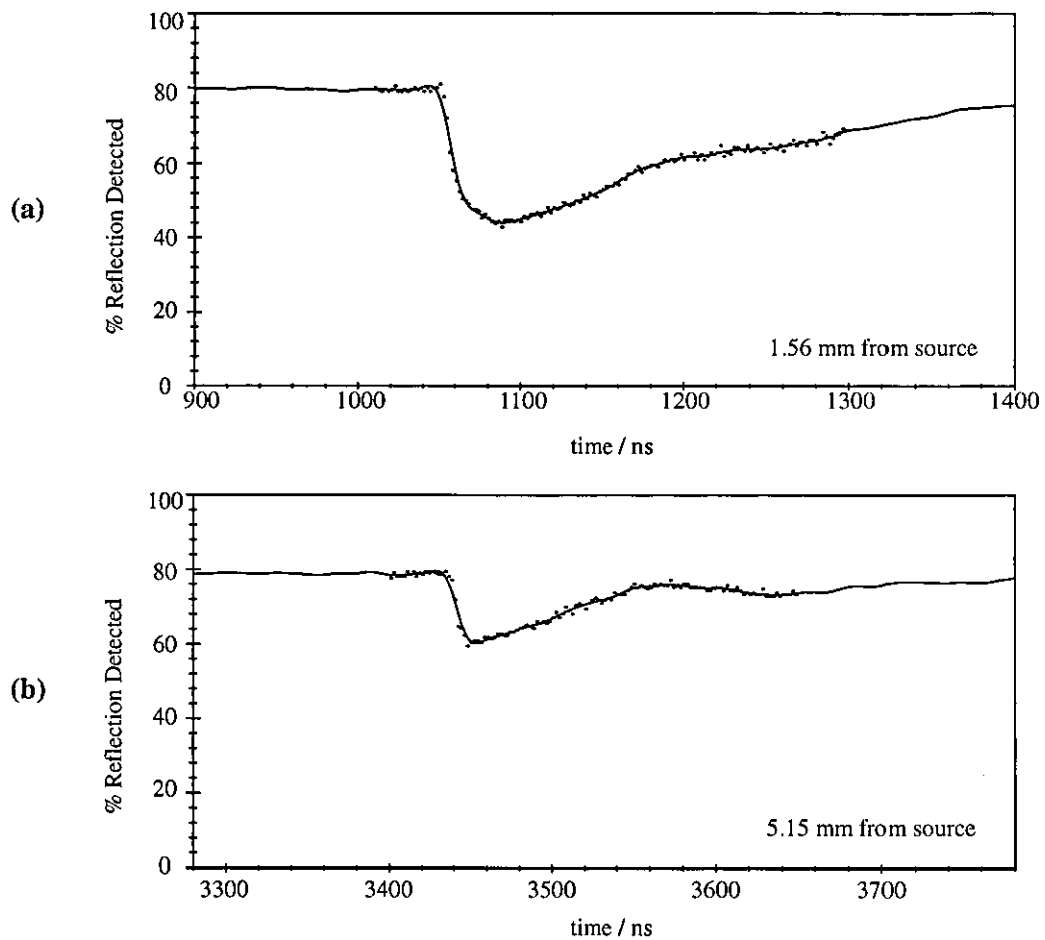


Figure 4.19 - Expansion of figure 4.18 showing fast shock rise times.

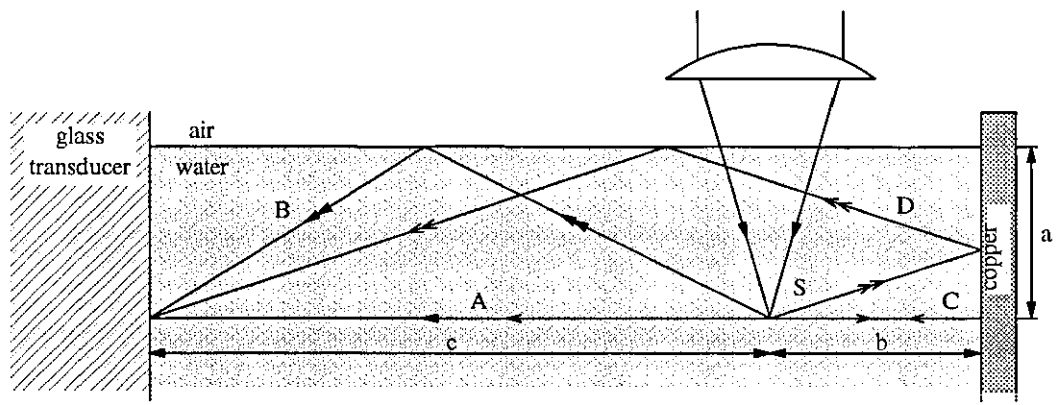
Finally figure 4.19(a) & (b) shows trace expansions of two of these transients generated at 1.56mm and 5.15mm from the transducer respectively. It can clearly be seen that the temporal profiles of the transients remain essentially unchanged from those measured using the perspex transducer, despite the relatively non-linear response of the glass transducer above 100bar. Furthermore the rise times of about 10ns and 4ns for transients in figure 4.19(a) & (b) respectively are also the same. Clearly the transient measured at the smaller radius is relatively undeveloped compared with the one measured at the larger radius, as was found using the perspex transducer. As a result it can be said that the glass fronted transducer should have many applications in the investigation of acoustic transient development in water.

4.7.2 - Negative or rarefaction waves

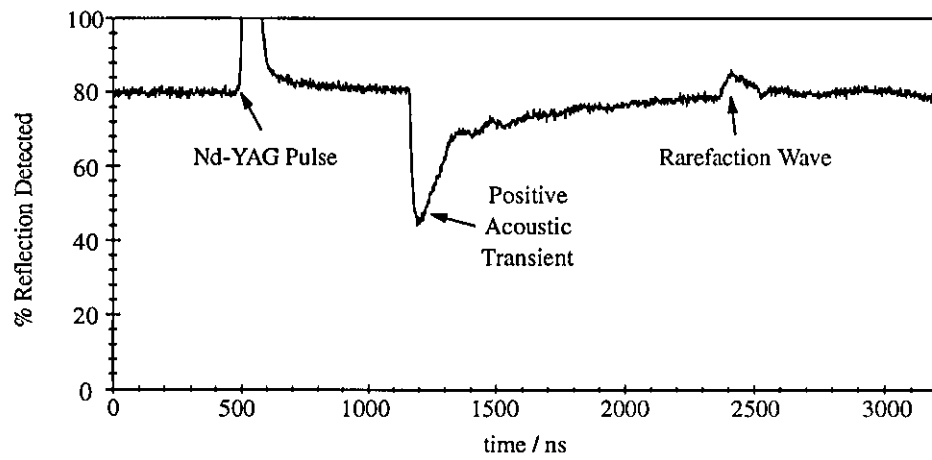
The glass fronted transducer has also been used to detect negative, or rarefaction, waves generated by the Nd-YAG laser acoustic transient source described. The rarefaction waves are produced very simply by reflecting the spherical acoustic transients off of the top water-air interface, as shown schematically in figure 4.20(a). As predicted by equation (2.20), phase inversion or negation of the wave occurs at the interface because the impedance of air ($Z_{\text{air}} \sim 430 \text{kgm}^{-2}\text{s}^{-1}$) is almost negligible compared with that of water ($Z_{\text{water}} \sim 1.5 \times 10^6 \text{kgm}^{-2}\text{s}^{-1}$).

Figure 4.20(b) shows a large amplitude acoustic transient measured by the glass transducer, as before, followed by a much smaller amplitude positive going peak which is the rarefaction wave. After generation at the source S in figure 4.20(a), the initial positive acoustic transient has here travelled the direct path A. Whereas a different part of the same spherical wave has travelled path B, has undergone phase inversion at the top water-air interface, and has given rise to the rarefaction wave detected later. Clearly the rarefaction wave has a smaller amplitude than the positive acoustic transient. Using the calibration graph in figure 4.12 the peak pressure has been measured here to be about -50bar. This is partly due to the fact that the rarefaction wave has travelled a greater distance than the positive acoustic transient, however it is also due to the rarefaction wave being incident upon the transducer obliquely.

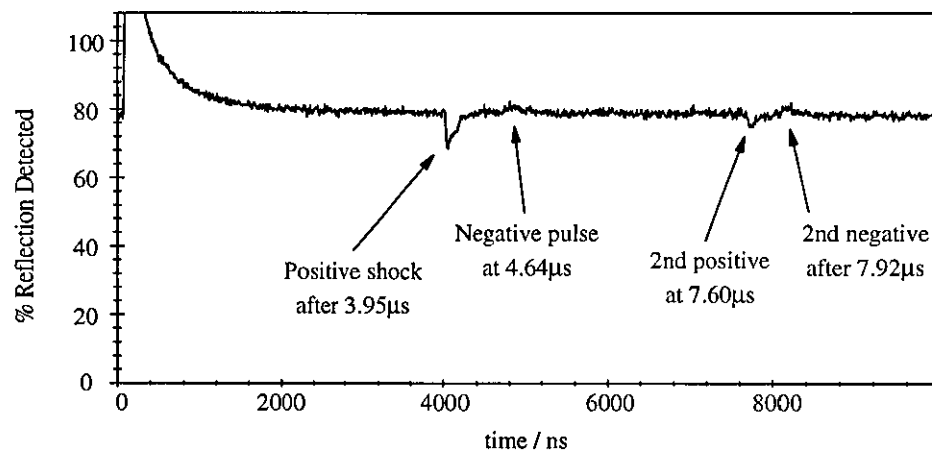
It is also clear that the rise time of the rarefaction wave is very much longer in duration than that of the positive acoustic transient. This is for two reasons: firstly that the wave is incident upon the transducer obliquely, and secondly the negative pressure acts upon the wave propagation to slow more negative parts of the wave. Eventually the negative



(a)



(b)



(c)

Figure 4.20 - Reflection of acoustic transients off of water-air and water-copper boundaries.

pressure will produce a positive going shock wave at the tail of the rarefaction wave, and this can just be identified at the end of the wave.

Reflections have been observed from a water-copper boundary and are seen in figure 4.20(c). In this case the acoustic impedance of copper ($Z_{\text{copper}} \sim 42.5 \times 10^6 \text{kgm}^{-2}\text{s}^{-1}$) is substantially higher than that of water, so equation (2.20) predicts that the incoming acoustic wave will be almost entirely reflected, and the resulting wave will be of the same phase as the incident wave (i.e. not inverted). As before the initial positive pressure acoustic transient is detected first having travelled the direct path A. A rarefaction wave is then detected which has travelled path B, followed later by a further positive wave which has travelled path C having been reflected off of the rear water-copper boundary. Finally a second rarefaction wave is detected which has travelled path D, having been reflected off of the rear water-copper boundary and the top water-air interface where has undergone phase inversion.

4.7.3 - Cavitation bubble phenomena

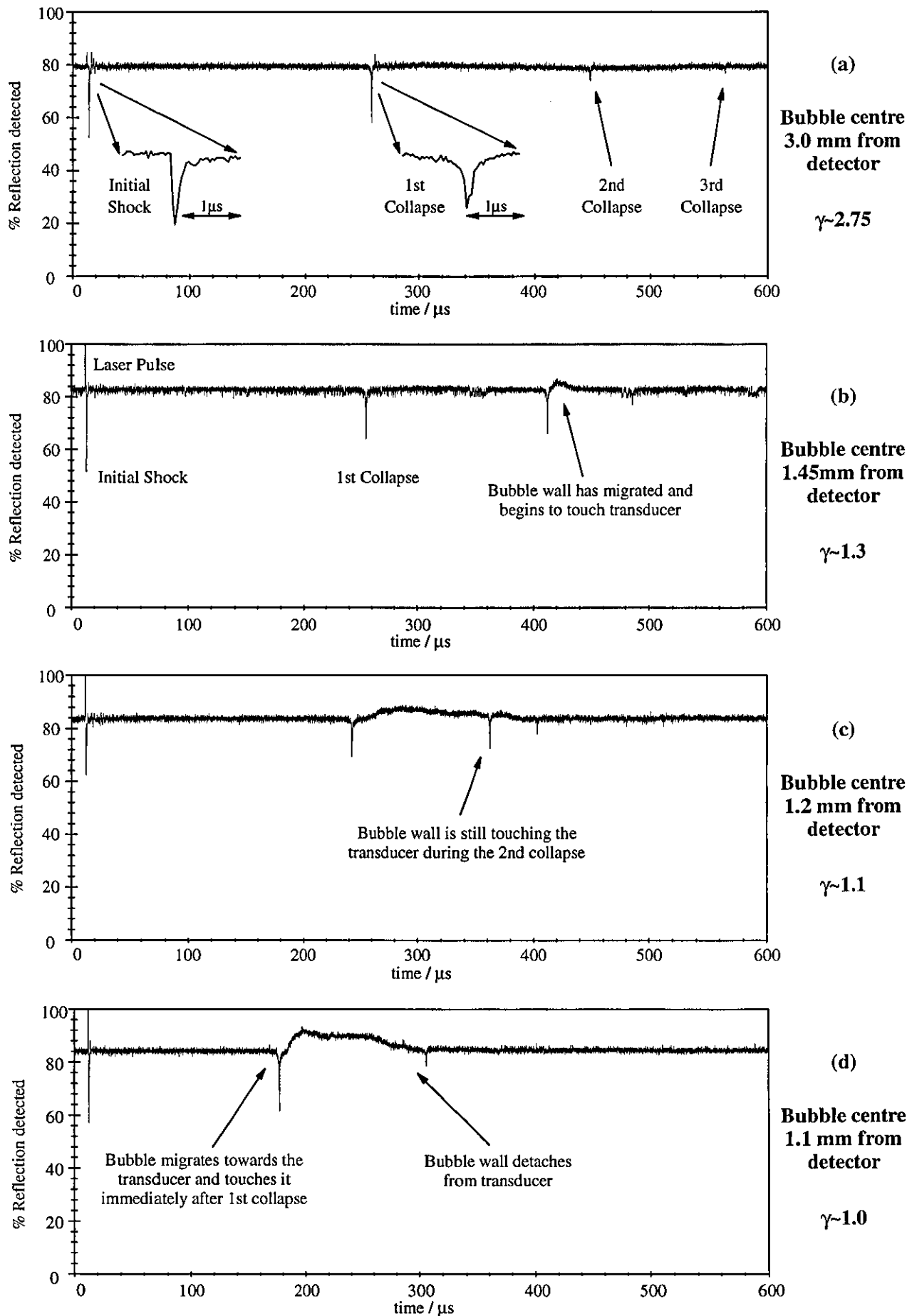
It has already been explained in section 4.6 that after the generation of the plasma in the water by laser assisted dielectric breakdown, a spherical cavitation bubble is produced which under free conditions then undergoes several cycles of expansion and collapse, producing further acoustic transients during each collapse. In recent years the study of cavitation bubble phenomena close to solid boundaries has attracted great interest because such bubbles are known to cause considerable damage to the solid under certain conditions. The mechanisms behind this damage are little understood, however through high speed photographic studies [36] the bubbles are known to undergo asymmetric collapse in which the bubble is initially attracted towards the boundary by Bjerknes force [36]. The bubble then collapses into an annular "donut" shape, where parts of the bubble which are initially furthest from the boundary are observed to collapse quicker than those close to the boundary. Furthermore the parts of the bubble furthest from the solid are also seen to form a narrow water jet which travels through the centre of the annulus and strikes the solid with great velocity. This is phenomena is sometimes termed *water hammer*, and is thought to be the major mechanism involved in the damage of the solid. Until very recently [37] very little experimental evidence has been found of high stresses which are directly attributable to water hammer. Infact the only stresses detected upon the surface of the solid has been due to acoustic transients associated with the collapse of the bubble, which on their own are thought not to be sufficiently intense to cause damage the solid.

A key factor in the study of cavitation bubble collapse close to solids is the value of γ , which is defined as the ratio between the initial distance of the source away from the surface and the maximum radius which the bubble achieves during its cycles of expansion and collapse. The prototype glass fronted optical transducer has been used to study cavitation bubbles generated by the focused Nd-YAG laser source close to a flat solid surface for a number of different γ values. This was done by keeping the energy of the Nd-YAG laser pulses constant at 55mJ (1060nm wavelength, 30ns duration) which consistently created bubbles which reached a maximum diameter of approximately 1.1mm (± 0.1 mm). Different values for γ were then achieved by varying the position of the source relative to the transducer.

Figure 4.21 shows the reflectance trace recorded experimentally for a variety of different values for γ and source distances. In figure 4.21(a) the acoustic transients arising from the first, second and third bubble collapses can be clearly identified for a source to transducer distance of 3mm ($\gamma \sim 2.75$), together with the initial transient. Clearly from the acoustic transient emission it can be said that the bubble undergoes three definite radial oscillations lasting just over 500 μ s before finally breaking up, the period of the first cycle being around 250 μ s. The acoustic emission recorded becomes weaker with each subsequent collapse which confirms that the cavitation bubble undergoes damped oscillations. Using the calibration curve (figure 4.12) the peak pressures have been measured to be 140bar, 100bar, 30bar and 15bar for the initial acoustic transient, first, second and third collapses respectively. Again it was observed experimentally that the peak pressures fluctuated by up to 20% for any one source-transducer distance.

A magnification of the reflectance trace around the first collapse is shown in figure 4.22(a). Each measurement point plotted represents a sample made every 40ns, and the solid line is a polynomial which has been fitted using the least squares method to remove some of the noise. It is clear that the pressure profile of the acoustic transient associated with the first collapse has temporal symmetry. Both the rise and fall times of the signal have been measured here to be typically about 80ns, the whole transient being approximately 300ns in duration. This is in agreement with results obtained using high speed Mach-Zehnder interferometry by Ward [38]. Clearly the rise time of this acoustic transient is substantially slower than that of the initial acoustic transient which was characterised earlier.

Using the temporal pressure profiles obtained, the energies of the transients have been calculated applying the following formula [3,5]:



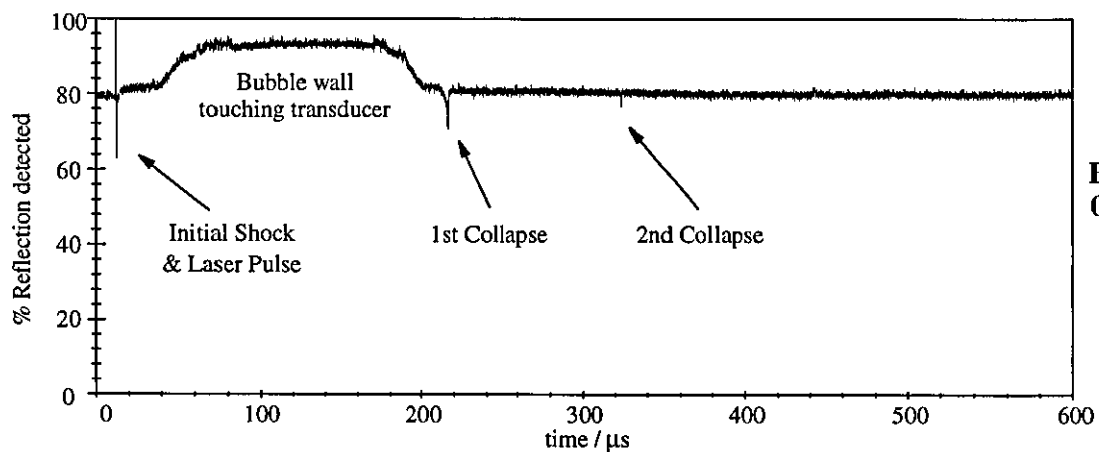
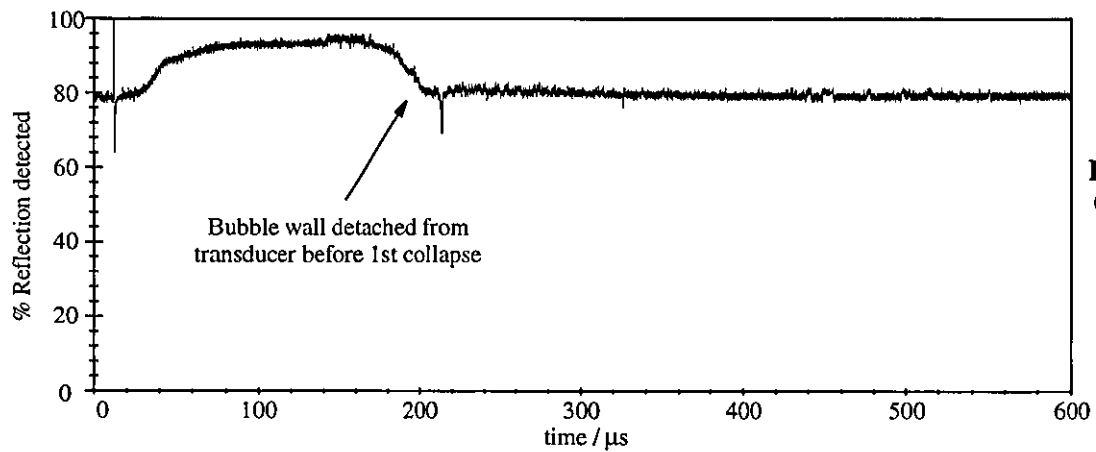
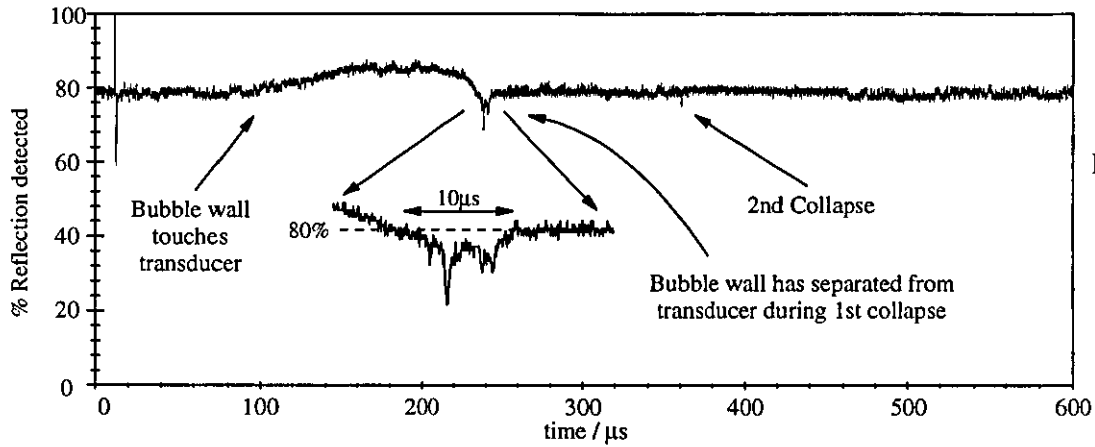
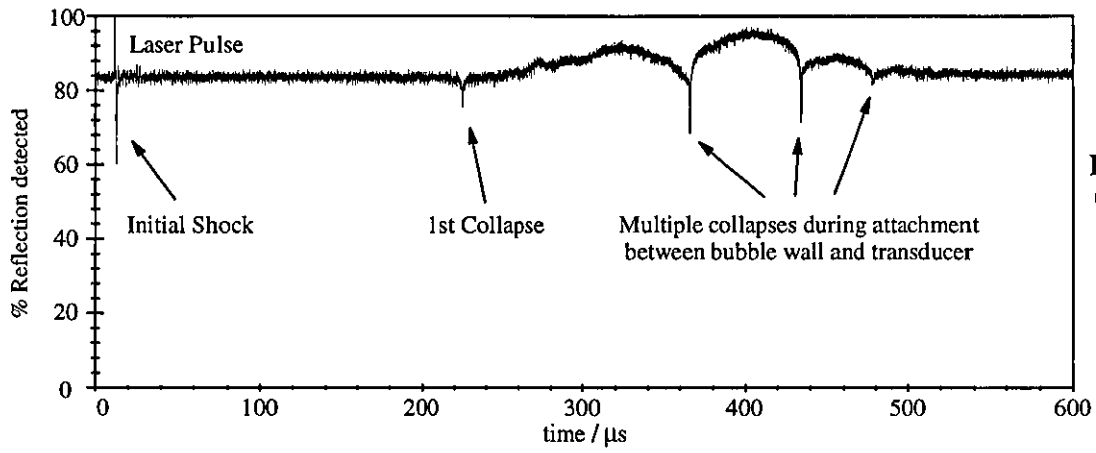


Figure 4.21 (continued) - Bubble detection at varying distances from the source.

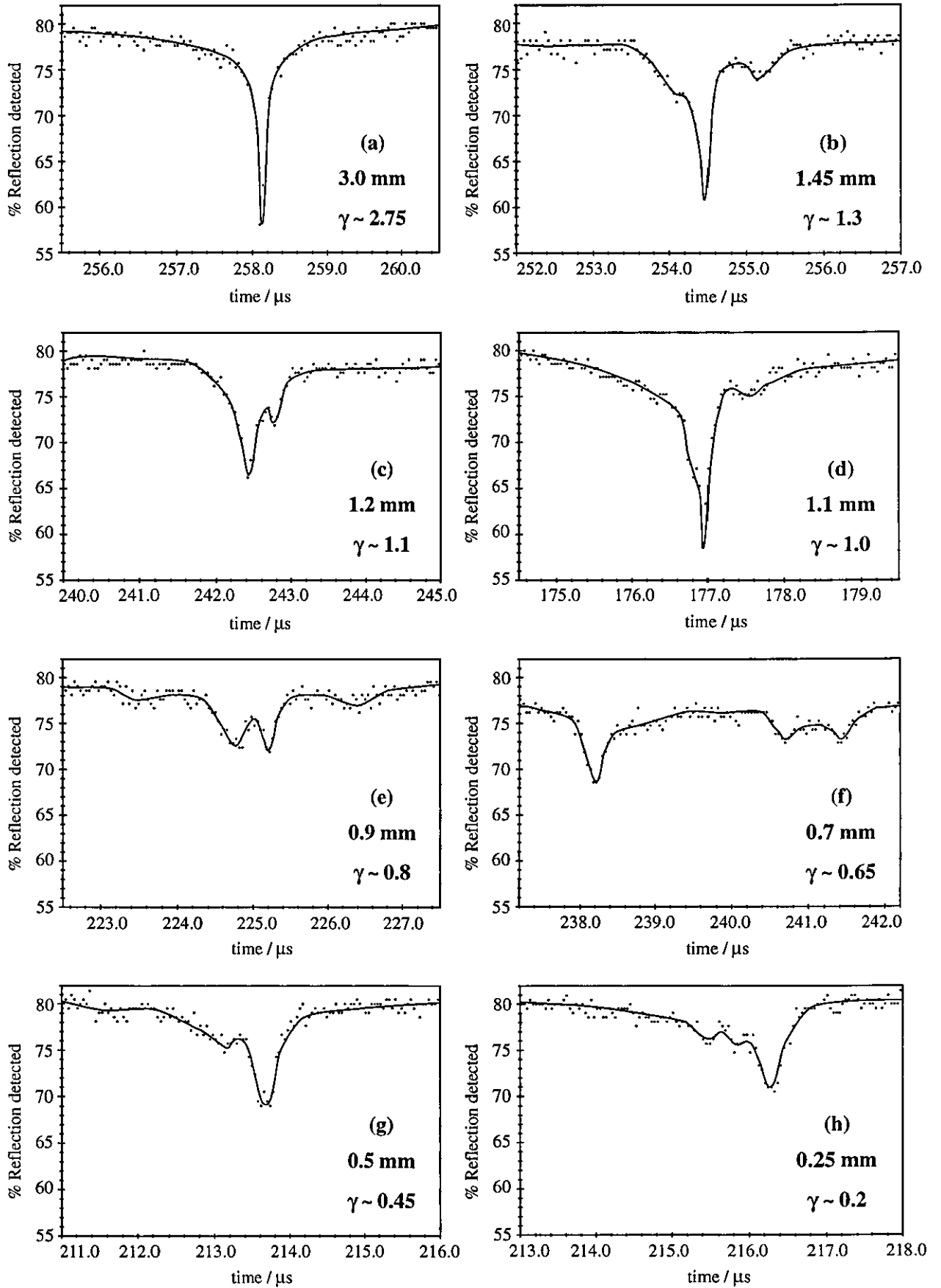


Figure 4.22 - Detection of acoustic transients during the 1st collapse of cavitation bubbles.
 (Taken from figures 4.21(a-h) respectively; each point represents a 40 ns sample)

$$E = \frac{4\pi r^2}{\rho c_w} \int P^2 dt \quad - (4.20)$$

This equation is a direct result of equation (2.11c) for spherically symmetric acoustic waves where the term $4\pi r^2$ is the surface area of the spherical acoustic transient, and the ρc_w term is the acoustic impedance of the water. The resulting energies have been calculated to be about 1.25mJ, 0.60mJ, 70 μ J and 17 μ J ($\pm 40\%$) for the transients associated with the initial event, first, second and third collapses respectively. This gives a total acoustic energy emitted of about 1.95mJ ($\pm 40\%$), which is just 3.5% of the energy provided by the 55mJ Nd-YAG laser pulse. The remainder of the incident laser energy was either not absorbed by the water or was dissipated throughout the volume of the liquid as heat.

A total energy of about 687 μ J ($\pm 40\%$) was emitted as the acoustic transients associated with the bubble collapse alone. This can be compared with the energy of the cavitation bubble which can be estimated using [3,5,35]:

$$E = \frac{4}{3}\pi (P_0 - P_v) r_b^3 \quad - (4.21)$$

where r_b is the maximum radius that the bubble achieves, P_0 the external static (atmospheric) pressure of 10⁵Pa, and P_v is the liquid vapour pressure within the bubble which is almost negligible compared with the external pressure. The maximum bubble radius has been estimated to be about 1.1mm (± 0.1 mm) using figure 4.21(d). Evidence supporting this includes the fact that the bubble begins to touch the front face of the transducer immediately after the first collapse, and also because the time of the first collapse is reduced somewhat. Using equation (4.21) it can then be estimated that the bubble energy is 560 μ J ($\pm 150\mu$ J). Within the limits of experimental error, this gives a remarkably good agreement with the calculated energy emitted by the bubble in the form of acoustic transients. Furthermore this complements the calibration of the transducer, the calibration graph shown in figure 4.12 being shown to be accurate to about 20%.

As the source is brought closer to the transducer, the value of γ reduced to 1.3 as in figure 4.21(b), it can be seen that the reflectance trace begins to rise over a relatively long period of time just after the 2nd collapse. This is not a rarefaction wave but the bubble migrating towards the interface so that it begins to touch the boundary. The bubble has a very low refractive index ($n_{air} \sim 1$) compared with glass, and therefore gives rise to total reflection of the probe beam at the transducer interface. It can also be seen that the reflectance does not reach 100%; this is because a thin film of liquid remains between the

bubble and transducer, which gives rise to frustrated total internal reflection at the transducer interface. Detection of the bubble wall touching the interface is hampered somewhat by misalignment of the bubble centre and the sensitive area of the transducer. This is partly due to the small distances involved and the associated difficulty of positioning the transducer, random instabilities in the laser beam, and also the bubble beginning to float upwards towards the water-air boundary.

When γ is about 1.1, as in figure 4.21(c), the bubble touches the transducer shortly after the first collapse and remains attached to the transducer even during the second collapse. In figure 4.22(c) a double peak structure can be seen to develop for the acoustic transient associated with the first collapse, and the main peak becomes smaller compared with that measured for $\gamma \sim 2.75$. Both effects are thought to be associated with the cavitation bubble losing its symmetry so that it does not collapse to a single point but into a more complicated pattern.

As γ is reduced further to unity the bubble is observed to touch the boundary immediately after the first collapse, which occurs unusually early $180\mu\text{s}$ after the Nd-YAG laser pulse. This is shown in figure 4.21(d). The bubble is also seen to detach itself from the transducer interface just before the second collapse.

An interesting result was recorded for $\gamma \sim 0.8$ and is shown in figure 4.21(e). The migration of the bubble towards the transducer begins about $40\mu\text{s}$ after the first collapse is detected. In figure 4.22(e) it can be seen that the acoustic transient associated with the first collapse has a double peak structure, both peaks having relatively low peak pressures. The bubble can then be seen to undergo three collapses in $\sim 140\mu\text{s}$ while being very close, perhaps even attached to the transducer. It can also clearly be seen that the second and third collapses emit comparatively intense acoustic transients.

Figure 4.21(f) shows an other interesting reflectance trace recorded for a cavitation bubble generated at $\gamma \sim 0.65$. In this trace it can clearly be seen that the bubble touches the transducer boundary approximately one third of the way through the first oscillatory cycle of the collapse. The reflectance can then be seen to drop below the nominal 80% zero pressure level for about $10\mu\text{s}$, and several short lived peaks are also detected during this. These short lived peaks are seen in more detail in figure 4.22(f), and are most likely to be due to acoustic transients created by the asymmetric collapse of the bubble. Whereas the relatively long drop in reflectance suggests a sustained build up of stress at the boundary.

This can possibly be attributed to effects observed for the same Nd-YAG source by Jin [36] and also later by Schiffers *et al* [37], who used a combination of high-speed photographic and piezoelectric transducer techniques to study the growth and collapse of similar cavitation bubbles generated close to a surface with $\gamma=0.82$. Using a 52 μm thick, 3mm diameter thin film PVDF transducer attached to the surface, they detected significant stress levels at the boundary which lasted for about 15 μs at the same time as the water jet is seen to form in a high speed schlieren photograph. On top of and close to the beginning of this stress pulse, a single 2 μs duration pressure pulse was detected which was attributed to acoustic transient. Both authors came to the conclusion that the longer duration pulse was caused by fluid travelling through the toroidal shaped collapsing bubble, that is a water jet forming within the bubble and impinging upon the surface. It is thought that the multiple peaks observed here using the prototype optical transducer were not seen by Jin and Schiffers because of the relatively large area, and resulting slow response time for non-planar waves, of the piezoelectric transducer used. Lastly it has been observed in figure 4.21(f), using the prototype optical transducer, that the peak pressure of the acoustic transient created during the second collapse is very small, and this suggests that almost all of the bubble energy has been dissipated during the first collapse.

Finally in figures 4.21(g) & (h) the collapse of cavitation bubbles for relatively small values of γ are recorded. Clearly the bubble wall touches the transducer boundary almost immediately after the generating Nd-YAG laser pulse, however it detaches shortly before the first collapse. Furthermore the bubble is not observed to touch the boundary again which suggests that during the first collapse cycle it bounced off of the surface. In figures 4.22(g) & (h) the reflectance traces show the acoustic transients associated with the first collapse have a single peak structure, however these are not temporally symmetric and possibly have several minor peaks. This is again thought to be due to loss of bubble symmetry during its encounter with the transducer boundary.

Conclusions

A prototype optical reflection transducer has been built to characterise the temporal pressure profile of acoustic transients by measuring the reflectance at a solid-liquid boundary. Initially the transducer was fabricated out of a semicircular perspex (PMMA) block which allowed the design to be assessed and proven experimentally. Theoretical modelling of the transducer showed that the response to acoustic transients was linear with pressure up to about 300bar. Initial experiments were performed which showed the

device to be capable of accurately measuring the pressure profile of incident acoustic transients generated by an optical cavitation event, and able to resolve fully the sub 10ns rise time of the shock fronts. Furthermore the profiles measured using the device agreed with those measured using other quantitative techniques, such as the Mach-Zehnder experiments performed by Ward [3-5].

At a later stage the front face of the perspex block was machined back and replaced with glass which improved the sensitivity of the transducer to changes in refractive index, giving a better signal to noise. It did however have a much more non-linear response to pressure, which was found theoretically to fall off for more intense acoustic transients. In addition to characterising acoustic transients associated with optical cavitation, the device was also capable of detecting rarefaction waves resulting from phase inversion at a water-air interface. Rise times of these negative pressure waves were however found to be much slower because such waves do not build into shock fronts, and also because the waves were measured obliquely.

The asymmetric collapse of laser cavitation bubbles close to a solid boundary has also been studied using the glass fronted transducer. This has been shown great interest in recent years since the mechanisms behind the cavitation damage of solids are not completely understood [36,37]. The migration of the bubble towards the interface was detected here as a rise in the reflectance signal towards saturation. Acoustic transients associated with the collapses of cavitation bubbles were also detected and studied. Furthermore a 10 μ s duration increase in stress at the transducer interface was detected for a bubble which grew to a maximum radius of 1.1mm and was generated 0.7mm from the transducer. This concurs with results obtained by Jin [36] and Schiffrers *et al* [37], who attributed this stress pulse to a water jet forming within the bubble which hits the transducer surface.

Finally an improved design for the optical transducer is shown schematically in figure 4.23. The device is based upon the same principles as the prototype transducers, in which a probe beam generated by a diode laser is partially reflected at a glass-water boundary. In this design however, the boundary is formed out of an equilateral glass (HC519604) prism in which a new front face is machined such that the light is reflected close to the critical angle of the interface. Furthermore the new device allows the probe beam preparation optics and the photodiode to be neatly placed behind the prism. The compact nature of this new design allows the device to be fully enclosed and could be commercially viable as a transducer. Although the device was constructed and

demonstrated to work in principle, time did not permit its use in characterising acoustic transients propagating in water, and this is suggested for further work.

In conclusion the transducer has been shown to be capable of measuring acoustic transients to nanosecond resolution with good sensitivity. Typically the glass fronted transducer had a minimum resolvable pressure of about 20bar (2MPa), and temporal resolution of about 1ns which was limited primarily by the photodiode detector. The device achieved a small sensitive area of just 20x80µm, which was entirely limited by the diffraction limit of the probe beam. Greater sensitivity could have been achieved with a more collimated beam, however at a cost of a larger sensitive area. Conversely a smaller measurement area and hence greater spatial resolution could have been achieved by using a more focused probe beam, but at the cost of sensitivity.

References

- [1] Preston, R. C., Bacon, D. R., Livett, A. J., and Rajendran, K. (1983) - *PVDF Membrane Hydrophone Performance Properties and Their Relevance to the Measurement of the Acoustic Output of Medical Ultrasonic Equipment*, J. Phys. E: Sci. Instrum. **16**, pp786-796.
- [2] DeReggi, A. S., Roth, S. C., Kenney, J. M. and Edelman, S. (1981) - *Piezoelectric Polymer Probe for Ultrasonic Applications*, J. Acoust. Soc. Am. **69**, pp853-859.
- [3] Ward, B. and Emmony, D. C. (1990) - *The Energies and Pressures of Acoustic Transients Associated with Optical Cavitation in Water*, J. Modern Optics **37**, pp803-811
- [4] Ward, B. and Emmony, D. C. (1991) - *Interferometric Studies of the Pressures Developed in a Liquid During Infrared Laser Induced Cavitation Bubble Oscillation*, Infrared Phys. **32**, pp489-515.
- [5] Ward, B. (1991) - *Generation of Acoustic Waves by Focused Infrared Neodymium-Laser Radiation*, PhD Thesis, Loughborough University.
- [6] Davidson, G. and Emmony, D. C. (1980) - *A Schlieren Probe Method for the Measurement of the Refractive Index Profile of Shock Wave in a Fluid*, J. Phys. E: Sci. Instrum. **13**, pp92-97.
- [7] Moffett, M. B., Powers, J. M, and Clay, W. L. (1988) - *Ultrasonic Microprobe Hydrophones*, J. Acoust. Soc. Am. **84**, pp1186-1194.
- [8] Staudenraus, J. and Eisenmenger, W. (1992) - *Fibre-Optic Probe Hydrophone for Ultrasonic and Shock-Wave Measurements in Water*, Ultrasonics **31**, pp267-273.

- [9] Dale, T. P. and Gladstone, J. H. (1858) - *On the Influence of Temperature on the Refraction of Light*, Phil. Trans. Roy. Soc. London **148**, pp887-894.
- [10] Gladstone, J. H. and Dale, T. P. (1863) - *Researches on the Refraction, Dispersion, and Sensitiveness of Liquids*, Phil. Trans. Roy. Soc. London **153**, pp317-343.
- [11] Waxler, R. M. and Weir C. E. (1963) - *Effect of Pressure and Temperature on the Refractive indices of Benzene, Carbon Tetrachloride, and Water*, Journal of Research of the National Bureau of Standards - A. Physics and Chemistry, **67A**, pp163-171.
- [12] Phillips, R. L. (1980) - *Proposed Fiber-Optic Acoustical Probe*, Optics Letters **5**, pp318-320.
- [13] Hecht, E. and Zajac, A. (1974) - *Optics*, Published by Addison-Wesley Publishing Company.
- [14] Partington, J. R. (1953) - *An Advanced Treatise on Physical Chemistry, Volume Four: Physico-Chemical Optics*, Published by Longmans, pp6-21.
- [15] Cariou, J. M., Dugas, J., Martin, L. and Michel, P. (1986) - *Refractive-Index Variations with Temperature of PMMA and Polycarbonate*, Applied Optics **25**, pp334-336.
- [16] Michel, P., Dugas, J., Cariou, J. M. and Martin, L. (1985) - *Thermal Variations of Refractive Index of PMMA, Polystyrene, and Poly(4-methyl-1-pentane)*, J. Macromol. Sci.-Phys., **B25**, pp379-394.
- [17] Houstoun, R. A. (1938) - *A Treatise on Light*, Published by Longmans, Green & Co.
- [18] Eykman, J. F. (1895) - Rec. Trav. Chim. **14**, pp177.
- [19] Lorentz, H. A. (1880), Ann. Physik **9**, pp641.
- [20] Lorentz, L. (1880), Ann. Physik **11**, pp70.
- [21] Harr, L., Gallagher, J. S., and Kell, G. S. (1984) - *NBS/NRC Steam Tables*, Published by Hemisphere.
- [22] Chen, C., Fine, R. A. and Millero, F. J. (1977) - *The Equation of State of Pure Water Determined from Sound Speeds*, J. Chem. Phys. **66**, pp2142-2144.
- [23] Dymond, J. H. and Malhotra, R. (1988) - *The Tait Equation: 100 Years On*, Int. J. Thermophysics **9**, pp941-951.
- [24] Schiebener, P., Straub, J., Leveit Sengers, J. M. H. and Gallagher, J. S. (1990) - *Refractive Index of Water and Steam as a Function of Wavelength, Temperature and Density*, J. Phys. Chem. Ref. Data **19**, pp677-717.
- [25] Waxler, R. M., Horowitz, D. and Feldman, A. (1979) - *Optical and Physical Parameters of Plexiglas 55 and Lexan*, Applied Optics, **18**, pp101-104.
- [26] *Perspex Acrylic Sheet: Technical Service Note PX127*, Produced by the Sheet Group, ICI Plastics Division.
- [27] *HC519604 Data Sheet*, Produced by Pilkington Glass.

- [28] Kaye, G. W. S. and Laby, T. H. (1995) - *Tables of Physical and Chemical Constants*, 16th Edition, Published by Longman.
- [29] Kennedy, G. C. and Keller, R. N. (1972) - *Compressibility*, Section 4d, American Institute of Physics Handbook, 3rd Edition, Edited by Gray, D. E., Published by McGraw-Hill Book Company, pp4-39 - 4-96.
- [30] Bridgman, P. W. (1948) - *The Compression of 39 Substances to 100,00 kg/cm²*, Proc. Am. Acad. Arts Sci. **78**, pp55-70.
- [31] Bridgman, P. W. (1948) - *The Compression of 177 Substances to 40,000 kg/cm²*, Proc. Am. Acad. Arts Sci. **78**, pp71-87.
- [32] Barker, L. M. and Hollenbach, R. E. (1970) - *Shock-Wave Studies of PMMA, Fused Silica, and Sapphire*, J. Appl. Phys. **41**, pp4208-4226.
- [33] *Centronics AEPX Series Photodetectors*, RS Data Sheet No. 842-422.
- [34] Wolf, A. V., Brown, M. G., and Prentiss, P. G. (1982) - *Concentrative Properties of Aqueous Solutions: Conversion Tables*, CRC Handbook of Chemistry and Physics, 62nd Edition, Edited by Weast, R. C., Published by the CRC Press Inc., ppD232-D233.
- [35] Vogel, A. and Lauterborn, W. (1988) - *Acoustic Transient Generation by Laser-Produced Cavitation Bubbles Near Solid Boundaries*, J. Acoust. Soc. Am. **84**, pp719-731.
- [36] Jin, Y. H. (1995) - *Optical Investigations of Cavitation*, PhD Thesis, Loughborough University.
- [37] Schiffers, W. P., Shaw, S. J., Jin, Y. H., and Emmony, D. C. (1997) - *High Speed Photographic Studies of the Interaction of Cavitation Bubbles with a Boundary*, High Speed Photography and Photonics, Proc. SPIE **2869**, pp308-315.
- [38] Ward, B., and Emmony, D. C. (1990) - *Interactions of Laser-Induced Cavitation Bubbles with a Rigid Boundary*, High Speed Photography and Photonics, Proc. SPIE **1358**, pp1035-1045.

Chapter Five

A Large Area Planar Piezoelectric Transducer for Measuring Spherically Symmetric Acoustic Transients

Introduction

This chapter will discuss the measurement of temporal pressure profiles of spherically symmetric acoustic transients propagating in water using a large flat piezoelectric film transducer. The theory behind the generation of voltage in such transducers is discussed in section 5.2 and, a mathematical function which describes the behaviour of the output voltage is derived. Simulations are then performed in section 5.3 which highlight the problems involved in the calculation of pressure-time profiles with limited signal resolution. The pressure-time relationships of acoustic transients created by optical cavitation are calculated experimentally, using voltage measurements made with transducers placed 1mm, 2mm and 4mm away from the event. Two thicknesses of polarised PVDF film transducer are used and the results discussed in sections 5.5 and 5.6. Finally the conclusion is made that the same technique could successfully be applied to acoustic transients produced with other non-planar sources, for example in systems with cylindrical symmetry.

5.1 - The problems of measuring acoustic transients from point sources

The accurate measurement and characterisation of acoustic transients generated by small events is in general extremely difficult. This is because devices for measuring such acoustic waves are usually required to be equally as small as the event and, have a wide signal bandwidth due to the short acoustic travel times and geometry involved. Many attempts have been made using a wide variety of techniques to characterise the acoustic transients associated with one such event - *optical cavitation*, which has already been discussed in chapter 2. Optical cavitation can be produced when light from a high power pulsed (Q-switched) laser is focused into a transparent liquid, such as water. The high intensity radiation causes *dielectric breakdown* to occur at the focal point, vaporising the surrounding liquid [1]. This region expands rapidly producing a spherically shaped cavitation bubble which undergoes several radial oscillations of expansion and collapse over a few hundred microseconds [2], before eventually breaking up and being absorbed in the liquid. Initially, and also during the subsequent collapses, the wall of the vapour

bubble expands at a velocity greater than that of the speed of sound in the liquid. This gives rise to a spherically symmetric acoustic transient, or shock wave, which propagates away from the centre of emission slowing after a few nanoseconds to the sound speed in the liquid [3].

Traditional methods for acoustic field time-profiling usually involve using either *spot poled piezoelectric membrane transducers* [4], or *needle hydrophones* [5]. Such techniques require the expanding acoustic wave to have travelled far enough so that its radius of curvature is large, thereby appearing planar to the small sensitive area of the transducer. The rise times of these devices are determined primarily by their geometry. For a planar acoustic transient which is incident upon a piezoelectric transducer with plates positioned perpendicular to the direction of propagation, the rise time is only dependant on the thickness of the device and the duration of the wave. When these factors are taken into account the time profile of the acoustic transient can be derived [6]. The apparent rise time can however be considerably longer for other orientations and non-planar transients, for example due to the considerable curvature of the acoustic wave front close to an optical cavitation event. This becomes most apparent in large area flat transducers where the curvature of the measured wave front is relatively large, as shown schematically in figure 5.1. This makes the measurement of such events by piezoelectric transducers impractical; however they have found uses in finding the total energy and peak pressure of the transients at large distances [7 & 8].

Optical methods have also been extensively used in the characterisation of optical cavitation events and the resulting spherically symmetric acoustic transients. One such technique is to study the deflection of a narrow probe laser beam traversed by the shock wave [9]. The light is deflected according to the local refractive index variations in the liquid, which is directly associated with the pressure characteristics of the transient. This and similar methods [7] provide extremely high bandwidth pressure-time profiles for small events.

High speed photographic techniques such as *Schlieren imaging* [7] and focused *Shadowgraphy* [2, 3 & 8] have also been used to give spatial characterisation of acoustic events. These methods have the obvious advantage of presenting clear visual evidence of the development of such acoustic transients and cavitation bubbles, however they cannot provide quantitative measurement of pressures developed within shock waves. Quantitative measurements can be made using high speed *Mach-Zehnder interferometry*. This can give both a visual display and, after subsequent analysis of fringes, the pressure time profile of the emerging acoustic transients [2,10]. The limitation of this technique is

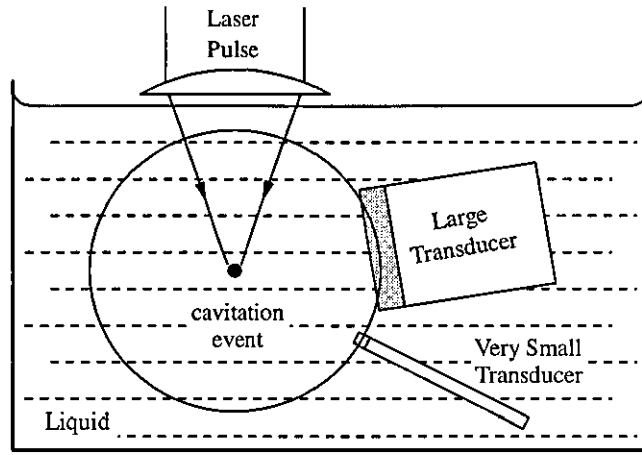


Figure 5.1 - Problems associated with the measurement of spherically shaped acoustic transients generated by optical cavitation.

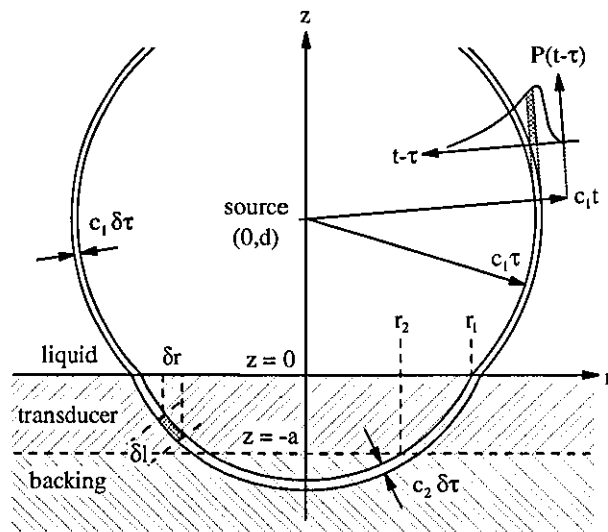


Figure 5.2 - Schematic diagram of the interaction between a spherically shaped acoustic transient and a piezoelectric transducer.

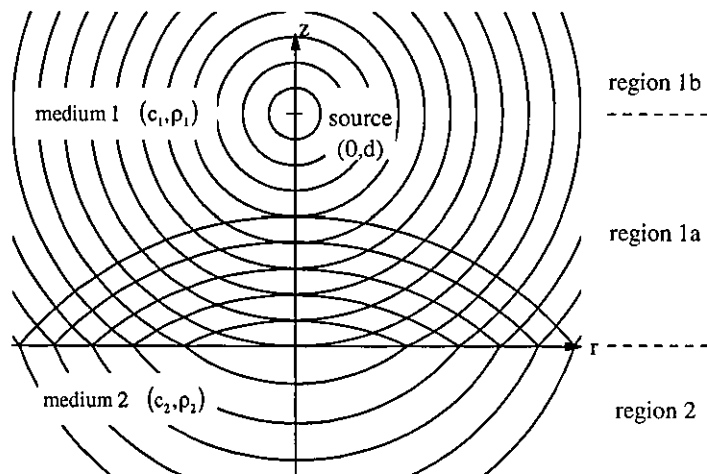


Figure 5.3 - Acoustic transmission and reflection for waves with spherical symmetry at a boundary between two media.

that it is difficult to accurately trace the fringe displacements at the rising edge of the shock wave [10], and hence derive the short rise time of the transient.

The approach described here uses a large area *Polyvinylidene fluoride* (PVDF) film piezoelectric transducer. Normally such a transducer is wholly unsuitable for small source acoustic transient profiling, due to its large size and resulting long signal rise times. In the technique described here the transducer is considered to be made up of a large number of small elements. Each of these elements measures the component of pressure normal to the film of a small section of the acoustic transient which is within the transducer. The voltage generated on the transducer plates is then essentially proportional to the sum of all of these pressure components. As a result if the spatial shape, or symmetry, of an acoustic transient is known as it progresses through the liquid, then its pressure-time profile can be derived from the voltage signal measured across the PVDF transducer electrodes as a function of time.

5.2 - Acoustic wave interactions with a large area thin film piezoelectric transducer

The temporal pressure profile of an acoustic transient can be defined as the relative values of pressure $P(t)$ measured with respect to time t , at an arbitrary point in space as the wave passes through it. The problem of measuring this using a device that is large in comparison with the dimensions of the transient is essentially one of convolution. The device can be split into many smaller volume elements which each have a respective acoustic pressure acting upon it. All of these contribute together towards the total charge developed on the plates of the transducer, and give rise to an output voltage $V(t)$ with respect to time.

Suppose that these elements follow the same spatial shape that an imaginary wave front takes as it travels through the various media involved, having travelled for a time τ after being emitted from an arbitrarily shaped imaginary source. The spatial position of any one of these elements will therefore be defined by the value of τ . Also, every point along the element will have the same acoustic pressure acting upon it, corresponding to a point in the pressure-time profile of $P(t-\tau)$ at a certain time t for a real acoustic transient emitted from the source. That is, as time increases the same element experiences pressure amplitudes that correspond to points later in the pressure profile curve. Each element contributes towards the total voltage $V(t)$ an amount $T(t)$ per unit pressure experienced, called the *impulse response* or *transducer function*. This amount is not only dependant on how much of the element is within the transducer and thus how much it affects the

total voltage, but also includes the reduction in magnitude that the acoustic transient undergoes as it travels further into the transducer. As a result the total voltage can be expressed in terms of a convolution:

$$V(t) = \int_{-\infty}^{\infty} P(t-\tau) \cdot T(\tau) d\tau \quad - (5.1)$$

If the source is small in comparison to the size of the measuring device, then it can be approximated to just a point. A system in which acoustic waves are emitted by a point source and measured by a large planar thin film transducer has cylindrical symmetry. This system can therefore be split into elements with cylindrical symmetry, each element having the same spatial shape that an acoustic transient emitted from the source forms after it has travelled for a time τ . In the source medium all of these elements will have a radius of $c_1\tau$ and thickness $c_1d\tau$, where c_1 is the propagation velocity of acoustic transients in that medium. This is shown in figure 5.2 where the cylindrical symmetry is about the z-axis. If the piezoelectric transducer has a thickness a , then only portions of elements existing within the range $-a < z < 0$ will affect the output voltage.

The effect that an element has on the output voltage can also include the reduction in magnitude that an acoustic transient experiences with distance. In order to find this, and also to compensate for distortion effects within the transducer due to refraction, the effect of each element is modelled using an imaginary thin step wave that has travelled to the same position. This wave will have duration $d\tau$ and, having travelled for a time τ after being emitted from the point source, has a pressure distribution $p(l, \tau)$ inside the transducer - where l is some relative position along the element from the z-axis. Since for a piezoelectric transducer the measured effect is primarily due to force components normal to the plates; then $T(\tau)$ can be defined in terms of a summation of annular segments along the element, or alternatively the wavefront:

$$T(\tau) \propto \int_{-\infty}^{\infty} \underbrace{p(l, \tau) \cos(\theta)}_{\text{component of pressure in the z - direction}} \underbrace{\delta \left\{ \begin{array}{l} -a < z < 0 \\ \text{elsewhere} \end{array} \right.}_{\text{function that describes if annulus is within transducer}} \underbrace{2\pi r \cdot dl}_{\text{area of annular segment}} \quad - (5.2)$$

where $l = f(z) = f(r)$ and represents the radius and position of annular segments. A simplification can then be made with the knowledge that $\delta r = \delta l \cdot \cos\theta$, which gives in the infinite limit:

$$T(\tau) \propto \int_{r_2}^{r_1} \rho(r, \tau) \cdot r \, dr \quad - (5.3)$$

where r_1 and r_2 are the radii at which an element (with position described by τ) intersects with the $z=0$ and $z=-a$ planes respectively. In order to evaluate $\rho(r, \tau)$ and hence $T(\tau)$, further knowledge of the position and decrease in magnitude of the imaginary step wave must be obtained as it travels through the transducer. This can be done by applying wave theory and will be discussed in the next section.

5.2.1 - The path of an acoustic wave from a point source

The evaluation of the field of spherical waves refracted by a second medium is one of practical significance in many physical cases, particularly in the areas of radio physics and acoustics. It was first studied in detail by Sommerfeld [11], who examined the field created by an electric dipole located close to a plane interface between two media. Previously consideration had only been given to conditions where the radius of curvature of the incident spherical wave front was large in comparison to the region under investigation. This was so that the evaluation could proceed by considering the waves as planar; which then allowed the already well established theories developed by Fresnel (optical & electromagnetic) and Lord Rayleigh [12] (acoustic) to be used to find the amplitude and intensity of the reflected and refracted waves at the interface. Of the many subsequent treatments [14,15], this section is based upon the one given by Officer [13] which takes full consideration of the curvature of the incident wave as it impinges on the transducer.

Suppose there is a source of spherically symmetric waves in a homogenous medium with sound velocity c_1 and density ρ_1 . If this is at a distance d away from a boundary with a second medium (c_2, ρ_2), then the diverging longitudinal waves in the two media will be described by the wave equation:

$$\nabla^2 \phi_{1,2} = \frac{1}{c_{1,2}^2} \frac{\partial^2 \phi_{1,2}}{\partial t^2} \quad - (5.4)$$

In order to solve this equation it will be assumed here that both media are loss-less and the first medium is a liquid (water), and that there will be no mode conversions to either

transverse or surface waves in the solid. In cylindrical co-ordinates, with symmetry about the z-axis, the fundamental solutions of equation (5.4) are of the form [13]:

$$\varphi = \exp(i\omega t) J_0(k.r) F(z)$$

where ω is the angular frequency of the source and k is the real wave number. In the three regions shown in figure 5.3, $F(z)$ is defined by:

$$\left. \begin{aligned} F_{1b} &= \underbrace{A.\exp(-i\beta_1 z)}_{\substack{\text{Emitted and} \\ \text{Reflected waves}}} \\ F_{1a} &= \underbrace{B.\exp(-i\beta_1 z)}_{\substack{\text{Reflected wave}}} + \underbrace{C.\exp(i\beta_1 z)}_{\substack{\text{Emitted wave}}} \\ F_2 &= \underbrace{D.\exp(i\beta_2 z)}_{\substack{\text{Transmitted wave}}} \end{aligned} \right\} \quad - (5.5)$$

where $\beta_1 = \left(\frac{\omega^2}{c_1^2} - k^2\right)^{1/2}$ and $\beta_2 = \left(\frac{\omega^2}{c_2^2} - k^2\right)^{1/2}$

In order to solve for the four unknown quantities A, B, C & D in equation (5.5), four boundary conditions are needed. Firstly it is known that the source is spherically symmetric about $r=0$ and $z=d$, so that there is:

- (i) a continuity of pressure along the $z=d$ plane,
- and (ii) a discontinuity of the component of particle velocity in the z-direction of $2k$ across the $z=d$ plane [13].

The second condition can be visualised, considering the source without the boundary, as pairs of particles at equal distances on opposite sides of the $z=d$ plane, that will be travelling at equal and opposite velocities in the z-direction away from the planes. Further boundary conditions may be found by considering the interface between the two media. That is there will be:

- (iii) a continuity of pressure along the $z=0$ plane,
- and (iv) z-component of particle velocity is continuous over the $z=0$ plane.

These four boundary conditions may be expressed mathematically as:

$$\left. \begin{array}{l}
z = d \left\{ \begin{array}{l}
1. \text{ pressure} \propto \rho_1 \frac{\partial \varphi_{1a}}{\partial t} = \rho_1 \frac{\partial \varphi_{1b}}{\partial t} \Rightarrow F_{1a} = F_{1b} \\
2. \text{ particle velocity in } z \text{ direction} : \frac{\partial \varphi_{1a}}{\partial z} - \frac{\partial \varphi_{1b}}{\partial z} = 2k \Rightarrow 2k = \frac{dF_{1a}}{dz} - \frac{dF_{1b}}{dz}
\end{array} \right. \\
z = 0 \left\{ \begin{array}{l}
3. \text{ pressure} \propto \rho_1 \frac{\partial \varphi_{1a}}{\partial t} = \rho_2 \frac{\partial \varphi_2}{\partial t} \Rightarrow \rho_1 F_{1a} = \rho_2 F_2 \\
4. \text{ particle velocity in } z \text{ direction} : \frac{\partial \varphi_{1a}}{\partial z} = \frac{\partial \varphi_2}{\partial z} \Rightarrow \frac{dF_{1a}}{dz} = \frac{dF_2}{dz}
\end{array} \right.
\end{array} \right\} - (5.6)$$

Using these conditions and upon solving for A, B, C & D it can be shown that for the transmitted wave:

$$D = \left(\frac{2\beta_1 b}{\beta_1 + b\beta_2} \right) \frac{k}{i\beta_1} \exp(-i\beta_1 d) \quad \text{where } b = \frac{\rho_1}{\rho_2} \quad - (5.7)$$

and the fundamental solutions for φ_{1a} , φ_{1b} and φ_2 can also be found. A complete solution for the transmitted wave can be obtained by adding together all the fundamental solutions with different k. That is for the transmitted wave:

$$\Phi_2(r, z < 0, \omega, t) = e^{i\omega t} \int_0^\infty J_0(kr) \frac{k}{i\beta_1} \left\{ \frac{2\beta_1 b}{\beta_1 + b\beta_2} \right\} \exp(-i[\beta_1 d - \beta_2 z]) dk \quad - (5.8)$$

It is worth noting here that the term in parentheses represents the Rayleigh transmission coefficient when both β_1 and β_2 are real. Finally if the solution is differentiated with respect to time, the pressure relationship can then be obtained:

$$p_{\text{trans}}(r, z < 0, \omega) \propto \int_0^\infty J_0(kr) \frac{k}{i\beta_1} \left\{ \frac{2b}{1 + b\left(\frac{\beta_2}{\beta_1}\right)} \right\} \exp\left(-i\beta_1 \left[d - \left(\frac{\beta_2}{\beta_1}\right) z \right] \right) dk \quad - (5.9)$$

5.2.2 - Evaluation of pressure in the high frequency limit

The complete solution described above in equation (5.9) cannot easily be solved analytically. It can however be simplified somewhat by assuming that the source emits only high frequency waves. This assumption is generally true for acoustic transients emitted from optical cavitation events, since they quickly develop into shock waves which have fast rise times and thus mainly contain high frequencies. An approximation can then be made for the ratio β_2/β_1 , such that in the high frequency limit:

$$\frac{\beta_2}{\beta_1} = \frac{c_1}{c_2} \sqrt{\frac{\omega^2 - (kc_2)^2}{\omega^2 - (kc_1)^2}} \xrightarrow{\omega \rightarrow \infty} \frac{\beta_2}{\beta_1} = \frac{c_1}{c_2} \quad - (5.10)$$

Hence the pressure function (5.9) simplifies to:

$$p_{\text{trans}}(r, -ve z, \text{large } \omega) \propto \frac{2b}{1 + b\left(\frac{c_1}{c_2}\right)} \int_0^\infty J_0(kr) \frac{k \cdot dk}{i\beta_1} \exp\left(-i\beta_1 \left[d - \left(\frac{c_1}{c_2}\right)z\right]\right)$$

It can be proved [16] that this integral is equal to:

$$p_{\text{trans}}(r, -ve z, \text{large } \omega) \propto \left\{ \frac{2b}{1 + b\left(\frac{c_1}{c_2}\right)} \right\} \frac{\exp\left(-\frac{i\omega}{c_1} \left[r^2 + \left(d - \left(\frac{c_1}{c_2}\right)z\right)^2\right]^{1/2}\right)}{\sqrt{r^2 + \left(d - \left(\frac{c_1}{c_2}\right)z\right)^2}} \quad - (5.11)$$

Suppose that a wavefront is emitted from the source such that in the first medium it has reached a spherical radius of $c_1\tau$. It can be seen from this equation that as the spherical wave enters the second medium its magnitude is altered by a constant factor of $2b/(1 + b.c_1/c_2)$. From thereon the wavefront locus follows the relationship:

$$\sqrt{r^2 + \left(d - \frac{c_1}{c_2}z\right)^2} = c_1\tau \quad - (5.12)$$

and decreases in amplitude according to $\left[r^2 + \left(d - \frac{c_1}{c_2}z\right)^2\right]^{-1/2}$. As a result equation (5.11) can be rewritten as:

$$p_{\text{trans}}(r, -ve z, \text{large } \omega) \propto \frac{\exp\left(\frac{2\pi i}{\tau c_1} \left[r^2 + \left(d - \left(\frac{c_1}{c_2}\right)z\right)^2\right]^{1/2}\right)}{\tau c_1}$$

giving finally: $p(r, \tau) = |p_{\text{trans}}(r, -ve z, \text{large } \omega)| \propto \frac{1}{\tau c_1} \quad - (5.13)$

5.2.3 - Accuracy of the high frequency approximation and piezoelectric materials

It is worth briefly investigating the limitations of the derivation above by considering the path of high frequency waves predicted using geometric optics. This can accurately describe the system of waves incident on a boundary at angles to the normal up to the critical angle $\theta_c = \arcsin(c_1/c_2)$, provided that the wavelength of the transient is small compared with d . Consider a portion of a wave front emitted from the point source in terms of a ray representation, as in figure 5.4. At a point in time when the wavefront in the first medium has travelled to a spherical radius of $c_1\tau$, it can easily be shown that the position of the ray in the second medium is:

$$\left. \begin{aligned} r &= \frac{d}{\cos(\theta_1)} \sin(\theta_1) + c_2 \left(\tau - \frac{dc_1}{\cos(\theta_1)} \right) \sin(\theta_2) \\ z &= -d - c_2 \left(\tau - \frac{dc_1}{\cos(\theta_1)} \right) \cos(\theta_2) \end{aligned} \right\} \quad - (5.14)$$

where angle θ_2 is given by Snell's law: $\sin(\theta_2) = \frac{c_2}{c_1} \sin(\theta_1)$.

Suppose the first medium is water ($c_1 = 1480\text{ms}^{-1}$) and the point source is chosen to be 1mm away from the boundary. The path of a transmitted acoustic transient can be plotted for various piezoelectric transducer materials, which will be assumed to be isotropic to begin with, using the geometric theory above and compared against the predictions made by the high frequency approximation. This has been done in 50ns time steps for the polymer *Polyvinylidene fluoride* (PVDF, $c_2=2200\text{ms}^{-1}$) and, the most commonly used piezoelectric ceramic material *Lead Zirconate Titanate* (PZT, $c_2= 4000\text{ms}^{-1}$), as shown in figures 5.5(a) & 5.5(b) respectively. It can be seen that the two models give similar results initially as the wave enters the transducer medium and is distorted by the increase in sound speed, for both materials. Later, however, the paths only coincide at small radial distances, the agreement breaking down as the incident angle θ approaches the critical angle $\theta_c = \arcsin(c_1/c_2)$. Therefore the high frequency approximation only holds for a finite duration $\Delta\tau$ after the wave has entered the isotropic transducer material, which can be defined as:

$$\Delta\tau \approx \tau(\theta = \theta_c) - \tau(\theta = 0) \approx \frac{d}{c_1} \left\{ \frac{1}{\cos(\theta_c)} - 1 \right\} \quad - (5.15)$$

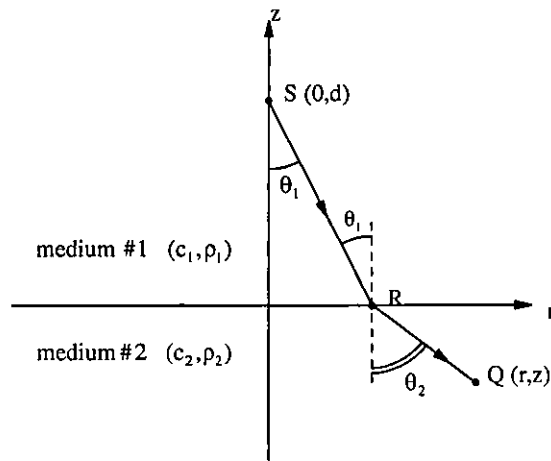
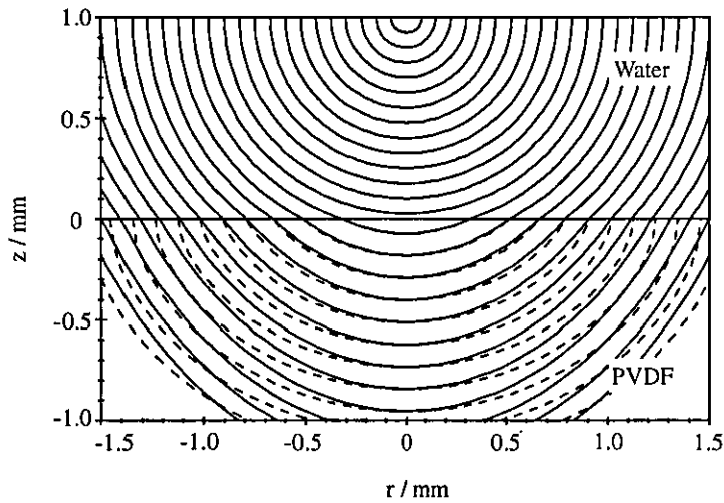
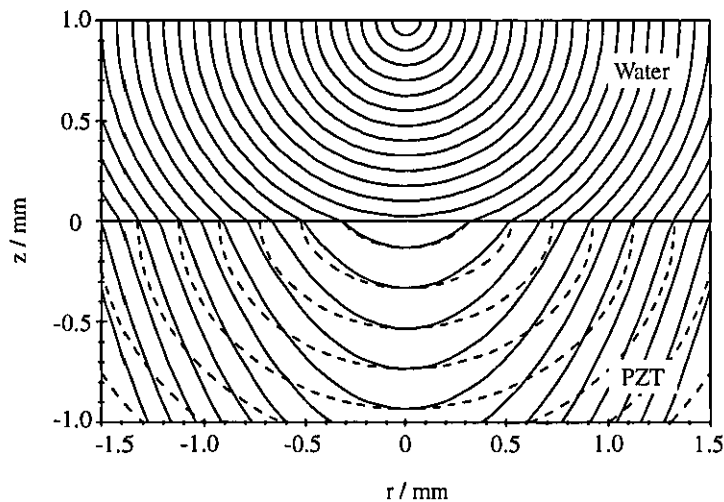


Figure 5.4 - Geometric wave approximation at boundary between two media.



(a) Waves in PVDF

— High frequency approximation } Wave crests shown
 - - - Geometric wave theory } with 50ns separation



(b) Waves in PZT

Figure 5.5 - Acoustic wave path predictions for a point source close to a boundary, using both geometric and wave equation approximations.

This gives a $\Delta\tau$ value of 250ns in PVDF ($\theta_c=42.3^\circ$) and 57ns in PZT ($\theta_c=22.7^\circ$). Therefore PVDF is likely to allow better accuracy in the development of a transducer function based upon the high frequency approximation, since the wave suffers less distortion in shape as it enters the transducer. Better approximations could be used in the derivation of the transducer function for isotropic materials, such as the one suggested by Brekhovskikh [17] based on geometric theory, but will not be discussed here.

One complicating factor is that polarised PVDF used in piezoelectric transducers tends to exhibit anisotropic behaviour [18], where the sound speed varies with the orientation of a wave in the material. In the case of Kynar piezoelectric film the direction of polarisation is perpendicular to the plates, the speed of sound being 2200ms^{-1} . Whereas in the directions parallel to the plates the sound speed is 1500ms^{-1} . This has the benefit that the distorted wave shape is closer to that of the prediction made by the high frequency approximation, thereby perhaps significantly increasing $\Delta\tau$ for polarised PVDF transducers with the direction of polarisation towards the source (i.e. along the Z-axis.)

There are further advantages in using PVDF as the transducer material. The impedance of PVDF (ρ_2c_2) is 2.6 times that of water ($\rho_1c_1=1.48\times 10^6\text{kgm}^{-2}\text{s}^{-1}$), allowing up to 75% of the energy of an incident wave to be transmitted into the material from water. This is in comparison to that of the ceramic Lead Zirconate (PZT), which has an acoustic impedance 15 times that of water and so allows only 23% of the energy to be transmitted [19]. Also the stress and strain constants (see chapter 2) are about 10 times higher in PVDF compared with ceramics, and therefore give rise to a higher voltage output for the same applied force [18,20].

5.2.4 - The transducer function

Having developed a theory to approximate the position and magnitude of a wave front entering a second medium, it is now possible to evaluate the transducer function using equations (5.3), (5.12) and (5.13), giving:

$$T(\tau) \propto \int_{\frac{1}{2}}^{r_1} \frac{1}{c_1\tau} r \, dr$$

where $r_1 = \left[(c_1\tau)^2 - d^2 \right]^{1/2}$ for $c_1\tau > d$, otherwise zero,

and $r_2 = \left[(c_1\tau)^2 - \left(d + \frac{c_1}{c_2}a \right)^2 \right]^{1/2}$ for $c_1\tau > d + a(c_1/c_2)$, otherwise zero.

Therefore, after simplification:

$$\left. \begin{aligned} T(\tau \leq d/c_1) &= 0 \\ T(d/c_1 \leq \tau \leq [d + \frac{c_1}{c_2}a]/c_1) &= \frac{(c_1\tau)^2 - d^2}{c_1\tau} \\ T(\tau \geq [d + \frac{c_1}{c_2}a]/c_1) &= \frac{\left(d + \frac{c_1}{c_2}a \right)^2 - d^2}{c_1\tau} \end{aligned} \right\} \quad - (5.16)$$

This is shown schematically in figure 5.6. Spherical elements that are outside of the transducer have no effect on the output voltage, which gives rise to the transducer function being zero for elements with radii $\tau c_1 \leq d$. As elements which begin to penetrate the transducer film are considered, $T(\tau)$ rises sharply peaking for the element that touches the boundary with the backing material. That is, every element portion within the transducer has an effect on the output voltage. This cap shaped element gives rise to a circular component of area in the plane of the transducer with a radius of $\sqrt{(c_1\tau)^2 - d^2}$. However the transducer function also takes into account the reduction in magnitude suffered by the transient as it propagates further, which here is proportional to the distance τc_1 . Finally, elements which penetrate the backing material (i.e. $\tau c_1 \leq d + \{c_1/c_2\}a$) have just an annulus shaped portion within the transducer film. The area presented in the plane of the transducer remains constant, giving rise to a fall in $T(\tau)$ with increasing element radius.

In summary, $T(\tau)$ is the effect that the individual volume elements have on the output voltage of the transducer per unit pressure applied. The spatial shape and position of each element corresponds to the form taken by a step wave at a time τ after being emitted by the point source. This source is a distance d away from the piezoelectric film transducer of thickness a . The transducer function ignores effects caused by acoustic absorption and it is only valid for the first 200ns of travel inside the second medium, due to the limitations of the high frequency approximation of $p(r, \tau)$.

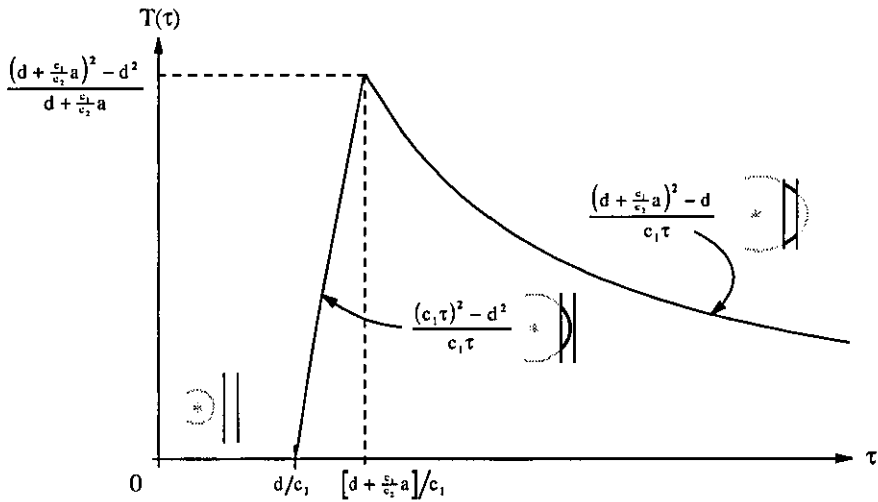


Figure 5.6 - The Transducer Function in terms of the parameter τ .

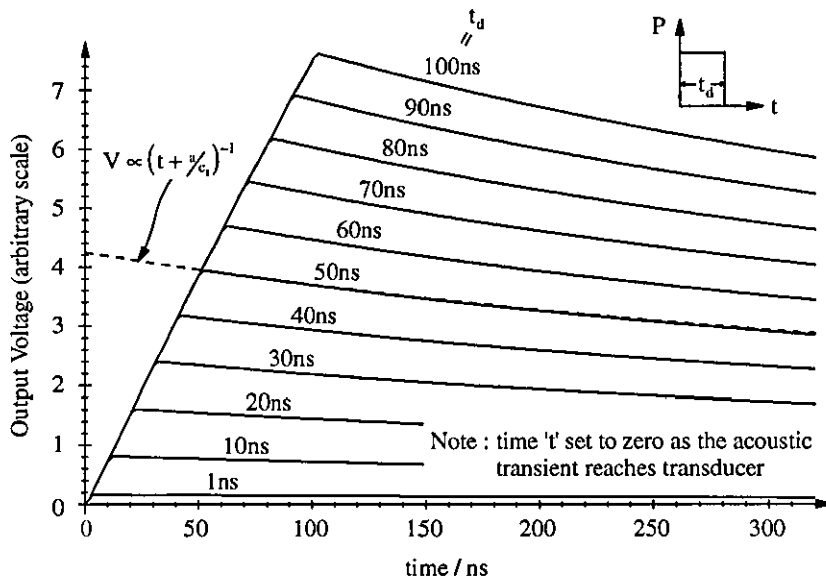


Figure 5.7 - Simulated voltage output for a $9\mu\text{m}$ thick transducer with varying step pressure pulse durations. (Source distance $d = 1\text{ mm}$ from transducer.)

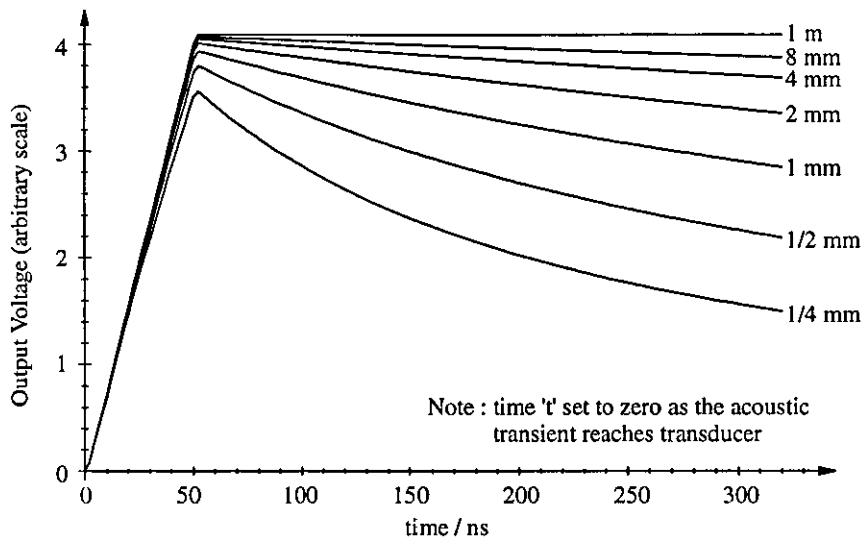


Figure 5.8 - Simulated voltage output of a $9\mu\text{m}$ thick transducer with varying distance between point source and transducer. (50ns step pressure pulse)

5.3 - Computer simulations

Before going onto discussing the experimental measurement of pressure profiles of spherically symmetric acoustic transients using the theory developed in the last section, it is helpful to simulate some of the problems involved. The voltage generated by large area piezoelectric transducers with different film thicknesses can be simulated quite easily using a numerical form of the convolution equation. This is done for a variety of source distances from the transducer, and also for several durations of a simple step-like pressure profile. The effects of signal noise and under-sampling of the measured voltage are added to the simulated voltage wave forms. Finally deconvolution is performed and the resulting pressure profiles studied.

5.3.1 - The discrete form of convolution and deconvolution

It is possible, with the aid of a computer, to simulate the voltage developed on the plates of the piezoelectric transducer due to some incident spherically symmetric pressure pulse profile. This can be achieved by using the discrete form of convolution:

$$V(t) = V(N\kappa) = \sum_{m=M}^N P(\kappa[N-m])T(m\kappa) \quad - (5.17)$$

$$\text{or} \quad V_N = \sum_{m=M}^N P_{N-m} T_m$$

where m and N are the integer equivalents of the integration variable τ and time t respectively in equation (5.1), linked by some multiplier κ which represents the time step between discrete measurements of V_N . It is assumed here that the pressure pulse is of a finite duration, such that $P(t < M\kappa) = P(t > N\kappa) = 0$, where M is some integer lower limit.

A simple form of deconvolution may be derived from equation (5.17) as a recursive series:

$$\left. \begin{aligned} P_M &= \frac{V_M}{T_M} \\ P_{M+1} &= \frac{1}{T_M} (V_{M+1} - P_M T_{M+1}) \\ &\vdots \\ P_N &= \frac{1}{T_M} \left(V_N - \sum_{m=M}^{N-1} P_{(N-1)-m} T_{m+1} \right) \end{aligned} \right\} - (5.18)$$

The pressure profile at time $t = N\kappa$ can thus be calculated provided that all voltages V_0 to V_N have been measured.

5.3.2 - Other techniques for evaluating a convolution

There are a number of different methods for calculating the voltage by convolution. The most common techniques apply an integral transformation to the voltage, transducer function and pressure. This transforms the respective function from time space t to some other space α in which the evaluation of the convolution or deconvolution is more easily achieved, before the reverse transform is applied. Forward integral transforms are usually of the form [21]:

$$\mathcal{F}(\alpha) = \int_a^b g(t)K(\alpha,t)dt$$

where $\mathcal{F}(\alpha)$ is the integral transform of $g(t)$ by the kernel $K(\alpha,t)$. The two most commonly used integral transforms applied to convolution are the *Fourier transform* and the *Laplace transform*. The Laplace transform has a kernel defined as $K(\alpha,t) = e^{-\alpha t}$ and is used primarily in the solving of differential equations, however evaluation of the reverse transform can often be extremely difficult. Alternatively the Fourier transform can be used, which has the kernel $K(\omega,t) = e^{-i\omega t}$ transforming to frequency space ω . This has a well defined inverse integral transform having the kernel $K(\omega,t) = e^{i\omega t}$. That is:

$$\left. \begin{aligned} \mathcal{F}(\omega) &= \text{FT}(f(t)) = \int_{-\infty}^{\infty} f(t)\exp(-i\omega t)dt \\ \text{and } f(t) &= \text{FT}^{-1}(\mathcal{F}(\omega)) = \int_{-\infty}^{\infty} f(t)\exp(i\omega t)dt \end{aligned} \right\} \quad - (5.19)$$

The convolution between the pressure profile $P(t-\tau)$ and the transducer function $T(\tau)$ can then be achieved using the *convolution theorem*:

$$V(t) = \int_{-\infty}^{\infty} P(t-\tau)T(\tau)dt = \int_{-\infty}^{\infty} \mathcal{P}(\omega)\mathcal{T}(\omega)\exp(i\omega t)d\omega$$

or alternatively:
$$\mathcal{V}(\omega) = \mathcal{P}(\omega)\mathcal{T}(\omega) \quad - (5.20)$$

That is, the convolution in frequency space is just the transformed pressure profile multiplied by the transducer function, the voltage then derived by applying the inverse Fourier transform. As a result deconvolution can be achieved using:

$$\mathcal{P}(\omega) = \frac{\mathcal{V}(\omega)}{\mathcal{F}(\omega)} \quad - (5.21)$$

Convolution of discrete values of voltage and pressure applying the Fourier transform can be achieved using an algorithm known as the *fast fourier transform* (FFT), which will not be detailed here but can be found in reference [22]. It is used extensively in signal processing due to the relatively small number of calculations required for large data sets and its ability to filter out noise in the frequency domain. The algorithm does however assume that the measured signal is repetitive, and as a result requires complete knowledge of both the measured voltage information and the transducer impulse response function. That is the data sets containing the calculated transducer function and the measured voltage must and start and finish with the same numerical values (i.e. zero). As a result this makes deconvolution of the voltage problematic, since it can be seen from equation (5.16) and figure 5.6 that the transducer function does not actually fall back to zero after the transient penetrates the film. In fact experimentally the transducer function does return to zero, however this is extremely difficult to model since the fall off is dependant on the active region of the transducer and its precise position relative to the points source. Even small discrepancies in the transducer function can cause large repetitive errors in the whole of the resulting pressure profile. This can in part be overcome by padding out the voltage data set with zeros, which also reduces aliasing problems, however at a cost of increasing the number of calculations required substantially. As a result the discrete form of the convolution described in the last section is more appropriate and will be applied here.

5.3.3 - Simulated voltage output of the transducer

The output of the large area transducer has been simulated for an incident spherically symmetric wave front using the basic convolution equation (5.17) and the transducer function developed earlier (equation (5.16)). Figure 5.7 shows the voltage as a function of time calculated for step like pressure pulses of varying duration created in water ($c_1=1500\text{ms}^{-1}$). The pressure pulses all have the same magnitude and originate from a point source 1mm from the transducer-water interface. It is assumed here that the transducer has infinite area and is fabricated out of thin film Polyvinylidene fluoride

material ($c_2=2200\text{ms}^{-1}$) which is $a=9\mu\text{m}$ thick (see figure 5.2). The transient takes a time d/c_1 to reach the transducer film after creation, which is much greater than the rise time of the resulting voltage. As a result the voltage is plotted here against the time after the acoustic wave has entered the film. It can be seen here that the output voltage rise time is directly proportional to the duration of the pressure pulse, as is the peak voltage. For a square pressure pulse the rise is also linear with time. The shape of the fall off in voltage is not however affected by the duration of the pulse, infact it is proportional to $(t+a/c_1)^{-1}$.

Figure 5.8 shows the simulated output voltage for a 50ns duration step pressure pulse, varying the distance d of the source from the transducer. From this it can be seen that the rise time is not a function of d and, the peak voltage slowly decreases with large reductions in the source distance. The rate of fall is however very much affected by the distance of the source from the transducer, the voltage falling faster when the source is close to the transducer, that is because of the large wave front curvature. When the source is at a large distance from the transducer the acoustic transient becomes almost planar, as a result the voltage remains almost constant after the wave front has reached the rear of the film. This is because the reduction in magnitude the transient suffers with distance is relatively small, given that it is inversely proportional to the distance from the source. It is also worth noting that the annular shaped component of area in the plane of the transducer, which is inside the film, is infact constant with time.

The simulated time relationship of the output voltage has also been investigated for a number of transducers with different film thicknesses. Figure 5.9 shows the ratio of the output voltage to PVDF film thickness simulated for a 50ns step pressure pulse created 1mm from the transducer, with film thicknesses of $a=9\mu\text{m}$, $28\mu\text{m}$, $52\mu\text{m}$ and $110\mu\text{m}$. It can clearly be seen here that the peak voltage is directly proportional to the transducer thickness. The rise time of the voltage signal is also a function of the transducer thickness, that is equal to the duration of the pressure pulse plus the time it takes the wave front to traverse the PVDF film (i.e. $t_{\text{rise}} = t_d + ac_2$). It is also apparent that the fall off in the voltage is unaffected by the thickness of the transducer.

The dependency of the voltage-time relationship on both the duration of the step pressure profile and the distance of the source have also been plotted for a $110\mu\text{m}$ thick transducer. This is shown in figures 5.10 and 5.11. Again the rise time is completely dependant on the duration of the pressure pulse added to the time for the wave front to traverse the thickness of the transducer. Also the peak voltage is affected primarily by

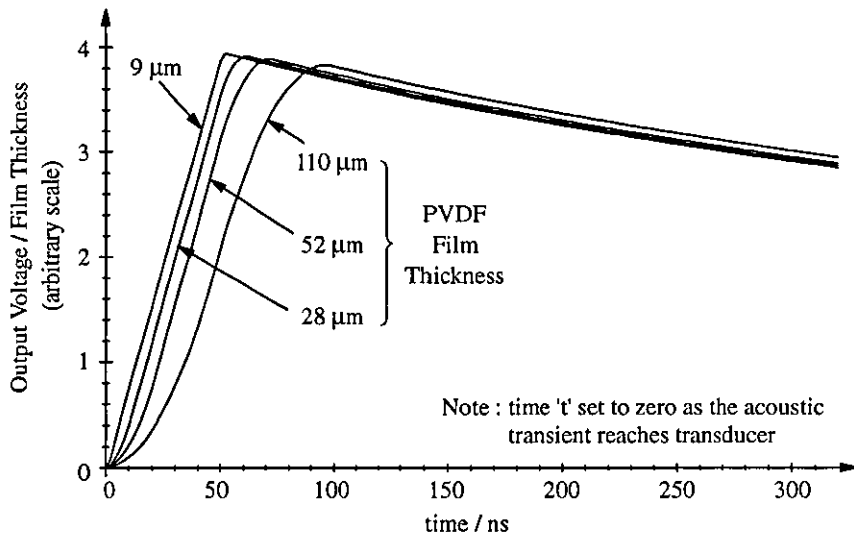


Figure 5.9 - Simulated voltage output of transducers with different film thicknesses. (for 50ns duration step pressure pulses, d=1mm.)

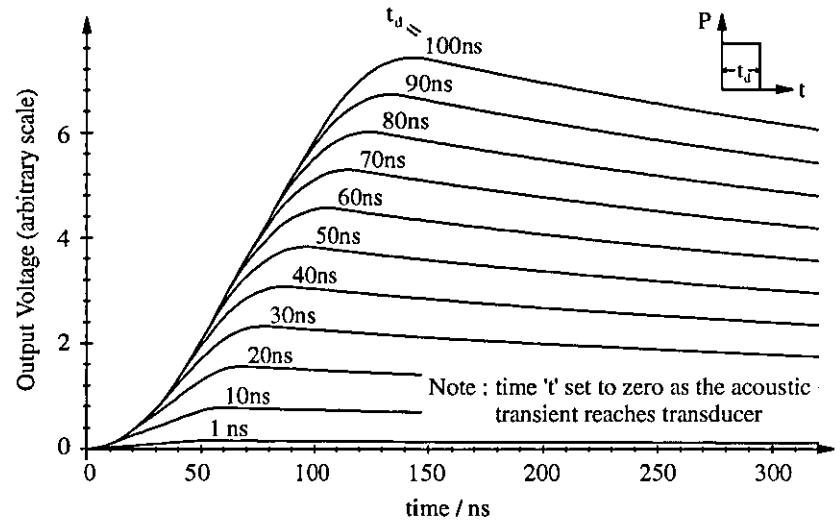


Figure 5.10 - Simulated voltage output for a 110 μm thick transducer with varying step pressure pulse durations. (Source distance d = 1 mm from transducer.)

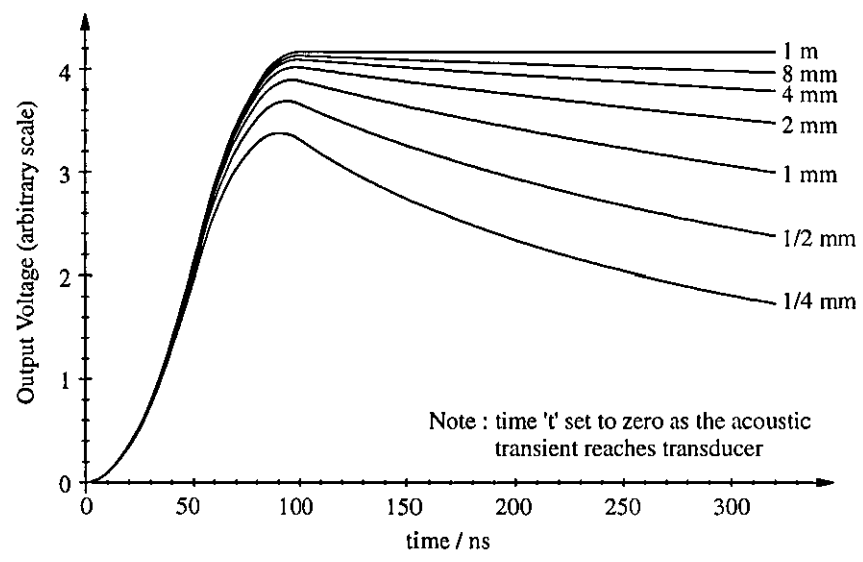


Figure 5.11 - Simulated voltage output of a 110 μm thick transducer with varying distance between point source and transducer. (50ns step pressure pulse)

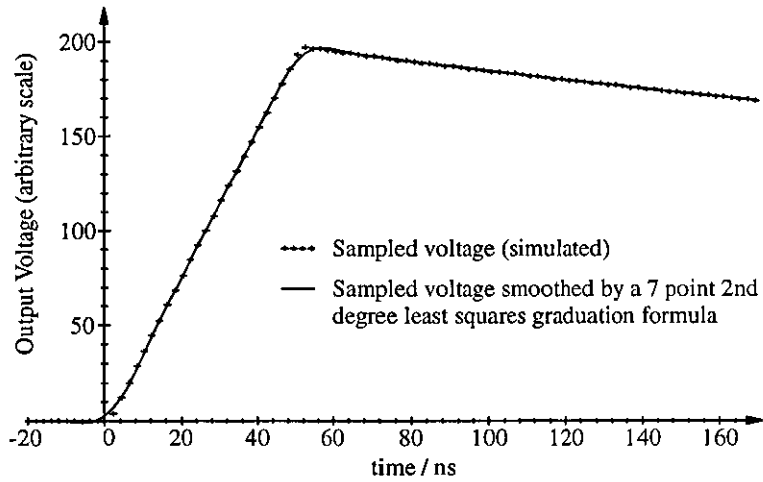
the pressure pulse duration and, the fall off is only dependant on the distance of the source from the transducer - or the curvature of the incident spherical transient.

5.3.4 - Deconvolution and the effects of a reduction in measurement accuracy

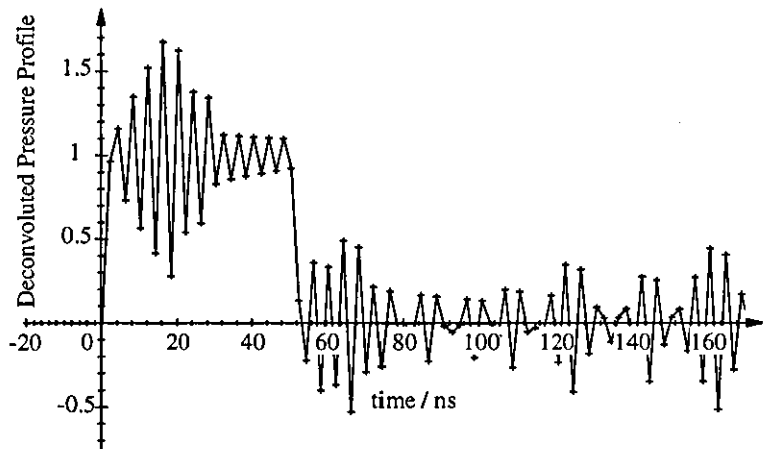
The voltage predicted using a 50ns duration step pulse can successfully be deconvolved using equation (5.18) provided that the calculations are precise. Suppose however that the voltage is measured on a device that does not have infinite precision, such as on a digital oscilloscope. Typically such devices only sample to a resolution of 8 bits, that is 256 different voltage levels, at a maximum acquisition rate of 500 mega-samples per second. The effect of this is illustrated in figure 5.12(a), where the simulated and sampled voltage has been plotted (represented by crosses) for a 50ns step pressure pulse created by a point source 1mm from a 9 μ m thick PVDF film transducer. It can be seen here that the voltage waveform appears virtually unchanged at this resolution. However when equation (5.18) is used to deconvolve the voltage, the resulting pressure profile becomes much more noisy than the original step function used, as shown in figure 5.12(b).

This situation can be improved with the application of *graduation formulae*. There are many smoothing algorithms, a few of which are shown in table 5.1 in order of their effect on the voltage values they are applied to. The simplest form of graduation involves averaging over several neighbouring voltage measurements with time. Whereas more complicated formulae can be derived by either least squares fitting of low order polynomials to the values of the voltage, or alternatively by neglecting higher order differences between the values - as performed by *Woolhouse's formula* and *Spencer's 21 point formula* [23]. The continuous line in figure 5.12(a) shows the 8 bit resolution voltage simulated above smoothed using two applications of a 7 point 2nd degree least squares formula. Applying the deconvolution algorithm to this waveform gives rise to the pressure profile shown as the continuous line in figure 5.12(c). It can clearly be seen that there is a substantial reduction in the noise on the calculated pressure profile. Comparing this to the original 50ns step-like pressure profile (shown as the line of circles in figure 5.12(c)), it can also be seen that there is some degradation in the rise and fall times of the signal caused by the application of the graduation algorithm.

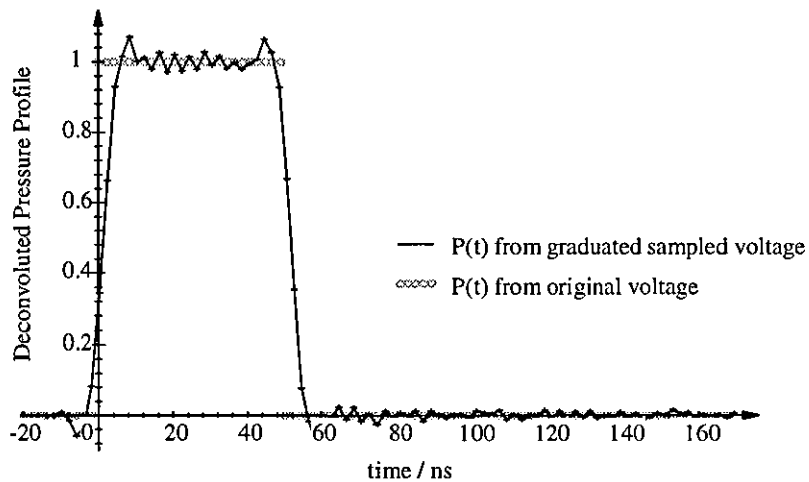
The effects of 'bit' noise increases with the thickness of the PVDF film. Figure 5.13 shows the effects of the 7 point 2nd order least squares graduation formula on a simulated 8 bit resolution voltage calculated for a 110 μ m thick PVDF transducer. Again the input



(a) The simulated voltage for a 50ns step pressure pulse created 1mm from a $9\mu\text{m}$ thick transducer is reduced in resolution to a maximum of 256 different values.



(b) Deconvolution of the reduced resolution voltage gives a noisy pressure profile.

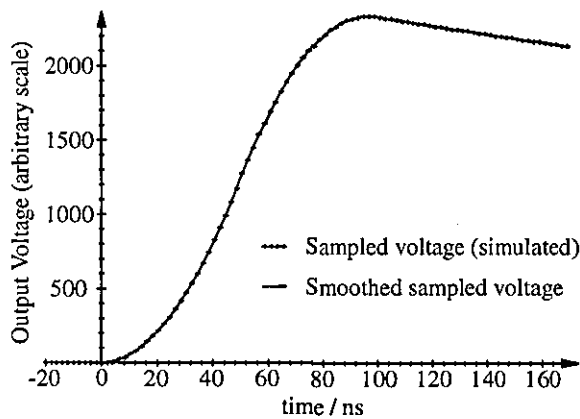


(c) Applying a graduation algorithm to the voltage gives improved results, here using a 7 point 2nd degree least squares formula applied twice.

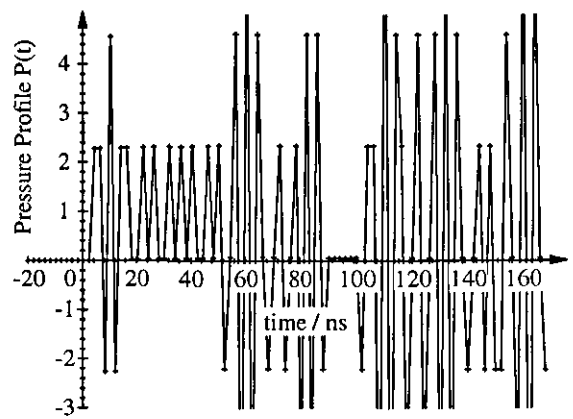
Figure 5.12 - Simulated problems associated with the deconvolution of a 'measured' voltage.

| Type | Equation |
|---|---|
| Averaging | $x'_m = \frac{1}{2n+1} \{x_m + (x_{m+1} + x_{m-1}) + (x_{m+2} + x_{m-2}) + \dots \dots + (x_{m+n} + x_{m-n})\}$ |
| Least squares fitting of a 2nd or 3rd degree parabola | $x'_m = p_0 x_m + p_1 (x_{m+1} + x_{m-1}) + p_2 (x_{m+2} + x_{m-2}) + \dots \dots + p_n (x_{m+n} + x_{m-n})$ where $p_s = 3 \frac{3n^2 + 3n - 1 - 5s^2}{(2n-1)(2n+1)(2n+3)}$ |
| Woolhouse's formula | $x'_m = \frac{1}{125} \left\{ \begin{aligned} &25x_m + 24(x_{m+1} + x_{m-1}) + 21(x_{m+2} + x_{m-2}) + 7(x_{m+3} + x_{m-3}) \\ &+ 3(x_{m+4} + x_{m-4}) - 2(x_{m+6} + x_{m-6}) - 3(x_{m+7} + x_{m-7}) \end{aligned} \right\}$ |
| Spencer's formulae | $x'_m = \frac{1}{350} \left\{ \begin{aligned} &60x_m + 57(x_{m+1} + x_{m-1}) + 47(x_{m+2} + x_{m-2}) + 33(x_{m+3} + x_{m-3}) + \\ &18(x_{m+4} + x_{m-4}) + 6(x_{m+5} + x_{m-5}) - 2(x_{m+6} + x_{m-6}) - 5(x_{m+7} + x_{m-7}) \\ &- 5(x_{m+8} + x_{m-8}) - 3(x_{m+9} + x_{m-9}) - (x_{m+10} + x_{m-10}) \end{aligned} \right\}$ |

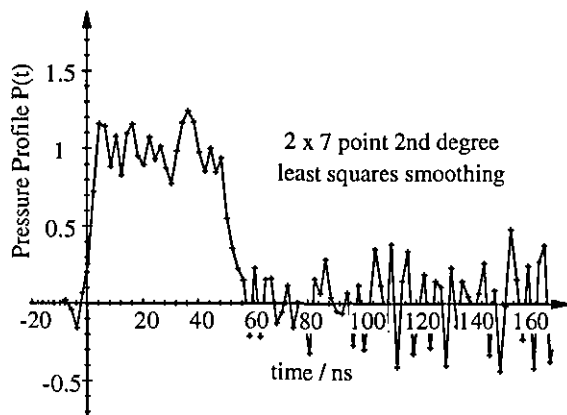
Table 5.1 - Graduation and smoothing formulae [Source: Whittaker & Robinson (1949)].



(a) Output Voltage for a 50ns test pressure pulse.



(b) Reduced resolution voltage results in a very noisy pressure profile.



(b) Improved result after graduation formulae applied to voltage.

Figure 5.13 - As in figure 5.12 but for a 110µm thick piezoelectric transducer, showing an increase in noise during the calculation of the pressure profile from a voltage waveform with low resolution.

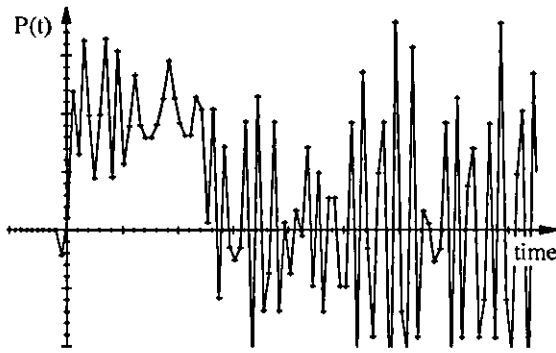
step pressure pulse has a duration of 50ns and the source is 1mm from the transducer. It is clear from figure 5.13(b) that deconvolution of the (unsmoothed) sampled voltage gives rise to a very noisy pressure profile, the step like signal being completely lost in the bit noise. Whereas in figure 5.13(c) it can be seen that two applications of the smoothing on the sampled voltage results in the step like pressure pulse being recovered somewhat, however not completely. Further applications of the same smoothing formula to the voltage data reduces the noise on the deconvolved pressure profile, as seen in figure 5.14. This is at some cost however, since it is apparent that as the number of smoothing iterations is increased the time resolution of the derived pressure profile is reduced. Greater smoothing of the sampled voltage can also be achieved by increasing number of points used by the least squares formula. The resulting pressure profiles are shown in figures 5.15(a) to (c), again showing improvements in the noise and reductions in the time resolution. Finally Spencer's 21 point formula may be applied, as in figure 5.15(d), but yet again the step-like pressure profile is resolved at the expense of time resolution.

In conclusion, it can be seen that the pressure profile may be calculated from discretely measured values of voltage. There is a problem however in that deconvolution amplifies the noise associated with limited measuring device resolution, as well as naturally occurring noise on top of the measured voltage. The effects can be counteracted by the use of graduation algorithms applied to the sampled voltage, however care has to be taken in that too much smoothing can result in the destruction of the signal through reductions in the time resolution.

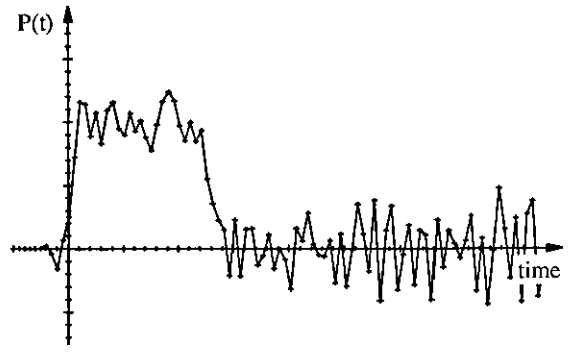
5.4 - Experimental set-up

An experiment to test the ability of the above theory to derive the pressure time profile of a spherically symmetric acoustic transient has been performed using optical cavitation in water. This has been practically achieved using a single pulse of light from a Q-switched Nd-YAG laser to create the event. The laser produces a 1060nm, 55mJ pulse of radiation 30ns in duration, which is focused by a 25mm, $f/1.56$ lens into water so that the focal point is ~ 5 mm below the surface. Dielectric breakdown occurs at the focal point over a region approximately $25\mu\text{m}$ in diameter, limited by both diffraction and spherical aberrations caused by the air-water interface. A plasma is formed which expands rapidly giving rise to an acoustic transient with spherical symmetry about the focal point.

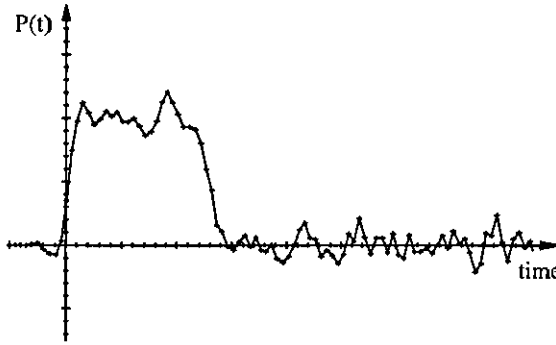
The expanding shock wave has been measured using a Polyvinylidene fluoride thin film transducer with Aluminium electrodes. This was placed at a variety of distances between



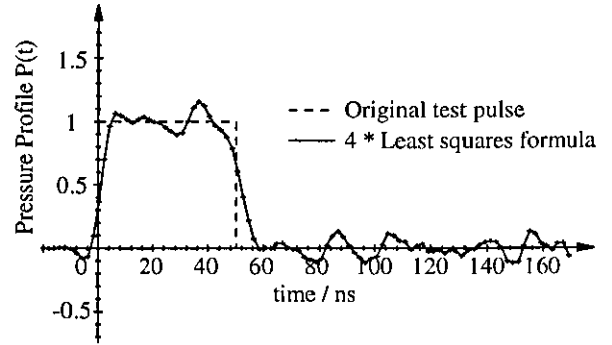
(a) 1 * 7pt 2nd order.



(b) 2 * 7pt 2nd order.

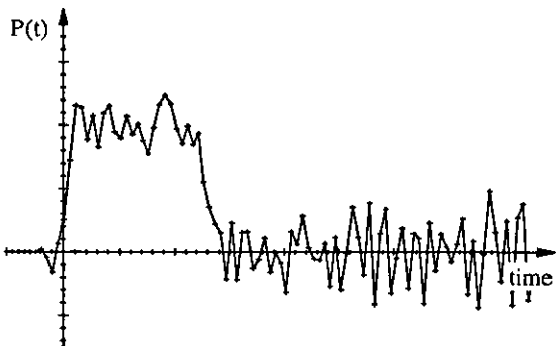


(c) 3 * 7pt 2nd order.

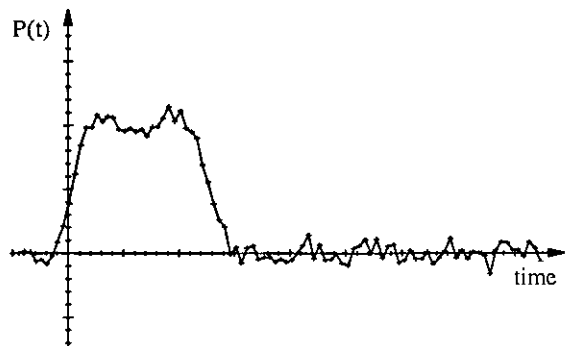


(d) 4 * 7pt 2nd order.

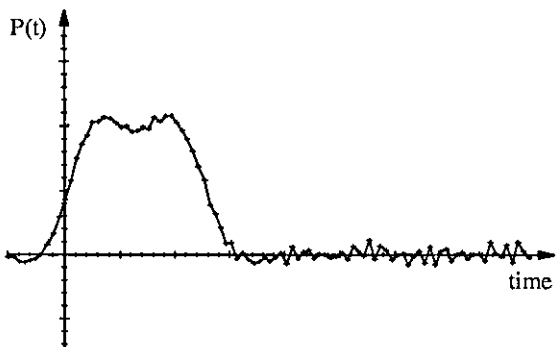
Figure 5.14 - Increasing number of applications of a least squares graduation formula reduces high frequency noise, but affects the temporal response of the transducer.



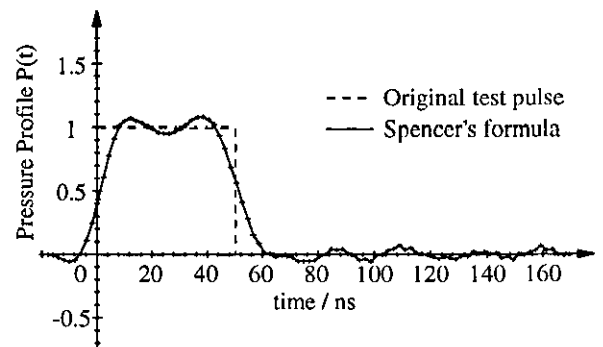
(a) 2 * 7 point, 2nd order least squares



(b) 2 * 11 point, 2nd order least squares.



(c) 2 * 15 point, 2nd order least squares.



(d) Spencer's 21 points formula.

Figure 5.15 - Increasing the number of points used in smoothing formula reduces noise further, however it affects the temporal response of the transducer greatly.

1 to 4mm from the focal region, as shown schematically in figure 5.16. A variety of thin film PVDF transducers were available commercially from Kynar [18], ready polarised and plated. Two size and thickness combinations were used - one of them $\phi=6.25\text{mm}$ in diameter, $a=9\mu\text{m}$ thick and the other $\phi=12.5\text{mm}$, $a=110\mu\text{m}$ thick. The Kynar PVDF film used here has a g_{33} stress constant of $\sim 0.34\text{Vm/N}$ and was used because of its relatively low acoustic impedance (2.6 times that of water,) giving a relatively high acoustic energy transmission (80% for a normally incident wave from water.) It exhibits anisotropic behaviour, having sound speeds of 2200ms^{-1} and 1500ms^{-1} in the directions perpendicular and parallel to the plates of the transducer respectively. The film is backed using a 5mm thick piece of unpolarised PVDF bonded to the film with Cyanoacrylate glue. This is to minimise the acoustic reflections back into the film at the transducer-backing interface.

The metalised plates of the transducer were connected to an Elantec EL2004 unity gain buffer amplifier, the reason for which will be discussed in detail in the next two sections. The electrical connections to the transducer plates were made through copper contacts clamped to the film. This was due to the delicate nature of the metalised plates. The output voltage from the amplifier was then sampled and recorded on a Tektronix TDS520 Digital Storage Oscilloscope at a sampling rate of 2ns. Finally the stored voltage data was transferred to a UNIX based Hewlett Packard mainframe computer where it was used to derive the pressure profile of the measured acoustic transient; that is by applying the discrete form of deconvolution (section 5.3.1, equation (5.18)) and the transducer function developed (section 5.2.4, equation(5.16)). A photograph of the transducer arrangement complete with buffer amplifier circuit can be found in appendix 3.

5.4.1 - The equivalent circuit of a piezoelectric transducer

The equivalent electronic circuit for the output characteristics of a PVDF film transducer is shown in figure 5.17. It is assumed here that the transducer is connected to a voltage measuring device such as an oscilloscope which has input capacitance C_i and resistance R_i . The output voltage V_{out} produced is essentially proportional to the charge Q developed on the plates of the piezoelectric film:

$$V_{\text{out}} = \frac{Q}{C_f + C_i} \quad - (5.22)$$

The capacitance of the transducer can be calculated from the area of the film A and its thickness a :

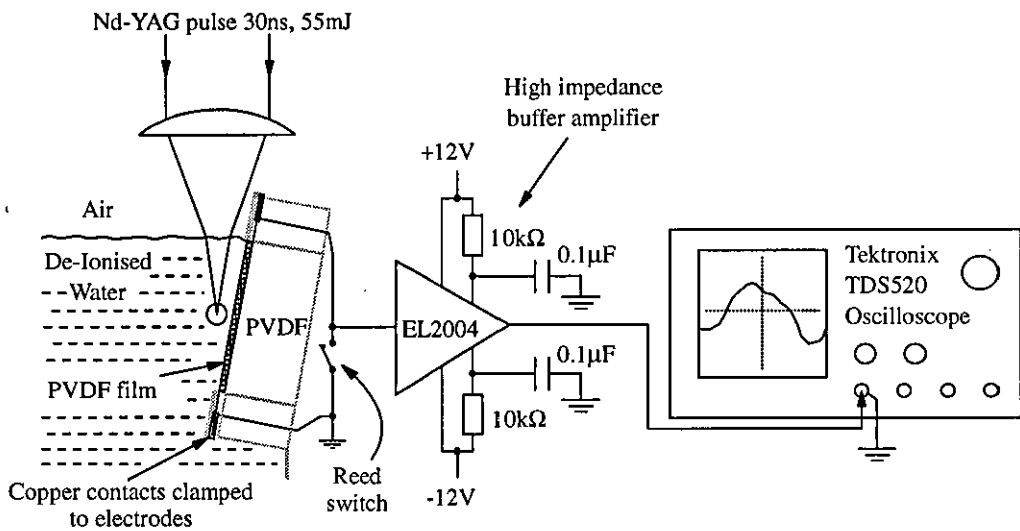


Figure 5.16 - Experimental setup for a PVDF thin film transducer measuring spherical acoustic transients from an optical cavitation event.

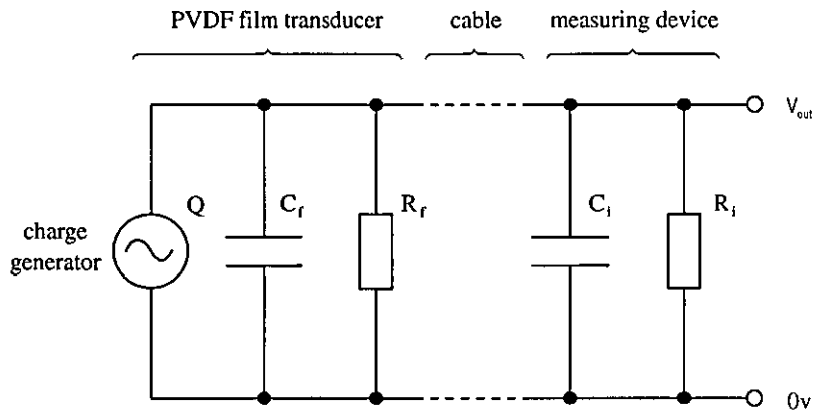


Figure 5.17 - Equivalent circuit of a PVDF film transducer connected to an amplifier.

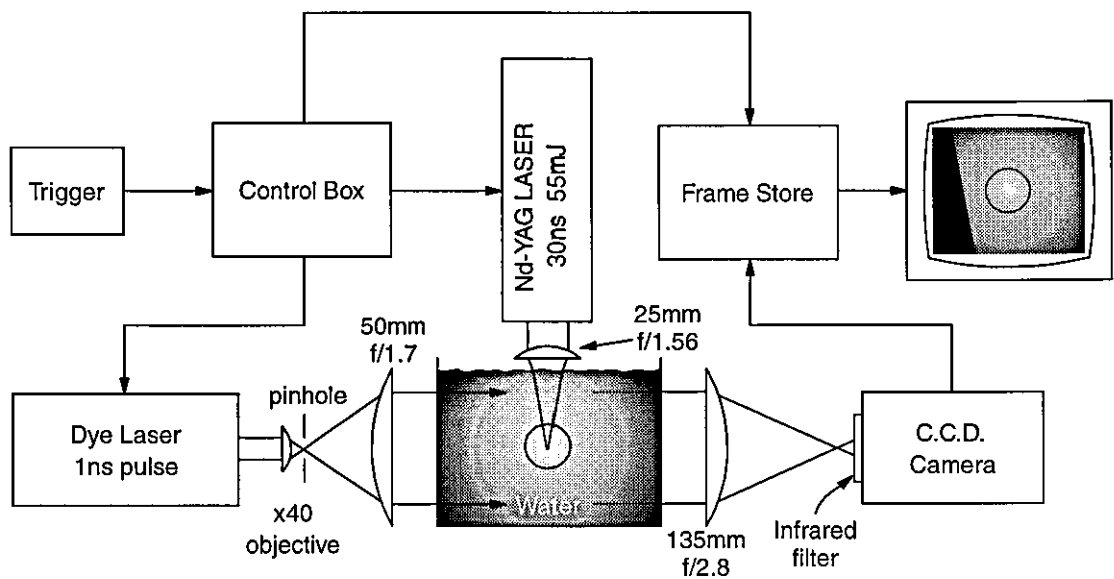


Figure 5.18 - Experimental setup for simultaneous high speed shadowgraphy.

$$C_f = \frac{A\varepsilon}{a} \quad - (5.23)$$

where the permittivity ε of PVDF is about 100pF/m. As a result the 9 μ m thick transducer, which has circular metalised plates 6.25mm in diameter, will have a capacitance of approximately 360pF. The 110 μ m thick, 12.5mm diameter transducer on the other hand will have a capacitance of about 120pF.

The charge developed on the plates of the transducer is directly proportional to the component of force F applied perpendicular to the plates, or alternatively the component of pressure P normal to the plates applied over its entire area:

$$Q = g_{33} \varepsilon F = g_{33} \varepsilon PA \quad - (5.24)$$

where g_{33} is the piezoelectric stress constant of the film, which is about 0.34Vm/N for PVDF. If it is assumed that the measuring device has negligible capacitance, then using the above equations:

$$V_{out} = g_{33} aP \quad - (5.25)$$

That is the output voltage is proportional to the thickness of the transducer and the pressure applied over the entire area of the film, however it is completely independent of the area of the film. If on the other hand a pressure P' is applied to an area A' that is only a fraction of the total area A of the piezoelectric film, then the remaining passive metalised film will act as a capacitor that is in parallel with the active film. As a result the output voltage developed will be:

$$V_{out} = g_{33} aP' \left(\frac{A'}{A} \right) \quad - (5.26)$$

The voltage developed on the plates as a spherically symmetric transient reaches the rear boundary of the transducer film can be estimated as follows, for point source placed at a distance d away from the transducer-water boundary. It is assumed here that the pressure profile of the acoustic transient is step-like and has duration which is longer than the time it takes the wave front to traverse the film. The average area over which pressure is applied to the piezoelectric material is approximately equal to the area mapped by the wave front locus half way into the film, which is parallel to the plates. This can be found by solving equation (5.12) for the radial coordinate $r_{1/2}$ of the transient half way into the

film (i.e. $z=-a/2$) when the wave front has travelled to the rear boundary (i.e. when $c_1\tau=d+a c_1/c_2$). After a little simplification:

$$A' \approx \pi r_{1/2}^2 \approx \pi \frac{c_1}{c_2} ad \quad - (5.27)$$

Note that it has been assumed here that the film thickness a is very much smaller than the source distance d . This allows the voltage developed as the transient reaches the rear of the film to be estimated using equation (5.26):

$$V_{out} \approx \frac{4g_{33} c_1 d a^2 P'}{c_2 \phi^2} \quad - (5.28)$$

where ϕ is the diameter of the active PVDF film. As an example, the output voltage can be estimated for a point source placed 1mm away from the film, the step-like pressure pulse having a peak pressure of 100MPa as it reaches the transducer. In the case of the 9 μ m, 6.25mm diameter transducer the output voltage will reach just $\sim 0.2V$ after 4ns; whereas for the 110 μ m, 12.5mm diameter transducer the output will be $\sim 7.2V$ after 50ns.

Finally output voltage is also frequency dependant since the measuring circuit forms a R-C high-pass filter, cutting off the signal at frequencies below:

$$f_c = \frac{1}{2\pi RC} = \frac{R_f + R_i}{2\pi(C_f + C_i)R_f R_i} \quad - (5.29)$$

That is, the charge developed on the film due to an applied force decays through R_i and R_f with a time constant of:

$$t_{RC} = \frac{C_f + C_i}{1/R_f + 1/R_i} \quad - (5.30)$$

As a result the perfect measuring device should have infinite input impedance and negligible capacitance. In such a case the decay time t_{RC} will be of the order of 1000 seconds for both transducers. This is not the case in reality however, the problems of which will be discussed in the next section.

5.4.2 - The use of a buffer amplifier

The comparatively high electrical volume resistivity ($10^{13}\Omega\text{m}$) and capacitance of PVDF transducers mean that the output voltage will be greatest when the capacitance of the measuring device is very small, as predicted by equation (5.22) in the last section. Also the signal is least distorted when the input resistance is very large. High sampling rate digital oscilloscopes have low input capacitance and work best with an input impedance of 50Ω (to avoid signal reflections at lead terminations) giving a time constant of $t_{rc}\sim 10\text{ns}$. This is considerably shorter than the duration of the acoustic transient t_p , which for optical cavitation found using Mach-Zehnder interferometry is $\sim 200\text{ns}$ (calculated from [10] using $t_p\sim r_d/c_2$, where r_d is the thickness of the acoustic transient.) Therefore a high input impedance buffer could be used to strengthen the signal and increase the time constant.

Practically such a device is the Elantec EL2004 unity gain buffer amplifier [24], which has a high input impedance of $10^{11}\Omega$ and low capacitance of 3pF . It is designed to drive a load resistance of 75Ω and passes frequencies from d.c. to 350MHz . The input of the amplifier is connected very close to the film transducer to keep the inductance of the circuit to a minimum, otherwise the circuit could oscillate. Also since the input impedance of the buffer amplifier is extremely high the input floats and can saturate, therefore a reed switch is incorporated sinking the input briefly to ground level before any measurements are taken.

The output of the buffer amplifier is connected to an oscilloscope which has a sampling rate at least as fast as the rise time of the acoustic transient ($<10\text{ns}$ [10].) Here a Tektronix TDS520 digital oscilloscope is used; which has an input impedance of 50Ω , capacitance of 10pF , bandwidth of 1GHz and a maximum sampling rate of 500M samples per second. The oscilloscope records the voltage signal with an 8 bit accuracy (256 voltage levels) and can store up to 15000 data points, which corresponds to $30\mu\text{s}$ at the maximum sampling rate. The data stored is transferred to a UNIX based Hewlett Packard mainframe computer where it is processed in exactly the same way as the simulations, using Maple 'V' symbolic programming language.

5.4.2 - Shadowgraphy

As a visual comparison and simultaneous to measurements made using the planar PVDF transducer, a focused shadowgraph of the acoustic transient has been taken using the set-up illustrated in figure 5.18. In this high speed photographic technique, the propagating acoustic transient is briefly illuminated by a collimated beam of laser light. This takes place a few hundred nanoseconds after the initiation of the optical cavitation event by the Nd-YAG laser and, the illumination pulse is sufficiently short so as to 'freeze' the propagating acoustic wave as it is being imaged onto a CCD camera. The output field from the camera which contains the illuminated image of the acoustic transient is then stored in a frame grabber and is subsequently viewed on a TV monitor. The transient refracts some of the illumination light away from its normal path, which is seen as a shadow on the resulting television picture.

In the experimental set-up here a PRA dye laser model LN102 operating with the dye Courmarin 500 is used as the pulsed illumination source. This produces an output pulse 500ps in duration with an energy of 15 μ J centred on the green visible wavelength of 514nm. The dye laser is pumped using a PRA 'Nitromite' model LN103TEA pulsed nitrogen laser operating in the near ultra-violet wavelength of 337nm. Before passing through a cell containing the cavitation event, the dye laser radiation is spatially filtered by a 40x microscope objective focused onto a 25 μ m pinhole. It is then collimated using 50mm f/1.7 SLR camera lens resulting in a 25mm diameter illumination beam.

The directly illuminated cavitation event is imaged onto a NEC NI-22C CCD camera using a 135mm f/3.5 telephoto camera lens. Since the radiation from the Nd-YAG laser ($\lambda=1060$ nm) is scattered by the plasma it creates during optical cavitation, it can be detected by the camera. It is therefore removed using a heat mirror placed just before the CCD camera. The camera outputs image information as a 20ms analogue field, which is stored by the frame grabber as a digital picture, made up of 256 horizontal by 256 vertical pixels with a grey scale resolution of 64 levels. According to the Gladstone-Dale relation [25,26] the change in refractive index is approximately linear with pressure for water up to 100MPa [27]. This results in a localised decrease in the light intensity (or grey scale of each pixel) recorded by the camera [28], which is due to light being refracted by the acoustic transient beyond the aperture of the imaging lens, as described in chapter 3, section 3.5.4.

Figure 5.19 shows a shadowgraph taken using the set-up described above. The acoustic transient can be clearly identified here as the dark circular ring in the centre of the

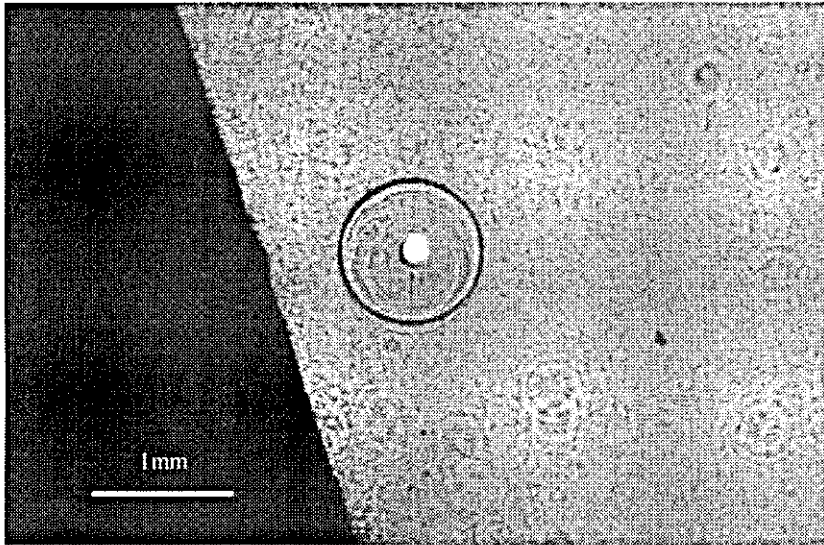


Figure 5.19 - Shadowgraph of the initial acoustic transient from optical cavitation event.

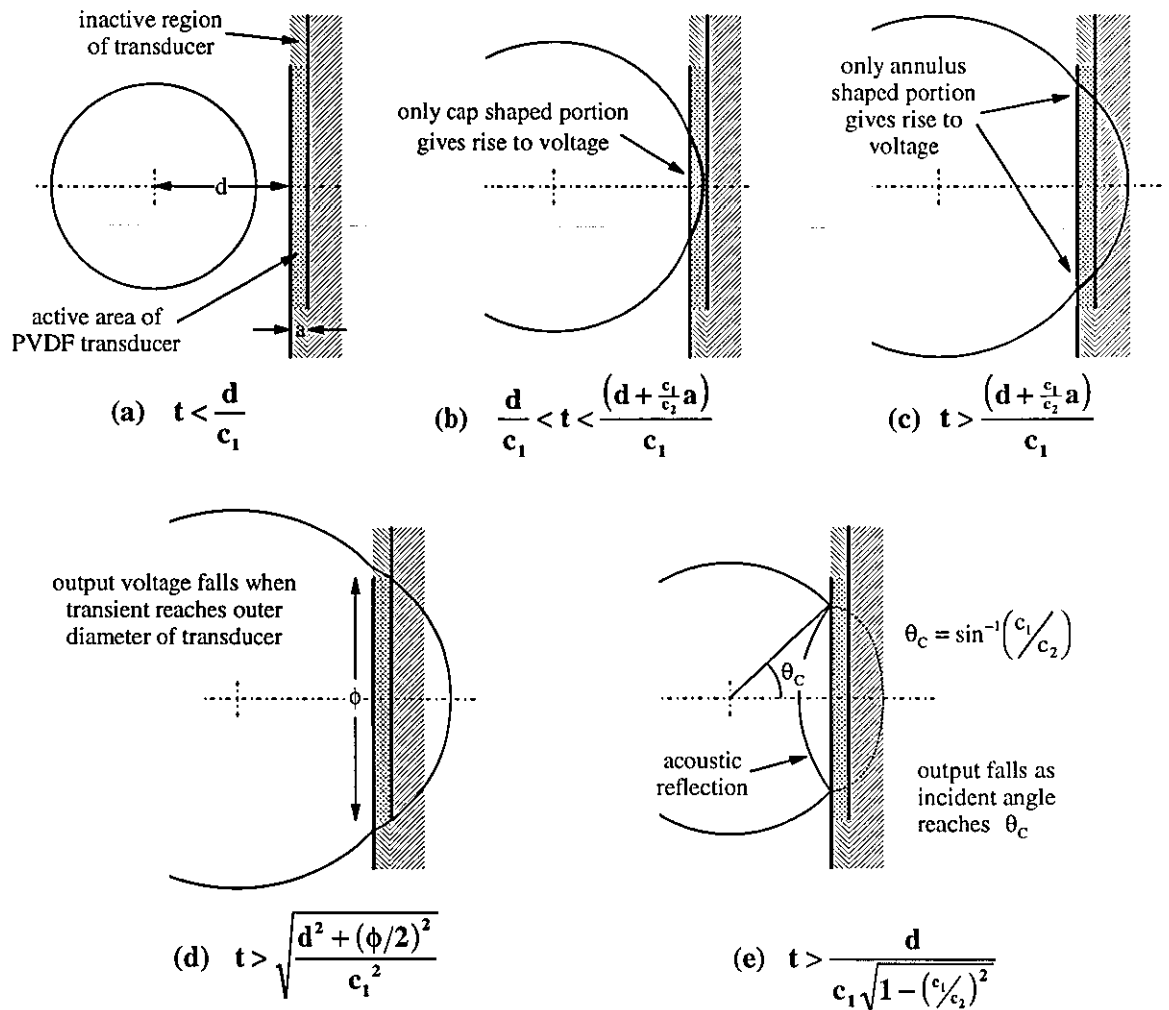


Figure 5.20 - Stages in the rise and fall of the output voltage.

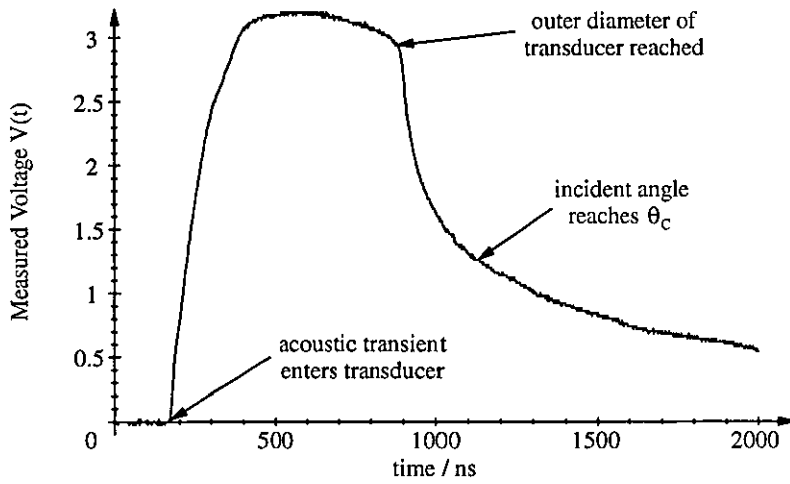
picture. Clearly the acoustic transient is spherically symmetric about the generating plasma, which is seen here as the circular white dot. The PVDF transducer can also be seen here on the left hand side of the image. Furthermore this set up was used to measure the source-transducer distance in the experiments that follow.

5.5 - Experimental results from 9 μ m thick PVDF transducer

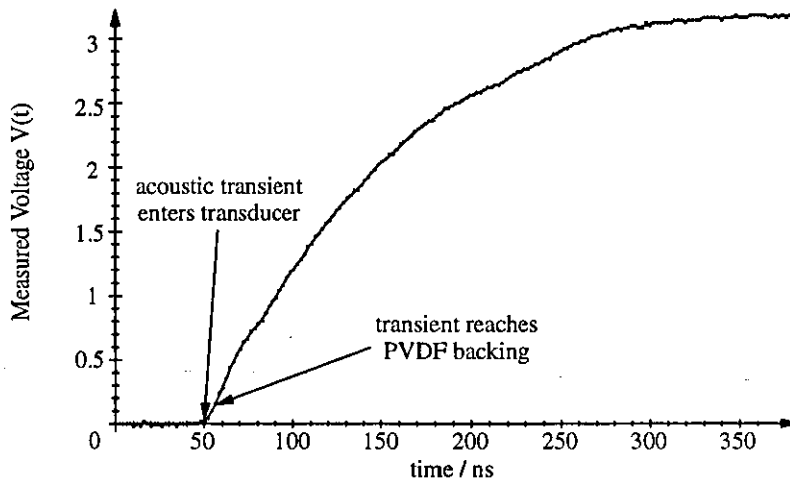
The voltage trace recorded from the 9 μ m thick, 6.25mm diameter polyvinylidene fluoride film transducer, placed about 4mm away from the dielectric breakdown source of acoustic transients can be seen in figure 5.21(a). The acoustic transient takes approximately 2.6 μ s to reach the transducer after its generation, which is much longer than the duration of the transient and the resulting voltage pulse. As a result the voltage trace has been plotted here starting shortly before the rise in voltage, and the time scale is not synchronised to the laser pulse. Furthermore the various stages in the progression of the transient through the transducer are shown in figure 5.20, and these can be used to describe the changes in the measured voltage.

An expansion of the voltage trace can be seen in figure 5.21(b), and again the time scale starts at an arbitrary point in time about 50ns before the voltage pulse from the transducer is detected. Each point represents a voltage sample made every 2ns by the oscilloscope. It can clearly be seen that the voltage rises over a period of approximately 200ns before reaching a peak of about 3V. The position of the shock front of the transient during this rise in voltage can be seen schematically in figure 5.20(b) and (c). Due to the relatively short time scale, no apparent change in gradient can be seen in the voltage trace when the leading edge of the transient reaches the backing material 4ns after the start of the voltage pulse.

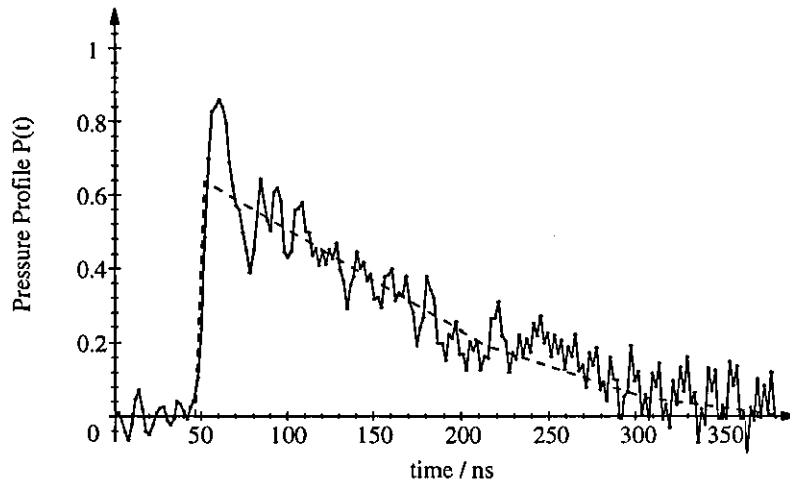
In figure 5.21(a) it can be seen that the voltage trace remains at about 3V for about 500ns decaying slightly, before falling off steeply and decaying to 0V several microseconds later. This fall off coincides with the point in time calculated for the locus of the transient to reach the outer diameter of the metalised transducer, as shown schematically in figure 5.20(d). When the incident angle of the transient at the water-transducer interface reaches the critical angle, as in figure 5.20(e), no significant decrease in the voltage can be seen. For isotropic media the acoustic transient should have been entirely reflected at the water-transducer boundary. This is most likely due to the anisotropic behaviour of the piezoelectric material, that is although the speed of sound of the PVDF film is about 2200ms⁻¹ in the direction perpendicular to the electrodes, it is about the



(a) Voltage measured experimentally using apparatus in figure 5.16.



(b) Expansion of voltage trace (a) around initial rise.



(c) Pressure Profile calculated from measured voltage, with 6 applications of a 5 point 2nd degree least squares graduation formula.

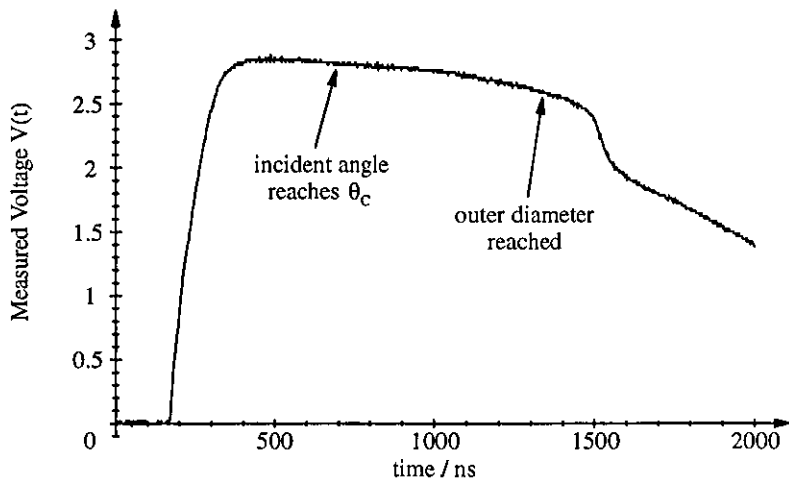
Figure 5.21 - Results from experiment with $9\mu\text{m}$ PVDF film transducer placed 4mm away from the source of an optical cavitation event.

same as that of water (1500ms^{-1}) parallel to the plates. Furthermore the acoustic reflection properties at the interface are somewhat complicated by the PVDF film being somewhat smaller than the thickness (or wavelength) of the acoustic transient.

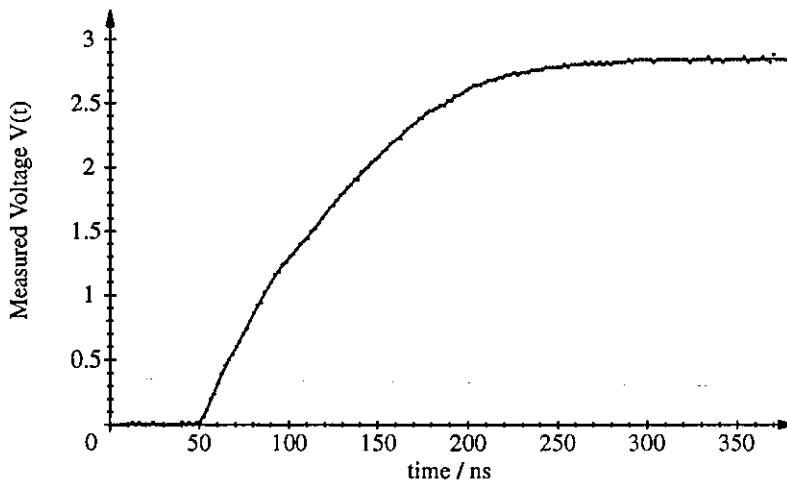
Using the transformations described earlier, the experimentally measured voltage trace has been deconvolved to give the temporal pressure profile shown in figure 5.21(c) by the solid line. In order to reduce the effects of noise and the limited resolution of the oscilloscope, the voltage was first smoothed using 6 applications of the 5 point 2nd degree least squares graduation formula described in section 5.3.4. Figure 5.21(b) shows the resulting graduated voltage as a solid line, which is clearly very similar to the data points measured. The resulting temporal pressure profile in figure 5.22(c) has the same time scale as the voltage trace in figure 5.21(b), and again each point represents a calculation made every 2ns. The vertical pressure axis on the other hand axis has an arbitrary scale.

Clearly this technique has resolved the acoustic transient together with the shock front. The temporal resolution has been estimated here to be about 4ns, this is limited by amount of smoothing used to reduce the effects of noise. The acoustic transient has a duration of about 250ns, and the shock front has been measured here to have a rise time of approximately 8ns, that is for a 10% to 80% rise in signal. Furthermore the shape of the acoustic transient agrees with that measured in chapter 4 using the prototype optical transducer, and also with that measured quantitatively by Ward [2,10,29] using high speed Mach-Zehnder interferometry. Interestingly, it can also be seen that the end of the transient pressure profile roughly coincides with the end of the rise in voltage. This was also observed for step like pressure profiles during the simulations performed earlier in section 5.3.3, figure 5.7.

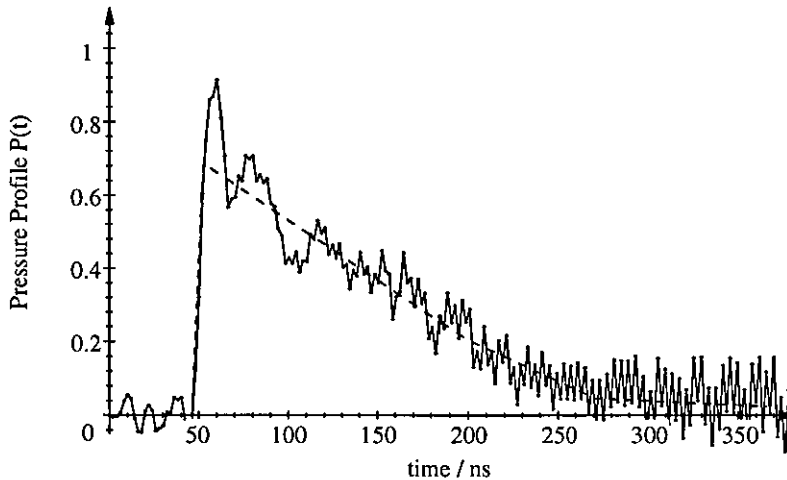
The voltage recorded for the same transducer moved to a slightly closer distance of 2mm away from the point source is shown in figures 5.22(a) & (b). Again it can clearly be seen that the voltage rises over approximately the same period of time, about 200ns, reaching a peak voltage of about 2.8volts. This concurs with the simulations made earlier in section 5.3.3, figure 5.8, where variations in the point source to transducer distance d were seen not to change the rise time and peak voltage significantly. In figure 5.22(a) the voltage then remains at about 2.8V for about $1\mu\text{s}$, although decaying slightly. When the incident angle of the acoustic transient is close to the calculated critical angle, as in figure 5.20(e), no change in the gradient of the signal can be identified. Again this is most likely to be due to the anisotropic nature of the PVDF film transducer. The voltage is finally observed to begin to fall off about 200ns after the transient reaches the outer



(a) Voltage measured experimentally for transducer 2mm from source.



(b) Expansion of voltage trace (a) around initial rise.



(c) Pressure Profile calculated from measured voltage, with 6 applications of a 5 point 2nd degree least squares graduation formula.

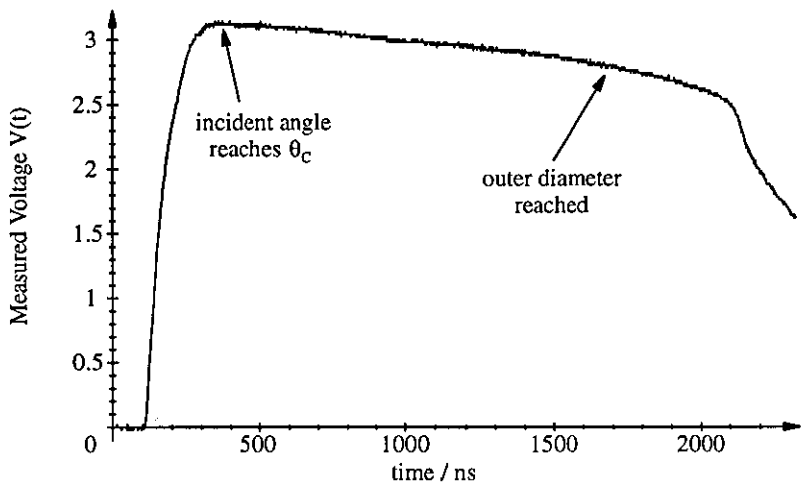
Figure 5.22 - Results from experiment with $9\mu\text{m}$ PVDF film transducer placed 2mm away from the source of an optical cavitation event.

metalised diameter of the transducer, as shown schematically in figure 5.20(d). In this case the voltage probably does not fall off immediately because of a slight misalignment between the point source of the acoustic transient and the central axis of the transducer.

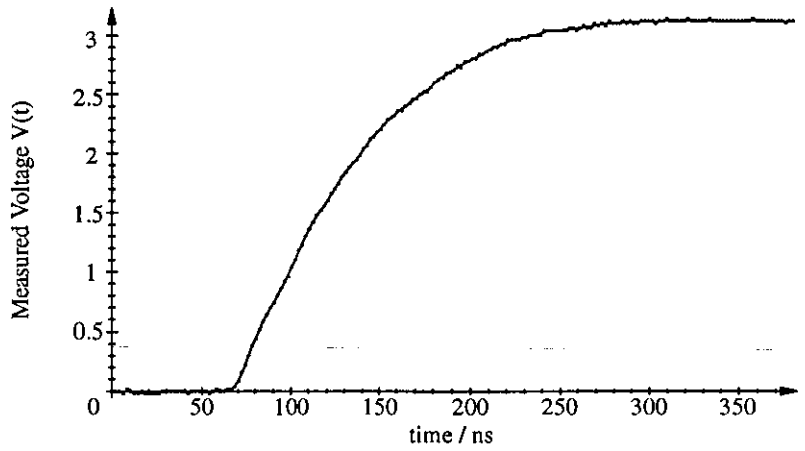
The temporal pressure profile calculated using the voltage data recorded is shown in figure 5.22(c). Again the voltage data was first smoothed using 6 applications of a 5 point 2nd degree least squares algorithm in order to reduce the adverse effects of noise. The same temporal scale has been used as the voltage data in figure 5.22(b), however the vertical axis has arbitrary scaling. Clearly the shape of the pressure profile is almost exactly the same as that obtained above for the larger transducer to source distance. The pressure pulse has a duration of about 200ns and a very sharp shock front, the rise time of which has been measured to be about 8ns. Again the temporal resolution is about 4ns, which is limited by the graduation algorithm used to improve the signal to noise ratio.

Finally the 9 μ m PVDF film transducer was moved even closer to the point source, to a distance of just 1mm away. This was the closest achievable distance experimentally without the focal cone of the generating Nd-YAG light being obstructed by the transducer. Furthermore the wavefront curvature at the transducer boundary is at its highest compared with the previous two experiments. As before a rise in voltage is seen over a period of 200ns, reaching a peak of about 3.1volts. At this source-transducer distance the incident angle of the acoustic transient reaches the critical angle very quickly, as marked on figure 5.23(a), however as before no significant fall off in the voltage can be seen. The voltage subsequently remains at the same level for a further 2 μ s, decaying slightly, before eventually falling off to zero volts several microseconds later. Again it is thought that the fall off is due to the transient reaching the outer metalised diameter of the transducer, although there appears to be some misalignment between the point source and the radial axis of the transducer.

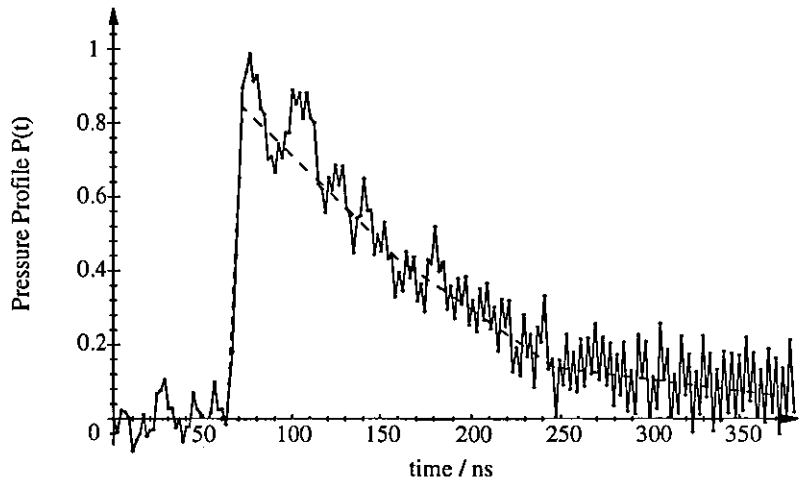
The temporal pressure calculated using the voltage data in figure 5.23(b), smoothed using the same algorithm as described above, is shown in figure 5.23(c). Clearly the shape of the curve is almost identical to that measured at the other source to transducer distances above. That is the shock front is clearly resolved and has a rise time of about 8ns, and it is followed by an approximately linear pressure decay lasting for approximately 200ns.



(a) Voltage measured experimentally for source distance 1mm from transducer.



(b) Expansion of voltage trace (a) around initial rise.



(c) Pressure Profile calculated from measured voltage, with 6 applications of a 5 point 2nd degree least squares graduation formula.

Figure 5.23 - Results from experiment with $9\mu\text{m}$ PVDF film transducer placed 1mm away from the source of an optical cavitation event.

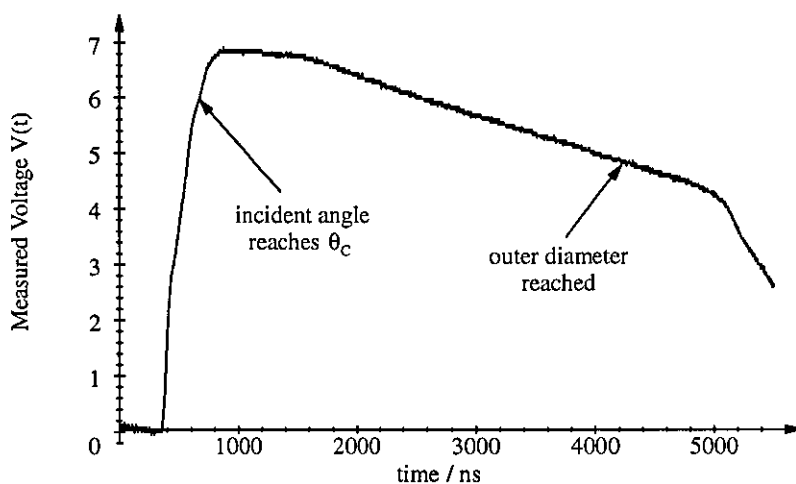
5.6 - Experimental results from 110 μ m thick PVDF transducer

A voltage trace recorded from the 110 μ m thick, 12.5mm diameter polyvinylidene fluoride film transducer is shown in figure 5.24(a). The transducer was placed just 1mm away from the optical cavitation source, and this was the smallest possible distance achievable experimentally without the Nd-YAG laser light being obstructed by the transducer. As with the traces measured using the 9 μ m thin film transducer in the last section, the time scale here starts about 400ns before the voltage pulse is detected and is not synchronised to the Nd-YAG laser pulse.

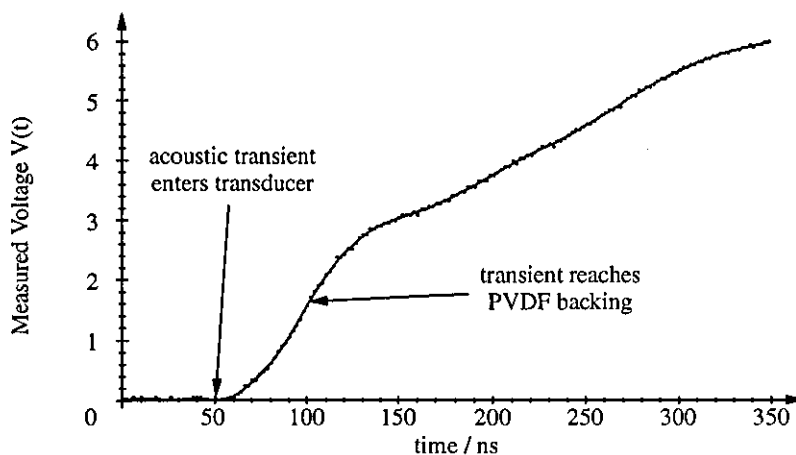
The initial rise in voltage occurs over a period of about 400ns which is considerably longer than that from the 9 μ m transducer placed at the same distance. This can to some extent be explained by the increase in the thickness of the transducer film, the transient taking about 50ns to traverse the film here compared with just 4ns for the 9 μ m film. Assuming that the acoustic transient has a similar pressure-time profile to the one measured in figure 5.23(c) using the 9 μ m transducer, the rise time should be around 250ns. It is thought that the extended rise time could be due to a small amount of acoustic reflection at the interface between the transducer film and the unpolarised backing material. This could be produced by ineffective bonding at the interface, or might alternatively be due to the slightly differing acoustic properties of the materials across the boundary. That is, in plane of the electrodes the polarised PVDF film has a lower wave propagation speed (1500ms⁻¹) compared to the direction normal to the plates (2200ms⁻¹). Whereas the unpolarised PVDF backing material is isotropic and has the same sound speed in all directions of 2200ms⁻¹, and it therefore has a different acoustic impedance to the transducer film in the direction parallel to the plates.

In this experiment the acoustic transient reaches the critical incident angle calculated using figure 5.20(e) before the output voltage reaches its peak. At this point the acoustic transient should be completely reflected at the water-transducer boundary, however as seen before no clear fall off in voltage can be identified. Again it is thought that this is due to the anisotropic wave propagation properties of the polarised PVDF piezoelectric material.

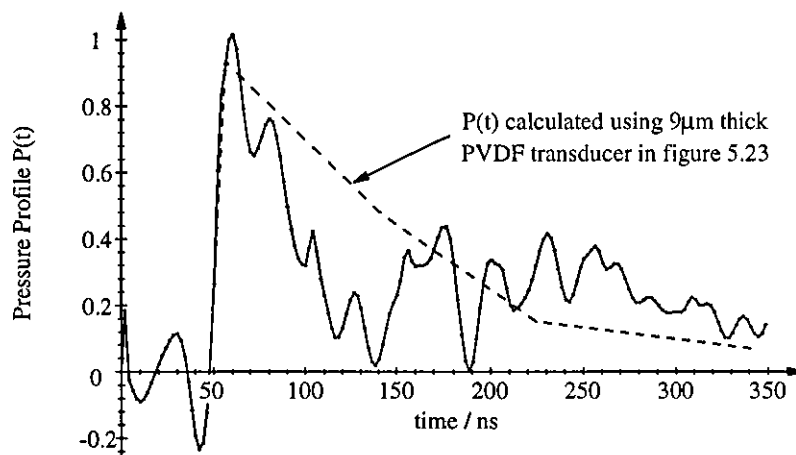
The voltage trace shown reaches a peak of approximately 6.9 volts, however over a number of successive acoustic transients measured experimentally this value was found to fluctuate by up to 20%. Although just over twice the magnitude of that recorded by the 9 μ m transducer, the peak voltage recorded by the 110 μ m thick transducer is significantly lower than can be expected given that the voltage response of a thin film



(a) Voltage measured experimentally for source distance 1mm from transducer.



(b) Expansion of voltage trace (a) around initial rise.



(c) Pressure Profile calculated from measured voltage, with 2 applications of Spencer's 21 point graduation formula.

Figure 5.24 - Results from experiment with 110 μm , 12.5mm ϕ PVDF film transducer placed 1mm away from the source of an optical cavitation event.

piezoelectric transducer is proportional to the piezoelectric film thickness. Typically this should give rise to a factor of 12 increase in the peak voltage. This can be explained by the fact that the transducer film utilised here has a metalised area 4 times the size of the $9\mu\text{m}$ film used in the last section. The acoustic transient generates charge on only a small portion of the transducer's plates, and the remaining passive metalised film then acts as a capacitor placed in parallel with the active film, giving rise to a reduced voltage output. The combined effect of increased metalised area and film thickness should therefore give rise to a factor of 3 increase in the peak voltage, which is within the limitations of experimental error is quite close to that observed.

After reaching a peak, the voltage trace is subsequently seen to decay 2.5 volts over a period of about $4\mu\text{s}$ before eventually falling off to zero volts. The voltage decay can be attributed here to the annular region that the locus of the transient forms within the transducer film, as shown schematically in figure 5.20(c). Although the annular region has a constant area in the plane of the transducer, the pressure of the spherical acoustic transient reduces in amplitude according to an inverse distance relationship which gives rise to the decay. Furthermore over such a long period of time the decay is probably added to by the leakage of charge in the transducer-amplifier circuit. As seen experimentally with the $9\mu\text{m}$ film transducer and shown schematically in figure 5.20(d), the final fall off in voltage is most likely due to the transient reaching the outer metalised diameter of the transducer electrodes. Again it is likely that central axis of the transducer and the source are slightly miss-aligned.

Figure 5.24(b) shows a magnification of the first part of the voltage rise, in which each data point plotted represents a sample made by the oscilloscope every 2ns. As before, the time scale shown starts about 50ns before the voltage pulse. The voltage signal was graduated using 2 applications of Spencer's 21 point formula described earlier in section 5.3.4, and this is shown by the solid line. Clearly there are no obvious departures between this and the measured data points. As commented in section 5.3.4, a more powerful graduation algorithm was used here because the $110\mu\text{m}$ film transducer was found to be significantly more susceptible to noise. The temporal pressure profile was then calculated using the smoothed voltage trace applying the theory developed earlier, and is shown in figure 5.24(c). Clearly the shock front has been resolved here and has a rise time of about 8ns. According to figure 5.24(c) the excess pressure subsequently falls to almost zero over a period of about 90ns, but then appears to rise again to approximately 30% of its peak value for a further 150ns. As commented in section 5.3.4, there is a trade off between the resolution of the derived pressure and the temporal resolution due to the effects of the graduation algorithm. The simulations made with a

step-like pressure profile found that the temporal resolution was reduced to ~ 8 ns, and from this it can be said that the shock front is only just resolved.

The dashed line in figure 5.24(c) shows the temporal profile calculated in the last section using voltage data recorded from the $9\mu\text{m}$ thick film transducer. Although both of the transducer films were used to detect similar acoustic transient generated at the same point source to transducer distance, there are clearly some distinct differences between the two temporal pressure profiles derived. Furthermore a great number of voltage traces were recorded of different transients and it was found to be very difficult to deduce a definite temporal profile due to the increased noise susceptibility of the thick transducer. Given that the profiles derived in the last section using the $9\mu\text{m}$ transducer concur with those measured in chapter 4 quantitatively measured with the prototype optical transducer, it is quite likely that the temporal pressure profile calculated here is inaccurate.

The apparent fall off in calculated pressure 50ns after the incidence of the transient can not be attributed to a small amount of acoustic reflection at the interface between the transducer film and backing material. Clearly only a small perturbation in the voltage is required to produce the relatively large fall off in pressure observed, and it is not entirely certain as to the cause of this effect. One possible cause is anisotropic piezoelectric behaviour of the piezoelectric material, the effect of which can be explained as follows. Each individual transducer element is subject to an excess pressure which acts in all directions. The theory developed in section 5.2 assumes that only stress components applied normal to the plates of the transducer give rise to a voltage output. This is in fact a simplification of the actual nature of piezoelectric transducers since although comparatively small, the components of stress applied in the plane of the film also give rise to a negative effect upon output voltage, counteracting the voltage developed by the components of stress normal to the plates. It is thought that this effect increases with the annular radius of the transient within the transducer film, and only just becomes apparent as the transient reaches the backing material - that is when the fall in pressure is observed. It is beyond the scope of this thesis to give a more detailed analysis of this effect, however, and it is suggested that for further work anisotropic behaviour of the PVDF film should be studied in more detail and the transducer function corrected accordingly.

Finally the peak pressure of the acoustic transient measured here can be estimated using equation (5.28), which was developed in section 5.4.1. From figure 5.24(b) the recorded output voltage reaches 1.5V as the acoustic transient reaches the unpolarised PVDF backing material. Using equation (5.28) this results in a peak pressure of about 225 bar,

which is in good agreement with the measurements made using the prototype optical transducer in chapter four with the same laser source. This value is however likely to be slightly higher than that calculated because in the development of equation (5.28) it was assumed that the acoustic transient had a step pressure profile.

Conclusions

In this chapter a technique for measuring spherically symmetric acoustic transients in water has been demonstrated using a relatively large area planar Polyvinylidene-fluoride (PVDF) film piezoelectric transducer. This has been done by first modelling the propagation of such a wave through the media involved. The transducer was considered to be made up of a large number of small elements which were shaped according to the locus of the transient at different points in time. Each element measures the component of pressure normal to the film of a small section of the acoustic transient which is within the transducer. The voltage output of the transducer was then calculated as a summation of all of these pressure components.

Using the theory developed, simulations were performed in which spherical acoustic transients with step-like pressure profiles are incident upon several piezoelectric film transducers with different thicknesses. The voltage output of such transducers were found to be determined by both the duration of the transient, and the propagation time of the leading edge of the transient across the thickness of the transducer. The fall off in voltage on the other hand was found to be very much longer and followed an inverse time relationship, which was attributed to an annular shaped portion of the transient remaining inside the transducer even after the leading edge has left the transducer.

The reverse process of deriving the temporal pressure profile of spherical acoustic transients from the simulated voltage traces has also been studied. It was found that the effects of signal noise and under-sampling of the measured voltage were significantly amplified during the inversion process, particularly for thick film transducers. The amount of noise could to some extent be reduced by the application of graduation algorithms on the measured voltage. It was found however that there is a trade off between the resulting temporal and spatial resolution of the derived pressure profile.

The same inversion process has also been demonstrated experimentally determining the temporal pressure profiles of spherically symmetric acoustic transients created by optical cavitation. These were measured using two thin film polyvinylidene-fluoride transducers

with different film thicknesses, which were placed at a range of distances away from the source. The results obtained showed that when a relatively thin transducer film is used, the temporal pressure profile of the acoustic transients can be resolved accurately. Furthermore the profiles agree with those measured earlier in chapter 4 using the prototype optical transducer. It was however found to be very difficult to deduce the pressure profile of the acoustic transients using a transducer film which is thick compared with the duration of the transient. This was thought to be due to the anisotropic behaviour of the piezoelectric material used. It is suggested that for further work these effects could be studied in more detail, and improvements could then be made to the model of the piezoelectric transducer which has been developed.

In conclusion this technique addresses the problem of characterising transients that originate from sources smaller than the measuring device. If the spatial shape, or symmetry, of an acoustic transient is known as it progresses through the liquid, then its pressure-time profile can be derived from the voltage signal measured by a relatively large planar piezoelectric transducer. As a result this technique could be extended to systems with other symmetries. For example, cylindrically symmetric acoustic transients generated, say, by a collimated pulsed laser beam passing through a slightly absorbing liquid could be characterised using this technique, and this is suggested for further investigation.

References

- [1] Felix, M. P. and Ellis, A. T. (1971) - *Laser-Induced Liquid Breakdown - A Step-By-Step Account*, Appl. Phys. Lett. **19**, pp484-486.
- [2] Ward, B. and Emmony, D. C. (1991) - *Interferometric Studies of the Pressures Developed in a Liquid During Infrared Laser Induced Cavitation Bubble Oscillation*, Infrared Phys. **32**, pp489-515.
- [3] Vogel, A. (1993) - *Time Resolved Measurements of Shock-Wave Emission and Cavitation-Bubble Generation in Intracocular Laser Surgery with ps- and ns-Pulses and Related Tissue Effects*, SPIE Ophthalmic Technologies III. **1887**, pp312-322.
- [4] DeReggi, A. S., Roth, S. C., Kenney, J. M., Harris, G. R., and Edelman (1981) - *Piezoelectric Polymer Probe for Ultrasonic Applications*, J. Acoust. Soc. Am. **69**, pp853-859.
- [5] Platte, M. (1985) - *A Polyvinylidene Fluoride Needle Hydrophone for Ultrasonic Applications*, Ultrasonics **23**, pp113-118.

- [6] Schoeffmann, H. (1988) - *Time-Resolved Investigations of Laser-Induced Shock Waves in Water by use of Polyvinylidene fluoride Hydrophones*, J. Appl. Phys. **63**, pp46-51.
- [7] Vogel, A. (1988) - *Acoustic Transient Generation by Laser-Produced Cavitation Bubbles Near Solid Boundaries*, J. Acoust. Soc. Am. **84**, pp719-731.
- [8] Sigrist, M. W. and Kneubuhl, F. K. (1978) - *Laser-Generated Stress Waves in Liquids*, J. Acoust. Soc. Am. **64**, pp1652-1663.
- [9] Davidson, G. and Emmony, D. C. (1980) - *A Schlieren Probe Method for the Measurement of the Refractive Index Profile of Shock Wave in a Fluid*, J. Phys. E: Sci. Instrum. **13**, pp92-97.
- [10] Ward, B. and Emmony, D. C. (1990) - *The Energies and Pressures of Acoustic Transients Associated with Optical Cavitation*, J. Mod. Opt. **37**, pp803-811.
- [11] Sommerfeld, A. (1909 & 1926) - *Über die Ausbreitung der Wellen in der drahtlosen Telegraphie*, Ann. Physik **28**, pp665, & **81**, pp1135.
- [12] Strutt, J. W. (Lord Rayleigh) (1945) - *The Theory of Sound*, Volume II, Published by Dover Publications / The Macmillan Company, pp78-86.
- [13] Officer, C. B. (1958) - *An Introduction to the Theory of Sound Transmission, with Application to the Ocean*, Published by McGraw-Hill book company, pp185-188.
- [14] Brekhovskikh, L. (1960) - *Waves in Layered Media*, Published by Academic Press, pp234.
- [15] Piquette, J. (1988) - *Spherical Waves Scattering by a Finite-Thickness Solid Plate of Infinite Extent, With Some Implications for Panel Measurements*, Acoust. Soc. Am. **83**, pp1284-1294.
- [16] as reference [13], p126-127
- [17] as reference [14], p292-295
- [18] Kynar data sheet, Supplied by AMP Piezo Film Sensors-Europe, Stanmore, UK.
- [19] Lancee, C.T. (1985) - *Ferro-electric ceramics versus polymer piezoelectric materials*, Ultrasonics, pp138-142.
- [20] Sessler, G.M. (1981) - *Piezoelectricity in Polyvinylidene fluoride*, J. Acoust. Am. **70**, pp1596-1608.
- [21] Arfken, G. (1985) - *Mathematical Methods for Physicists*, 3rd Edition, Published by Academic Press Inc., pp794-864.
- [22] Press, W. H., Teukolsky, S. A., Vetterling, W. T., and Flannery, B. P. (1992) - *Numerical Recipes in Fortran*, 2nd Edition, Published by Cambridge University Press.
- [23] Whittaker, Sir E., and Robinson, G. (1949) - *The Calculus of Observations, A Treatise on Numerical Mathematics*, 4th Edition, Published by Blackie & Son Ltd., pp285-296.

- [24] 1993 Data Book, Elantec Inc., pp2.50-2.63.
- [25] Dale, T. P. and Gladstone, J. H. (1858) - *On the Influence of Temperature on the Refraction of Light*, Phil. Trans. Roy. Soc. London **148**, pp887-894.
- [26] Gladstone, J. H. and Dale, T. P. (1863) - *Researches on the Refraction, Dispersion, and Sensitiveness of Liquids*, Phil. Trans. Roy. Soc. London **153**, pp317-343.
- [27] Waxler, R. M. and Weir C. E. (1963) - *Effect of Pressure and Temperature on the Refractive indices of Benzene, Carbon Tetrachloride, and Water*, Journal of Research of the National Bureau of Standards - A. Physics and Chemistry, **67A**, pp163-171.
- [28] Holder, D. W., and North, R. J. (1963) - *Schlieren Methods*, National Physical Laboratory Notes on Applied Science No. 31, Published by Her Majesty's Stationary Office.
- [29] Ward, B., and Emmony, D. C. (1990) - *Conservation of Energy in the Oscillations of Laser-Induced Cavitation Bubbles*, J. Acoust. Soc. Am. **88**, pp434-441.

Chapter Six

Conclusions and Further Work

This thesis has been concerned with the design and development of measuring devices for the characterisation of acoustic transients with high temporal and spatial resolution. Three new techniques have been demonstrated: high speed multiple exposure photography using a semiconductor laser, a highly sensitive optical transducer based upon changes in reflectivity at a solid-fluid interface, and a large area piezoelectric transducer for characterising spherically symmetric acoustic transients.

In chapter three it was demonstrated that a pulsed semiconductor laser can be used effectively in high speed photography as a flash light source capable of resolving acoustic transients. A multiple exposure system incorporating a Northern Telecom LJ30 semiconductor laser was built, and was used to photograph transients initiated by Rhodamine 6G Dye laser ablation in air, Nd-YAG laser assisted dielectric breakdown in air, and optical cavitation in water. The system was capable of producing up to 10 pulses of light at a maximum repetition rate of 5MHz with a timing accuracy of ~ 5 ns. Each of these semiconductor laser light pulses had a full width half maximum duration of 50ns, peak power of 30W, and wavelength of 860nm. A CCD camera was used to integrate several successive 'dark field' schlieren images, and the propagation of single acoustic transients were subsequently displayed on the same output picture.

The spatial resolution of the recorded images was found to be limited by the 50ns duration of the semiconductor laser pulses and the velocity of the acoustic transients. This resulted in the system having spatial resolutions of $17\mu\text{m}$ for air born acoustic transients, and $75\mu\text{m}$ for water born transients which propagate at speeds of 330ms^{-1} and 1500ms^{-1} respectively. Although capable of clearly resolving transients propagating in air, the system was not able to completely resolve the shock front of water born acoustic transients. A conclusion was made that improvements in the spatial and temporal resolution can only be made with shorter laser pulse durations. It is thought that this should be possible in the near future with further developments in semiconductor laser technology.

In summary the system has been proven to be very useful for investigating the development of single acoustic transients with time, provided that a dark field imaging technique such as schlieren is used. As a result the system allowed the study of events

which are either non-repetitive or are not repeatable. The experiments conducted showed that the semiconductor laser used is an excellent source for schlieren photography, and is compact, relatively cheap, very reliable and has simple low voltage electronic drive circuitry. Furthermore the technique has the potential to be applied in other high speed photographic diagnostic techniques including Interferometry, Electronic Speckle Pattern Interferometry (ESPI), and Particle Image Velocimetry (PIV). This not only allows the study of acoustic transients but also other fast moving mechanical phenomena such as cavitation, fluid flow in engines, ballistics and surface vibrations.

In chapter four an optical transducer was constructed to measure the temporal pressure profiles of acoustic transients. The device was based upon the measurement of the reflectance of a solid-liquid boundary, and used a probe beam which was incident close to the critical angle. The transducer was initially fabricated out of a semicircular perspex (PMMA) block which allowed the design to be assessed and proven experimentally. At a later stage the front face of the perspex block was machined back and replaced with glass which improved the sensitivity of the transducer to changes in refractive index, giving a better signal to noise. It did however have a non-linear response to pressure, which was found theoretically to fall off for more intense acoustic transients.

Experiments were performed which showed the optical transducer to be capable of accurately measuring the pressure profile of incident acoustic transients generated by an optical cavitation event, and able to resolve fully the sub 10ns rise time of the shock fronts. The pressure profiles measured agreed with those measured using other quantitative techniques such as Mach-Zehnder interferometry. In addition to characterising acoustic transients associated with optical cavitation, the device was also capable of detecting rarefaction waves resulting from phase inversion at a water-air interface.

It was found that the glass fronted transducer had a minimum resolvable pressure of about 20bar (2MPa), and temporal resolution of about 1ns which was limited primarily by the response of the photodiode detector. The device achieved a small sensitive area of just 20x80 μ m, which was limited by diffraction of the probe beam. Greater sensitivity could have been achieved with a more collimated beam, however at a cost of a larger sensitive area. Conversely a smaller measurement area and hence greater spatial resolution could have been achieved by using a more focused probe beam, but at the cost of sensitivity.

The asymmetric collapse of laser cavitation bubbles close to a solid boundary was also studied using the glass fronted transducer. The migration of the bubbles towards the interface was detected as a rise in the reflectance signal towards saturation, and the acoustic transients associated with the bubble collapses were also studied. A $10\mu\text{s}$ duration increase in stress at the transducer interface was also detected for a bubble which grew to a maximum radius of 1.1mm, and was generated 0.7mm from the transducer. This agrees with results obtained by other authors, and this has been attributed to a water jet forming within the bubble which hits the transducer surface.

Furthermore the optical transducer was redesigned to incorporate an equilateral glass prism. A new front face was machined on the prism such that probe beam light was reflected close to the critical angle of the interface, and this face formed the boundary at which reflectivity measurements were made. The new design allowed the probe beam preparation optics and the photodiode to be placed neatly behind the prism, and the compact nature of the device allowed it to be fully enclosed making it commercially viable as a transducer. Although the device was demonstrated to work in principle, time did not permit it to be used for the measurement of acoustic transients, and this is suggested for further work.

In chapter five a technique for measuring spherically symmetric acoustic transients in water was demonstrated using a relatively large area planar Polyvinylidene-fluoride (PVDF) film piezoelectric transducer. This was achieved by first modelling the propagation of such a wave through the media involved. The transducer was considered to be made up of a large number of small elements which were shaped according to the locus of the transient at different points in time. Each element was considered to measure only the component of pressure normal to the film of a small section of the acoustic transient which is within the transducer, and the output voltage was then calculated as a summation of all of these pressure components.

Simulations were then performed using the theory developed. The output voltages of several piezoelectric transducers with different film thicknesses were calculated for incident spherical acoustic transients with step-like pressure profiles. It was found that the rise time of the voltage is dependant upon the duration of the transient, and the propagation time of the leading edge of the transient across the thickness of the transducer. The fall off in the voltage was however found to be very much longer and followed an inverse time relationship. This was attributed to an annular shaped portion of the transient remaining inside the transducer even after the leading edge has left the transducer. The reverse process of calculating the temporal pressure profile of spherical

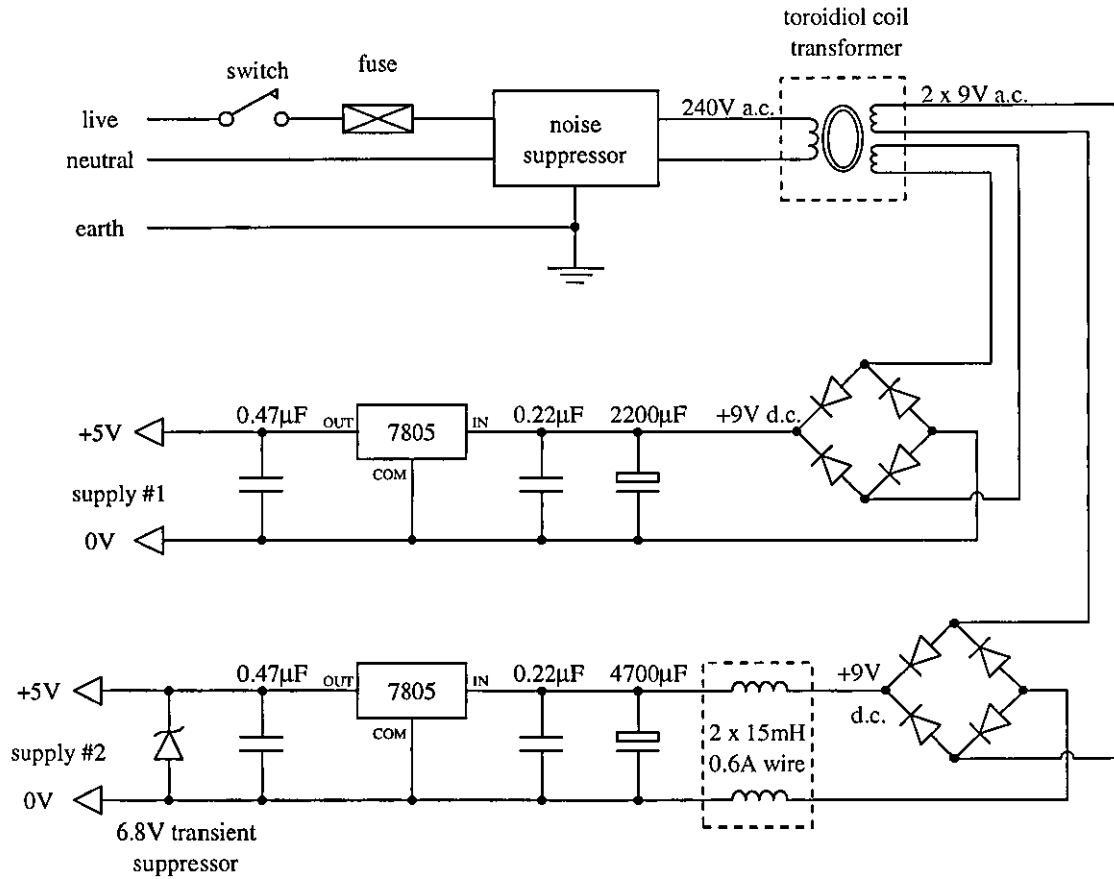
acoustic transients from measured voltage traces was also simulated. It was found that the problems of signal noise and under-sampling of the measured voltage are significantly increased during the inversion process, particularly for thick film transducers. These effects were reduced somewhat by the application of graduation algorithms to the measured voltage, however it was found that there is a trade off between the temporal and spatial resolution of the derived pressure profile.

The inversion process developed was also used to determine the temporal pressure profiles of spherically symmetric acoustic transients created experimentally during optical cavitation. Measurements were made using two thin film polyvinylidene-fluoride transducers with different film thicknesses, which were placed at a range of distances away from the source. The results obtained showed that the temporal pressure profiles of the acoustic transients could be accurately resolved when a relatively thin transducer film is used, and the derived profiles agreed with those measured earlier using the prototype optical transducer. It was however found to be quite difficult to deduce the pressure profiles of the acoustic transients using a thick film transducer, and it was thought that this was due to the anisotropic behaviour of the piezoelectric material used. It was suggested that for further work these effects could be studied in greater detail, and appropriate improvements made to the piezoelectric transducer model which has been developed.

Finally the technique described here addresses the problem of characterising transients that originate from sources which are smaller than the measuring device. The conclusion has been made that if the spatial shape, or symmetry, of an acoustic transient is known as it propagates through a medium, then its pressure-time profile can be derived from the voltage signal measured by a relatively large planar piezoelectric transducer. As a result it is thought that this technique can be extended to systems with other symmetries, such as laser generated cylindrically symmetric acoustic transients, and further investigation into this has been recommended.

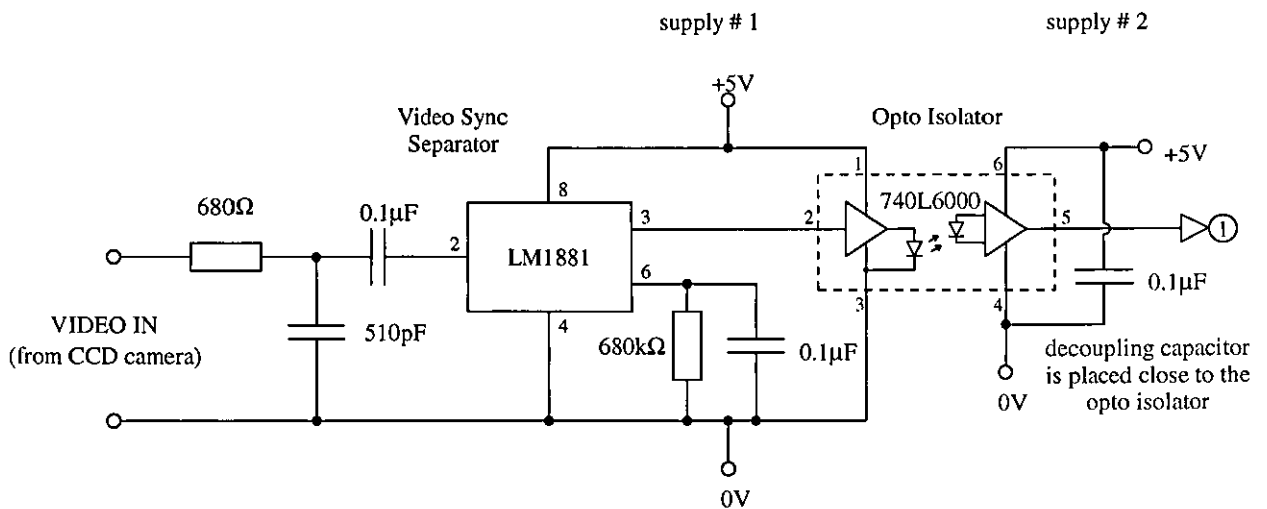
Appendix One - Digital Timing Circuitry

A1.1 - Power supply.



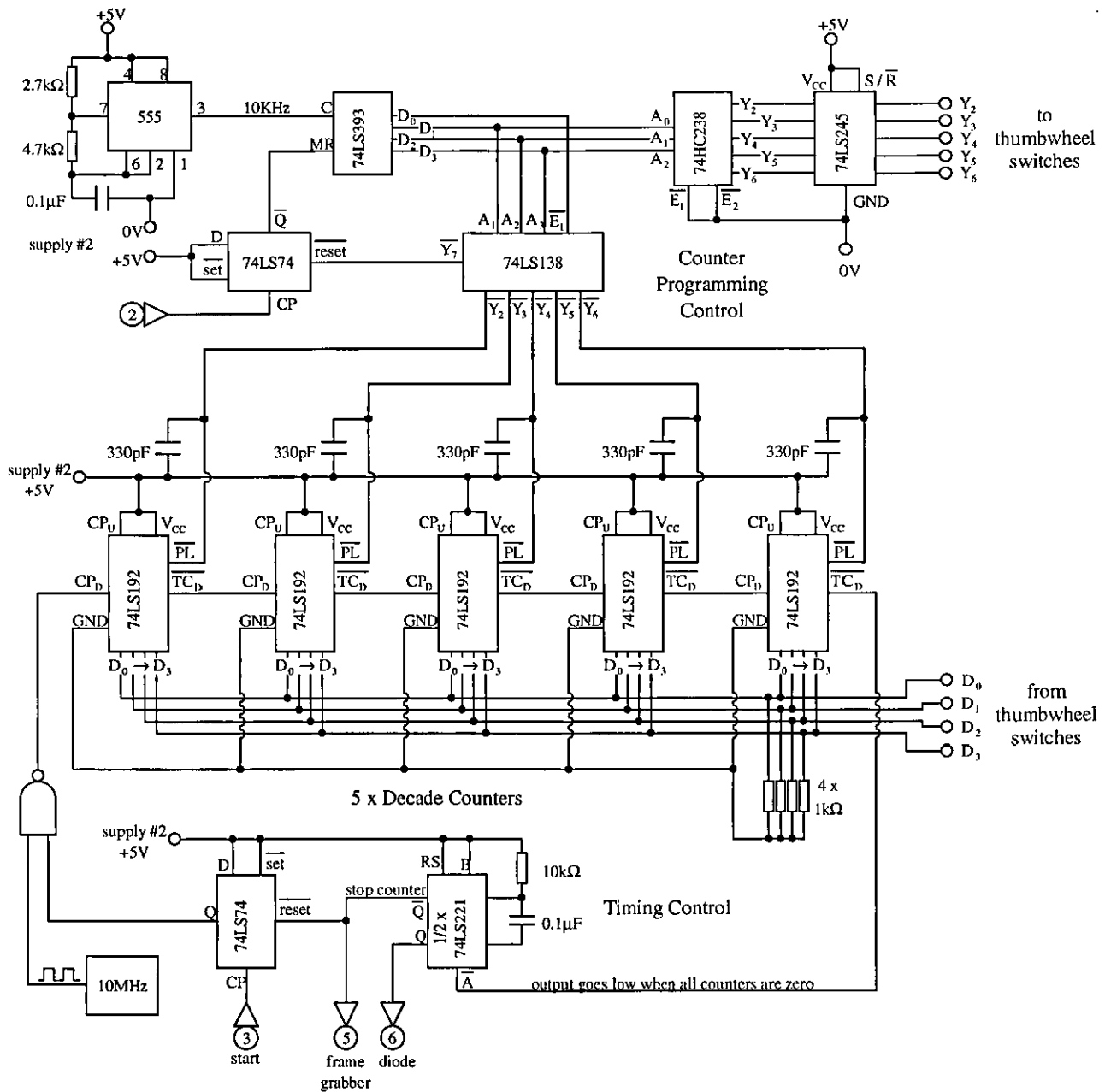
Note: Both supplies are isolated from earth to avoid earth loops in supply #1. This is due to the inputs are common to 0V on supply #1, and avoids transmitting noise through to supply #2.

A1.2 - Video sync. separation and detection circuit with optical isolator.

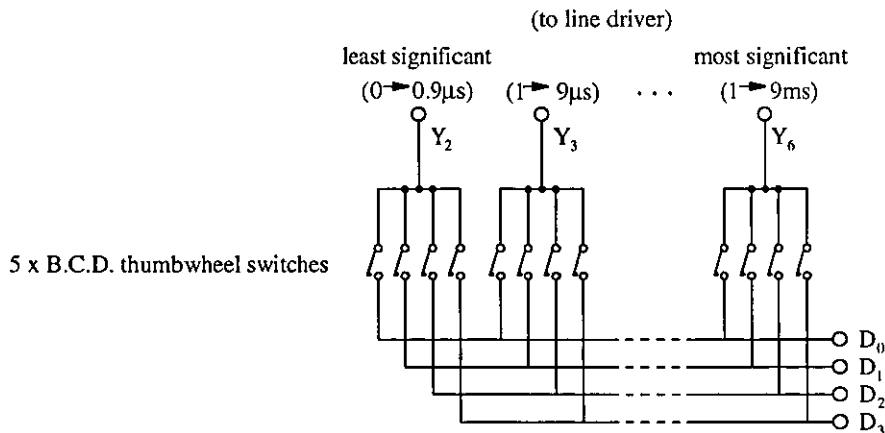


Note : Output ① gives opto isolated vertical sync signal for synchronisation of timing circuitry to CCD camera.

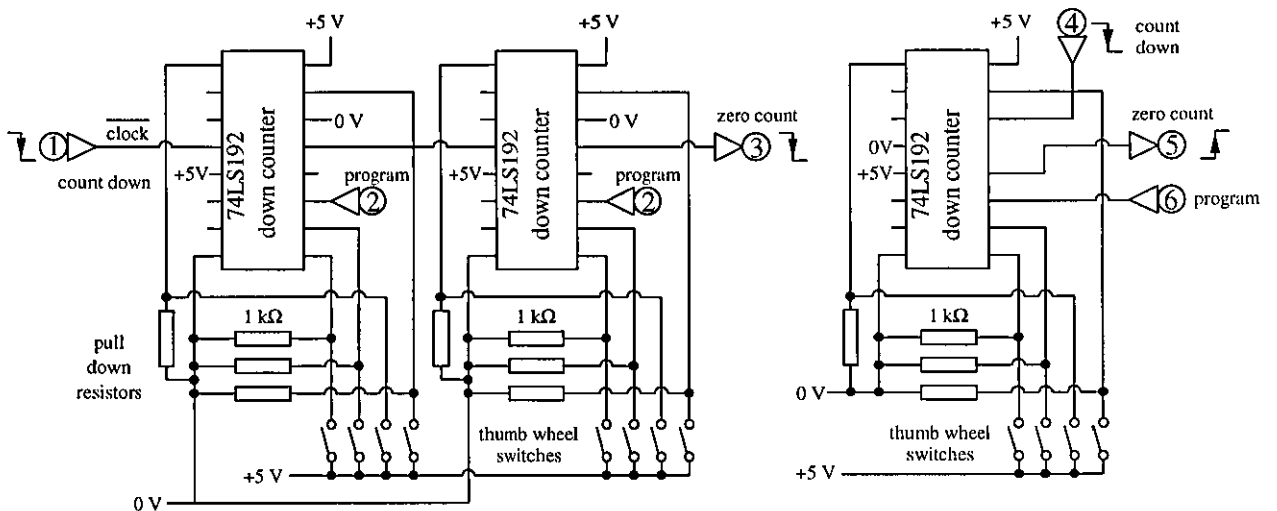
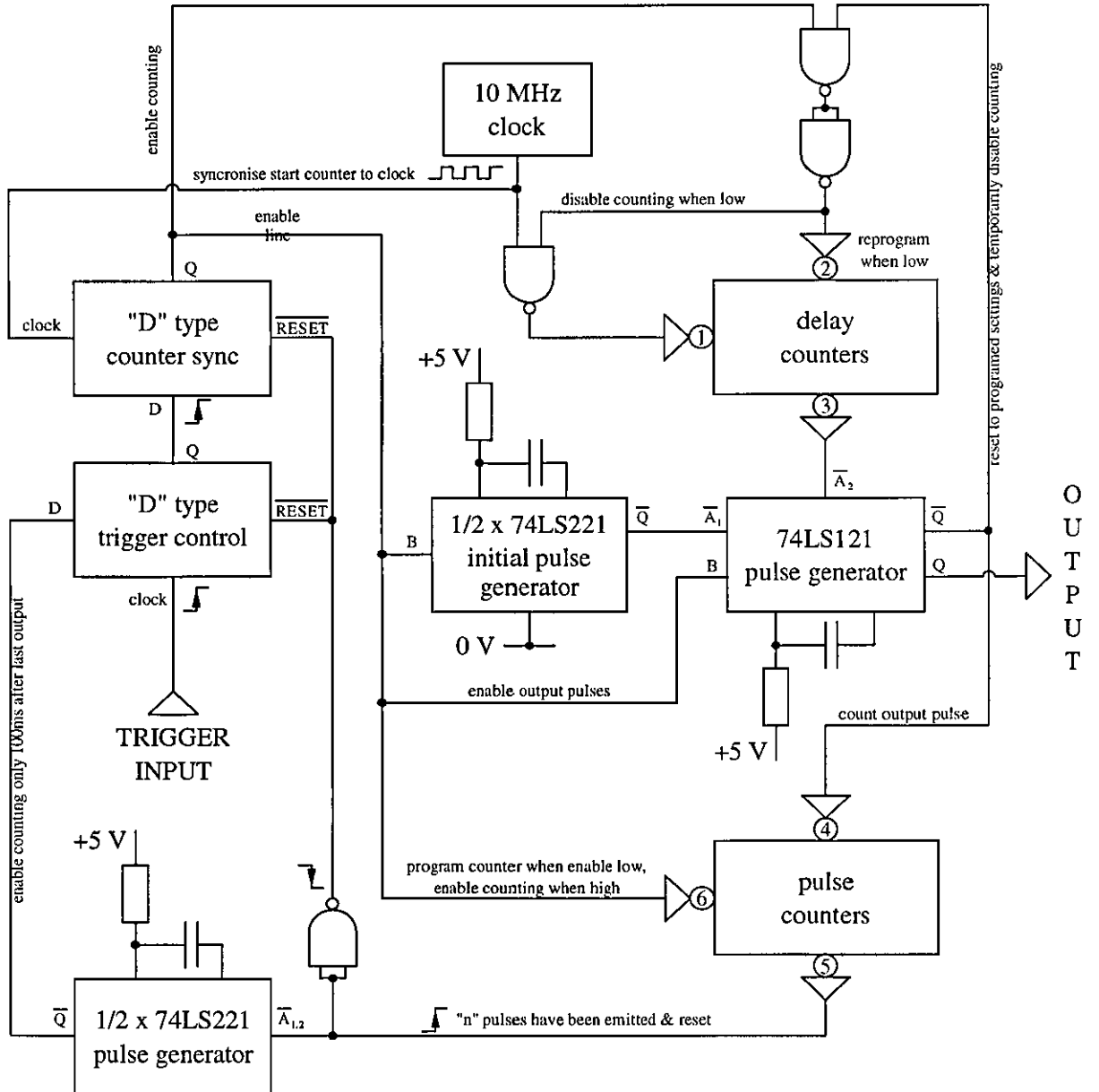
A1.6 - Digital delay circuit.



A1.7 - BCD thumbwheel switches.



A1.8 - Multiple pulse timing circuitry.



Appendix Two - Maple Routines

A2.1 - Pwav(Tar1,pc1,pc2,S)

Maple routine for plotting voltage or pressure values entered in array 'Tar1' against time in intervals of 2ns. The output is a plot viewed between two points in time defined by 'pc1' and 'pc2'. This is displayed as a series of points if the value of 'S' is 'P', otherwise as a line.

```
> Pwav:=proc(Tar1,pc1,pc2,S) local temp,n,N2,N;
> N:=nops(Tar1); N2:=round(pc2*N): temp:=array(1..2*N2):
> for n from 1 to N2 do temp[2*n-1]:=(n-1)/(N-1)*N*2: temp[2*n]:=Tar1[n]: od:
> if S='P' then RETURN(plot(convert(temp,list),pc1*N*2..pc2*N*2,style=POINT));
> else RETURN(plot(convert(temp,list),pc1*N*2..pc2*N*2,style=LINE)); fi; end;
```

A2.2 - filter(xx,d,a)

Maple routine describing the behaviour of a spherically shaped element of an acoustic transient incident on a large planar piezoelectric transducer. The value of 'xx' represents the time (or distance) that the element has travelled from the source. The parameters 'd' and 'a' represent in time units the distance that the transducer is away from the source and the transducer film thickness respectively. For example, if the transducer is made out of PVDF, is 9µm thick and is placed 1mm from the point source (in water) then $d=1(\text{mm})/1.5(\text{mm}/\mu\text{s})=665\text{ns}$ and $a=9(\mu\text{m})/2.2(\text{mm}/\mu\text{s})=4\text{ns}$.

```
> filter:=proc(xx,d,a) local x;
> x:=xx+d:
> if x<d then RETURN(0); elif x<d+a then RETURN(x*(1-d^2/x^2));
> else RETURN( (((d+a)^2-d^2)/x) ); fi; end;
```

A2.3 - Invert(tar1,pc1,pc2,d,a)

This maple routine deconvolves the voltage entered as an array 'tar1' using the 'filter(xx,d,a)' function above. Each array value constitutes a voltage measurement in 2ns steps. The output is in terms of an array and represents the pressure profile in relative values, also in 2ns steps. The parameters 'd' and 'a' are as in A2.2.

```
> Invert:=proc(tar1,pc1,pc2,d,a) local tx,temp,res,n,m,ofs,N;
> N:=nops(tar1): temp:=array(1..N): res:=array(1..N): ofs:=tar1[1]:
> for n from 1 to N do temp[n]:=tar1[n]-ofs: res[n]:=0: od:
> for n from 1 to round(N*pc2) do res[n]:=temp[n]/(filter(2,d,a)):
>   for m from (n+1) to round(N*pc2) do
>     tx:=2*(m-n)+2: temp[m]:=temp[m] - (res[n]*filter(tx,d,a)); od:
> od: RETURN(eval(convert(res,list))): end;
```

A2.4 - Test(a,N,t0)

Maple routine that simulates the voltage generated by a piezoelectric transducer, in $2ns$ steps, for a step pressure profile of duration 't0'. The transducer of thickness 'a' is placed a distance 'd' from the point source, both of these parameters being expressed in time units (see A2.2.)

```
> Test:=proc(d,a,N,t0) local n,m,tar,t0a;
> tar:=array(1..N): t0a:=round(t0/2);
> for n from 1 to N do tar[n]:=sum('filter((n-m)*2,d,a)',m=1..t0a); od:
> RETURN(eval(convert(tar,list))); end:
```

A2.5 - SpencerSmooth(T)

This subroutine takes a list of numbers 'T', say the voltage values with time, and graduates them using Spencer's Formulae. (See "The Calculus of Observations - A Treatise on Numerical Mathematics" by Sir Edmund Whittaker and G. Robinson, Fourth Edition 1949, page 290.)

```
> Smoothy:=proc(T) local n,N,TA,TB,i;
> N:=nops(T): TA:=array(1..N): TB:=array(1..N+20); for n from 1 to N do
  TB[n+10]:=T[n]: od:
> for n from 1 to 10 do TB[n]:=TB[11]: TB[N+10+n]:=TB[N+10]: od:
> for n from 11 to N+10 do
> TA[n-10]:= (60*TB[n] + 57*(TB[n-1]+TB[n+1]) + 47*(TB[n-2]+TB[n+2])
  + 33*(TB[n-3]+TB[n+3]) + 18*(TB[n-4]+TB[n+4]) + 6*(TB[n-5]+TB[n+5])
  - 2*(TB[n-6]+TB[n+6]) - 5*(TB[n-7]+TB[n+7]) - 5*(TB[n-8]+TB[n+8])
  - 3*(TB[n-9]+TB[n+9]) - (TB[n-10]+TB[n+10]) )/350; od:
> RETURN(eval(convert(TA,list))); end:
```

A2.6 - LeastSqr(kk,nn)

Maple subroutine returning coefficients of a polynomial that is fitted to a list of unknown data points using the method of least squares. The number of data points 'N' is entered in terms of 'nn' where $N=2*nn+1$, and the degree of the polynomial to be fitted as 'kk'. Note that N should always be larger than $kk+1$. It is used with the maple routine 'LSqrSmooth' found in A2.7. (See "The Calculus of Observations - A Treatise on Numerical Mathematics" by Sir Edmund Whittaker and G. Robinson, Fourth Edition 1949, pages 291-296; and also "Applied Numerical Analysis" by C.F. Gerald, Second Edition 1970, pages 81-86 & 468-474.)

```
> with(linalg):
> LeastSqr:=proc(kk,nn) local N,aa,bb,cc,k1,k2,m,values:
> N:=nn*2+1: aa:=array(1..(kk+1),1..(kk+2)): values:=array(1..(nn+1)):
> for k1 from 0 to kk do
> for k2 from 0 to kk do
```

```

> if k1=0 and k2=0 then aa[1,1]:=N:
> else
> aa[k1+1,k2+1]:=sum(m^(k1+k2),m=-nn..nn):
> fi: od:
> aa[k1+1,kk+2]:=sum(m^k1*y[m],m=-nn..nn): od:
> bb:=gausselim(aa);
> cc:=backsub(bb)[1];
> for k1 from 0 to nn do values[k1+1]:=coeff(cc,y[k1]): od:
> RETURN(eval(values)); end:

```

A2.7 - LSqrSmooth(T,kk,nn)

*This routine graduates a list of data points 'T' by applying a Least Squares fitted polynomial algorithm calculated using the 'LeastSqr' subroutine found in A2.6. The degree of the polynomial used is entered as 'kk', and the number of points covered by the graduation algorithm 'N' is controlled by parameter 'nn' where $N=2*nn+1$.*

```

> Smoothing:=proc(T,kk,nn) local n,m,N,TA,TB,equ;
> N:=nops(T): TA:=array(1..N): equ:=array(1..nn+1);
> equ:=LeastSqr(kk,nn):
> TB:=array(1..(N+(2*nn))); for n from 1 to N do TB[n+nn]:=T[n]: od:
> for n from 1 to nn do TB[n]:=TB[nn+1]: TB[N+nn+n]:=TB[N+nn]: od:
> for n from nn+1 to N+nn do
> TA[n-nn]:=sum(equ[m+1]*(TB[n-m]+TB[n+m]),m=1..(nn)) + equ[1]*TB[n];
> od: RETURN(eval(convert(TA,list))): end:

```

A2.8 - Noise Example Program.

This program illustrates the problems encountered with low resolution voltage values.

```

> V:=Test(665,110/2.2,160,50):
Create a perfect 50ns step pressure pulse and calculate the simulated voltage, as a list in 2ns intervals, for a 110µm thick transducer placed 1mm from the source.
> mx:=max(op(V)); V256:=array(1..nops(V)):
> for m from 1 to nops(V) do V2[m]:=256*round(V[m]/mx): od:
> V256:=convert(eval(V2),list):
Reduces the accuracy of the voltage values to 256 bit resolution.
> Vspen:=eval(V256): for m from 1 to 2 do Vspen:=SpencerSmooth(Vspen): od:
Apply Spencer's graduation formula twice to the reduced resolution voltage.
> display({Pwav(Vspen,0,0.7,P),Pwav(V256,0,0.7,L)});
Compare the reduced resolution simulated voltage with the voltage graduated by Spencer's formula on a graph.
> Res:=Invert(V,0,1,665,110/2.2):
Perform the inverse transform or deconvolution on the "perfect" simulated voltage.
> Res256:=Invert(V256,0,1,665,110/2.2):
Perform deconvolution on the reduced resolution simulated voltage.

```

```
> ResSpn:=Invert(Vspen,0,1,665,110/2.2):
Perform the inverse transform on the graduated voltage.
> display({Pwav(Res,0,1,L),Pwav(ResSpn,0,1,P)});
Display the pressure profile calculated from the simulated "perfect" voltage together
with the pressure profile derived from the graduated voltage.
> display({Pwav(Res,0,0.7,P)});
Display the noisy pressure profile derived from the reduced resolution voltage.
```

A2.9 - Example Deconvolution Program

This program reads in experimentally measured voltage data points from a file, graduates them, deconvolves them, and finally plots a graph of the resulting pressure profile.

```
> read(volts); V:=convert(evalm(Volts-Volts[200]),list):
Read in data file 'volts' containing an array 'Volts' of experimentally measured voltage
values and converts them into a list of data values 'V' with zero volts set at the 200th
value of 'Volts'.
> Pwav(V,0,0.5,L):
Plot a graph of the experimentally measured voltage (see A2.1.)
> n:=190: VV:=array(1..n): o:=200: for m from 1 to n do VV[m]:=V[m+o]: od:
> VV:=convert(evalm(VV),list): VV1:=eval(VV):
Select a smaller range of voltage values (190 of them, starting at 200th value of 'V') and
store them in array 'VV', then convert 'VV' to a list and duplicate it in 'VV1'.
> for m from 1 to 6 do VV1:=LSqrSmooth(VV1,2,2): od:
Graduate voltage list 'VV1' using 6 applications of a 5 point 2nd order least squares
formula (see A2.6 and A2.7.)
> display({Pwav(VV,0,1,P),Pwav(VV1,0,1,L)},view=[0..380,-0.05..3.2]);
Plot a graph comparing the graduated voltage with the original voltage values.
> Res:=Invert(VV1,0,1,665,9/2.2):
Deconvolve the graduated voltage values for 9µm thick transducer placed 1mm from
source (see A2.2 and A2.3.)
> display({Pwav(Res,list),0,1,P},Pwav(Res,list),0,1,L));
Finally display a graph of the pressure profile calculated from the graduated voltage.
```

Appendix Three - Photographs

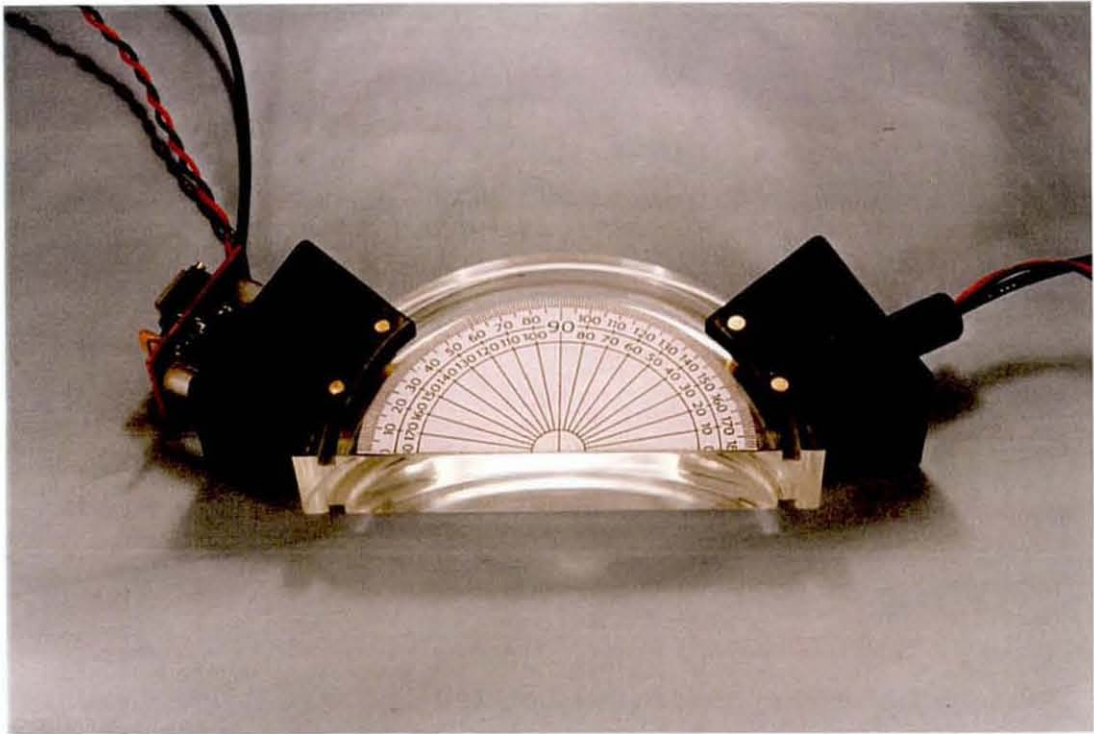


Figure A3.1 - Photograph of the prototype perspex semicircular optical transducer.

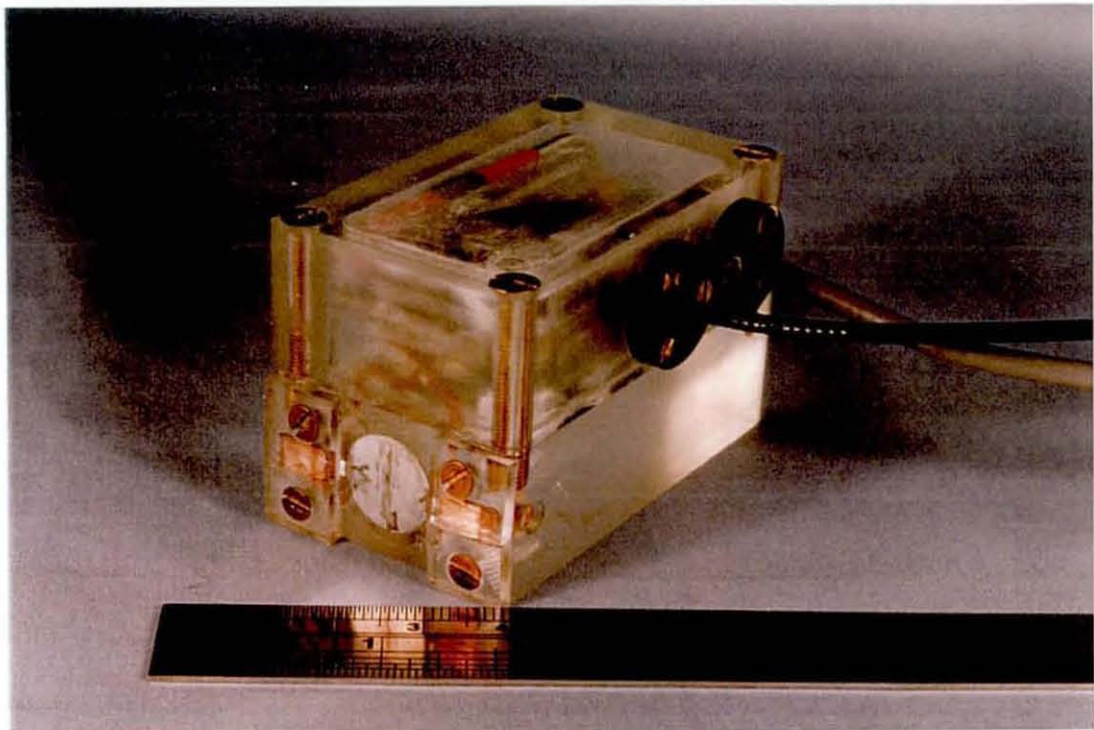


Figure A3.2 - Photograph of the large area piezoelectric transducer with the high impedance amplification electronics attached.

